

DETERMINING THE DYNAMIC SCALES OF THE BOUNDARY LAYER AND
FLOW SEPARATION INCEPTION:
ANALYSIS TOWARDS EFFICIENT FLOW CONTROL

A Dissertation

Submitted to the Faculty

of

Purdue University

by

Jorge Saavedra Garcia

In Partial Fulfillment of the
Requirements for the Degree

of

Doctor of Philosophy

December 2018

Purdue University

West Lafayette, Indiana

**THE PURDUE UNIVERSITY GRADUATE SCHOOL
STATEMENT OF DISSERTATION APPROVAL**

Dr. Guillermo Paniagua, Chair

School of Mechanical Engineering

Dr. Jonathan Poggie

School of Aeronautics and Astronautics

Dr. Amy Marconnet

School of Mechanical Engineering

Dr. Sally Bane

School of Aeronautics and Astronautics

Dr. John Clark

Air Force Research Laboratory

Approved by:

Dr. Jay P. Gore

Head of the School Graduate Program

To my family, thank you for your support, without you none of this would have
been possible.

ACKNOWLEDGMENTS

The copyright of part of the material presented in the chapters 3 and 5 belongs to ASME and has been presented in Transient Performance of Separated Flows: Characterization and Active Flow Control, Journal of Engineering for Gas Turbine and Power, Vol.141(1) 2018 [DOI: 10.1115/1.4040685]

The copyright of part of the material presented in the Chapter 2 belongs to ASME and has been presented in Thermal Boundary Layer Response to Periodic Fluctuations for Turbulent Flow, Journal of Engineering for Gas Turbine and Power, [DOI: 10.1115/1.4041138]

The copyright of part of the material presented in the Appendix D.4 belongs to ASME and has been presented in Experimental Characterization of the Vane Heat Flux Under Pulsating Trailing-Edge Blowing, Journal of Turbomachinery Vol.139,(6) 2017 [DOI: 10.1115/1.4035211]

The material presented in this dissertation is based upon work supported by the Air Force Office of Scientific Research, Air Force Material Command, USAF under Award No. FA9550-16-1-0120. Computer time for the direct numerical simulations presented in section 2.4 was provided by the Air Force Research Laboratory DoD Supercomputing Resource Center.

I would like to also thank all the members of the Purdue Experimental Turbine Aero-thermal Lab who contributed to the commissioning the facility and the integration of the data acquisition system.

TABLE OF CONTENTS

	Page
LIST OF TABLES	viii
LIST OF FIGURES	x
SYMBOLS	xx
ABBREVIATIONS	xxiv
ABSTRACT	xxv
1 INTRODUCTION	1
1.1 Motivation and Bibliographic Review	1
1.2 Research Objectives	6
1.3 Research methodology	7
1.4 Dissertation guideline	9
2 BOUNDARY LAYER RESPONSE TO MEAN FLOW VARIATIONS	11
2.1 Strategy	16
2.2 Sudden flow acceleration	26
2.3 Periodic mean flow oscillations	34
2.4 Detailed simulation on the boundary layer reaction to sudden flow acceleration	51
2.4.1 Description of numerical approach	51
2.4.2 Boundary layer and wall fluxes evolution after sudden flow ac- celeration	60
2.4.3 Free-stream transient evolution impact on near wall region eval- uation	67
3 TRANSIENT PERFORMANCE OF SEPARATED FLOWS	85
3.1 Methodology	90
3.2 Separated flow region reaction to sudden flow start-up	104
3.3 Flow separation performance under fluctuating inlet conditions	109

	Page
4 EMPIRICAL ANALYSIS OF MEAN FLOW ACCELERATION IMPACT ON THE BOUNDARY LAYER DETACHMENT	118
4.1 Wind tunnel design and operation	118
4.2 Wind tunnel flow conditioning	121
4.2.1 Flow discharge into the settling chamber	125
4.2.2 Stilling section	128
4.2.3 Honeycomb	128
4.2.4 Contraction area	132
4.2.5 Detailed analysis of the 3D flow features	141
4.2.6 Experimental assessment of the facility flow conditioning . . .	149
4.3 Facility Calibration	161
4.3.1 Calibration methodology	163
4.3.2 Experimental characterization of the performance envelope . .	167
4.3.3 Experimental envelope comparison to isentropic performance model	168
4.3.4 Uncertainty Analysis	169
4.4 Test article design and instrumentation	172
4.4.1 Test article design	172
4.4.2 Test article assembly and instrumentation	178
4.5 Steady State Performance of Flow Separation Domain	182
4.6 Flow separation performance under sudden flow discharge	192
5 FLOW SEPARATION CONTROL THROUGH TRANSIENT SUCTION AND INJECTION	202
6 CONCLUSION	217
REFERENCES	221
A Fluent Validation	236
A.1 Unsteady strong interactions in a turbine transonic turbine	236
A.2 Sod Shock Tube Validation	236
B Domain numerical discretization	239

	Page
B.1 Isothermal Flat Plate domain verification	239
B.2 Isothermal separation domain verification	240
C Momentum Integral Equations reduction	242
D Instruments Calibration and Uncertainty Evaluations	247
D.1 Pressure sensor calibration and drift pressure correction	247
D.2 Hotwire calibration	248
D.3 Thermocouple calibration	249
D.4 Heat transfer calculation	251
D.4.1 One-Dimensional Numerical Heat Flux Approach to Solve Con- duction	251
D.4.2 Adiabatic Convective Heat Transfer Coefficient	254
D.5 Uncertainty Evaluation	256
VITA	267

LIST OF TABLES

Table	Page
2.1 Grid convergence analysis	19
2.2 Range of Strouhal numbers analyzed	37
2.3 Mean values during the periodic excitation	40
2.4 Maximum amplitude of the oscillations during the periodic excitation	40
2.5 Steady Initial and Final flow conditions	55
2.6 Mesh sensitivity for 2D URANS simulations	58
2.7 DNS vs URANS for steady flow conditions	59
3.1 Boundary conditions for $Re/\rho, 8.9 \times 10^5$	93
4.1 Pressure loss coefficient of different honeycomb cross sectional configurations	129
4.2 Contractions shape performance	137
4.3 Contractions shape performance	139
4.4 Turbulence, integral length scale and dissipative length scale at various Reynolds	154
4.5 Facility performance envelope calibration sensors absolute uncertainty	170
4.6 Mach number uncertainty during facility calibration experiments	171
4.7 Reynolds uncertainty during facility calibration experiments	172
4.8 Reported Experimental points	183
5.1 Flow momentum deficit driving the flow detachment	204
5.2 Dynamic pressure loss for various inlet frequencies	206
5.3 Dynamic pressure loss for various injection total pressure amplitudes keeping a constant upper level	211
5.4 Dynamic pressure loss for various injection total pressure amplitudes keeping a constant upper level	214
D.1 Material properties	252
D.2 Sensors Uncertainty	258

Table	Page
D.3 Massflow Uncertainty	259
D.4 Reynolds Uncertainty	260
D.5 Stream wise velocity Uncertainty	261
D.6 Hotwire Calibration A factor	262
D.7 Hotwire Calibration n factor	263
D.8 U from Hotwire Calibration	264
D.9 Heat Flux Calibration	265
D.10 Adiabatic Heat Transfer Coefficient Calibration	266

LIST OF FIGURES

Figure	Page
1.1 a) Boundary layer establishment following an impulsive start; b) Experimental testing of a blowdown process; c) Boundary layer establishment after the passage of a shock wave.	3
1.2 Flow field and wall fluxes evolution during a blow down start-up	4
1.3 Momentum boundary layer development after the passage of a pressure wave front	5
2.1 a) Numerical domain for URANS flow acceleration research; b) Inlet total pressure profile for sudden flow acceleration analysis; c) Inlet total pressure profile for periodic perturbation analysis	17
2.2 a) Axial velocity at (0.4,0.07) for different mesh resolutions; b) Grid convergence indicator	18
2.3 a) Free stream axial velocity evolution; b) Wall shear stress evolution: during a sudden flow acceleration	27
2.4 a) Inlet total pressure profile for instantaneous discharge analysis; b) Acoustic characteristics propagation in a domain with discharge to low pressure reservoir	28
2.5 Total pressure, characteristics and axial velocity evolution after a total pressure step.	29
2.6 a) Free stream axial velocity b) Skin friction coefficient c) Heat flux: evolution during a flow acceleration after characteristics delay correction	30
2.7 Momentum boundary layer profile at different acceleration phases for both steady and transient evaluation	31
2.8 Thermal boundary layer profile at different acceleration phases for both steady and transient evaluation	32
2.9 Diffusion delay across the boundary layer a) Wall shear stress establishment delay; b)Boundary layer profile; c) Turbulent viscosity distribution across the near wall flow region	34

Figure	Page
2.10 a) Drag coefficient evolution during the transient simulation; b) Drag coefficient representation for two consecutive periods after convergence; c) Cross correlation factor between two consecutive periods after convergence	35
2.11 Flow and wall fluxes response to periodic excitation at $x/L = 0.5$: a) Axial free stream velocity b) Static pressure c) Skin friction coefficient d) Heat transfer coefficient e) Acceleration parameter	39
2.12 Static pressure contour along the domain, a) 5Hz excitation; b) 100 Hz excitation	41
2.13 Axial velocity contour along: a) Aggressive flow expansion through a nozzle contour; b) Flat plate configuration	43
2.14 Acceleration parameter effect on the aero-thermal boundary layer: a) Acceleration parameter b) Skin friction c) Heat transfer coefficient	44
2.15 Boundary layer profiles at several axial locations for flat plate and sudden expansion domain (black and blue respectively)	45
2.16 Wall non-dimensional boundary layer profiles at several axial locations for flat plate and sudden expansion domain (black and blue respectively)	46
2.17 a) Numerical replication of experimental test section for boundary layer reverse transition validation b) Velocity magnitude contour along the simulated test section c) Skin Friction coefficient over test article	48
2.18 Boundary layer displacement thickness temporal evolution at $x/L = 0.5$ for various excitation frequencies	49
2.19 Momentum boundary layer profiles evolution along the excitation period, transient periodic excitation and quasi-steady comparisons	49
2.20 Thermal boundary layer profiles evolution along the excitation period, transient periodic excitation and quasi-steady comparisons	50
2.21 Direct Numerical Simulations numerical domain	53
2.22 Inlet boundary conditions; a) P_0 transient profile, b) Initial momentum boundary layer, c) Initial thermal boundary layer	54
2.23 Boundary layer transition enhancement through the addition of a momentum source that mimics the presence of an obstacle	56
2.24 Steady State Comparison DNS vs URANS for initial and final conditions	59
2.25 2D contour of density along center plane for several time steps along the transient evolution	61

Figure	Page
2.26 Temporal evolution of free-stream flow conditions through the transient for DNS, laminar and URANS simulations; a) Axial free-stream velocity, b) Flow acceleration parameter, c) Local flow acceleration	62
2.27 Acoustic propagation of flow characteristics driving the flow acceleration	63
2.28 Impact of mean flow sudden acceleration on wall fluxes for DNS, laminar and URANS evaluations; a) Heat flux evolution, b) Stream-wise wall shear stress at L^*	64
2.29 Near wall flow region temporal evolution through the flow acceleration for DNS, laminar and URANS simulations; a) Boundary layer momentum thickness, b) Integral flow momentum inside of the boundary layer along the transient at L^*	65
2.30 Boundary layer profiles during the sudden flow acceleration a) Inner units axial velocity, b) Stream-wise velocity profile in outer units, c) Density profile d) Non-dimensional temperature profile	66
2.31 Wall normal velocity at different instances during the acceleration	67
2.32 Turbulent and laminar boundary layer evolution after a sudden flow acceleration based on Rayleigh flow start-up assumption	72
2.33 Evaluation of similarity based on the URANS simulations at three different axial locations, $x=0.6$, $x=0.7$ and $x=0.8$; a) Stream-wise velocity, b) Flow density, c) Boundary layer momentum thickness	74
2.34 Momentum Integral Equation terms order of magnitude evaluation	76
2.35 Integral Reynolds Stress across the boundary layer during the sudden flow acceleration	77
2.36 Reduced Momentum Integral Equation terms order of magnitude evaluation	78
2.37 Boundary layer ratios throughout the transient	78
2.38 Free-stream conditions input for simplified model evaluation; a) Stream-wise velocity, b) Gas density, c) Static Pressure	80
2.39 Simplified model prediction of the boundary layer transient evolution 10 ms	80
2.40 Simplified model prediction of the boundary layer transient evolution 25 ms	81
2.41 Skin friction prediction correction based on boundary layer transient evolution, a) 10 ms transient, b) 25 ms transient	83

Figure	Page
2.42 Reynolds analogy application to find the transient evolution of the heat transfer coefficient after the sudden flow acceleration	84
3.1 Domain generation for flow separation dynamic scales analysis: a) Geometry definition based on Bezier curve; b) Slope distribution along the test article; c) Curvature distribution along the hump surface	91
3.2 2D numerical domain for flow separation dynamics investigation	92
3.3 Separation domains axial velocity contours at $Re/m\ 8.9 \times 10^5$	94
3.4 Test article 11 performance at $Re/m\ 1.1 \times 10^6$ a) Free Stream Axial Velocity; b) Acceleration Parameter; c) Skin Friction coefficient along hump domain	95
3.5 Boundary layer profiles for different axial position along the flow separation domain	96
3.6 2D numerical domain for flow separation dynamics at $Re/m\ 1.1 \times 10^6$	97
3.7 Mesh sensitivity analysis: a) Grid convergence index, b) Momentum boundary layer profiles at various axial locations: 0.15, 0.3 and 0.45 m; c) Wall shear stress evolution along the hump surface	99
3.8 Validation of the numerical methodology on separated flow aero-thermodynamics	100
3.9 Large Eddy Simulations numerical domain for separated flow dynamics analysis	104
3.10 a) Inlet boundary condition for sudden flow acceleration; b) Inlet boundary condition for periodic flow perturbation; c) Massflow through the domain and d) drag coefficient during the sudden flow acceleration	106
3.11 Free stream, wall fluxes and separated region evolution during the sudden flow acceleration	107
3.12 Axial velocity contours at various instances during the blowdown compared to steady evaluations along the transient	109
3.13 Mean flow, separated region and wall fluxes evolution at various excitation frequencies	111
3.14 Axial velocity profiles at various instances during the periodic disturbance at $x=0.25m$	112
3.15 Integral drag along the plate for various excitation frequencies, a) Drag signal after periodic convergence, b) FFT of the drag signal for 8 periods	113
3.16 Averaged axial velocity and thermal profiles for various # periods	114

Figure	Page
3.17 Root mean square deviation of axial velocity and temperature along the normal plane for different # periods	115
3.18 a) Energy spectra on the domain at 3 given points b) Axial velocity contour at $t/p = 0.75$ with q-criterion iso-surfaces display	116
3.19 Large Eddy Simulation vs 2D SST Transitional results, a) bubble length, b) separation inception, c) heat transfer coefficient at $x=0.25m$ during the periodic oscillation	117
4.1 Linear wind tunnel; a) Test section visual access dimensions; b) Test section assembly; c) Mach and Reynolds subsonic envelope	118
4.2 Sketch of the Purdue Experimental Turbine Aerothermal Laboratory facility	120
4.3 Re/m and Mach number envelope of the linear test section	121
4.4 Linear Wind tunnel design; a) CAD model, b) Wind tunnel installed at Zucrow Laboratories	122
4.5 Blow-down wind tunnel layout	124
4.6 Flow discharge topologies	126
4.7 Flow straightener a,b,c) Available cell configurations; d) cell structure; e) Rectangular screen configuration	131
4.8 a) 3D Contraction Area, circular to rectangular cross section b) Abbot et al. [172] length to aspect ratio design limits	135
4.9 Mesh sensitivity analysis: RMS-Deviation of axial flow velocity in the outlet plane for different meshes	136
4.10 Numerical domain for contraction area design, a) Design based on Bezier curve, b) Numerical domain for 2D URANS analysis	137
4.11 Left) Axial velocity contour of the analyzed contraction types, Right) Flow velocity profiles at the outlet plane of the domain	138
4.12 a) Curvature of contraction shapes; b) Static pressure distribution along the contraction wall	139
4.13 Wall pressure distribution along the contraction for various design angles	140
4.14 2D Contours of axial velocity of different contraction angles	141
4.15 a) Axial velocity profile; b) RMS-D (u) of different contraction angles at a plane 0.0 5m downstream of the contraction outlet	141
4.16 3D Numerical domain for complete settling chamber URANS simulations	143

Figure	Page
4.17 3D Velocity contours with streamlines comparing 4 and 8 radial discharge slots	144
4.18 Evolution of mass-flow averaged axial velocity, temperature, pressure and total pressure during blow-down operation at the outlet plane of the settling chamber	146
4.19 3D Static Temperature contour during sudden flow discharge numerical experiment	147
4.20 Velocity Magnitude contour during blow-down numerical experiment	148
4.21 Total pressure, total temperature and stream-wise velocity temporal evolution at the outlet plane during the sudden flow discharge transient simulation	149
4.22 Settling chamber velocity magnitude contours at normal operation compared to a case when one of radial discharge slots is obstructed, robustness analysis	150
4.23 Facility mass-flow stability	151
4.24 Flow Conditioning performance, temporal uniformity of main quantities in the test section	152
4.25 Total flow temperature stability measured along the centerline of the test section	153
4.26 Hot Wire temporal stability at several conditions	153
4.27 a) Stream wise velocity profile across the height of the test section and b) Root Mean Square Deviation profile of the axial velocity component	155
4.28 a) Total temperature and b) Total Temperature Root Mean Square Deviation profiles across the test section height	156
4.29 a) Total Pressure and b) Total Pressure Root Mean Square Deviation profiles along the test section height at Reynolds 1.5×10^5	157
4.30 a) Total Pressure and b) Total Pressure Root Mean Square Deviation profiles along the test section height at Reynolds 3.4×10^5	158
4.31 Dynamic response and replicability characterization of the flow conditioning system, Sudden flow discharge and valve cyclic actuation experiments.	159
4.32 a) Reynolds/m b) Mach number maps achieved in the linear test section	162

Figure	Page
4.33 a) Complete envelope of Re/m and Mach numbers of the linear test section compared with the envelope tested in the experiments. b) Tested envelope in function of the two control variables: the area of the throat and the mass-flow through the test section.	165
4.34 a) Comparison between the Re/m map and the Kriging meta-model in function of the massflow and the throat area with the representation of the points resulted from the optimization methodology. b) Comparison between the Mach number map and the Kriging meta-model in function of the massflow and the throat area with the representation of the points resulted from the optimization methodology. c) Root mean squared error of the Mach number and Re/m number using 20, 36 and 50 points in the Kriging interpolation optimization methodology. pressure amplitude effect on the separated flow region and thermal isolation	166
4.35 a) PETAL Linear Test Section; b) Instrumentation location for facility envelope characterization	167
4.36 a) Comparison of the isentropic model with the experimental data; a)Mach number map (front view). b) Mach number map (rear view). c) Re/m number map (front view). d) Re/m number at several mass-flow levels.	169
4.37 Mass-flow, Total and static pressure, Mach and Reynolds/m number evolution during a performance characterization experiment	170
4.38 Extruded 3D Domain for Experimental analysis; a) Numerical domain replication for performance assessment analysis b)Wall shear stress contour for operation at Re/m 2×10^6	173
4.39 Comparison of 3D extruded domain against 2D numerical analysis	174
4.40 Contoured 3D Domain for Experimental analysis; a) Numerical domain , b) Wall shear stress contour for operation Re/m 2×10^6	174
4.41 Comparison of 3D contoured domain against 2D URANS analysis	175
4.42 3D Flow Separation Domain Performance assuming boundary layer development from the test section inlet	176
4.43 Test section geometry integration in the flow conditioning system	177
4.44 3D Flow Separation Domain performance with prescribed inlet momentum and thermal boundary layer profiles	178
4.45 Flow Separation Domain Test Article integration in the PETAL Linear Wind Tunnel	179
4.46 Flow Separation Domain test article	180

Figure	Page
4.47 Test article instrumentation distribution for separated flow dynamic response experimental campaign	181
4.48 Flow Separation Domain wall pressure distribution and reattachment location at several Reynolds numbers	184
4.49 Test conditions repeatability	184
4.50 Test article performance at high Reynolds Environments, CO-20	185
4.51 3D Flow behaviour at CO-7, a) Static pressure contour, b) Static pressure distribution along the test article at various span locations	186
4.52 Unsteady Reynolds Average Navier Stokes prediction of separated flow regions compared against experimental results operating at CO-4	187
4.53 CO-4 Hotwire Traverse	188
4.54 CO-7 Hotwire Traverse	189
4.55 Hot flow experiments mean flow Conditions	190
4.56 Wall temperature evolution at different axial locations along the hump surface for hot flow conditions	190
4.57 Heat Transfer Coefficient distribution along the hump surface during operation at two different Reynolds numbers, comparison between experimental and numerical results	191
4.58 Sudden flow discharge experiment CO-5 conditions, mass-flow, total pressure, total temperature and axial free stream velocity evolution	193
4.59 Surface pressure evolution during CO-5 sudden discharge experiment	194
4.60 Stream-wise velocity transient evolution during CO-5 sudden flow discharge at different wall distances.	195
4.61 Local stream-wise velocity unsteadiness during CO-5 Sudden Flow Discharge Experiment	196
4.62 Sudden flow discharge experiment at CO-8 Conditions, mass-flow, total pressure, total temperature and axial free stream velocity evolution	197
4.63 Surface pressure evolution during CO-8 sudden discharge experiment	198
4.64 Stream-wise velocity transient evolution during CO-8 sudden flow discharge at different wall distances.	199
4.65 Local stream-wise velocity unsteadiness during CO-8 Sudden Flow Discharge Experiment	200

Figure	Page
4.66 Stream-wise velocity profile at several time-steps along the sudden flow discharge, experimental profiles (1-D Hotwire) vs. URANS numerical prediction	201
5.1 Flow momentum deficit driving the flow detachment	203
5.2 Numerical domain for flow control analysis	204
5.3 Flow separation control envelope for different slot pressures	206
5.4 Slot pressure fluctuation effect on the separated flow region with an actuation amplitude of 4 kPa	207
5.5 Momentum boundary layer profiles at $x=0.25$ m for various injection frequencies	208
5.6 Thermal boundary layer profiles at $x=0.25$ m for various injection frequencies	210
5.7 Injection pressure amplitude effect on the separated flow region and thermal isolation	212
5.8 Injection pressure amplitude effect on the separated flow region and thermal insulation	213
5.9 Mass-flow averaged axial velocity and skin friction evolution at plane $x = 0.25$ m for transitional and full turbulent periodic injection	215
5.10 Averaged 2D contour of Turbulent Kinetic Energy for transitional and fully turbulent case with flow aspiration and injection	216
A.1 Transonic stator geometry for validation	237
A.2 Left) Isentropic Mach number distribution along suction and pressure side, current CFD vs. experiments; Right)Mach number contour along the stator passage	237
A.3 Sod Shock tube solution; Left) 2D Pressure contour 10ms after the membrane burst Right)Pressure and density distribution across the domain 100 ms after the membrane burst (Analytical and Current CFD tool)	238
B.1 Domains to compare for flat plate research, Left) Regular flat plate (inlet at plate LE); Right) Extended inlet making use of symmetry plane	239
B.2 Skin friction distribution along the flat plate (Red, regular plate plate, Dashed-black, domain with symmetry plane upstream)	240
B.3 Domains to compare for flow separation research, Top) Regular domain (inlet at plate LE); Bottom) Extended inlet making use of symmetry plane	241

Figure	Page
B.4 Skin friction distribution along the separation domain (Black regular plate, Blue, domain with symmetry plane upstream)	241
D.1 Pressure Stability correction	248
D.2 TC calibration	250
D.3 Thermocouple Uncertainty	251
D.4 (Left) Heat conduction across multilayered substrates, (Right) Heat flux data reduction based on 1D semi-infinite assumption with a Crank Nicholson scheme	253
D.5 Validation of the code developed to solve the transient heat transfer	254
D.6 Heat transfer coefficient computation based on heat flux data and adiabatic wall temperature definition	255
D.7 Methodology application	257

SYMBOLS

α_t	Thermal diffusivity (m^2/s)
α_h	Wire resistance temperature coefficient (Ohm/K)
A	Area (m^2)
A_c	Constant on skin friction correlation
A_h	Constant on hotwire calibration
Al	Aluminum
β	Porosity
c	Speed of sound (m/s)
C	Covariance (m/s)
CCF	Cross Correlation Function
c_f	Skin friction
c_d	Drag coefficient
c_p	Specific heat (J/kg/K)
c_v	Specific heat (J/kg/K)
c_k	Cerakote
d	Model Order
Δ	Boundary layer dimensional factor (m)
δ	Boundary layer thickness (m)
δ^s	Boundary layer displacement thickness (m)
δ_p	Pressure Boundary layer thickness (m)
δ_ρ	Density Boundary layer thickness (m)
δ_0	Initial Boundary layer thickness (m)
ϵ	Internal Energy ($kg/m^2/s^2$)
f	Frequency ()

F	Boundary layer evolution function
f_i	Momentum source (m^2/s)
Φ_h	Hydraulic diameter (m)
Γ	Required precision ()
H	Domain Height (m)
htc	Heat transfer coefficient ($W/m^2/K$)
k	Acceleration Parameter
kn	Number of independent variables
κ	Thermal conductivity (W/m/K)
λ	Dissipative length scale (m)
Λ	Integral length scale (m)
L	Domain Length (m)
μ	Dynamic molecular viscosity (kg/m/s)
N_c	Cell Count
N	Contraction ratio
n_h	Exponential factor on Hotwire calibration
n_q	Adiabatic Heat transfer coefficient exponential factor
ν	Kinematic viscosity (N/m^2)
P	Pressure (Pa)
p	Period
Pr	Prandtl number
q''	Heat Flux rate (W/m^2)
R	Gas Constant
ρ	Gas density (kg/m^3)
S	Energy source ($kg/m^2/s^2$)
S_e	temperature dependent function of the material (V/K)
\sum_{ji}	Total Stress Tensor (N/m^2)
σ	Standard Deviation
t	Time (s)

T	Temperature (K)
ϑ	Total Energy ($kg/m^2/s^2$)
τ	Wall Shear Stress (Pa)
θ	Momentum Boundary layer thickness (m)
xv	Axial velocity (m/s)
$Tu\%$	Turbulence Intensity (%)
ξ	Dimensionless temporal/axial indicator (K)
x	Axial distance (m)
y	Normal distance (m)
V_{CTA}	Constant Temperature Anemometry Voltage (V)
W	Domain Width (m)
w	Wire
ζ	Axial location for boundary layer tripping
Subscripts	
0	stagnant conditions
ax	axial
aw	adiabatic wall
c	contact
δ	boundary layer edge
dyn	dynamic
exc	excitation
i	inlet
o	outlet
r	reattachment
ref	reference
s	surface
th	thermal
x	streamwise direction
y	normal direction

w	wall
∞	free stream conditions

Superscripts

+	wall units
*	Observation location
—	Mass flow averaged

ABBREVIATIONS

CCf	Cross Correlation Factor
DBD	Dielectric Barrier Discharge
FFT	Fast Fourier Transform
FSD	Flow Separation Domain
DNS	Direct Numerical Simulation
GCI	Grid Convergence Indicator
HP	High Pressure
LP	Low Pressure
LES	Large Eddy Simulations
MIE	Momentum Integral Equation
PETAL	Purdue Experimental Turbine Aerothermal Lab
RMS	Root Mean Square
RMSE	Root Mean Square Error
RMSD	Root Mean Square Deviation
RTD	Resistance Temperature Detector
SST	Shear Stress Transport
TE	Trailing Edge
TRL	Technology Readiness Level
URANS	Unsteady Reynolds Average Navier Stokes Simulations

ABSTRACT

Saavedra Garcia, Jorge PhD, Purdue University, December 2018. Determining the Dynamic Scales of the Boundary Layer and Flow Separation Inception: Analysis Towards Efficient Flow Control . Major Professor: Guillermo Paniagua.

The dynamic performance of the momentum and thermal boundary layer linked to the acoustic response dictate the efficiency of heat exchangers and the operational limits of fluid machinery. The specific time required by the boundary layer to establish or adapt to the free stream variations is vital to optimize flow control strategies as well as the thermal management of fluid systems. The proper understanding of the wall fluxes, separated flow regions and free stream response to transient conditions becomes the fulcrum of the further improvement of fluid machinery performance and endurance. Throughout this dissertation the establishment sequence and the main parameters dictating the acoustic response and the boundary layer settlement are quantified together with their implication on the wall fluxes and boundary layer detachment.

Unsteady Reynolds Average Navier Stokes evaluations, Large Eddy Simulations, Direct Numerical Simulations and wind tunnel experiments are exploited to analyze the transient behavior of attached and detached flow aerodynamics. The core of the research is built upon URANS simulations allowing the realization of multiple detailed parametric analyses. Thanks to its reduced computational cost, hundreds of transient flow evaluations are carried out, enabling the determination of the establishment sequence, the main flow features and relevant non-dimensional numbers. The URANS methodology is verified against experimental and analytic results on the flow conditions of the study. The Large Eddy Simulations and Direct Numerical Simulations allow further characterization of the near wall flow region behavior with much

higher resolution while providing an additional source of verification for the coarser numerical tools. An experimental campaign on a novel full visual access linear wind tunnel explores the impact of mean flow sudden accelerations on the boundary layer detachment and reattachment phenomena over an ad-hoc wall mounted hump. The wind tunnel is designed based on the premises of: full visual access, spatial and temporal stability of total and static pressure together with the total temperature and fast flow settlement, minimizing the start-up phase duration of the wind tunnel. A wall mounted hump that mimics the behavior of the aft portion of a low pressure turbine is inserted in the wind tunnel guaranteeing a 2D flow separation phenomena. After steady state test article characterization series of sudden flow discharge experiments reveal the impact of mean flow transients on the boundary layer detachment inception. Finally, taking advantage of the knowledge on transient flow performance, optimum flow control mechanisms to abate boundary layer detachment are proposed. The recommended control approach effectively prevents the boundary layer separation while minimizing the energy requirement.

1. INTRODUCTION

1.1 Motivation and Bibliographic Review

The boundary layer establishment was previously identified in theoretical and analytical studies of various degrees of complexity. Several authors proposed analytical solutions of the unsteady boundary layer development. Stewartson [1] [2] focused on the impulsive start of motion of semi-infinite flat plates. Considering short time scales, the boundary layer over the flat plate could be divided in two regions sketched in Figure 1.1 a). In the downstream segment the boundary layer is independent of the axial position along $x > u_w t$, because the effect of the leading edge has not arrived there yet. The boundary layer in this region corresponds to a Rayleigh profile [3]. At axial positions closer than the convection threshold, $x < u_w t$, near wall flow is independent of time and responds to a Blasius profile [4] growing from the leading edge of the plate. By contrast, in cases of larger flow time scales, the whole plate is affected by the leading edge presence and the solution of the boundary layer should be expressed as a function of the axial position. Moore [5] performed a dimensionless analysis of the establishment of the flow over a flat plate, set into motion with a time-dependent velocity. Considering a quasi-steady approach, the response of the boundary layer is thereby driven by the diffusion across the boundary layer thickness: $\tau_{flow,establishment} = \delta^2/\nu$, where δ boundary layer thickness, and ν the molecular viscosity. Similarly, Ostrach [5] analyzed the effect of the heat transfer in the aerodynamic boundary layer establishment. A wall temperature larger than the free stream temperature (temperature ratio $TR = T_\infty/T_w$ lower than 1) leads to thinner boundary layers, consequently leading to higher skin friction coefficients and faster establishments. Smith [6] studied the starting process in a reflected shock tunnel, which evidenced experimentally the relevance of the unsteady flow phenomena on the

boundary layer settlement. Based on their derivations a characteristic parameter was proposed:

$$\Psi_{transient} = x \frac{\partial u / \partial t}{u^2} \quad (1.1)$$

This parameter identifies how fast can a boundary layer react to free stream change as a function of the actual acceleration exerted. For values of $\Psi_{transient} \ll 1$ a quasi-steady flow behaviour is expected, however for larger values of $\Psi_{transient}$ the boundary layer evolution may be affected by the transient performance. Wen and Huang [7] analytically demonstrated the prime influence of the acceleration rate on the boundary layer development, derived from the skin friction coefficient and heat transfer rate on an isothermal flat plate. Based on the exact solution of the Navier-Stokes equations for two-dimensional incompressible laminar flow, Watson [8] predicted the boundary layer growth during the starting process. In Watson's analysis, the skin friction establishment was modeled as $\tau_{cf} = (\delta^{*2}/\nu)$, while the time required by the aerodynamic flow to reach the steady-state regime was estimated to be three times τ_{cf} . Davies and Bernstein [9] divided the flow around a test article when exposed to sudden mean flow changes in three different regions: external mean flow field, boundary layer and the wake. The inviscid of external mean flow field adjustment to the new conditions will be established following the acoustic settlement of the flow, uniquely driven by the settlement of the compression and/or expansion waves that initiated the regime change. Inside of the boundary layer the adjustment is only promoted by the diffusion across the boundary layer height and thus a much slower process. The previous studies were done for a laminar boundary layer, where only molecular diffusion was considered.

Lighthill performed analytic studies on the boundary layer response to mean flow variations, pointing out the main differences between subsonic and supersonic flow regimes [10]. In this investigation the onset of separation was also assessed as function of the dynamic pressure distributions along the surface and their influence on the boundary layer development was carefully determined. At supersonic regimes [11],

the impact of expansion and compression disturbances was examined. Where the interaction between the main stream and the boundary layer was treated mathematically by perturbing pure parallel flow neglecting the viscous forces. Including the energy equation through von Misess formulation the effect of random free stream conditions and wall temperature distributions on the heat transfer rate across laminar incompressible boundary layers was also tackled [12].

Still all previous studies considered a laminar boundary layer. Moreover, most analytic investigations available in the literature adopt a quasi-steady approach. Their applicability is limited to the range of impulsive starts or specific unsteady evolution, for which the second derivatives of the flow speed are negligible compared to the mean stream velocity. For turbulent flows, the time required for the boundary layer to be established should be reduced due to the increased mixing of the flow, which can be modeled as an increase in fluid viscosity. To my knowledge, there are no published analytically studies on the turbulent boundary layer establishment.

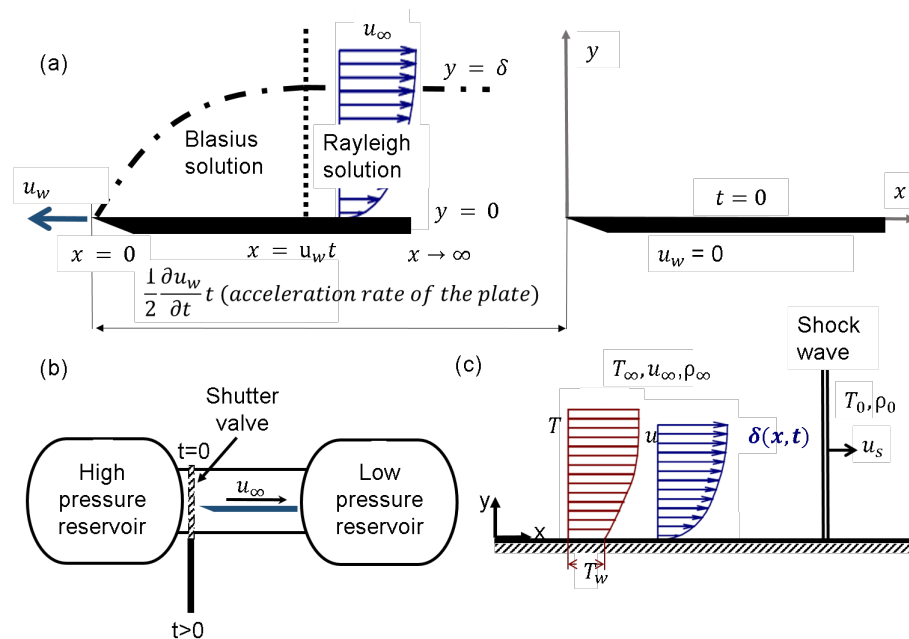


Fig. 1.1. a) Boundary layer establishment following an impulsive start; b) Experimental testing of a blowdown process; c) Boundary layer establishment after the passage of a shock wave.

The development of a turbulent model would find a myriad of practical applications, where the flow is characterized by chaotic regimes. Heat transfer research in aerospace components is typically performed in short-duration wind tunnels because they offer large temperature gradients and hence better accuracy than the continuous running facilities. In blow-down wind tunnels (Figure 1.1 b and c), the flow is set into motion following the passage of a pressure wave. The Figure 1.2 represents the numerical evolution of total pressure, massflow and wall shear stress at half cord of a flat plate during the initial phase of a blow down experiment. All the values are referenced to their magnitude at steady state conditions. On that representation the rise of the total pressure determines the duration of the start-up phase. The final settlement of the massflow and the wall shear stress takes place only after the total pressure has reached its final steady value. There is an evident delay between the establishment of the total pressure and the massflow and wall shear stress.

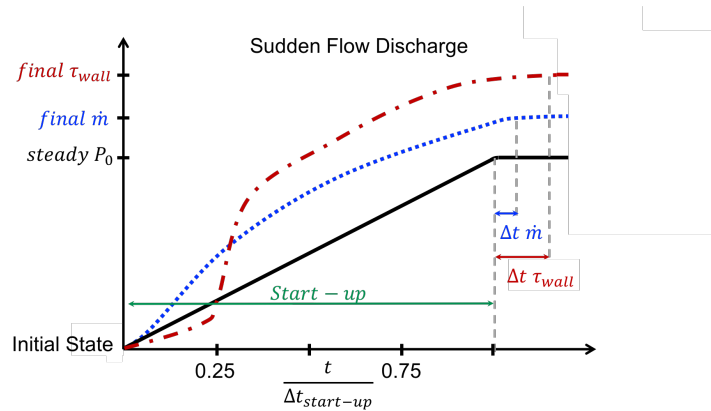


Fig. 1.2. Flow field and wall fluxes evolution during a blow down start-up

In this sense, Mirels [13] analyzed the boundary layer growth after the passage of a shock-wave, as depicted in the Figure 1.1 c. While Holden [14] studied experimentally the establishment of detached flows in the supersonic regime, and reported that the establishment time is function of the flow speed, Reynolds number, Mach number and the gas to wall temperature ratio: $\tau(u/L) = f(M, Re, T_w/T_\infty)$. Lee and Lewis [15] performed several numerical simulations that validated Holdens model and provided

establishment time predictions over a wider range of objects. Similarly Davies and Bernstein [9] conducted experiments in order to investigate the establishment of a shock-induced boundary layer on a semi-infinite flat plate. Using the same establishment parameter defined by Holden, it was found that the heat flux attains the steady-state level after a characteristic time defined as $\tau(u/L) = 3.3$.

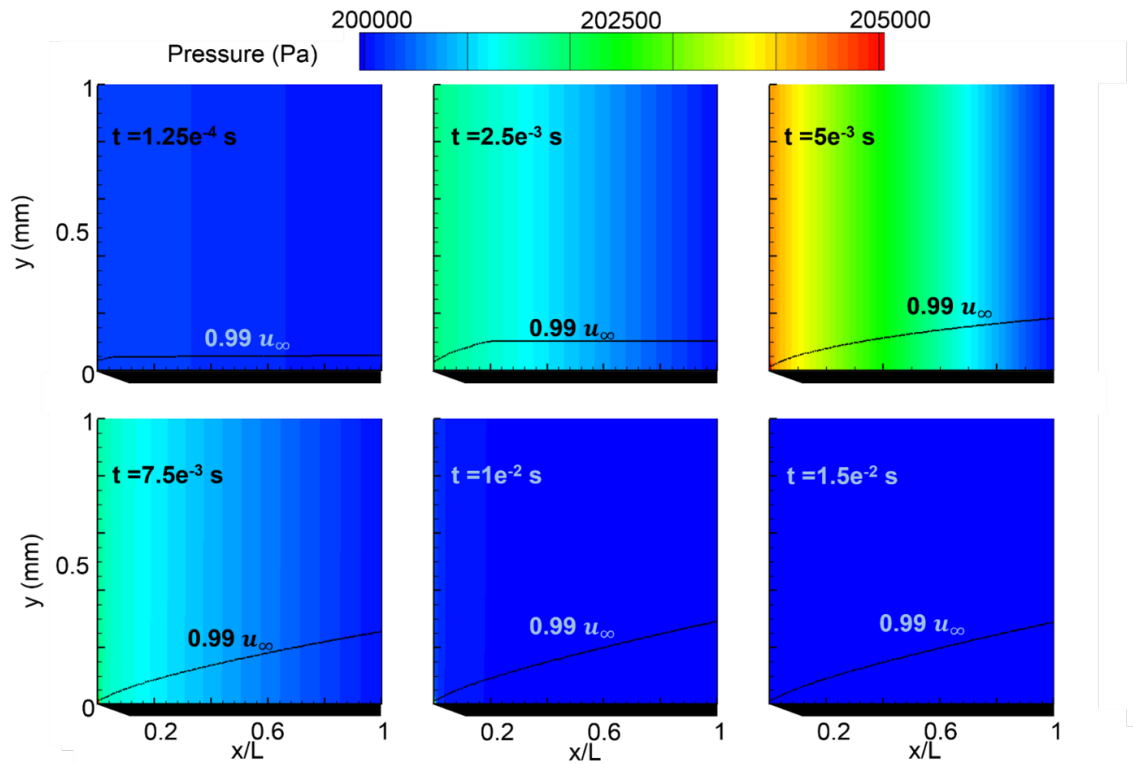


Fig. 1.3. Momentum boundary layer development after the passage of a pressure wave front

Apart from pure analytic and experimental investigations Jacobs [16] performed advanced numerical simulations to characterize the establishment of the near wall region in specific geometries. Also numerically, Li and Nalim [17] addressed the response of the thermal boundary layer to a sudden change in free stream flow temperature, maintaining a constant flow velocity. Through their analysis transient heat transfer correlations were presented in terms of Nusselt and Prandtl numbers. The Figure 1.3 depicts the response of the momentum boundary layer to a sudden total pressure

rise and the subsequent generation of a Rayleigh boundary layer. In following, the presence of the plate leading edge is convected downstream and the boundary layer acquires a nominal profile. However, the final phase of the boundary layer settlement is dictated by the diffusion of the information across the near wall flow. Based on this preliminary numerical analysis clear different phases on the momentum boundary layer settlement are identified.

1.2 Research Objectives

The ultimate goal of this research is to improve the performance of flow control approaches to abate the boundary layer separation, considering the mean flow unsteadiness and benefiting from the dynamic response of the momentum and thermal boundary layers. To achieve such goal the following objectives are proposed:

At first, the response of the near wall flow region under sudden flow acceleration or periodic flow perturbations must be described to **characterize the dynamic response of the momentum and thermal boundary layer**. Identifying the establishment sequence of the boundary layer and the main parameters driving its settlement. Additionally, the influence of the main dimension-less numbers, (Reynolds, Mach, Strouhal) must be recognized. In this line, the implication of the boundary layer transient performance on the distribution of the wall fluxes has to be identified.

Once the evolution of the momentum and thermal boundary layer are characterized, the next objective is to **determine the effect of the mean flow transients on the boundary layer detachment and reattachment process**. Illustrating how the near wall flow under adverse pressure gradient is affected by sudden flow acceleration, deceleration or periodic flow disturbances.

In order to demonstrate experimentally the dynamic behavior of recirculated flow regions, **a modular wind tunnel must be designed to perform transient experiments over separated flow regions in a wide regime of Reynolds and Mach numbers**, ranging from 1×10^5 up to 1.9×10^8 Re/m and from Mach 0.01 up

to Mach 6. The wind tunnel must provide uniform and stable experimental conditions with a minimum start-up time to allow transient test article characterization. An ad-hoc wall mounted hump will be used a reference test-case for steady and transient experiments on separated flow aero-thermodynamics.

Finally, the knowledge on the dynamic response of both, zero-pressure gradient boundary layers and boundary layers exposed to adverse pressure gradients, will be used to **propose optimum flow control techniques to abate boundary layer detachment during unsteady operation.**

Such objectives will contribute to describe the impact of transient flow operation on the performance of fluid-machinery, together with its consequence on the wall fluxes distribution and the flow detachment-reattachment phenomena.

1.3 Research methodology

To achieve the first objective series of Unsteady Reynolds Average Navier Stokes simulations over a flat plate geometry are evaluated. Verifying the impact of free-stream sudden or periodic flow changes on the near wall region and wall fluxes. The numerical simulations are used to describe the different phases present during the acceleration and illustrate the behaviour of the heat flux and shear stress under different periodic excitation frequencies. The performance of the URANS model is assessed through comparison against experimental cases. Additionally, Direct Numerical Simulations are exploited to further explore the dynamic performance of the URANS $k\omega$ SST transitional model while taking a closer look at the physics behind the response of the boundary layer to mean flow accelerations. Based on the Momentum Integral Equations of the boundary layer and supported by the Direct Numerical Simulations results, a simplified model is derived to predict the evolution of the momentum boundary layer under free-stream transients. Given the transient progression of free-stream flow parameters: pressure, density and axial velocity; the proposed ordinary differen-

tial equation provides the temporal evolution of the boundary layer from which wall shear stress and heat flux trends can be derived.

Regarding the second objective, an ad-hoc wall mounted hump is designed to investigate the evolution boundary layer detachment and reattachment process under mean flow transients. The wall mounted hump behaves like the aft portion of a suction side blade, where flow separation occurs at low Reynolds number operation but fully attached flow is present at high Reynolds numbers. URANS and LES simulations are exploited for the analysis of the free-stream transient evolution impact on the boundary layer detachment and reattachment phenomena. The URANS simulations enable the characterization of the transient evolution features when compared to a quasi-steady evolution. Similarly, the analysis of mean flow fluctuation at several frequencies and sudden flow release over the wall mounted hump depict the dynamic response of the boundary layer detachment process. Experimental results over a backward facing step verify the accuracy of the numerical model on predicting the wall fluxes evolution on recirculated flow regions. While Large Eddy Simulations are used to verify the dynamic performance of the URANS $k\omega$ SST under these circumstances.

The design of the modular wind tunnel follows a sequential methodology from zero-dimensional to three-dimensional unsteady Computational Fluid Dynamic analysis. The operational limits are based on isentropic flow relations. While 3D URANS simulations are evaluated to optimize the flow conditioning system and guarantee its functionality under the operating premises. Such facility, will be used to empirically prove the impact of mean flow transients over recirculated flow regions. The experimental campaign explores the evolution of sudden flow discharge over the wall mounted hump and provides another verification case for the numerical effort. The experimental performance is monitored with total pressure and total temperature probes, 1D hotwire sensors, wall mounted thermocouples and wall pressure readings.

Finally, in the quest towards optimum flow actuation approaches that benefit from near wall flow dynamic evolution, URANS simulations over the wall mounted hump

with flow injection and ingestion are evaluated. A slot is added to the hump geometry that allows the aspiration of the boundary layer or the addition of flow momentum by blowing. The envelope of effective flow control will be analyzed with steady state simulations. In conclusion, URANS simulations will be used to identify the optimum flow control techniques to abate flow separation while minimizing the energy input.

1.4 Dissertation guideline

The core of the report is structured in 5 different chapters. The first chapter provides an insight of the previous studies on the boundary layer establishment and dynamic evolution research. The rest of the thesis extends the analysis of the boundary layer dynamic response to turbulent flows and its impact on the boundary layer detachment-reattachment phenomena.

The following chapter dives into the dynamic response of the boundary layer to transient flow conditions. Focusing first on the reaction of the near wall flow to a sudden flow acceleration and then analyzing its behavior under periodic free stream fluctuations. Through the realization of Direct Numerical Simulations we take a closer look into the near wall region evolution under sudden flow discharge. In addition, a simplified model is developed to predict the evolution of the momentum boundary layer under mean flow transients.

The third chapter aims to analyze the performance of flow detachment and reattachment under unsteady free stream flow. As disposed for the attached flow analysis, it will begin looking into the boundary layer separation phenomena after a sudden flow variation. To finally analyze its dynamic response to intermittent mean flow conditions.

To assess experimentally the dynamic reaction of flow separated regions to transient mean flow conditions, the wall mounted hump will be tested on an ad-hoc designed linear wind tunnel. The fourth chapter of this report outlines the design guidelines of the wind tunnel with particular attention to its flow conditioning system.

This chapter also summarizes the calibration procedure to describe the operational envelope of the facility. The actual layout of the test article, instrumentation and steady state test article operation are discussed. Finally, the performance of the flow separation domain under sudden flow discharge experiments is described based on wall pressure readings and hotwire traverses.

Once characterized the dynamic response of the separated flow regions, that knowledge will be used to search the optimum flow actuation approach to prevent boundary layer detachment. The fifth chapter describes the flow control approach that take advantage of the dynamic response of the flow through flow injection and absorption. Looking into the optimum actuation strategy, maximizing its effectiveness while minimizing the energy requirement.

2. BOUNDARY LAYER RESPONSE TO MEAN FLOW VARIATIONS

Nowadays many power generation devices which involve the use of a working fluid are submitted to periodic flow oscillations or transient mean flow conditions dictated by their operating regime. The nature of those flow transients may vary, ranging from different angle incidences, mass-flow or even temperature. For instance, in turbochargers for automotive power plants the turbomachinery is exposed to pulsating flow conditions dictated by the engine operating regime which may severely affect the performance and incur on endurance detriments.

Traditionally, the performance of such devices is characterized based on steady state experimental evaluations. However, in the quest towards performance improvement, the researchers have found that the transient response of the turbomachinery and its associated elements is one of the main area that still demands more understanding [18] [19]. As a consequence many studies have been performed on the comprehension of the pulsating flow conditions on the radial turbomachinery [20], [21], [22] [23]. As an example, Binder et al. [24] analyzed the influence of the stator wakes on the rotor performance through series of laser-2-focus velocimetry measurements. Revealing that the wake impingement on the rotor blades modifies the flow turning across the rotor, generating overturning on the wake region. Similar conclusions were withdrawn by Arndt [25] on a multistage low pressure turbine. The interaction of the periodic stator wakes with the rotor results in strong amplitude modulations of the flow velocity and turbulent intensity, altering the secondary flows through the rotor and modifying the radial distribution of the flow turning. Numerically, Giles [26] looked into the propagation and reflection of the shocks generated on the stator trailing edge across the rotor row, which induce large variations on the rotor lift performance. Chaluvadi et al. [27] analyzed the wake and stator pas-

sage vortices influence on the rotor behavior through smoke flow visualizations and hotwire measurements. Describing the influence of the incoming perturbations on the rotor secondary flows and its final contribution on the rotor performance loss. Moss et al. [28] characterized the heat flux over the suction and pressure side of the rotor airfoils through various experimental campaigns in a rotating annular facility with and without stator vanes. The effect of the incoming wakes on the heat flux along the rotor blade was highlighted thanks to the comparison of the forward and reverse rotation experiments. Completely different trends and magnitudes of heat flux take place in the rear suction side blade because of the presence of the stator wakes. Similarly, the comparison of the rotation results with cascade experimental data, further supports the strong influence of the upcoming wakes and its relevant role in the boundary layer transition.

In this regard, as new combustion approaches are explored for propulsion concepts, like pulse detonation or rotating detonation combustors [29], new fluid machinery components are developed [30, 31]. The performance of such units under pulsating conditions becomes a fulcrum for future technology integration. Sousa et al [32] described the transient flow behavior experienced across internal flow passages exposed to variable inlet flow conditions in supersonic flow conditions. The impact of transient mean flows with the exhaust propulsive elements requires more understanding to ensure efficient energy usage and optimal performance [33, 34].

The boundary layer transient growth was previously documented in fundamental and analytic studies for laminar flow conditions. Several authors proposed numerical solutions of the unsteady boundary layer development. Stewartson [1, 2] studied the impulsive start of motion of semi-infinite flat plates. Rott [35] also looked into the theory of time dependent laminar flows, describing the evolution of laminar boundary layers driven by free-stream flow changes. In a similar analysis, Moore [36] carried a dimensionless evaluation of the flow establishment over a flat plate. The response of the boundary layer to mean flow changes is dictated by the diffusion across its height. Starting from the exact solution of the Navier-Stokes equations for 2-D in-

compressible laminar flow, Watson derived a model that could predict the skin friction establishment time. Theoretically, Wen and Huang [7] highlighted the prime role of the acceleration rate on the boundary layer transient evolution. Schetz and Oh [37] analyzed the transient development of the near wall flow region driven by the impulsive start of motion of the surrounding fluid. Taking advantage of the unsteady momentum integral equations and using an ad-hoc boundary layer profile with the Howarth-Dorodnitzin transformation and Crocco Integral relations they predicted the momentum and thermal boundary layer evolution.

Most of the heat transfer, supersonic and hypersonic research in aerospace components is empirically evaluated in short-duration wind tunnels. Their use is optimal for this application due to the large temperature gradient that can be instantaneously imposed between the flow and the test article, enabling high accuracy measurements. On the other hand, the test duration is generally constrained to a few milliseconds due to the demanding upstream flow conditions required for the experimental operation. In sudden flow release wind tunnels, the flow is set into motion following a rapid valve opening or diaphragm burst causing pressure waves to travel across the test section. Mirels [13, 38] analyzed the boundary layer growth during the flow start-up after the passage of a shock-wave. Similarly, Holden [14, 39] experimentally studied the flow establishment of flows in the supersonic regime, describing that the time to reach steady state is a function of the flow speed, Reynolds number, Mach number and the gas to wall temperature ratio. In this line, Lewis [15] performed numerical evaluations that agreed with Holden's model and provided predictions of the boundary layer development time. Also experimentally, Davies [9] described the formation of a shock-induced boundary layer on a semi-infinite flat plate. Focusing on the starting phase of sudden flow release wind tunnels, Smith [6] studied the starting process in a reflected shock tunnel. In their experiments a relation between the mean flow evolution and the boundary layer transient development was clearly exposed. In a similar research, Lam and Crocco [40] focused their analysis on the shock induced unsteady laminar compressible boundary layer on a flat plate.

In the turbulent flow regime, Horlock and Evans [41] analyzed the influence of turbulence and ordered unsteadiness in the free-stream on the boundary layer development. Additional terms related to the shear stress and the kinetic energy in the edge of the boundary layer appeared to be of relevance on the 2D momentum integral equations. The turbulent kinetic energy and shear stress at the boundary layer edge must be considered in order to capture the influence of such transient turbulent structures on the near wall region. In this line, low-order models were also applied to model the low-frequency motions observed in reflected shock-wave boundary layer interactions by Toubert and Sandham [42], using results of direct numerical simulation to determine the relevant parameters from the 3-D momentum integral equations. In attempt to predict the turbulent boundary layer establishment time Saavedra et al. performed an extensive parametric analysis on the development of the boundary layer under sudden flow discharge based on URANS blow-down simulations [43]. Through the isolation of the independent effect of each one of the driver parameters a correlation was derived to predict the boundary layer establishment time.

In the field of boundary layer response to continuous flow fluctuations, Uchida [44] revealed the influence of the dynamic pressure gradients travelling along the pipe on the wall fluxes on laminar flows. Similarly, Mizushima et al. [45] experimentally characterized the instantaneous profiles of velocity and turbulence intensity for pulsating flows. Based on their empirical investigation, two main regimes were distinguished. At low frequencies the turbulence levels remained unaltered, but the mean flow conditions suffered high variations. In contrast, for higher frequencies, the mean flow quantities were stable while the turbulent characteristics suffered strong oscillations. Towards a better understanding of the nature of pulsating flow in a pipe, Shemer et al. [46] conducted an extensive analysis on turbulent and laminar pulsating flows at identical frequencies and Reynolds numbers for small amplitude perturbations. They found that the radial distribution on the flow velocity amplitude and phase were strongly dependent of the flow regime, whether laminar or turbulent. The turbulent cases depicted a faster response than the laminar flow at some radial locations due to

the influence of the eddy viscosity. Regarding the impact of free-stream fluctuations on the wall heat flux, Moschandreu and Zamir [47] depicted the main role of Prandtl and Strouhal number on the heat flux rate oscillation magnitude driven by the free-stream changes. The ratio between the thermal to momentum boundary layer has a strong influence on the heat flux transient evolution, as also analyzed by Saavedra et al [48].

Focusing in axial turbomachinery, unsteady effects impact the aerothermal performance of the turbine blade rows, originating noise, mechanical and thermal fatigue. Blade row interactions are due to the relative motion between nearby rows of airfoils, and in particular, due to the periodic encounter of flow distortions generated by combustion chambers and upstream or downstream airfoil rows. Hence, the detailed characterization of the thermal boundary layer, wall heat fluxes and the skin friction is vital to improve the performance of cooled turbine airfoils. In order to determine the aerodynamic and thermal time scales involved in this phenomena, series of Unsteady Reynolds Averaged Navier-Stokes simulations were performed. This simulations will be used to investigate the wall heat flux response to periodic flow velocity fluctuations over a flat plate. Because of the flow acceleration the boundary layer is first stretched, resulting in an increase of the wall shear stress. Later on, due to the viscous diffusion, the low momentum flow adjusts to the new free stream conditions. The behavior of the boundary layer at low frequency is similar to the response to an individual deceleration followed by one acceleration. However, at higher frequencies the mean flow topology is completely altered. One would expect that higher acceleration rates would cause a further stretching of the boundary layer that should cause even greater wall shear stresses and heat fluxes. Two counteracting effects influence the response of both the momentum and the thermal boundary layer. In one hand, the stagnant flow quantities propagate at characteristic velocities guiding the establishment of the mean flow conditions. On the other hand, the diffusion across the boundary layer leads the final response of the near wall region. Additionally, the dynamic pressure

gradients imposed in the mean flow modulate the viscous properties of the boundary layer through local flow acceleration, transforming the expected pattern.

2.1 Strategy

In order to characterize the transient flow conditions and the near wall flow properties during the flow acceleration the Navier-Stokes equations are exploited. Presented in the following order: conservation of mass, momentum and energy.

$$\frac{\delta}{\delta t}(\rho) + \frac{\delta}{\delta x_i}(\rho u_i) = 0 \quad (2.1)$$

$$\frac{\delta}{\delta t}(\rho u_i) + \frac{\delta}{\delta x_i}(\rho u_i \rho u_j - P_{ij}) = 0 \quad (2.2)$$

$$\frac{\delta E}{\delta t} + \frac{\delta}{\delta x_i}(u_i E - u_j P_{ij} + \dot{q}_i) = 0 \quad (2.3)$$

Where ρ is the density, u the velocity and P_{ij} is the stress tensor, E is the energy density and \dot{q} is the heat flux. Where

$$P_{ij} = -\frac{\rho}{m} k_b T \delta_{ij} - 2/3 \mu \frac{\delta u_k}{\delta x_k} \delta_{ij} + \mu \left(\frac{\delta u_i}{\delta x_j} \frac{\delta u_j}{\delta x_i} \right) \quad (2.4)$$

and $E = 3/2 \frac{\rho}{m} k_b T + 1/2 \rho u^2$. Being m the mass and T the temperature. To tackle the solution of the previous set of equations, Reynolds decomposition is commonly performed, where an instantaneous quantity is split into its time averaged and fluctuating quantities [49]. This decomposition guides towards the formulation of the Reynolds Average Navier Stokes equations RANS. Which are primarily used to predict the behavior of turbulent flows.

$$\frac{\delta}{\delta t}(\rho \bar{u}_i) + \rho \bar{u}_i \frac{\delta \bar{u}_i}{\delta x_j} = \rho f + \frac{\delta}{\delta x_j} \left(-\bar{P} \delta_{ji} + \mu \left(\frac{\delta \bar{u}_i}{\delta x_j} \frac{\delta \bar{u}_j}{\delta x_i} \right) - \rho \overline{(u'_i u'_j)} \right) \quad (2.5)$$

These equations can incorporate approximations based on the turbulent flow properties in order to accommodate the chaotic turbulent effects.

$$\rho(\overline{u'_i u'_j}) = 2\mu_t S_{ij} - 2/3\rho k\delta_{ij} \quad (2.6)$$

To account for turbulent diffusion phenomena the molecular viscosity is supplemented by the eddy viscosity. Where the dynamic eddy viscosity μ_t is modeled making use of different turbulent models. To reduce the computational burden most of the numerical investigations were carried out in a 2D geometry. The domain, Figure 2.1 a), was meshed following a blocking strategy with ANSYS ICEM . A grid sensitivity study was completed following the approach outlined by Celik et al. [50], guaranteeing a proper geometrical discretization. For this purpose, the axial flow velocity just outside of the boundary layer and the boundary layer height were acquired for all the different grids, as depicted in Figure 2.2 a). A summary of the different mesh properties is also presented in table 1.

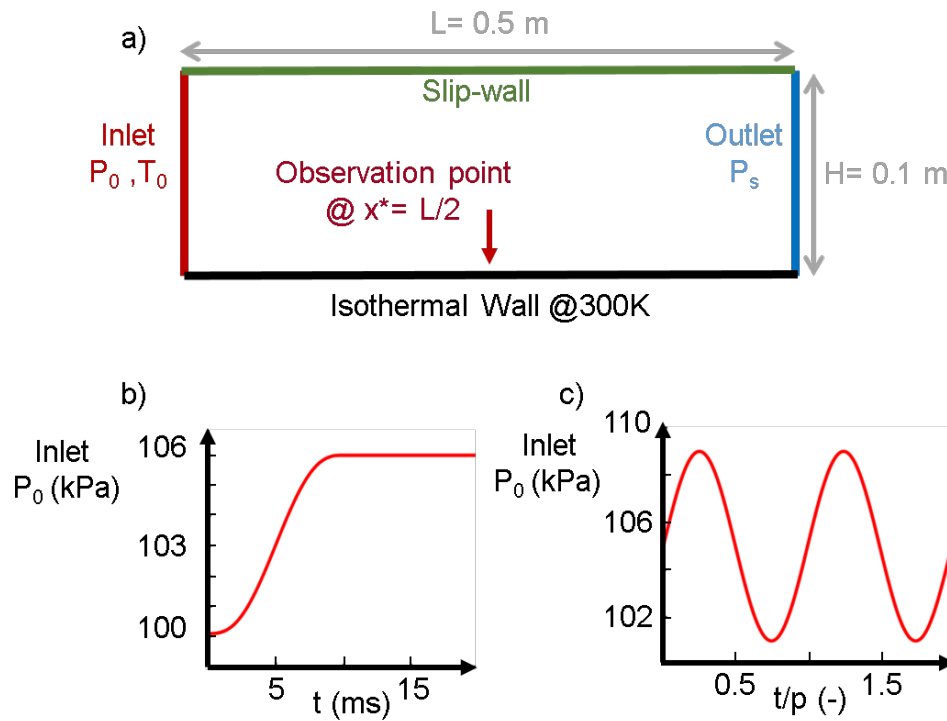


Fig. 2.1. a) Numerical domain for URANS flow acceleration research; b) Inlet total pressure profile for sudden flow acceleration analysis; c) Inlet total pressure profile for periodic perturbation analysis

Figure 2.2 b) displays the grid convergence index for all the different meshes under scrutiny. The results for the mesh of forty thousand cells show a relative uncertainty around 0.25% and a convergence indicator below 0.006. Therefore, that grid resolution was selected for the rest of the numerical analysis. The grid convergence indicator (GCI) is a parameter that quantifies the concurrence of the fine grid. Selecting a target value of 0.006 the confluence of the discretization level to the finest accuracy is guaranteed. To enhance correct near wall flow prediction the y^+ was maintained below 0.5 along the entire plate. Similarly, the grid expansion ratio was fixed at 1.15, in order to ensure correct near wall resolution for all the cases. Due to the non-stationary flow behavior, and in order to resolve quantitatively the aerodynamic structures and the wall fluxes evolution Unsteady Reynolds Averaged Navier-Stokes simulations were performed with ANSYS Fluent .

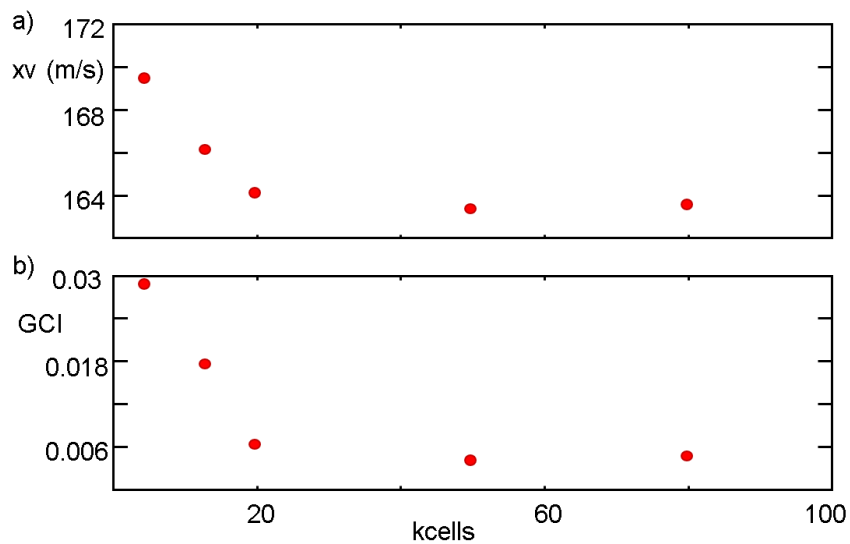


Fig. 2.2. a) Axial velocity at (0.4,0.07) for different mesh resolutions;
b) Grid convergence indicator

The time step and inner iterations used for the simulations were selected based on a benchmark analysis keeping a minimum frequency resolution of 40 kHz. As a

result, the time step was initially set to 5×10^{-7} s with up to 14 inner iterations for internal time step convergence.

Table 2.1.
Grid convergence analysis

Cells	xv (m/s)	δ (mm)	Average Cell Size,h	Area Ratio $r = h_c/h_f$
5000	168.269	6.981	0.003606	1.41
10000	166.269	7.067	0.002550	1.41
20000	165.256	7.115	0.001803	1.41
40000	164.384	7.219	0.001275	1.41
80000	164.121	7.223	0.000901	1.41
120000	164.022	7.224	0.000637	1.41

The static pressure level was fixed in the outlet boundary condition at 100 kPa. The inlet of the domain was modeled as an inlet pressure boundary condition where the total temperature was kept constant at 500K. The inlet flow variations were imposed following total pressure transient profiles, $P_0(t)$

The top wall of the domain was modeled as an adiabatic inviscid wall. While the plate was simulated as a viscous isothermal surface at 300K with uniform roughness. The wall fluxes and both momentum and thermal boundary layer were monitored at $x/L = 0.5$ (x^*). For this numerical research the turbulence closure was achieved through the use of the Langtry-Menter 4 equation Transitional SST model [51] [52]. Following this procedure the laminar to turbulent transition effects on the thermal boundary layer response are taken into account. For this particular turbulent closure the turbulent kinematic viscosity is evaluated as function of 2 parameters, κ and ω

$$\nu_t = \frac{k}{\omega} \quad (2.7)$$

The shear stress transport (SST) model was developed by Menter [53] [54] as a blend method between the k- ω and the k- ϵ models. Taking advantage of their superior

performance on different regions. The wall is robustly and accurately modeled making use of the k - ω formulation, while the free stream is independently modeled by the k - ϵ model. To overcome the blending both models are weighted with a function that takes into account the wall distance. The SST model includes damped cross diffusion derivatives in the k - ω and the definition of the turbulent viscosity takes into account the turbulent shear stress.

The k - ω SST has been proven as a robust and reliable model to accurately predict: adverse pressure gradients, transonic airfoils and shock waves and for both near wall and far-field zones. [55] [56]; while the core flow propagation numeric behavior is unaltered. Two different solver validations were performed prior to the research to verify the performance of the numerical tool under relevant flow features. The validations can be found in the Appendix 1, Fluent Validation. The SST k - ω shares part of its formulation with the standard k - ω model where the conservation equations for k and ω are:

$$\frac{\delta}{\delta t}(\rho k) + \frac{\delta}{\delta x_i}(\rho k u_i) = \frac{\delta}{\delta x_j}(\Gamma_k \frac{\delta k}{\delta x_j}) + \tilde{P}_k - D_k + S_K \quad (2.8)$$

$$\frac{\delta}{\delta t}(\rho \omega) + \frac{\delta}{\delta x_i}(\rho \omega u_i) = \frac{\delta}{\delta x_j}(\Gamma_\omega \frac{\delta \omega}{\delta x_j}) + \tilde{P}_\omega - D_\omega + Y_\omega + S_\omega \quad (2.9)$$

Here \tilde{P}_k and \tilde{P}_ω represent the generation of turbulent kinetic energy and ω due to mean velocity gradients. Γ_k and Γ_ω represent the effective diffusivity of both terms and D_k, D_ω the turbulent dissipation. While S_k and S_ω represent user defined source terms and Y_ω the cross diffusion term.

The effective diffusivities are modeled by

$$\Gamma_K = \mu + \frac{\mu_t}{\sigma_k} \quad (2.10)$$

$$\Gamma_\omega = \mu + \frac{\mu_t}{\sigma_\omega} \quad (2.11)$$

Where σ accounts for the turbulent Prandtl number and the turbulent viscosity is computed as follows:

$$\mu_t = \frac{\rho_k}{\omega} \frac{1}{\max(\frac{1}{\alpha^*}, \frac{SF_2}{a_1\omega})} \quad (2.12)$$

Being S the strain rate magnitude and

$$\sigma_k = \frac{1}{\frac{F_1}{\sigma_{k,1}} + \frac{1-F_1}{\sigma_{k,2}}} \quad (2.13)$$

$$\sigma_\omega = \frac{1}{\frac{F_1}{\sigma_{\omega,1}} + \frac{1-F_1}{\sigma_{\omega,2}}} \quad (2.14)$$

$$\alpha^* = \alpha_\infty^* \left(\frac{\alpha_0^* + \frac{Re_t}{Re_k}}{1 + \frac{Re_t}{Re_k}} \right) \quad (2.15)$$

Where,

$$Re_t = \frac{\rho k}{\mu\omega}, \quad R_k = 6, \quad \alpha_0^* = \beta_i/3, \quad \beta_i = 0.072$$

The blending functions are given by:

$$F_1 = \tanh(\Phi_1^4) \quad (2.16)$$

$$\Phi_1 = \min\left(\max\left(\frac{\sqrt{k}}{0.09\omega y}, \frac{500\mu}{\rho y^2\omega}\right), \frac{4\rho k}{\sigma_{\omega,2} D_\omega^+ y^2}\right) \quad (2.17)$$

$$D_\omega^+ = \max\left(\frac{2\rho}{\sigma_{\omega,2}\omega} \frac{\delta_k}{\delta x_j} \frac{\delta\omega}{\delta x_j}, 10^{-10}\right) \quad (2.18)$$

$$F_2 = \tanh(\Phi_2^2) \quad (2.19)$$

$$\Phi_2 = \max\left(2\frac{\sqrt{k}}{0.09\omega y}, \frac{500\mu}{\rho y^2\omega}\right) \quad (2.20)$$

Where y is the distance to the closest surface and D_ω^+ is the positive portion of the cross diffusion term. The production of turbulent kinetic energy \tilde{P}_k is defined

as $\tilde{P}_k = \min(P_k, 10\rho\beta^*k\omega)$. Where P_k represents the production of turbulent kinetic energy in its pure form, consistent with the Boussinesq hypothesis

$$P_k = -\overline{\rho u'_i u'_j} \frac{\delta u_i}{\delta x_j} = \mu_t S^2 \quad (2.21)$$

The production of ω energy \tilde{P}_ω is defined as $\tilde{P}_\omega = \alpha P_k n u_t$. Where α is again derived based on the blending functions:

$$\alpha = F_1 \alpha_{\infty,1} + (1 - F_1) \alpha_{\infty,2} \quad (2.22)$$

$\alpha_{\infty,1} = \frac{\beta_{i,1}}{\beta_\infty^*} - \frac{\kappa^2}{\sigma_{\omega,1} \sqrt{\beta_\infty^*}}$, $\alpha_{\infty,2} = \frac{\beta_{i,2}}{\beta_\infty^*} - \frac{\kappa^2}{\sigma_{\omega,2} \sqrt{\beta_\infty^*}}$; Being κ the von Karman constant 0.4.

The dissipation rates are modeled as $D_K = \rho\beta_\infty^*k\omega$ and $D_\omega = \rho\beta\omega^2$. In these expressions the value of $\beta = F_1\beta_{i,1} + (1 - F_1)\beta_{i,2}$. Whereas the cross-diffusion term is defined by $Y_\omega = 2(1 - F_1)\rho\sigma_{\omega,2}\frac{1}{\omega}\frac{\delta k}{\delta x_j}\frac{\delta \omega}{\delta x_j}$. Finally, the model predefined constants are:

$$\sigma_k = 2.0, \sigma_\omega = 2.0, \sigma_{k,1} = 1.176, \sigma_{\omega,1} = 2.0, \sigma_{k,2} = 1.0, \sigma_{\omega,2} = 1.168, a_1 = 0.31, \beta_{i,1} = 0.075, \beta_{i,2} = 0.0828, \alpha_\infty = 0.52, \alpha_\infty^* = 1, \alpha_{\infty,0} = 1/9, \beta_i = 0.072, \beta_\infty^* = 0.09, R_k = 6, R_\omega = 2.95, R_\beta = 8;$$

The transition formulation is introduced by the Boussinesq assumption [57] [58]

$$\tau_{ij} = 2\mu_i \left(S_{ij} - 1/3 \delta_{ij} \frac{\delta u_k}{\delta x_k} \right) \quad (2.23)$$

This models is also known as the γ -Re θ SST because it uses the evolution of γ (intermittency) and the Reynolds based on the momentum boundary layer thickness (θ). It is a four equation model based on the k- ω SST with the additional two equations to describe the laminar turbulent transition process.

$$\frac{\delta}{\delta t} + \frac{\delta}{\delta x_i} = \frac{\delta}{\delta x_j} \left((\mu + \sigma_\omega \mu_t) \frac{\delta \omega}{\delta x_j} \right) = \tilde{P}_\omega - D_\omega + \frac{2(1 - F_1)\rho\sigma_\omega}{\omega} \frac{\delta k}{\delta x_j} \frac{\delta \omega}{\delta x_j} \quad (2.24)$$

$$\frac{\delta}{\delta t} + \frac{\delta}{\delta x_i} (\rho\gamma u_i) = \frac{\delta}{\delta x_j} \left((\mu + \frac{\mu_t}{\sigma_f}) \frac{\delta Y}{\delta x_j} \right) + \tilde{P}_\omega - E_\gamma \quad (2.25)$$

$$\frac{\delta}{\delta t}(\rho Re_{\theta t}) + \frac{\delta}{\delta x_i}(\rho Re_{\theta t} u_i) = \frac{\delta}{\delta x_j} \left((\sigma_{\theta t}(\mu + \mu_t) \frac{\delta \mathfrak{R}_{\theta t}}{\delta x_j}) \right) + \tilde{P}_{\theta t} \quad (2.26)$$

The source terms are:

$$P_\gamma = F_{length} c_{\alpha 1} \rho S (\gamma F_{onset})^{0.5} (1 - c_{e1} \gamma) \quad (2.27)$$

$$E_\gamma = c_{\alpha 2} \rho \Omega F_{turb} (c_{e2} \gamma - 1) \quad (2.28)$$

Where the blending functions are defined by

$$\begin{aligned} F_{onset1} &= \frac{Re_v}{2.193 Re_{\theta,c}}; Re_v = \frac{\rho S D^2}{\mu}; F_{onset2} = \min(\max(F_{onset1}, F_{onset1}^4), 2.0) \\ R_T &= \frac{\rho k}{\mu \omega}; F_{onset3} = \max(1 - \frac{R_t^3}{2.5}, 0), F_{onset} = \max(F_{onset2}, F_{onset3}, 0) \\ F_{turb} &= \exp(-\frac{R_T^4}{4}); F_{length} = F_{length,1} (1 - F_{SubLayer}) + 40.0 F_{SubLayer} \end{aligned}$$

$$E_\gamma = c_{\alpha 2} \rho \Omega F_{turb} (c_{e2} \gamma - 1) \quad (2.29)$$

$$F_{length1} = \begin{cases} 39.8139 - (119.27 \times 10^{-4}) Re_{\theta,t} - \\ (132.5672 \times 10^{-6}) Re_{\theta,t}^2, & \text{if } Re_{\theta,t} < 400 \\ 263.404 - (123.939 \times 10^{-2}) Re_{\theta,t} + \\ (194.458 \times 10^{-5}) Re_{\theta,t}^2, & \\ -(101.695 \times 10^{-5}) Re_{\theta,t}^3, & \text{if } 400 < Re_{\theta,t} < 596 \\ 0.5 - (3 \times 10^{-4}) (Re_{\theta,t} - 596), & \text{if } 596 < Re_{\theta,t} < 1200 \\ 0.3188, & \text{if } Re_{\theta,t} > 1200 \end{cases} \quad (2.30)$$

$$F_{sublayer} = \exp\left(-\left(\frac{Re_\omega}{200}\right)^2\right); Re_\omega = \frac{\rho \omega d^2}{\mu}$$

$$Re_{\theta c} = \begin{cases} 396.035 \times 10^{-2} + (10120.656 \times 10^{-4})Re_{\theta t} - \\ (868.23 \times 10^{-6})Re_{\theta t}^2 \\ + (696.56 \times 10^{-9})Re_{\theta t}^3 - (174.105 \times 10^{-12})Re_{\theta t}^4 & \text{if } Re_{\theta t} < 1870 \\ Re_{\theta t} + (593.11 \times 10^{-6} + 0.482(Re_{\theta t} - 1870)) & \text{if } Re_{\theta t} > 1870 \end{cases} \quad (2.31)$$

$$S = \sqrt{(2S_{ij}S_{ij})}; S_{ij} = \frac{1}{2} \left(\frac{\delta u_i}{\delta x_j} + \frac{\delta u_j}{\delta x_i} \right);$$

$$\omega = \sqrt{(2w_{ij}W_{ij})}; W_{ij} = \frac{1}{2} \left(\frac{\delta u_i}{\delta x_j} - \frac{\delta u_j}{\delta x_i} \right);$$

$$P_{\theta t} = \frac{c_{\theta t} \rho}{T} (Re_{\theta t}^{eq} - Re_{\theta t})(1 - F_{\theta t}); T = \frac{500\mu}{\rho U^2}; U = \sqrt{u_k u_k}$$

$$F_{\theta c} = \min \left(\max \left(F_{wake} \exp\left(-\left(\frac{d}{\delta}\right)^4\right), 1 - \frac{c_{e2}\gamma - 1}{c_{e2} - 1} \right), 1 \right) \quad (2.32)$$

$$\delta = \frac{375\Omega\mu d Re_{\theta t}}{\rho U^2};$$

$$F_{wake} = \exp\left(-\left(\frac{Re_w}{1 \times 10^5}\right)^2\right);$$

$$\lambda_{\theta} = \frac{\rho \theta_t^2 d U}{\mu d S};$$

$$Tu = \frac{100\sqrt{\frac{2k}{3}}}{U}$$

$$\frac{dU}{dS} = u_m u_n \frac{\delta u_m}{\delta x_n} \quad (2.33)$$

$$Re_{\theta c}^{eq} = \begin{cases} (1173.51 - 589.428Tu + 0.2196Tu^2)F(\lambda_{\theta}) & \text{if } Tu < 1.3 \\ (1331.5(Tu - 0.5658))^{-0.671}F(\lambda_{\theta}) & \text{if } Tu > 1.3 \end{cases} \quad (2.34)$$

$$F(\lambda_{\theta}) = \begin{cases} 1 + (12.986\lambda_{\theta} + 123.66\lambda_{\theta}^2 + 405.689\lambda_{\theta}^3)\exp\left(\left(\frac{Tu}{1.5}\right)^{1.5}\right) & \text{if } \lambda_{\theta} < 0 \\ 1 + 0.275(1 - \exp(-35.0\lambda_{\theta}))\exp\left(\frac{-Tu}{0.5}\right) & \text{if } \lambda_{\theta} > 0 \end{cases} \quad (2.35)$$

$$Re_{\theta t}^{eq} = \frac{\rho U \theta t}{\mu}$$

Making use of the following calibration constants

$$c_{a1} = 2; c_{a2} = 0.06; c_{a3} = 1.0; c_{e2} = 50; c_{\theta t} = 0.03; s_1 = 2; \sigma_f = 1.0 \text{ and } \sigma_{\theta t} = 2$$

The boundary conditions for γ and $Re_{\theta t}$ are set by

$$\frac{\delta\gamma}{\delta n_{wall}} = 0; \gamma_{farfield} = 1; \frac{\delta Re_{\theta t}}{\delta n_{wall}}$$

$$Re_{\theta t farfield} = \begin{cases} (1173.51 - 589.428Tu + 0.2196Tu^{-2})F(\lambda_{\theta}) & \text{if } Tu < 1.3 \\ 1331.5(Tu - 0.5658)^{-0.671}F(\lambda_{\theta}) & \text{if } Tu > 1.3 \end{cases} \quad (2.36)$$

The effects of laminar to turbulent transition are introduced into the SST model by modifying the turbulent-kinetic-energy terms as

$$\tilde{P}_k = \gamma_{eff}P_{k,SST}; D_k = \min(\max(\gamma_{eff}, 0.1), 1)D_{k,SST}; \gamma_{eff} = \max(\gamma, \gamma_{sep})$$

$$\gamma_{sep} = \min(s_1(\max(0, \frac{Re_v}{3.235Re_{\theta c}})) - 1)F_{reattach}, 2); F_{reattach} = \exp(-(\frac{R_t}{20})^4)$$

Where the subscript SST refers to the original values following the SST pure formulation. The form of the specific dissipation is unaltered. However, the blending functions need to be slightly modified

$$R_y = \frac{\rho d\sqrt{k}}{\mu}; F_3 = \exp\left(-\left(\frac{R_y}{120}\right)^5\right); F_1 = \max(F_1, SST, F_3)$$

For numerical robustness the following limits are enforced $-0.1 < \lambda_{\theta} < 0.1$; $Tu > 0.027$; $Re_{\theta t} > 20$

To analyze the behavior of developed turbulent boundary layers the transition was numerically enhanced in the leading edge of the plate. However, using the transitional model, the turbulent to laminar reverse transition effects on the thermal boundary layer response are taken into account. The working fluid was air, modeled as an ideal gas. Where the Sutherland law was used to include the effect of the temperature on the molecular fluid viscosity. Second order upwind schemes were adopted for the flow and turbulent kinetic energy. Similarly, second order implicit schemes were used for the transient formulation. ¹

¹Material Published on Thermal Boundary Layer Response to Periodic Fluctuations for Turbulent Flow, J. Eng. Gas Turbine Power 141 (1), 2018

2.2 Sudden flow acceleration

The first analysis consisted on the reaction of the boundary layer to a sudden mean flow acceleration. The sudden flow discharge was set imposing a smoother step rise profile on the inlet total pressure P_0 , represented in Figure 2.1 b). The use of this sort of rising profile is preferred since it guarantees the continuity of the input signal. The initial pressure level $P_0(t < 0)$ was equal to 100.1 kPa. The overall pressure rise had a duration of 10 ms and the final level was $P_0(t > 0.01) = 106$ kPa. Based on the total to static pressure ratio the flow velocity in the domain accelerates from 16.5 m/s up to 128.8 m/s. In order to characterize the dynamic response of the boundary layer during the sudden flow acceleration the free stream quantities and wall fluxes along the transient evolution were monitored. For comparison purposes, some steady state simulations were evaluated along the total pressure rise, mimicking a quasi-steady evolution of the case during the transient. At those simulations, the total pressure level at the inlet is maintained constant. Once the case reached convergence the local wall fluxes and mean flow conditions were recorded.

Figure 2.3 depicts the comparison of free stream velocity a) and wall shear stress b) at the observation location, $x = L/2$. Looking at the axial velocity comparison between the transient evolution and the steady evaluations there seems to be an evident delay on the mean flow settlement Δ_{t1} . For the same values of inlet total pressure, the axial velocity predicted by the steady evaluations appears to happen at a later phase during the transient evolution. In a similar manner, for the wall shear stress, the delay is even larger. The results suggest that there is an additional delay related with the viscous propagation effects across the boundary layer. ($\Delta_{t2} = \Delta_{t1} +$ viscous propagation effects).

The temporal delay Δ_{t1} , is due to the characteristics propagation and can be approximated based on the speed of sound and the flow velocity upstream and downstream of the compression and expansion wave fronts. Aiming the understanding of the mean flow establishment nature, a pure pressure step inviscid simulation was

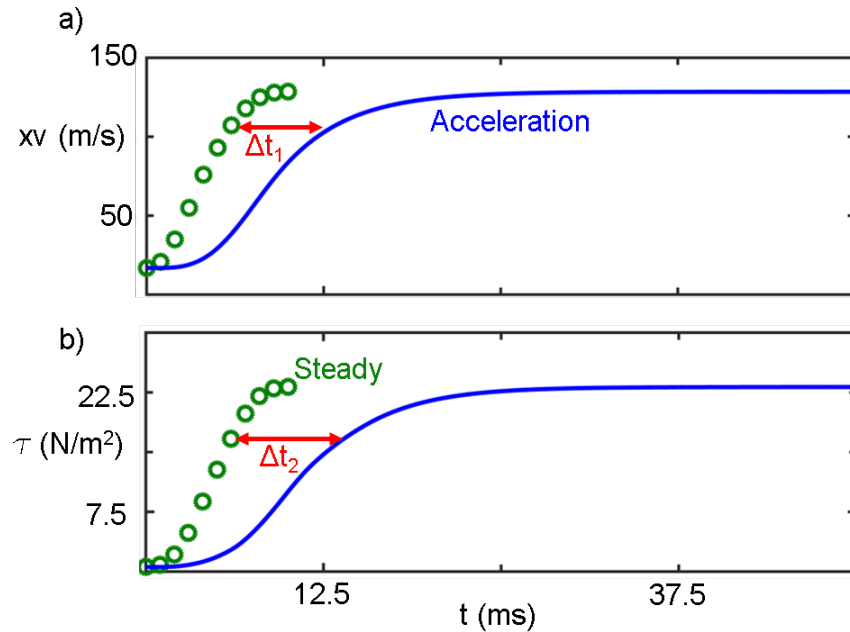


Fig. 2.3. a) Free stream axial velocity evolution; b) Wall shear stress evolution: during a sudden flow acceleration

performed. For this analysis the domain and the mesh that were used followed the same guidelines. As for the sudden flow acceleration both the total temperature and back pressure were kept constant at a level of 500K and 100 kPa respectively. While the top wall was modeled as an inviscid adiabatic surface and the plate was kept isothermal at 300K. The initial total pressure level for this analysis was 100.1 kPa leading to an initial flow velocity of 16.5 m/s. In this case, a sudden total pressure rise at $t=0$ of $\Delta P_0 = 900$ was imposed following the profile depicted in Figure 2.4 a).

As outlined by Lighthill, [11] [59] [60], the acoustic response of an open end flow passage is depicted in Figure 2.4 b). Due to the total pressure rise in the inlet, pressure waves are generated and propagated downstream at a speed $c+xv$, transmitting to the rest of the flow domain the new total pressure level. Figure 2.5 represents the total and static pressure levels, the characteristics propagation and the free stream axial velocity at several time steps along the transient evaluation. Prior to the total pressure step, the static and total pressure are uniform, as well as the free stream velocity,

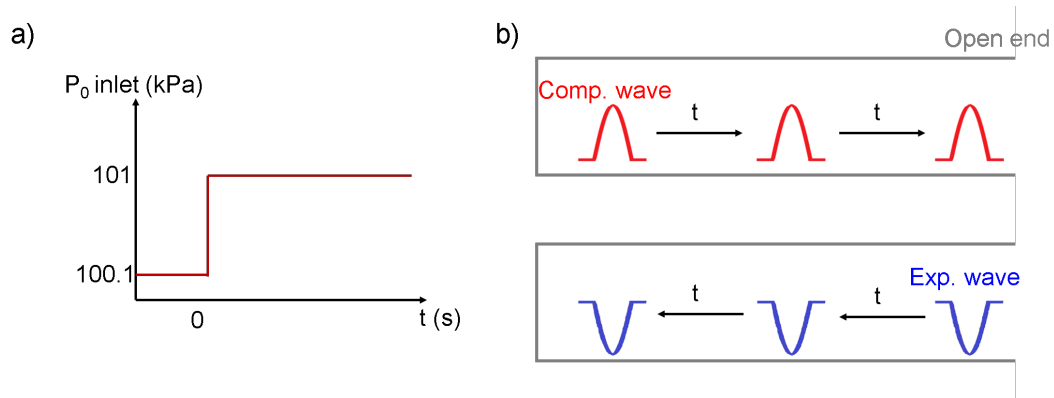


Fig. 2.4. a) Inlet total pressure profile for instantaneous discharge analysis; b) Acoustic characteristics propagation in a domain with discharge to low pressure reservoir

and there are no characteristics being propagated across the domain. The following snapshot, 0.5 ms after the pressure step, right running characteristics (pressure waves) travel along the domain introducing the new total pressure level. As the updated total pressure information is released the flow suddenly increases its velocity. This process is similar to the reaction of the flow after the passage of a shock wave

Later on, once the pressure waves reach the open end of the domain ($t \geq 1\text{ms}$), modeled as a pressure outlet, the pressure waves are reflected backward, as expansion waves and they become pure left running characteristics. As the expansion front travels upstream of the domain the actual static pressure is set. Following the arrival of the expansion wave, traveling at a speed $c+xv$, the static pressure level is reduced to match the outlet boundary conditions. Consequently, the difference on the total and static pressure (dynamic pressure) is now in agreement with both inlet and outlet conditions. Once the actual dynamic pressure is set, the legitimate flow velocity is established in agreement with the total pressure increase that generated the pressure wave. Following this sequence, in the last snapshot ($t = 2\text{ms}$) the expansion wave front has travelled backward almost the entire domain instituting the final flow velocity in all the pipe except for the leading edge region.

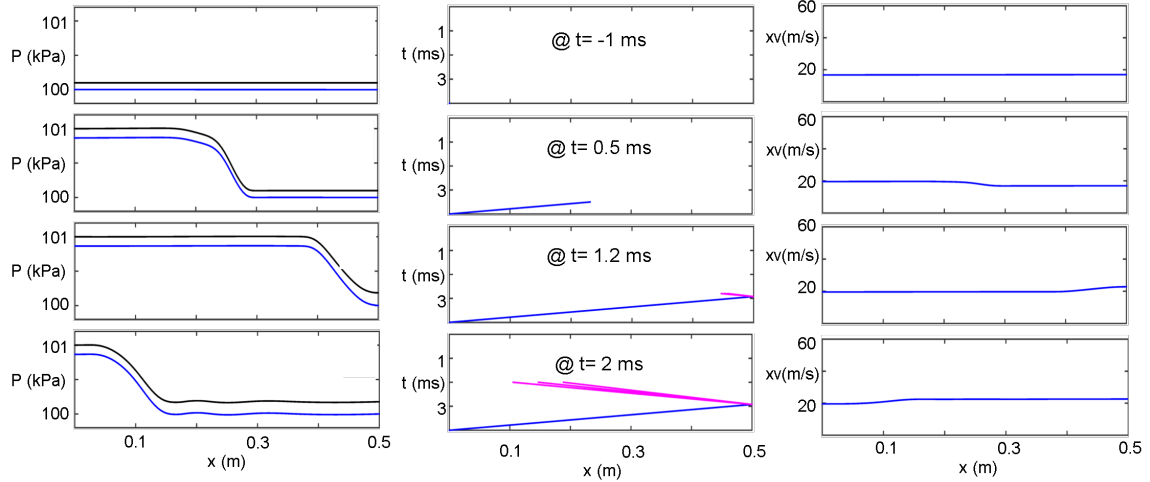


Fig. 2.5. Total pressure, characteristics and axial velocity evolution after a total pressure step.

As reasoned for a pressure step, in subsonic flows the settlement of the actual free stream flow conditions happens just once the pressure and expansion waves travel along the domain. Hence, the delay that was noticed in Figure 2.3 a) is due to the time required for the characteristics (pressure and expansion waves) to go through the domain and update the entire pipe on the actual total and static pressure levels.

By shifting the steady point evaluations with the time required for the characteristics to establish the mean flow conditions, a better representation is obtained. The transient profile values are then compared with steady evaluations for the same free stream conditions, as depicted in Figure 2.6 a) for the free stream velocity.

Figure 2.6 b) represents the skin friction coefficient compared with the steady evaluations. Two different trends are observed during the flow acceleration. At first, the transient evaluation overshoots the steady skin friction values. Under this circumstance, Figure 2.6 a) depicts the boundary layer for both steady and transient run at half of the pressure rise. During the initial phase of the acceleration the inertia of the fluid close to the wall stretches the boundary layer. For the same axial velocity, a strained boundary layer with shorter height leads to higher skin friction values.

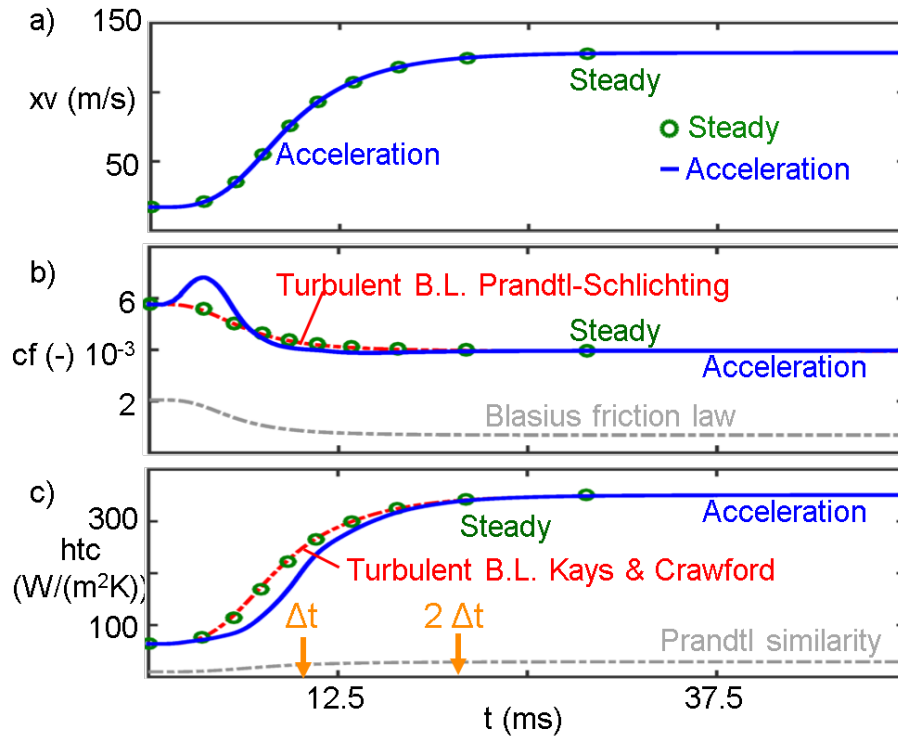


Fig. 2.6. a) Free stream axial velocity b) Skin friction coefficient c) Heat flux: evolution during a flow acceleration after characteristics delay correction

Laminar and turbulent boundary layer skin friction correlations are also included in Figure 2.6 b) for comparison purposes. Due to the inertia of the flow in the first phase of the acceleration the skin friction slightly overshoots the turbulent prediction. However, during the latter phases of the flow stimulation, the transient evaluation undergoes the prediction for turbulent flow without reaching laminar boundary layer character. This phenomena is a consequence of the turbulence settlement delay. In the steady evaluations the turbulence inside of the boundary layer has been completely established. While during the acceleration, the boundary layer is continuously evolving and it suffers some temporal shifting due to the diffusion delay. This phenomenon can also be recognized in the momentum boundary layer profile in Figure 2.7 c).

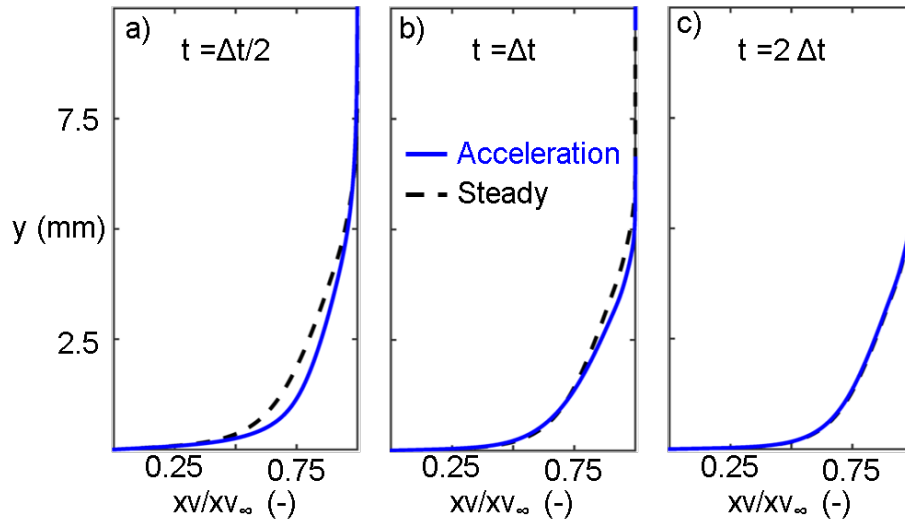


Fig. 2.7. Momentum boundary layer profile at different acceleration phases for both steady and transient evaluation

Figure 2.6 c) represents the heat flux rate during the flow acceleration compared with the steady conditions. Laminar and turbulent boundary layer heat transfer coefficients derived from Nusselt correlations are also included in the figure. The wall heat fluxes during the transient evolution depict smaller values than the ones acquired in the independent steady evaluations, which are in agreement with the ones predicted for turbulent flow. Those smaller heat transfer values are the symptoms of thermal distribution delay across the near wall flow. In this sense, Figure 2.8 represents the thermal boundary layer profiles for both transient and steady evaluations during three different phases of the flow acceleration. The first set of thermal boundary layer profiles at half of the total pressure rise, ($t=t/2$), show similar thicknesses but different slopes near the wall. During the transient evaluation, the boundary layer profiles have not been adjusted yet to the new Reynolds conditions. Therefore, the slope at the wall is still lagging behind, adjusting from a thicker boundary layer. By the end of the pressure rise ($t=\Delta t$), this lag is further augmented and the slope near the wall during the unsteady evaluation is much smaller than the one found in the steady state condition. This could also be perceived in Figure 2.6 c), where the

difference between the steady and the transient evaluation reaches its maximum, at $t=10\text{ms}$. Afterwards, the differences between the transient and steady profiles are gradually mitigated.

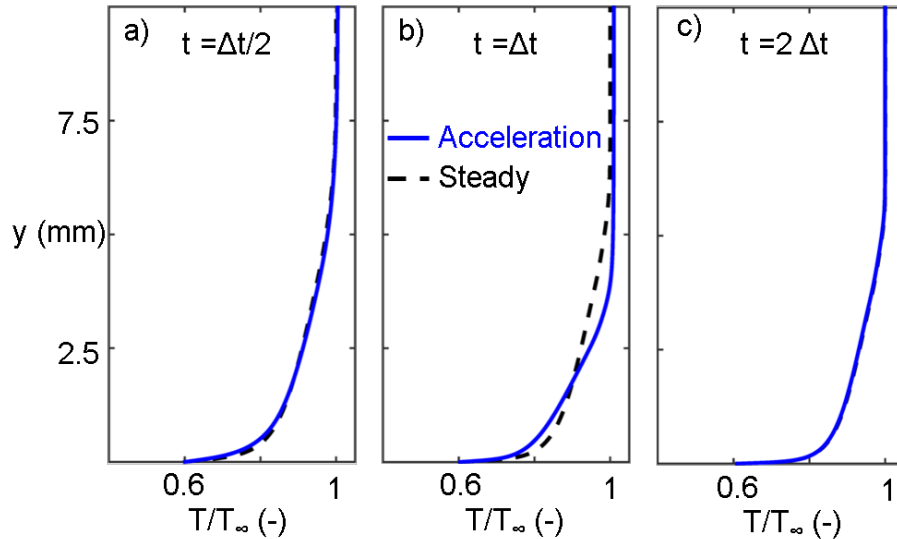


Fig. 2.8. Thermal boundary layer profile at different acceleration phases for both steady and transient evaluation

By looking at figures Figure 2.3 b) or Figure 2.3 c) it is clear the effect of the diffusion delay on the settlement of the wall fluxes compared to the free stream quantities. That delay leads to wall fluxes values lower than the ones found for the steady state evaluations after the mean flow establishment correction. Which implies that for the same free stream conditions, (Reynolds number), the transient evolution reaches the wall flux values determined in the steady evaluations with a certain time shift. To look further into this matter, Figure 2.9 left) depicts the referenced evolution of the wall shear stress and the free stream velocity. Both magnitudes are referenced to their final steady state value after the flow acceleration has taken place. It becomes apparent that once the free stream velocity reaches its final value there is still some time, Δt_{est} , for the wall shear stress to acquire its ultimate rate. That temporal shifting is the consequence of the diffusion delay across the boundary layer. The

mean flow quantities are transferred convectively and acoustically along the domain. However, the propagation of the information across the normal direction to the wall into the boundary layer happens mainly in a diffusive manner. The temporal delay due to the diffusive propagation across the boundary layer (Δt_{est}) can be estimated based on the viscosity distribution along the momentum boundary layer thickness with the following expression.

$$\Delta t_{est} = \int_0^{\delta} \frac{y}{\max(\mu, \mu_t)} \rho \partial y \quad (2.37)$$

For illustration purposes Figure 2.9 represents the non-dimensional velocity profile and the turbulent viscosity distribution along it. The turbulent viscosity distribution across the boundary layer will be a consequence of the mean flow turbulence, the Reynolds and the wall surface roughness among other things. The eddy viscosity distribution could be addressed following the guidelines of any of the well-known turbulent closure formulations (Baldwin-Barth [61], Spalart-Allmaras [62], $k - \epsilon$ [63], $k - \omega$, [53]). As introduced in the previous equation the diffusion rate will be determined by the maximum viscosity value being either the laminar or turbulent one. Following this procedure, the diffusion across the inner viscous sublayer is properly modeled as well as the pure laminar boundary layer cases. It must be highlighted that by integrating the viscosity profile along the boundary layer also the temperature effects on the molecular viscosity are considered as they could be of main relevance.

In the case of the heat flux, the delay is driven by the diffusion of the information across the thermal boundary layer height. As reasoned by the Prandtl analogy [64], for fluid with Prandtl numbers below the thermal boundary layer results thicker than the aerodynamic one ($\delta_{th} = \delta / Pr^{1/3}$). As derived for the momentum boundary layer, the thermal boundary layer establishment delay could be inferred as :

$$\Delta t_{est,th} = \int_0^{\delta_{th}} \frac{y}{\max(\alpha, \alpha_t)} \partial y \quad (2.38)$$

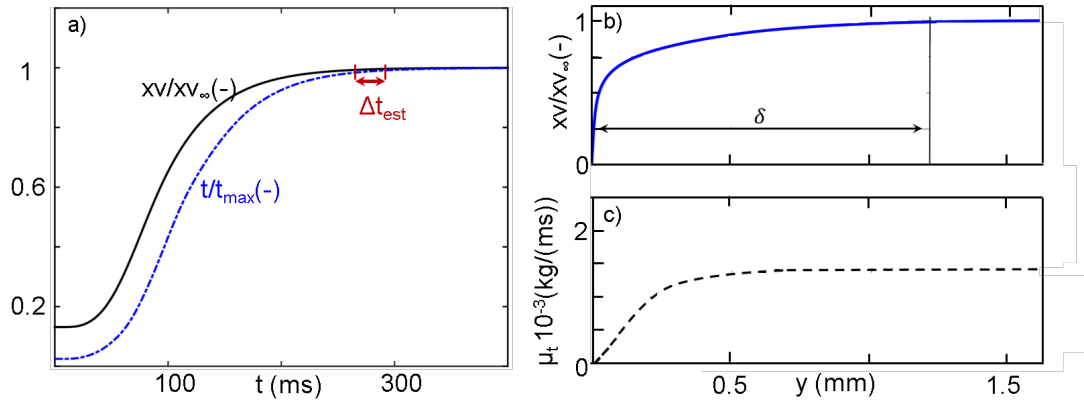


Fig. 2.9. Diffusion delay across the boundary layer a) Wall shear stress establishment delay; b) Boundary layer profile; c) Turbulent viscosity distribution across the near wall flow region

As a consequence of the higher boundary layer thickness, the thermal boundary layer establishment will happen only after the aerodynamic boundary layer establishment. Which is conducive to a later settlement of the final heat flux rate compared to the wall shear stress or the mean flow quantities.

2.3 Periodic mean flow oscillations

For the analysis of the boundary layer response to periodic perturbations the same numerical domain displayed in Figure 2.1 a) was used. Where the inlet total pressure followed a pure sinusoidal profile with a mean level of 105 kPa and an absolute amplitude of 4 kPa, ($P_0 \in [101 \text{ } 109 \text{ kPa}]$). Figure 2.1 c) represents two consecutive periods of the imposed total pressure. To analyze the phenomena at low and moderate pulsating flow regimes, the following frequencies were explored: 5, 10 20 50,100 and 1000 Hz. For comparison purposes 80 steady evaluations were performed at various total pressures along the period to mimic the performance of the transient assuming quasi-steady behavior.

The unsteady convergence of the simulations for all the excitation frequencies was ensured prior to the data acquisition based on the methodology outlined by Clark

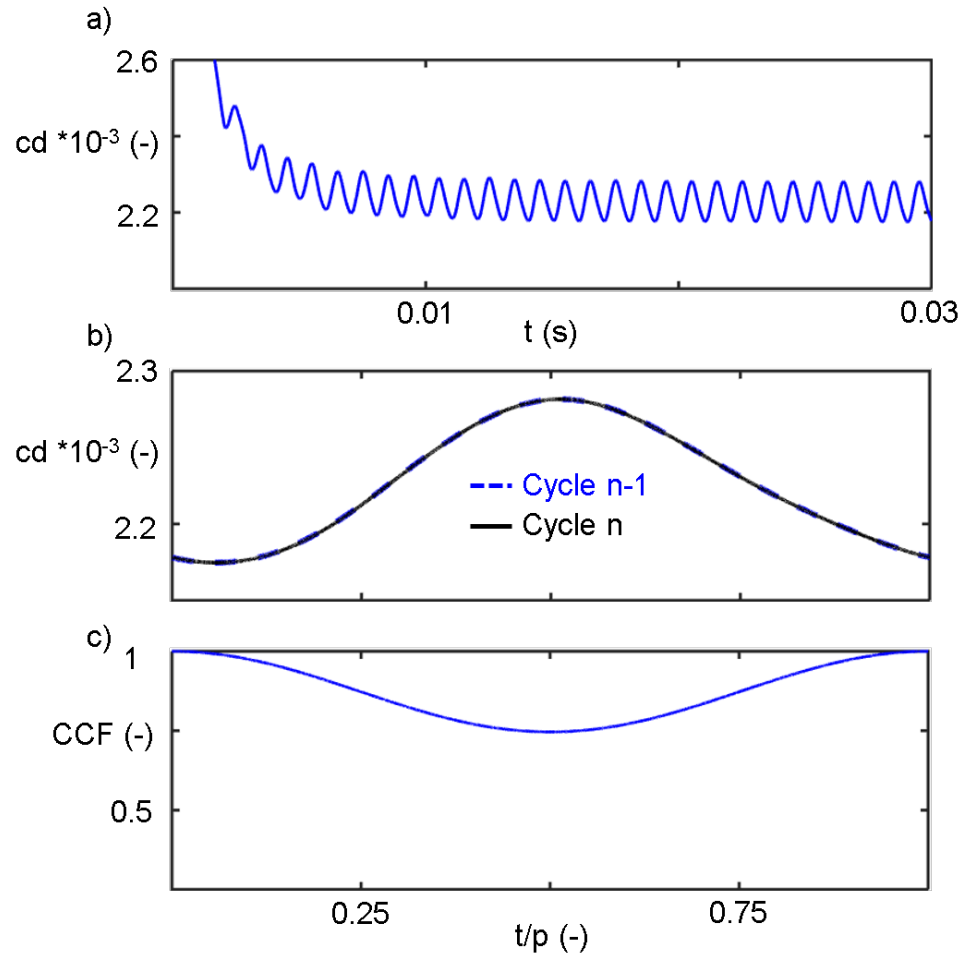


Fig. 2.10. a) Drag coefficient evolution during the transient simulation; b) Drag coefficient representation for two consecutive periods after convergence; c) Cross correlation factor between two consecutive periods after convergence

and Grover [65]. Which evaluates, the phase, amplitude, mean value and the cross correlation for each single cycle. Figure 2.10 a) represents the drag integration along the entire plate domain for the transient evaluation. There is a clear phase where the drag suffers substantial variations, symptoms of non-converged conditions until approximately $t=0.01$ ms. Later on, the cycle to cycle variations are mitigated.

Taking advantage of the periodic convergence definition of Clark and Grover once a negligible difference between two consecutive cycles is identified, the solution is

considered periodic. Figure 2.10 b) represents two consecutive periodic cycles after the convergence assessment. Similarly, Figure 2.10 c) depicts the cross correlation between them, which further supports the periodic convergence status. The cross correlation is a measure of similarity of the two signals as a function of the temporal shifting of one relative to the other. Consequently, when both signals are out of phase, as for instance when one is temporally displaced half a period with respect to the other $t/p = 0.5$, their correlation factor is reduced. However when the temporal displacement is again a complete period, the signals are in phase and the correlation factor is one, which further supports the periodic convergence status. Instead of referring to the various frequencies analyzed it results more convenient to use the non-dimensional Strouhal number of the domain. Where the frequency of excitation is divided by the frequency response of the domain:

$$St_{domain} = \frac{f_{excitation}}{f_{domain}} \quad (2.39)$$

The frequency response of the domain is defined as the time that the fastest characteristic takes to travel from the inlet to the outlet of the domain:

$$f_{domain} = \frac{L_{domain}}{c + \bar{x}v} \quad (2.40)$$

Using the mass-flow averaged velocity over an entire period the frequency response of the domain is approximately 1100 Hz. Each one of the excitation frequencies is translated into a Strouhal number (St_{domain}) as presented in Table 2.2.

Figure 2.11 a) represents the free stream axial flow velocity at $x=L/2$ for all the Strouhal numbers under analysis compared to the steady state cases. For low Strouhal numbers the results are similar to the steady state cases. However, as the Strouhal number gets closer to one the deviation from the steady state increases. Figure 2.11 b) represents the static pressure in the same location for the steady evaluations, and for three different Strouhal numbers, 0.009, 0.091 and 0.909. For low Strouhal numbers the acoustic and convective characteristics can travel along the domain multiple times before new changes are applied in the inlet. Consequently, the flow can smoothly ad-

Table 2.2.
Range of Strouhal numbers analyzed

Excitation Frequency	St_{domain}
5	0.0045
10	0.009
20	0.018
50	0.045
100	0.0921
1000	0.909

just to the new inlet conditions. However, for Strouhal numbers closer to unity, there is not enough time for the characteristics to commute across the domain and an average value is settled. In terms of static pressure, for the low Strouhal numbers there are moderate pressure and expansion waves travelling across the domain to establish the new flow conditions. While for larger Strouhal numbers, the strength of these waves is increased. Revealing that for actuation frequencies similar to the frequency response of the domain, the plate suffers the passage of strong pressure and expansion waves that rapidly accelerate and decelerate the flow. Figure 2.11 c) represents the skin friction evolution for the same set of Strouhal numbers. Laminar and turbulent boundary layer skin friction correlations are also included in the representation. For low Strouhal numbers (0.009), during the final total pressure rise ($0 < t/p < 0.25$) the skin friction clearly underscores the prediction for turbulent flow, reaching values of almost laminar boundary layer conditions. On the contrary, for the latest total pressure decay ($0.5 < t/p < 0.75$), the skin friction exceeds the predicted turbulent boundary layer. However, for moderate or closer to unity Strouhal numbers, the deviations from the turbulent boundary layer prediction are much smaller and the value oscillates around the steady state simulations data. Nonetheless, the larger Strouhal

number result does not follow the skin friction predicted for turbulent boundary layer on the flow acceleration and deceleration.

Figure 2.11 d) depicts the heat transfer coefficient evolution over the entire actuation period. It also includes the heat transfer coefficient predictions from turbulent and laminar Nusselt correlations. For low Strouhal numbers the amplitude variations perceived on the heat flux are similar to the ones predicted for turbulent boundary layers, and on the same order of magnitude that the steady state evaluations. Although, there exists a phase lag associated with the settlement of the mean flow conditions and the diffusion of the information across the thermal boundary layer. For larger Strouhal numbers, the amplitude of the variations on the heat transfer coefficient are mitigated. The heat transfer coefficient on larger actuation frequencies tends to a mean level which is always above the laminar boundary predictions but also in disagreement with the turbulent prediction. Displaying lower values during the flow acceleration and larger during the flow deceleration. Table 2.3 and Table 2.4 summarize the mean level and amplitude of the fluctuations.

As the Strouhal number increases the mean level of the axial flow velocity, wall shear stress and heat transfer coefficient ascents. However, the amplitude of the variations of such quantities is reduced. Once the actuation frequency approaches the frequency response of the domain, the variables tend to a period averaged value. The raise of the mean levels with the Strouhal seems to follow a logarithmic evolution. In this sense, using a logarithmic least squares fitting, the mean level evolution for the wall shear stress and heat flux are derived. The predictions are referenced to the lowest Strouhal number results.

$$\bar{\tau}_{St} = \bar{\tau}_{0.0045} \times (0.036 \times \ln(St) + 0.19) + \bar{\tau}_{0.0045} \quad (2.41)$$

$$\bar{q}_{St} = \bar{q}_{0.0045} \times (0.013 \times \ln(St) + 0.07) + \bar{q}_{0.0045} \quad (2.42)$$

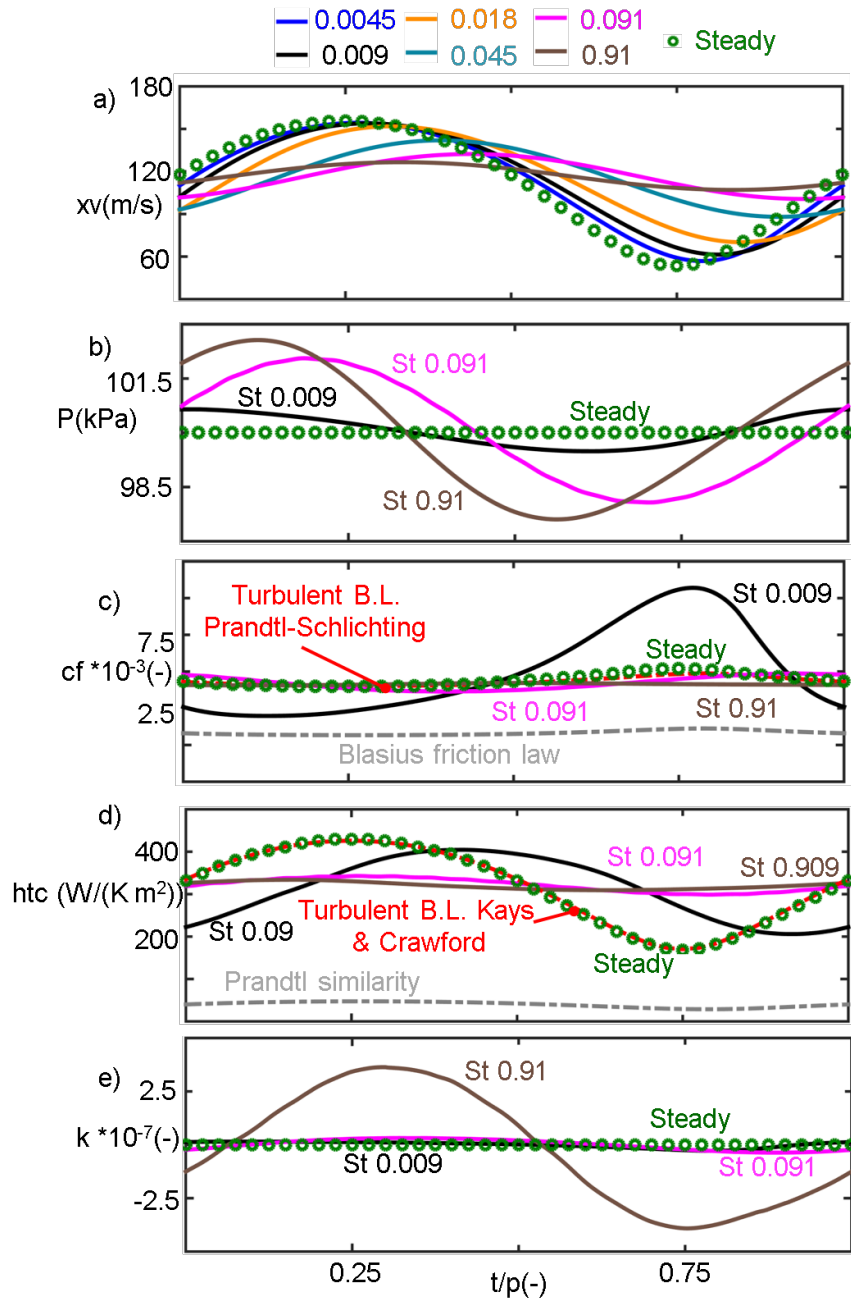


Fig. 2.11. Flow and wall fluxes response to periodic excitation at $x/L = 0.5$: a) Axial free stream velocity b) Static pressure c) Skin friction coefficient d) Heat transfer coefficient e) Acceleration parameter

The coefficient of determination for the wall shear stress and heat flux mean levels are 0.986 and 0.983 respectively. Taking advantage of this expression, the mean level of heat flux and wall shear stress for different excitation frequencies could be predicted.

Table 2.3.
Mean values during the periodic excitation

St_{domain}	$\overline{xv}(m/s)$	$\overline{\tau}(N/m^2)$	$\overline{htc}(W/m^2)$
Steady	117.7	20.54	329.6
0.0045	111.5	18.19	322.2
0.009	112.1	18.49	323.5
0.018	113.2	18.97	326.2
0.045	115.4	19.76	330.6
0.0921	116.5	20.04	332.5
0.909	116.9	20.05	331.5

Table 2.4.
Maximum amplitude of the oscillations during the periodic excitation

St_{domain}	$\Delta xv(m/s)$	$\Delta \tau(N/m^2)$	$\Delta htc(W/m^2)$
Steady	51.1	14.68	143.3
0.0045	48.7	9.88	124
0.009	46.3	8.98	109.1
0.018	40.9	7.31	83.8
0.045	27	4.49	41
0.0921	15.9	2.87	24.7
0.909	9.7	3.21	9.4

In terms of heat transfer, for the larger Strouhal numbers the deviations from the turbulent prediction could be a consequence of the boundary layer nature. In a similar way, based on the sudden flow acceleration analysis, we could expect that the fastest fluctuations will display higher skin friction coefficients since the inlet flow conditions changes happen at much faster rates. However, based on the results shown in Figure

2.11 c) we observe the contrary. For the highest frequencies, the amplitude of the skin friction coefficient is minimized; with values at least one order of magnitude smaller than the ones found for the slowest fluctuating rates. Trying to understand such behavior, Figure 2.12 represents the 2D contour of static pressure represented at 20% of the period ($t/p = 0.2$) for $St = 0.0045$ and $St = 0.091$ (top and bottom respectively).

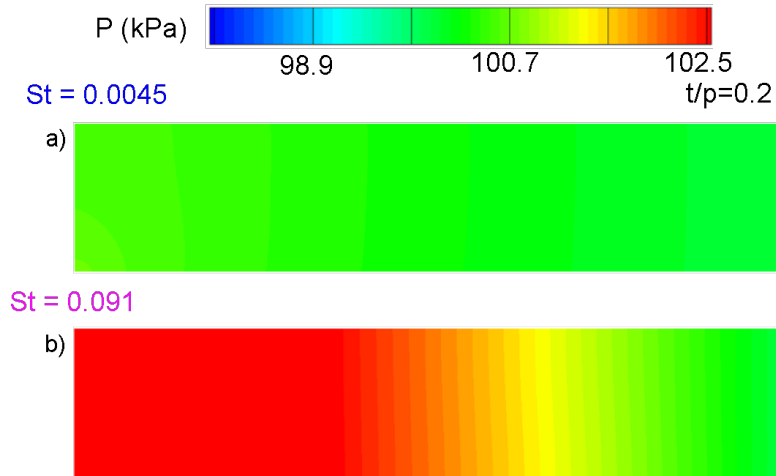


Fig. 2.12. Static pressure contour along the domain, a) 5Hz excitation; b) 100 Hz excitation

Based on the static pressure distribution it is clear that for the lower Strouhal number the domain gradually adjusts to the new inlet boundary conditions. Although, for larger Strouhal numbers there are relatively strong pressure waves that travel across the domain to adjust the flow to the inlet changes. The presence of strong positive and negative pressure gradient leads to sudden free stream flow decelerations and accelerations. The strength or rate of acceleration is quantified by the acceleration parameter (K).

$$K = \frac{\mu}{\rho x v_{\infty}^2} \frac{\partial x v}{\partial x} \quad (2.43)$$

The acceleration parameter is commonly used to determine the likelihood of flow re-laminarisation as studied by Launder and Jones [66] [67] and Spalart [67]. Fol-

lowing this formulation, for small fluctuating frequencies the acceleration along the plate results negligible with values around 10^{-15} , Figure 2.11 e). However, as the frequency increases the acceleration parameter reaches higher values getting closer to the threshold of flow re-laminarisation, which is set by most authors in the range of 3×10^{-6} to 3.5×10^{-6} [68]. For the analyzed frequencies, the maximum acceleration parameter found at mid cord was 4×10^{-7} , which is not enough to cause re-laminarisation but could have a significant influence on the wall fluxes by means of turbulence mitigation.

In the quest towards a better understanding on the effect of the acceleration parameter two different numerical domains are compared, Figure 2.13. The domain on the top simulates a plate submitted to a geometrically imposed negative pressure gradient, whereas the lower one is just a flat plate under uniform free stream conditions. Both domains were meshed following the guidelines set for the previous section. In this analysis the length of the domain is equal to 0.7m and the top wall is also modeled as a viscous isothermal wall at 300 K. The total pressure in the inlet for both domains was set at 100.7 kPa. The static pressure in the outlet of the straight domain was equivalent to atmospheric pressure at ground sea level, conducive to a free stream flow velocity of 36.64 m/s. The back pressure in the outlet of the accelerated domain was 85.78 kPa which lead a final flow velocity of 164.28 m/s. The area reduction was particularly designed to set an inlet flow velocity similar to the one in the straight domain.

Figure 2.14 represents the effect of a strong acceleration on the wall shear stress and heat transfer coefficient over a flat plate. While Figure 2.14 b) and c) depict the skin friction coefficient and the heat transfer coefficient respectively. The predictions for turbulent and laminar boundary layer correlations for flat plates are also included for comparison purposes. Natural transition onset takes place at about $x = 200\text{mm}$ and at approximately $x = 280\text{ mm}$ the boundary layer is fully turbulent. Right after that point, the flow starts being accelerated. As the acceleration parameter exceeds 1×10^{-7} ($x=350\text{mm}$) the skin friction coefficient and heat transfer coefficient deviate

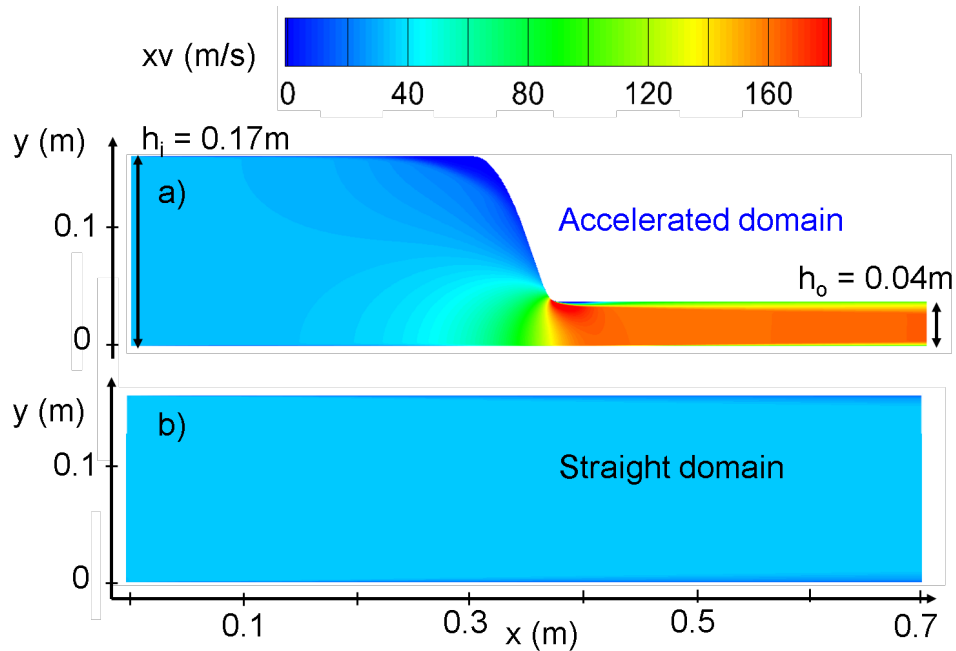


Fig. 2.13. Axial velocity contour along: a) Aggressive flow expansion through a nozzle contour; b) Flat plate configuration

from the turbulent prediction. Eventually, once the acceleration parameter reaches the threshold of 3×10^{-6} the boundary layer suffers re-laminarisation and the skin friction coefficient achieves almost laminar boundary layer values. In a similar way, the heat flux also experiences a decay because of the flow re-laminarisation. The reverse transition is the consequence of the turbulence mitigation due to the flow acceleration. Which freezes the eddies breakup and dumps the turbulence dissemination. Once the acceleration is completed, the near wall flow rapidly recovers its turbulent nature and the skin friction coefficient exhibits again similar values to the turbulent prediction.

As the flow is accelerated the boundary layer is initially stretched, as depicted in the boundary layer profiles in Figure 2.15, consequently the wall shear stress rises abruptly. At $x=0.35$ there exists an inflection point in the wall shear stress and suddenly it starts to decay. Looking at the profiles in Figure 2.15 there is not any evident symptom for such a sudden decrease in the wall shear stress since the boundary layer

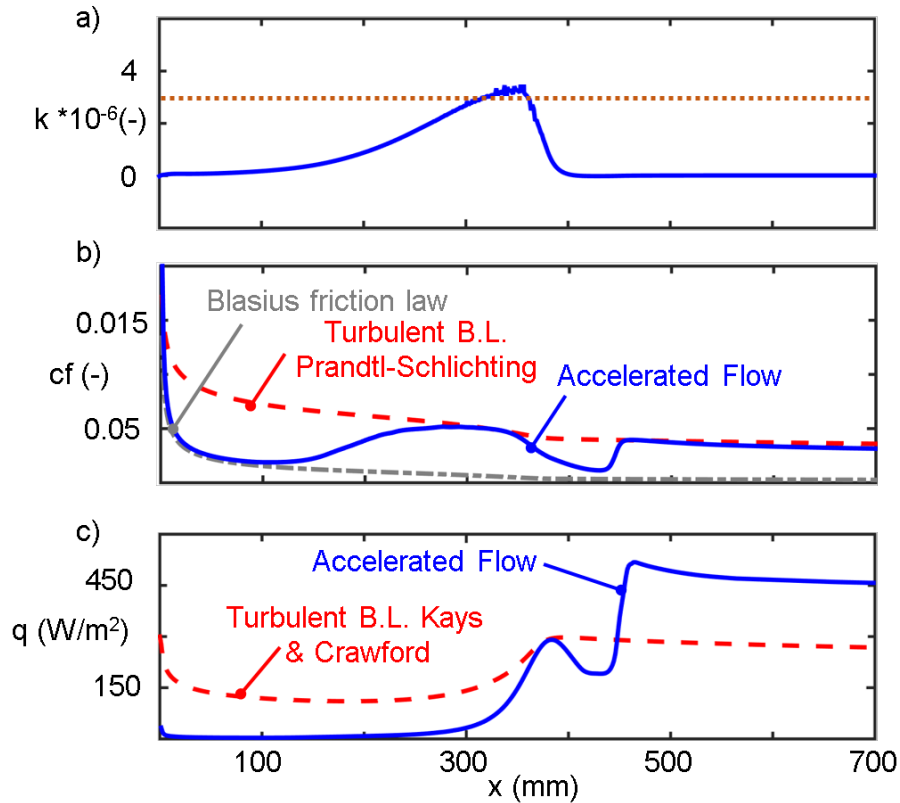


Fig. 2.14. Acceleration parameter effect on the aero-thermal boundary layer: a) Acceleration parameter b) Skin friction c) Heat transfer coefficient

profile still seems to depict a much narrower boundary layer. Although if we look at the wall non-dimensional velocity profiles displayed in Figure 2.16 a clear difference is disclosed for the axial location $x=0.3$ and 0.4 m. Figure 2.16 compares the velocity profile in non dimensional wall units for the straight and the accelerated domain for the log-law [4] and the nominal Blasius profile [3] [69]. At $x = 0.3$ and 0.4 m the boundary layer of the accelerated domain reveals a similar profile compared to the Blasius boundary layer, which clearly denotes the reverse transition phenomena.

Due to the flow acceleration the turbulent eddies break up is frozen and the wall shear stress is reduced. Downstream in the plate, at $x = 0.45$ the wall shear stress suddenly increases reaching a much higher value than the one prior to the boundary

layer re-laminasization. That point coincides with the end of the convergent section in the domain and reveals that once the flow acceleration is over the flow turbulence is suddenly released conducting towards nominal turbulent wall fluxes.

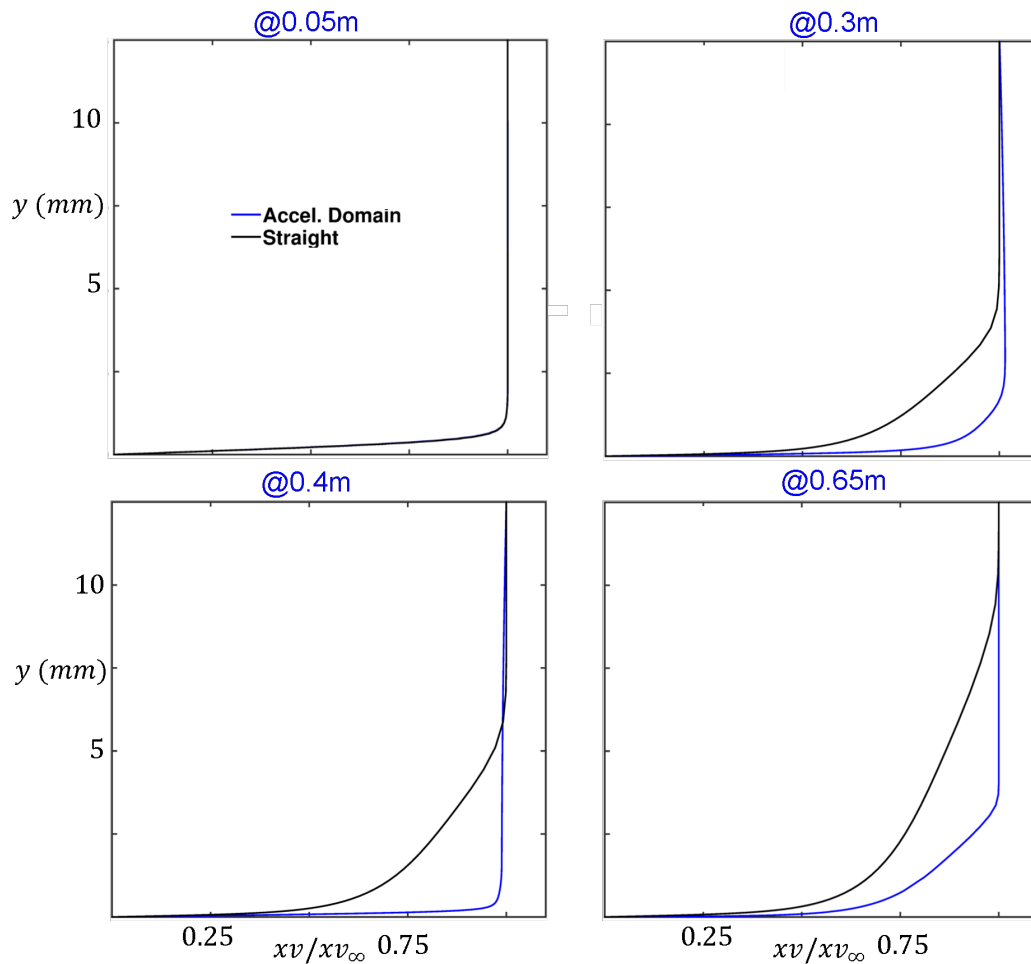


Fig. 2.15. Boundary layer profiles at several axial locations for flat plate and sudden expansion domain (black and blue respectively)

This analysis represents the effect of a static pressure gradient over the flat plate. Translating this analogy onto dynamic pressure gradients across the flat plate, it reveals the strong influence of mean flow variations on the wall fluxes distribution along the plate. By means of the local flow acceleration, the dynamic pressure gradients alter the nature of the boundary layer and its turbulent status.

In order to verify the accuracy of our numerical model resolving the near wall flow and predicting reverse transition, the experimental analysis performed by Bader et al. [70] on the flat plate boundary layer in accelerated flow was numerically replicated. Figure 2.17 a) represents the numerical discretization of the experimental test section of Graz University. Where the boundary conditions are: $xv_\infty = 4.824\text{m/s}$, $T = 318\text{ K}$, $P_s = 97.7\text{ kPa}$ and $Tu = 5.45\%$.

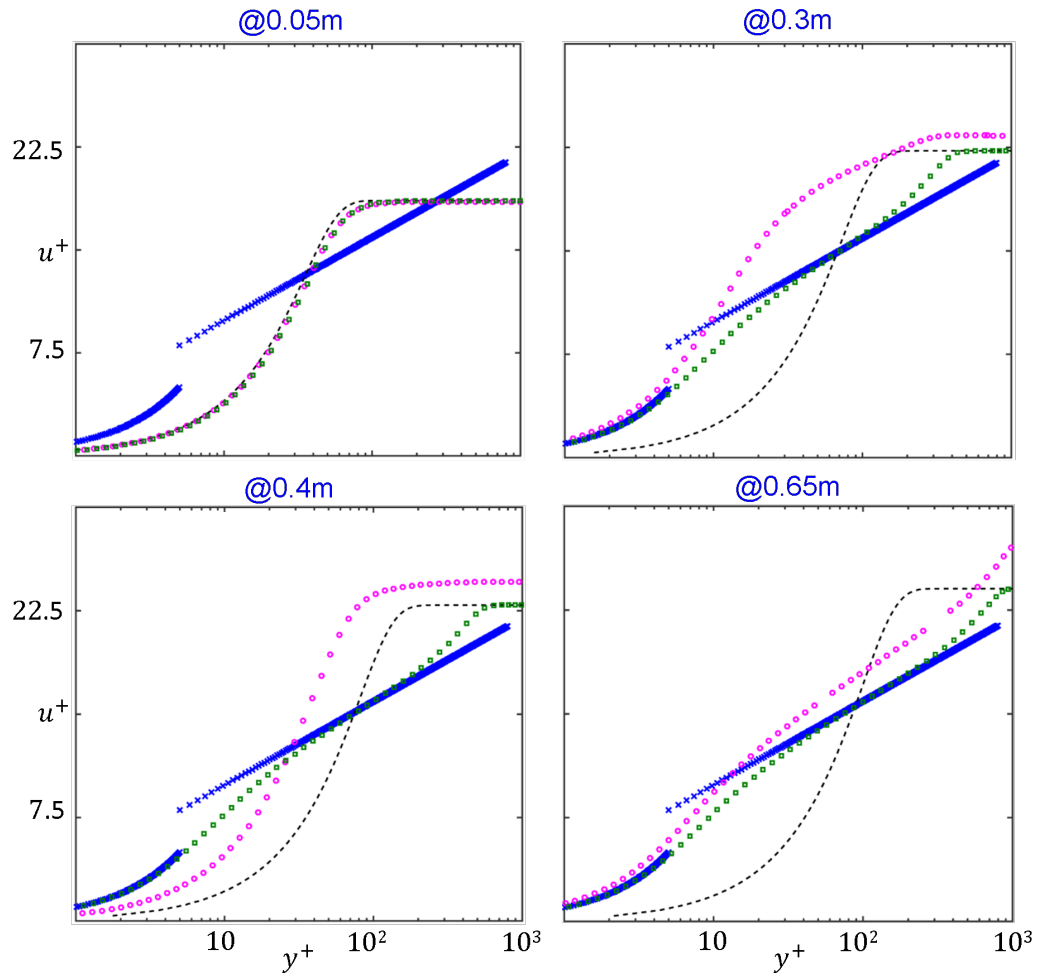


Fig. 2.16. Wall non-dimensional boundary layer profiles at several axial locations for flat plate and sudden expansion domain (black and blue respectively))

Figure 2.17 b) represents the velocity magnitude contour in the modeled test section. While Figure 2.17 c) compares the skin friction coefficient retrieved with the current numerical set-up to the experimental results of Bader et al.; including laminar and turbulent boundary layer skin friction correlations. Overall, there is an excellent agreement between the numerical and the experimental results. The only discrepancy takes place on the transition tripping, where the numerical results overshoot the experimental findings due to the differences on the tripping approaches. However, in terms of capturing the boundary layer re-laminarisation the comparison of the results is satisfactory. Further validations of the numerical solver and the selected settings can be found in Appendix 1, Fluent Validation.

Looking again at the flat plate exposed to periodic inlet fluctuations. Under constant inlet temperature and fixed back pressure, the variations on the free stream velocity drive the evolution of the Reynolds number. Which eventually determines the boundary layer height. Figure 2.18 represents the boundary layer displacement thickness along the periodic inlet fluctuation, suffering the highest amplitude variations for the smaller Strouhal numbers. Similarly, Figure 2.19 represents the momentum boundary layer profiles for all the frequencies and the steady evaluations at different time steps along the period.

Comparing the boundary layer displacement thickness evolution against the skin friction representation in Figure 2.11 c) there is a considerable phase lag of about half a period between the mean flow maximum speed and highest wall fluxes for the smallest Strouhal number. This phase lag is a consequence of the diffusion delay across the boundary thickness. There is shrinkage of the boundary layer at the velocity profiles for $t/p = 3/4$ as a consequence on the flow inertia after the sudden flow acceleration driven by the pressure rise.

The boundary layer stretching is maximum for the low Strouhal numbers where the absolute velocity variation amplitudes are larger. As the excitation frequency increases, the magnitude of the velocity fluctuation is reduced, and the boundary layer suffers less contraction. On the other hand, at $t/p = 1/4$ the boundary layer

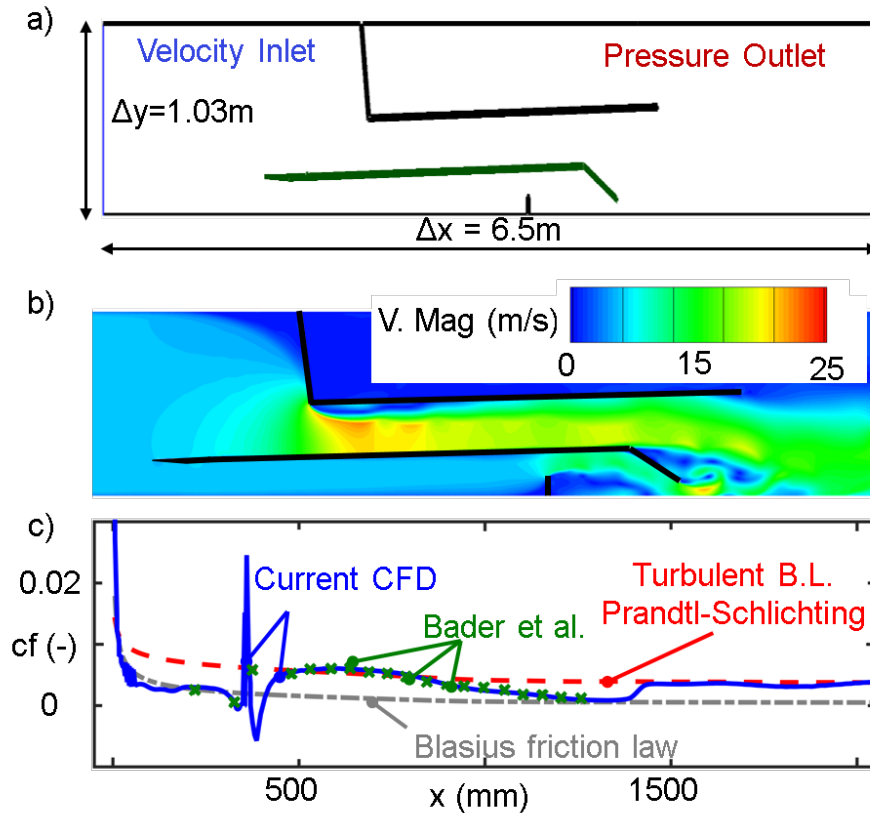


Fig. 2.17. a) Numerical replication of experimental test section for boundary layer reverse transition validation b) Velocity magnitude contour along the simulated test section c) Skin Friction coefficient over test article

has its maximum thickness, associated with the slowest flow velocity condition and a decelerating trend. For the smaller Strouhal numbers the deviations from the steady state evaluations boundary layer thickness are at its maximum. The profiles of larger Strouhal number do not seem to depart much from the steady boundary layer results and preserve a constant boundary layer thickness because of the averaging of the inlet flow conditions.

Figure 2.20 represents the thermal boundary layer profile for all the Strouhal number under scrutiny at various phases of the evolution. For lower excitation frequencies, the thermal boundary layer thickness suffers notorious variations as a con-

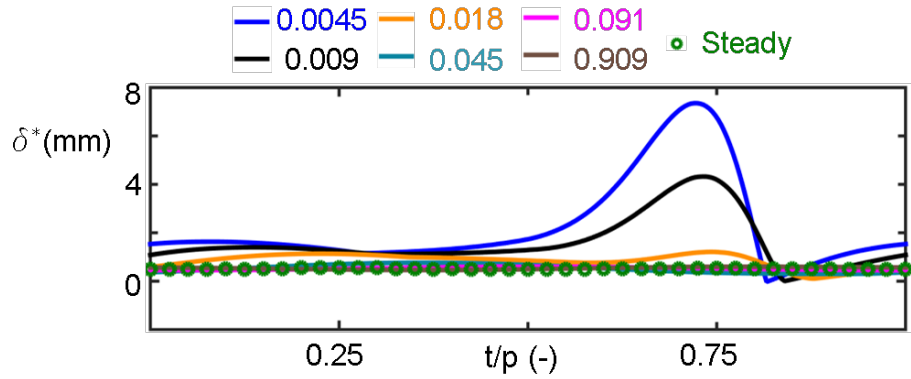


Fig. 2.18. Boundary layer displacement thickness temporal evolution at $x/L = 0.5$ for various excitation frequencies

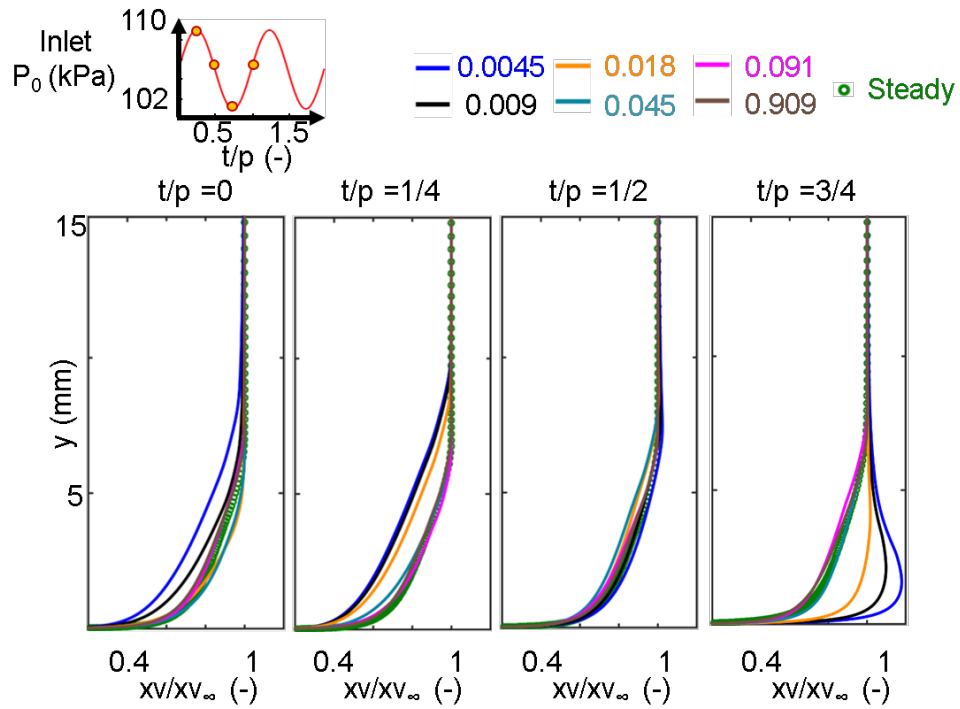


Fig. 2.19. Momentum boundary layer profiles evolution along the excitation period, transient periodic excitation and quasi-steady comparisons

sequence of the mean flow acceleration and deceleration, dictating the span of the heat transfer coefficient amplitude. It is notorious how even displaying much thinner

thermal boundary layers, like the ones at $t/p = 3/4$ the near wall region does not completely adjust to this conditions because of the diffusion delay. Consequently, the heat transfer coefficient during these phases does not overshoot the turbulent boundary prediction or the steady state result. Hence, the thermal diffusion delay prevents the near wall flow to generate much higher heat flux rates than the steady turbulent evaluations. On the other hand, for the higher excitation frequencies, although displaying similar boundary layer thickness to the ones exhibited in the steady state evaluations, their heat flux rates do not follow the same trend. This is the consequence of the sudden flow variations effect modulating the boundary layer nature. Where the steady evaluations reflect their higher heat transfer coefficient, the larger Strouhal numbers experienced their larger acceleration parameter, which mitigates the turbulence and reduces the heat flux rate.

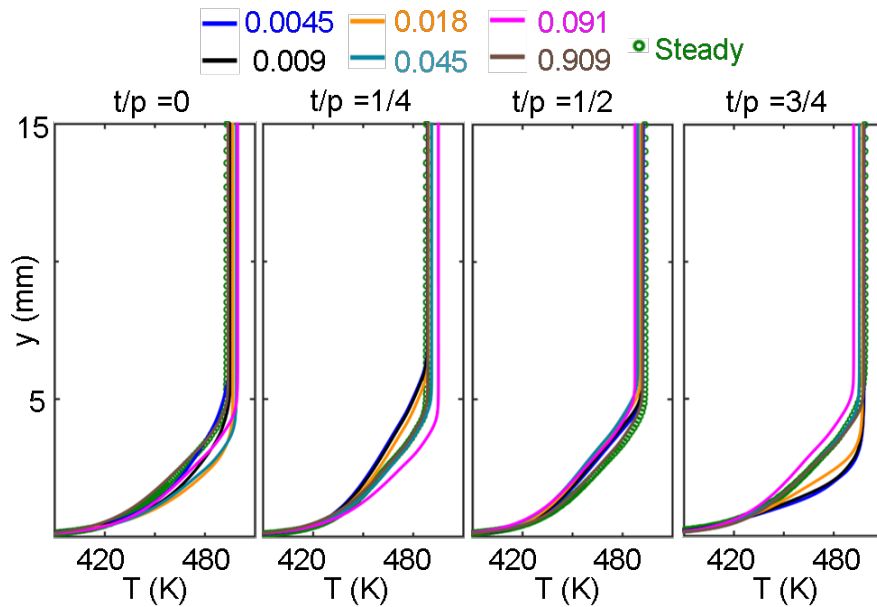


Fig. 2.20. Thermal boundary layer profiles evolution along the excitation period, transient periodic excitation and quasi-steady comparisons

2.4 Detailed simulation on the boundary layer reaction to sudden flow acceleration

In order to verify the modeling capabilities of the selected URANS methodology and take a closer look at the physics involved in the boundary layer dynamic reaction, a sudden flow acceleration from Mach 0.3 to Mach 0.6 will be compared to the results of a Direct Navier Simulation, [71] [72]. Based on Direct Numerical Simulations (DNS), both the mean properties and integral boundary layer properties are analyzed. Taking advantage of the higher resolution analysis and the 3D boundary layer momentum integral equations a simplified integral model is developed to predict the compressible turbulent boundary layer growth under free-stream transient behavior. Finally, taking advantage of the transient boundary layer development model and current skin friction correlations, the shear stress evolution along the transient can also be estimated.

2.4.1 Description of numerical approach

Numerical Domain

The analysis is focused on a flat plate geometry that allows the extrapolation of the results to a myriad of configurations. Figure 2.21 depicts the numerical domain for the transient evaluation of the compressible turbulent boundary layer evolution driven by sudden flow acceleration. The total length of the domain (L) was equal to 128.5 times the height of the inlet boundary layer ($\delta_0=8$ mm). The global length of the domain determines the acoustic response of the test geometry and constrains the establishment time of the mean flow characteristics. For the Direct Numerical Simulations the finely resolved region ended at $100 \delta_0$ (Lx), and grid stretching was employed in the remainder of the domain to support the outflow boundary condition (a sponge layer). The total height of the domain (H) was equal to $125 \delta_0$, ensuring minimal influence of the boundary layer displacement thickness (δ^*) growth on the

free-stream velocity, ($H > 150 \delta^*$). For the direct numerical simulations, the mesh was finely resolved till $7 \times \delta_0$ (Hx), with grid stretching employed for the rest of the domain in the wall-normal direction. The width of the domain (W) is $28 \times \Delta_0$. The Direct Numerical Simulations results are averaged across the span wise direction to provide smoother 2-D transient conditions throughout the acceleration.

The computational mesh consisted of about 376 million points arranged in a $2026 \times 326 \times 569$ structured mesh. The sponge layers at the top and end of the domain consisted of 25 points, with a stretching factor of 1.2. An overlap layer of 9 points was used to enforce a periodic boundary condition in the spanwise direction. Since the free-stream flow conditions varied, so did the non-dimensional grid spacing. For the flow conditions most challenging for numerical accuracy, the grid resolution in the resolved region was $\Delta x^+ = 32$ in the stream-wise direction and $\Delta z^+ = 32$ in the span-wise direction. The resolution in the wall-normal direction varied from $\Delta y^+ = 0.7$ at the wall to $\Delta y^+ = 24$ at the boundary layer edge. These parameters correspond to the final boundary layer state; the values for the initial boundary layer state were about half as large. The largest non-dimensional time step for the calculations was about $\Delta t^+ = 0.3$ with an equivalent dimensional time step of $0.5 \mu s$.

The Direct Numerical Simulations were carried out on 4320 cores, with 360 sub-domains ($20 \times 3 \times 6$) parallelized using MPI, and with 12 OpenMP threads per MPI rank. Data for computing turbulence statistics were saved every 200 computational steps (every 0.1 ms) for the following planes: $x/\delta_0 = 100$, $y/\delta_0 = 0$, $z/\delta_0 = 14$. For the 10 ms rise time, at total of 198000 time steps (99 ms) were computed, while 300000 time steps (150 ms) were evaluated for the 25 ms rise time.

Boundary conditions

In order to model the sudden flow acceleration in the numerical domain the static pressure level was fixed at 16 kPa in the outlet, right boundary. The inlet of the domain was modeled as a pressure boundary condition where the total temperature

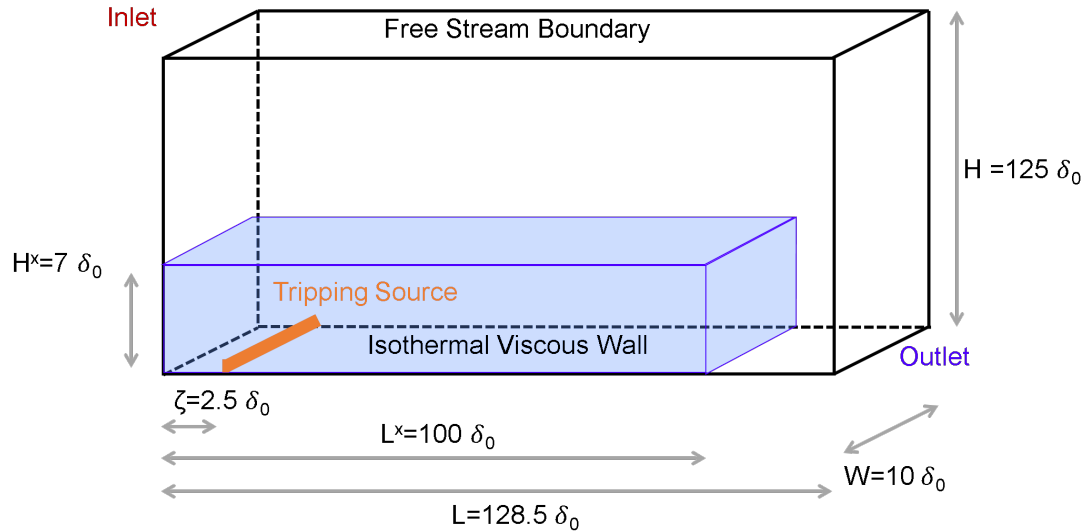


Fig. 2.21. Direct Numerical Simulations numerical domain

was kept constant at 500K. The free-stream flow acceleration was imposed following total pressure transient profile, $P_0(t)$. The total pressure rise in the inlet was modelled following the smoother step function [73] evolution 2.44, as depicted in Figure 2 a). The use of the smoother step function guarantees the continuity of the signal through the pressure rise. For the first 36.4 ms of the simulation, $t < t_0$, the total pressure was set at 17 kPa simulating the steady state conditions for Mach 0.3 flow, where the Reynolds number based on the momentum thickness is 1202 at L^* . Then the total pressure was raised to 20.5 kPa over 10 ms following the smoother step profile. Finally, the total pressure was kept at 20.5 kPa up to $t = 100$ ms to reach steady flow conditions at Mach 0.6. The steady flow conditions at the initial and final status are summarized in Table 2.5. A second transient acceleration with a rise time of 25 ms was evaluated to explore the impact of the acceleration rate and to verify the accuracy of the developed model. The top wall of the domain was modeled as an adiabatic inviscid wall. (employing extrapolation during the DNS evaluations) While the plate was simulated as a viscous isothermal surface at 300 K. A periodic boundary condition was imposed in the span-wise direction for the lateral boundaries of the domain.

$$P_0(t) = \begin{cases} & \text{if } t < t_0 \\ 17 + 3.5 \left(6 \left(\frac{t-t_0}{\Delta t} \right)^5 - 15 \left(\frac{t-t_0}{\Delta t} \right)^4 + 10 \left(\frac{t-t_0}{\Delta t} \right)^3 \right) & \text{if } t_0 < t < (t_0 + \Delta t) \\ 20.5 & \text{if } t > (t_0 + \Delta t) \end{cases} \quad (2.44)$$

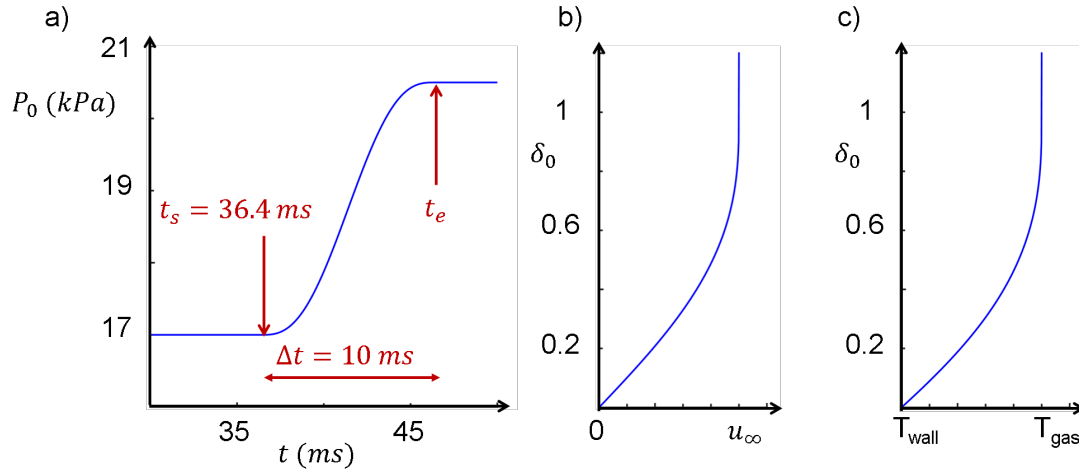


Fig. 2.22. Inlet boundary conditions; a) P_0 transient profile, b) Initial momentum boundary layer, c) Initial thermal boundary layer

An initial laminar boundary layer was imposed at the inlet with a height of 8 mm, δ_0 . The momentum boundary layer followed a Polhausen profile, eq. 2.45. Similarly, the thermal boundary layer was derived from the momentum one taking advantage of the Crocco relation for temperature, eq. 2.46. Both momentum and thermal boundary layer are depicted on Figure 2.22 b) and c) respectively.

$$u = u_\infty \left(2 \left(\frac{y}{\delta_0} \right) - 2 \left(\frac{y}{\delta_0} \right)^3 + \left(\frac{y}{\delta_0} \right)^4 \right) \quad (2.45)$$

$$u = T_{wall} + (T_{gas} - T_{wall}) \left(\frac{u}{u_\infty} \right) + \frac{1}{2} \sqrt{Pr} (\gamma - 1) M^2 T_{gas} \left(\left(\frac{u}{u_\infty} \right) - \left(\frac{u}{u_\infty} \right)^2 \right) \quad (2.46)$$

Table 2.5.
Steady Initial and Final flow conditions

	P_0 (kPa)	P (kPa)	T_0 (K)	M	Re_θ
Initial condition	17	16	500	0.2968	1202
Final condition	20.5	16	500	0.6061	2162

Boundary Layer Trip

To resolve the impact of the sudden flow acceleration on a fully developed turbulent boundary layer a trip model was employed to promote the transition of the initial laminar boundary layer. The artificial body force term used here was similar to the one applied by Mullenix et al. [74] and Bisek et al [75]. A counter-flow body force was enforced near the wall, $2.5 \delta_0$ downstream of the inlet plane. For the Unsteady Reynolds Average Navier Stokes computations, the source term imposed a 5 kN body force with an angle α of 5 degrees over a rectangular region of $1.25 \times 0.125 \delta_0$ cross section. The source term was continuously applied uniformly across the span of the domain, as displayed in Figure 2.23. For the Direct Numerical Simulation, the trip had the following form:

$$F = \frac{F_0}{\pi x_r y_r} \exp\left(-\left(\frac{x-x_0}{x_r}\right)^2 - \left(\frac{y-y_0}{y_r}\right)^2\right) \quad (2.47)$$

$$f_x = F \cos \alpha \quad (2.48)$$

$$f_y = F \sin \alpha \quad (2.49)$$

Where the non-dimensional values of the parameters are: $F_0=0.03$, $x_0=2.5$, $x_r=0.17$, $y_0=0$, $y_r=0.01$, $\alpha = 1$. The non-dimensional values are based on reference parameters of $\delta_R=0.11 \frac{kg}{m^3}$, $U_R=131.9$ m/s, $\delta_0=8.0$ mm.

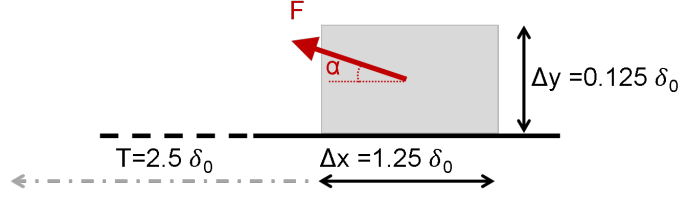


Fig. 2.23. Boundary layer transition enhancement through the addition of a momentum source that mimics the presence of an obstacle

Solvers

Regarding the numerical solvers, the three-dimensional compressible Navier-Stokes equations are solved directly without modeling using the code HOPS (Higher Order Plasma Solver), developed by Professor Poggie [71, 72]. The physical model consists of the perfect-gas, compressible-flow formulation. The conservation of mass, momentum, and energy are formulated as:

$$\frac{\partial \rho}{\partial t} + \frac{\partial}{\partial x_j}(\rho u_j) = 0 \quad (2.50)$$

$$\frac{\partial \rho u_i}{\partial t} + \frac{\partial}{\partial x_j}(\rho u_j u_i - \sum_{ij}) = f_i \quad (2.51)$$

$$\frac{\partial \vartheta}{\partial t} = \frac{\partial}{\partial x_j}(u_j \vartheta - \sum_{ij} u_i - Q_j) = f_i u_i + S \quad (2.52)$$

where ρ is the gas density, u_i is the velocity, \sum_{ij} is the total stress tensor, $\vartheta = \rho(\epsilon + u_k u_k/2)$ is the total energy of the fluid, ϵ is the internal energy and Q_j is the heat flux. The additional terms f_i and S are included to account for optional body force and energy sources.

The total stress tensor \sum_{ij} is given by the constitutive equation for a Newtonian fluid, and the heat flux Q_j follows Fourier's heat conduction law.

$$\sum_{ij} = -p\delta_{ij} + \mu \left(\frac{\partial u_i}{\partial x_j} + \frac{\partial u_j}{\partial x_i} \right) - 2/3\mu \frac{\partial u_k}{\partial x_k} \delta_{ij} \quad (2.53)$$

$$q_i = -\kappa \frac{\partial T}{\partial x_i} \quad (2.54)$$

Being p the pressure, μ the viscosity and κ the thermal conductivity. The transport coefficients were evaluated using the correlations given by White [76]. The working fluid (air) was assumed to be a calorically and thermally perfect gas such that $\epsilon = c_v T$ and $p = \rho RT$, where T is the temperature, c_v is the specific heat and R is the gas ideal constant. The spatial derivatives were evaluated with sixth-order compact differences, and stability was enforced with an eighth-order Pade-type filter. Near the domain boundaries, the filter order was reduced in steps of two, with no filtering at the boundary itself. Similarly, the accuracy of the spatial scheme was reduced to fifth-order and fourth-order accuracy near boundaries. Time marching was carried out using a second-order implicit scheme. Further details on the numerical methods of the solver are given in [71]. For validation of the numerical model the experimental results of Elena and Lacharme [77], Alving [78] and Konrad [79] for the streamwise velocity profile of a turbulent boundary layer and the Reynolds normal stress were used, as presented in [71] and [72].

To assess the capabilities of Reynolds-averaged Navier-Stokes solvers modelling the free-stream transient evolution impact on the near wall region the commercial software ANSYS Fluent was used. To reduce the computational burden the simulations on this solver were carried out on a 2D version, considering the center-plane of the domain. The plane was meshed following a blocking strategy with ANSYS ICEM. In order to guarantee a proper geometrical discretization, a grid sensitivity study was accomplished following the approach outlined by Celik et al. [50]. For this purpose, the axial flow velocity just outside of the boundary layer and the boundary layer momentum thickness were acquired for all the different grids. The different spatial discretization models were tested at the final steady state condition, $P_0 = 20.5$ kPa, $T_0 = 500$ K, $T_{wall} = 300$ K, $P = 16$ kPa. A summary of the different mesh properties is also presented in Table 2.5.

Table 2.6.
Mesh sensitivity for 2D URANS simulations

Cell Count	N_x	N_y	u_∞ (m/s)	θ (mm)	GCI %
48600	270	180	260.90	2.60	33.8
83200	320	260	261.60	2.40	10.8
140000	400	350	261.94	2.34	1.8
235200	560	420	261.98	2.33	1.7
400000	800	500	261.95	2.34	

The mesh with 140000 cells was selected for the transient evaluation given its accuracy compared to the finer cases and its grid convergence indicator. To enhance correct near wall flow prediction the y^+ was maintained below 0.5 along the entire plate. In this approach the turbulence closure was achieved through the use of the Langtry-Menter four-equation Transitional SST model [51]. The working fluid was air, modeled as an ideal gas. The Sutherland law was implemented to include the effect of the temperature on the molecular fluid viscosity. Second-order upwind schemes were adopted for the flow and turbulent kinetic energy, while second order implicit schemes were used for the transient formulation. This methodology was previously verified against experimental results on flat plate accelerated flow, presented in [43].

Figure 2.24 a) and b) compare the axial velocity and density boundary layer profiles for URANS and DNS simulations at the initial and final steady flow conditions of the evolution. The URANS results slightly depart from the DNS profiles near the wall region, which falls within the accuracy of the URANS models on predicting the near wall region under this low Reynolds number environment. In terms of the momentum boundary layer thicknesses the integral values obtained are displayed in Table 2.7; the URANS have only a 5% deviation from the DNS results. Figure 2.24 c) depicts the shear stress profiles at initial and final conditions for both solvers. For the initial steady flow condition URANS transitional model predicts an earlier

fully developed turbulent boundary layer and the magnitude of shear stress along the plate does not deviate much from the DNS. However, for the final flow condition at higher Reynolds number the URANS also predict an earlier complete transition but the axial shear stress magnitude deviates about 30% from the Direct Numerical Simulation results. In addition to the turbulent simulations laminar evaluations were carried out to compare the impact of sudden free-stream variations over laminar and turbulent boundary layers.

Table 2.7.
DNS vs URANS for steady flow conditions

	P_0 (kPa)	T_0 (K)	T_w (K)	P (kPa)	θ (mm)
DNS	17	500	300	16	2.8
URANS	17	500	300	16	2.89
DNS	20.5	500	300	16	2.24
URANS	20.5	500	300	16	2.34

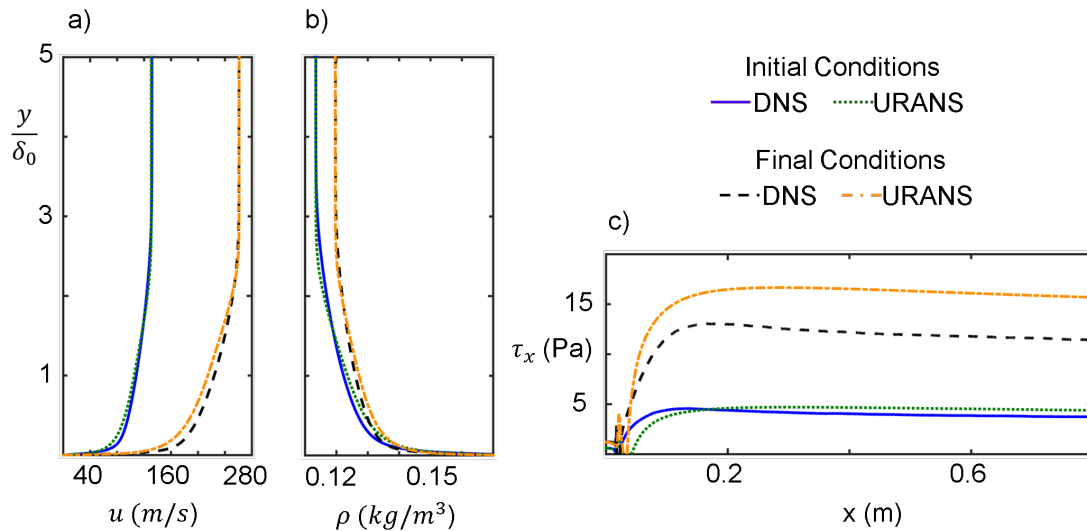


Fig. 2.24. Steady State Comparison DNS vs URANS for initial and final conditions

2.4.2 Boundary layer and wall fluxes evolution after sudden flow acceleration

Figure 2.25 represents the evolution of the gas density across the center-plane of the domain for several time steps along the flow acceleration. The first image corresponds to the conditions prior to the total pressure rise. The boundary layer transition is enhanced by the tripping near the domain inlet and fully developed turbulent boundary layer flow is present in the second half of the domain. The second time step depicts the density contour at half of the total pressure rise. Due to the passage of the pressure waves slightly larger density is present near the plate leading edge. This phenomenon is further enhanced once the final total pressure is set at $t=46.4$ ms. As a consequence of the delay on the arrival of the expansion waves from the outlet, the density at the front of the domain is up to 15% larger than at the trailing edge of the plate. Finally, the domain establishes at the final condition as depicted for $t = 99$ ms.

Figure 2.26 a) depicts the axial free-stream velocity (u_∞) temporal evolution at $y = 7\delta_0$ at the end of the resolved region, L_x . The results from DNS, URANS and the laminar simulation fall on top of each other, depicting the same acoustic response in the three numerical setups for the imposed transient. Similarly, Figure 2.26 b) displays the flow acceleration parameter, (k), at the same location. The acceleration parameter:

$$k = \frac{\mu}{\rho x v_\infty^2} \frac{\partial x v}{\partial x} \quad (2.55)$$

represents the acceleration rate progress along the transient at the end of the resolved region. This factor is commonly used for the prediction of flow re-laminarisation [66,67]. There are two different phases present in the acceleration. At first, following the arrival of the initial pressure wave the acceleration parameter displays negative magnitude. Figure 2.27 represents the propagation of the characteristics along the domain following the total pressure raise at the inlet. As the total pressure increases

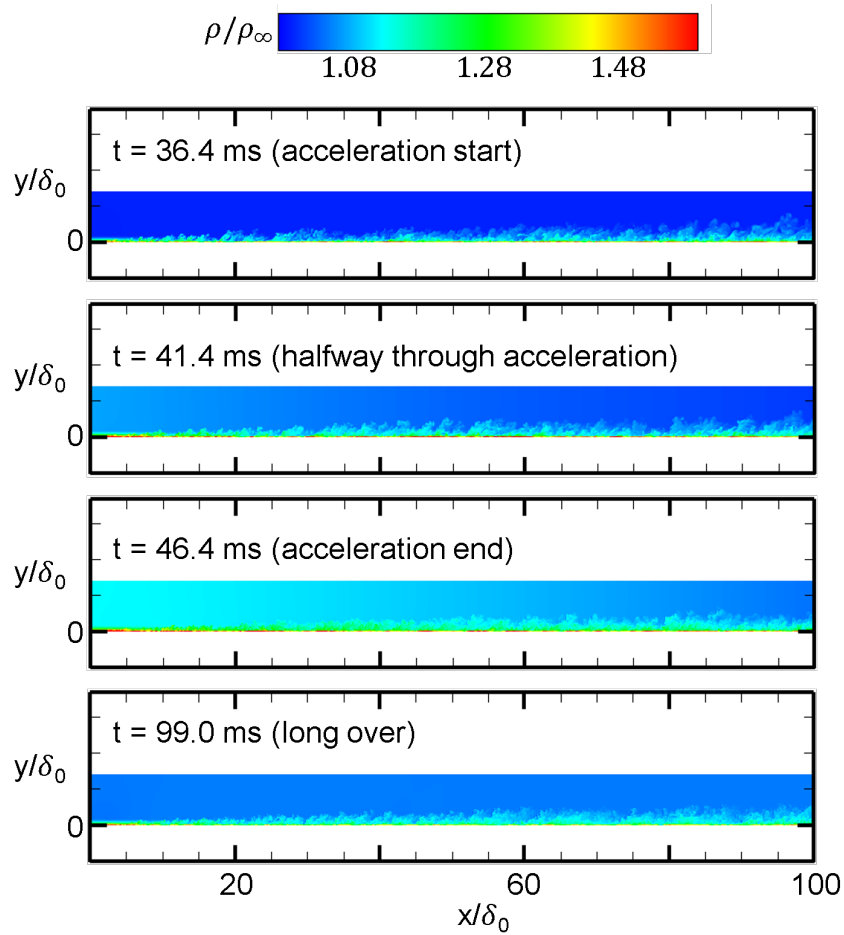


Fig. 2.25. 2D contour of density along center plane for several time steps along the transient evolution

in the inlet to initiate the acceleration a pressure wave is released. The pressure wave travels along the domain at the speed of sound (c) plus the actual free-stream velocity (xv). As the pressure wave cruises over the plate it accelerates the flow, and consequently faster flow is present behind it, driving a negative acceleration parameter. Once the pressure front reaches the domain outlet it is reflected as an expansion wave that travels upstream at $c - xv$. The arrival of the expansion wave at the observation plane is represented by the increment of the acceleration parameter. The peak of acceleration parameter takes place for the final phases of the acceleration after the final steady state total pressure is set at the inlet. Figure 2.26 c) shows the local

free-stream flow temporal acceleration throughout the transient. The maximum local acceleration takes place at $t = 44$ ms, right at the inflection point on the acceleration parameter, when compression and expansion waves meet at the edge of the finely resolved region.

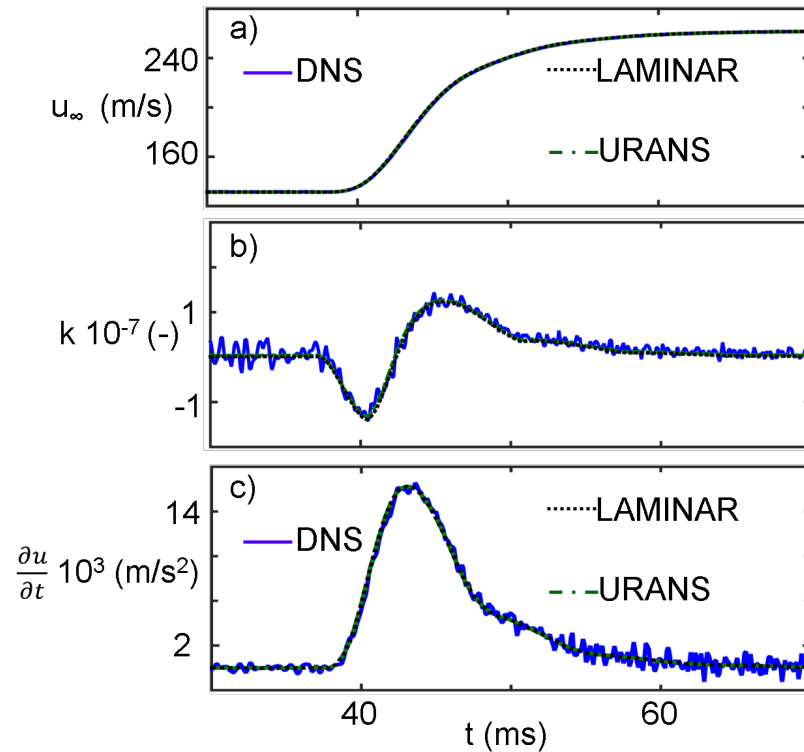


Fig. 2.26. Temporal evolution of free-stream flow conditions through the transient for DNS, laminar and URANS simulations; a) Axial free-stream velocity, b) Flow acceleration parameter, c) Local flow acceleration

The impact of the free-stream flow conditions is directly reflected in the near wall region as represented in Figure 2.28 a) and b) for the wall shear stress and heat flux respectively. Figure 2.28 a) depicts the evolution of the axial wall shear stress at the end of the finely resolved region. Both turbulent simulations display similar trends, although as already discussed in the comparison for steady conditions the k-SST model over predicts the wall flux magnitude at this low Reynolds number. There are two different phases present on the evolution of the heat flux, at first once the flow

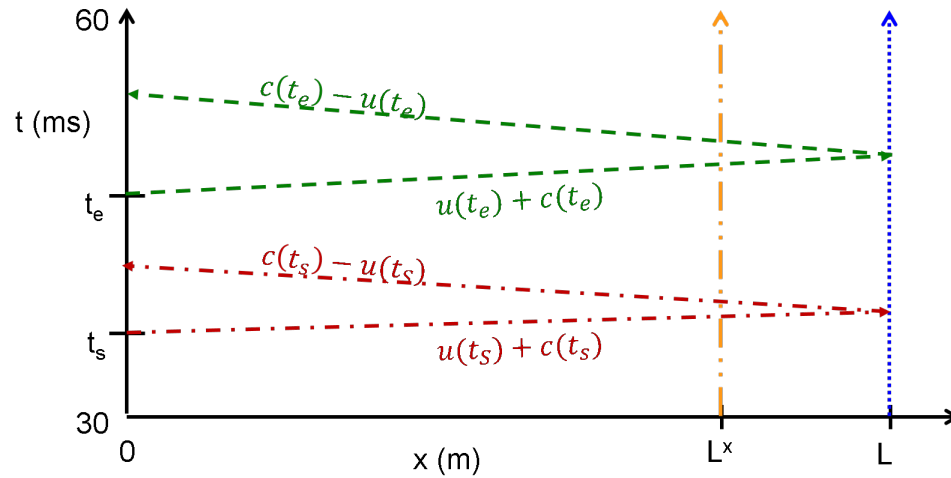


Fig. 2.27. Acoustic propagation of flow characteristics driving the flow acceleration

starts to react to the acceleration at L_x , $t > 37.8$ ms, the wall shear stress rapidly increases as a consequence of the free-stream velocity change and the boundary layer height reduction. Then for $t > 49$ ms the slope of the shear stress growth starts to decay. Finally, the drag approaches its final steady state in a logarithmic way. Figure 2.29 a) depicts the evolution of the momentum boundary thickness throughout the transient. The boundary layer suffers an initial rapid shrinkage driven by the passage of the compression waves, leading towards a minimal thickness at $t = 48.5$ ms. The shrinkage is a consequence of the flow inertia, as the flow accelerates it pushes the low momentum flow inside of the boundary layer against the wall, reducing the overall boundary layer height and boosting the skin friction. After the minimum thickness the boundary layer height gradually approaches its final status. The overall change on the axial shear stress increase rate is driven by the interaction of the boundary layer thickness and free-stream velocity temporal evolution.

In terms of the heat flux, as depicted in Figure 2.28 b) there is an intermediate phase on the temporal evolution driven by the reduction of the free-stream gas temperature. Throughout the simulation a constant total temperature is imposed at the inlet, consequently as the Mach number rises the static temperature of the flow is

reduced. The change on the free stream temperature is convected downstream at the mean flow velocity and then diffused across the thermal boundary layer.

In the laminar boundary layer temporal evolution there are also two clear trends after the acceleration outset. During the first segment of the local acceleration, $t < 44$ ms, the wall fluxes magnitude increase following the reduction of the momentum boundary layer thickness and the increase on the local free-stream acceleration. While for $t > 44$ ms the shear stress follows a gradual decay towards the final steady state condition. The laminar case actually overshoots the final value of wall fluxes during the transient driven by the sudden mean flow velocity change, depicting a stronger influence of the acceleration on the shear stress and heat flux. The laminar boundary layer also displays a slower adaptation or larger establishment delay to the final conditions as the propagation of the information across the near wall region is promoted only by the molecular diffusion.

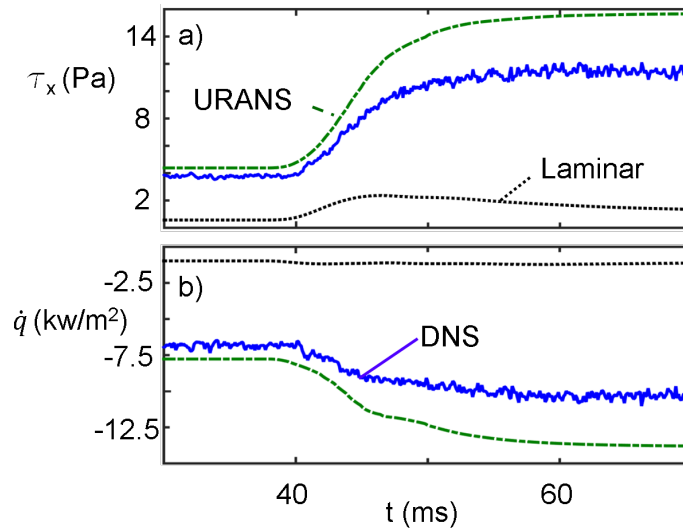


Fig. 2.28. Impact of mean flow sudden acceleration on wall fluxes for DNS, laminar and URANS evaluations; a) Heat flux evolution, b) Stream-wise wall shear stress at L^*

Figure 2.29 b) represents the temporal evolution of the flow momentum contained inside of the boundary layer thickness. The definition used here for the boundary

layer thickness is the height at which the local axial velocity is 99% of the free-stream one. Regardless of the boundary layer status, either turbulent or laminar, the flow momentum in the near wall region is boosted along the flow acceleration.

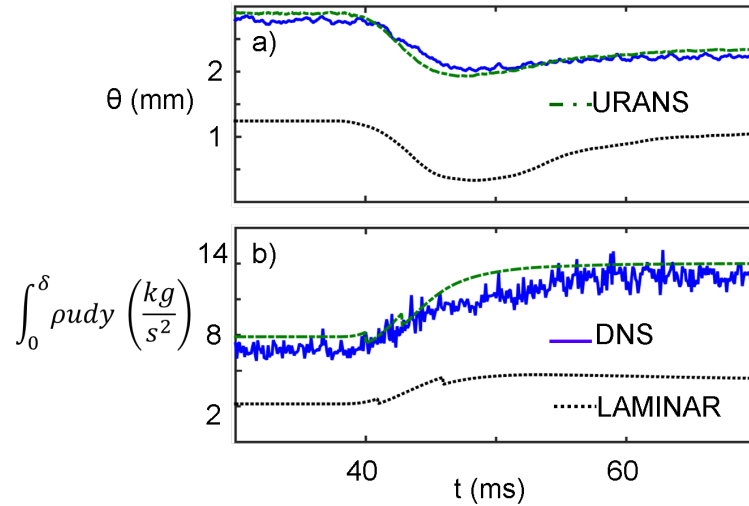


Fig. 2.29. Near wall flow region temporal evolution through the flow acceleration for DNS, laminar and URANS simulations; a) Boundary layer momentum thickness, b) Integral flow momentum inside of the boundary layer along the transient at L^*

Figure 2.30 a) and b) represent the axial velocity profiles in inner and outer units for several time steps along the transient acceleration. All the profiles collapse in the viscous sublayer, depicting a negligible effect of the acceleration parameter on the inner boundary layer status during the phases of stronger acceleration. On the other hand, inside of the logarithmic region the profiles depart from each other, indicating that the distribution of hairpin-type vortices might be affected by the flow acceleration, and probably preventing the application of a universal von Karman constant under these circumstances, [80,81]. In the outer stream wise velocity profiles all the time steps collapse for the near wall region $[y/\delta]_0 < 0.2$. However, the profiles at $t = 0.0485$ s and 0.053 s depict slightly higher velocities than the other profiles at $0.2 < y/\delta]_0 < 2$ suffering the influence from the mean flow acceleration.

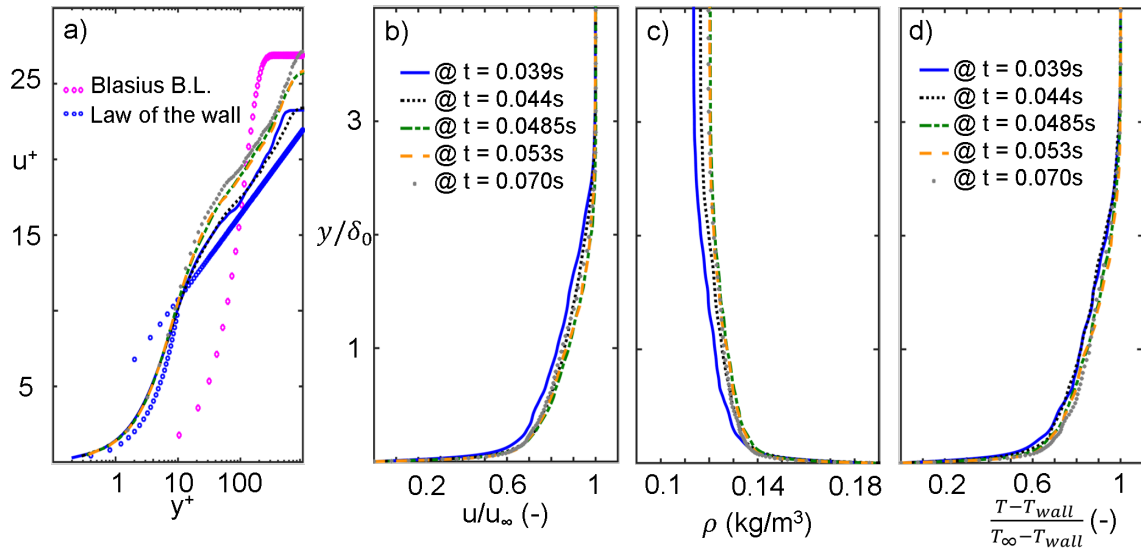


Fig. 2.30. Boundary layer profiles during the sudden flow acceleration
a) Inner units axial velocity, b) Stream-wise velocity profile in outer units, c) Density profile d) Non-dimensional temperature profile

Figure 2.30 c) and d) depict the profiles of density and referenced temperature along the wall normal direction at the end of the finely resolved region, $x = L_x$. The changes on the referenced temperature profiles are mainly driven by the evolution of the boundary layer thickness along the flow acceleration. The profiles at $t = 0.0485$ s and 0.053 s depict the smaller thermal boundary layer thickness of the transient, which is consistent with the evolution of the momentum boundary layer thickness considering the Reynolds analogy. However, in the density profiles representation further differences are observed when comparing different phases of the acceleration. The shifts on the density profiles are motivated by the travelling compression and expansion fronts carrying out the total pressure changes and its natural reflections at the domain outlet.

Figure 2.31 represents the normal velocity profiles obtained at L_x during several time steps along the acceleration. At stable free-stream conditions the integral normal flow velocity along the boundary layer has positive magnitude as a consequence of the axial growth of the displacement thickness. However, during the sudden flow

acceleration for the profiles at maximum acceleration rate ($t = 0.044$ and $t = 0.0485$), the integral value of the normal velocity component is negative. Which remarks that the due to the passage of the compression wave passage the flow is being pushed against the wall, shrinking the boundary layer size.

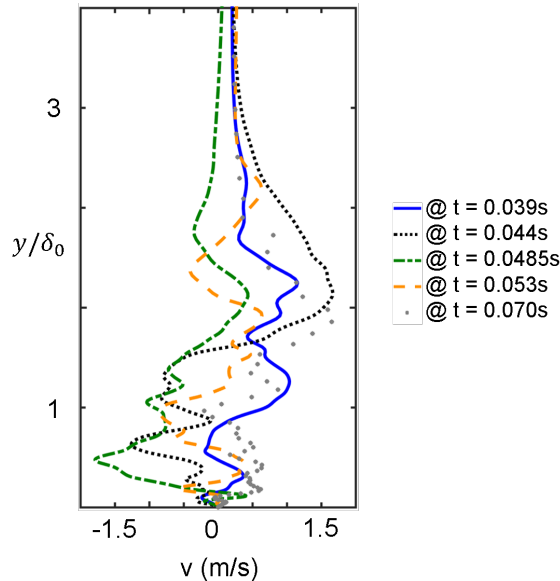


Fig. 2.31. Wall normal velocity at different instances during the acceleration

2.4.3 Free-stream transient evolution impact on near wall region evaluation

The computational cost of performing Direct Numerical Simulations becomes overwhelming for practical or industrial purposes. Although, the temporal evolution of the boundary layer and wall fluxes results of primary interest on the design of aeromechanic devices that operate under transient or periodically perturbed free-stream conditions. For this reason, in the quest towards a cheaper alternative to predict the transient evolution of the boundary layer a simplified model is derived from the momentum integral equations.

Impulsive start of motion model

In the past several models have been elaborated considering the impulsive start of motion or 1st Stokes problem as defined by Rayleigh [82], [37,83]. Starting from a 2-D boundary layer near the edge and the established compressible Momentum Integral Equation:

$$\frac{\tau_w}{\rho x v_\infty^2} = \frac{1}{x v_\infty^2} \frac{\partial(xv\delta^*)}{\partial t} + \frac{\partial\theta}{\partial x} + \left(\frac{2\theta + \delta^*}{xv}\right) \frac{\partial xv}{\partial x} + \frac{\theta}{\rho} \frac{\partial\rho}{\partial x} \quad (2.56)$$

Based on the impulsive start of motion of the flow above the plate, for all $t > 0$,

$$\frac{\partial xv_\infty}{\partial x} = \frac{\partial xv_\infty}{\partial t} = 0 \quad (2.57)$$

the momentum integral equation can be represented as

$$\mu \frac{\partial xv}{\partial y}_{y=0} = \frac{\partial(\rho\delta^*)}{\partial t} + \frac{\partial\rho\theta}{\partial x} \in (t > 0) \quad (2.58)$$

By integrating across the boundary layer height:

$$\mu \frac{\partial xv}{\partial y}_{y=0} = \frac{\partial}{\partial t} \left(\rho \int_0^\delta \left(1 - \frac{\rho xv}{\rho_\delta x v_\delta}\right) dy \right) + \frac{\partial}{\partial x} \left(\int_0^\delta \rho \frac{xv}{xv_\infty} \left(1 - \frac{xv}{xv_\infty}\right) dy \right) \quad (2.59)$$

Then assuming that the boundary layer profile follows a profile of the form:

$$\frac{xv}{xv_\infty} = f(\eta) \quad (2.60)$$

Where $\eta = y/\partial(x, t)$. Introducing the definition of the momentum and displacement boundary layer thickness, the integral terms can be expressed as:

$$\delta^* = \delta \int_0^1 (1 - f(\eta)) d\eta = \alpha_1 \delta \quad (2.61)$$

$$\theta = \delta \int_0^1 f(\eta)(1 - f(\eta)) d\eta = \alpha_2 \delta \quad (2.62)$$

In addition, the slope of the axial velocity profile at the wall could be obtained based on the prescribed profile:

$$\frac{\partial xv}{\partial y}_{y=0} = \frac{xv_{\infty}}{\delta} f'(0) \quad (2.63)$$

Finally, substituting all this in 2.59:

$$\alpha_1 \delta \frac{\partial \delta}{\partial t} + \alpha_2 \delta xv_{\infty} \frac{\partial \delta}{\partial x} = \nu f'(0) \quad (2.64)$$

With the boundary conditions

$$\delta(0, t) = 0, t > 0 \quad (2.65)$$

$$\delta(x, 0) = \delta_0, t < 0 \quad (2.66)$$

The solution of this partial derivative equation is of the form:

$$\delta = \frac{\sqrt{2} \sqrt{f'(0) \nu x + \alpha_2 u_{\infty} C(1) \left(\frac{\alpha_2 t x v_{\infty} - \alpha_1 x}{\alpha_2 x v_{\infty}} \right)}}{\sqrt{\alpha_2} \sqrt{x v_{\infty}}} \quad (2.67)$$

Applying the 1st boundary condition 2.65, $\partial/\partial t = 0$ for $t > 0$, equation 2.64 can be simplified as:

$$\alpha_2 x v_{\infty} \delta \frac{\partial \delta}{\partial x} = \nu f'(0) \quad (2.68)$$

Which solution follows the Blasius boundary layer growth

$$\delta_a = \sqrt{\frac{2 \nu f'(0) x}{\alpha_2 x v_{\infty}}} \quad (2.69)$$

To retrieve the value of the constant on equation 2.67 the second boundary condition is applied, where the 1st boundary condition is also employed to find the thickness at the initial status

$$\sqrt{\frac{2 \nu f'(0) x}{\alpha_2 x v_{\infty}}} = \frac{\sqrt{2} \sqrt{f'(0) \nu x + \alpha_2 u_{\infty} C(1) \left(\frac{\alpha_2 t x v_{\infty} - \alpha_1 x}{\alpha_2 x v_{\infty}} \right)}}{\sqrt{\alpha_2} \sqrt{x v_{\infty}}} \quad (2.70)$$

$$C(1) = \frac{f'(0)\nu}{\alpha_1} \left(1 - \frac{xv_\infty}{xv_{\infty,1}}\right) \quad (2.71)$$

Inserting the constant [C(1)] in equation 2.67:

$$\sqrt{\frac{2 nu f'(0)x}{\alpha_2 xv_\infty}} = \frac{\sqrt{2} \sqrt{f'(0)\nu x + \alpha_2 xv_\infty \frac{f'(0)\nu}{\alpha_1} \left(1 - \frac{xv_\infty}{xv_{\infty,1}}\right) \left(\frac{\alpha_2 xv_\infty - \alpha_1 x}{\alpha_2 xv_\infty}\right)}}{\sqrt{\alpha_2} \sqrt{xv_\infty}} \quad (2.72)$$

The solution provided by this model is not continuous and the time to change from one solution to the other can be found when both methods provide the same boundary layer height: $\delta_a = \delta_b$. The blending time is then defined by:

$$t^c = \frac{\alpha_1 x}{\alpha_2 u_\infty} \quad (2.73)$$

if $t < t^c$ the Rayleigh solution δ_b must be used, whereas if $t > t^c$ the Blasius solution δ_a must be used.

For a laminar boundary layer of the type

$$f(\eta) = 2\eta - 2\eta^3 + \eta^4 \quad (2.74)$$

$$f(0) = 0; f'(\eta) = 2 - 6\eta^2 + 4\eta^3; f'(0) = 2 \quad (2.75)$$

$$\alpha_1 = \int_0^1 (1 - f(\eta)) d\eta = 3/10 \quad (2.76)$$

$$\alpha_2 = \int_0^1 f(\eta)(1 - f(\eta)) d\eta = 37/115 \quad (2.77)$$

On the other hand, a turbulent prediction can be inferred if using the 1/7th law. In the case of the 1/7th law profile, the wall shear stress near the wall cannot be directly derived. However, the wall shear stress evolution found in the numerical evaluations exposed in section 2.4.2 is used to test the model.

$$f(\eta) = \eta^{\frac{1}{7}} \quad (2.78)$$

$$\alpha_1 = \int_0^1 (1 - f(\eta))d\eta = 1/8 \quad (2.79)$$

$$\alpha_2 = \int_0^1 f(\eta)(1 - f(\eta))d\eta = 7/72 \quad (2.80)$$

Figure 2.32 depicts the temporal evolution of the boundary layer thickness during the transient acceleration for the DNS and laminar simulations compared to the model derived from the Rayleigh flow behavior for both laminar and turbulent boundary layer. The laminar impulsive start of motion model follows up to some extent the trend depicted by the laminar simulation with an offset on the actual magnitude of the boundary layer height. For a laminar boundary layer, the model can predict the duration of the transient and the trend followed throughout the temporal evolution.

However, in the case of the turbulent boundary layer the model cannot predict the actual trend, nor the magnitude of the changes perceived on the boundary layer along the acceleration. The turbulent impulsive start of the flow predicts an early boundary layer height increase for the initial phase of the acceleration and then a rapid decay till the establishment of the final condition. The overall duration of the transient development of the boundary layer is under predicted in the Rayleigh model, which envisions an establishment equivalent to a 15% of the actual time taken for the boundary layer to reach the ultimate steady state.

Momentum Integral Equations model

In order to capture the impact of the free-stream flow transients on the near wall region further terms seem to be required on a reduced order model. Considering the continuity 2.81 and stream wise momentum 2.82 equation:

$$\frac{\partial \rho}{\partial t} + \frac{\partial \rho u}{\partial x} + \frac{\partial \rho v}{\partial y} + \frac{\partial \rho w}{\partial z} = 0 \quad (2.81)$$

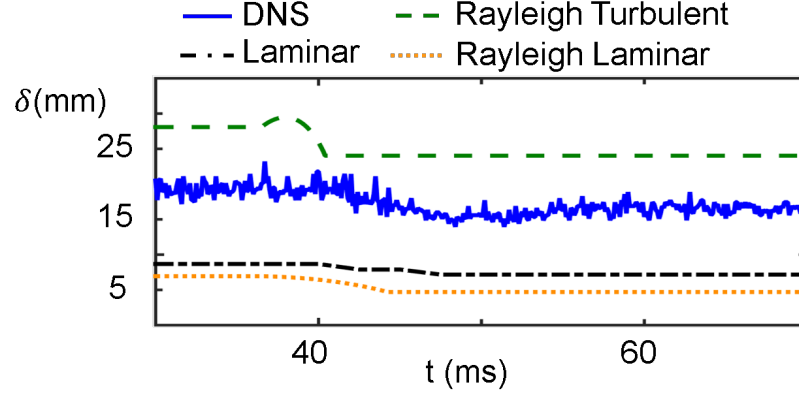


Fig. 2.32. Turbulent and laminar boundary layer evolution after a sudden flow acceleration based on Rayleigh flow start-up assumption

$$\rho \frac{\partial u}{\partial t} + \rho u \frac{\partial u}{\partial x} + \rho v \frac{\partial u}{\partial y} + \rho w \frac{\partial u}{\partial z} = -\frac{\partial p}{\partial x} + \frac{1}{Re} \left(\frac{\partial \tau_{xx}}{\partial x} + \frac{\partial \tau_{xy}}{\partial y} + \frac{\partial \tau_{xz}}{\partial z} \right) \quad (2.82)$$

Where the shear stresses (τ_{ij}) are computed as:

$$\tau_{ij} = \mu \left(\frac{\partial u_j}{\partial x_i} + \frac{\partial u_i}{\partial x_j} - \frac{2}{3} \delta_{ij} \frac{\partial u_k}{\partial x_k} \right) \quad (2.83)$$

Integrating the stream wise momentum equation with respect to the normal direction from the wall to the boundary layer edge

$$\int_0^\delta \left(\rho \frac{\partial u}{\partial t} + \rho u \frac{\partial u}{\partial x} + \rho w \frac{\partial u}{\partial z} \right) dy + \int_0^\delta \left(\rho v \frac{\partial u}{\partial y} \right) dy = \int_0^\delta \left(-\frac{\partial p}{\partial x} + \frac{1}{Re} \left(\frac{\partial \tau_{xx}}{\partial x} + \frac{\partial \tau_{xy}}{\partial y} + \frac{\partial \tau_{xz}}{\partial z} \right) \right) dy \quad (2.84)$$

After rearranging the terms and some algebra that can be followed in Appendix C, equation 2.84 is rewritten as:

$$\begin{aligned}
& \rho_\delta(\delta - \delta^*) \left(\frac{\partial u_\delta}{\partial t} + u_\delta \frac{\partial u_\delta}{\partial x} \right) + u_\delta \frac{\partial \left(\rho_\delta(\delta_\rho - \delta^*) \right)}{\partial t} - \frac{\rho_\delta u_\delta^2 \theta}{\partial x} + \frac{\partial \left(\int_0^\delta \rho u w dy \right)}{\partial z} \\
& - u_\delta \frac{\partial \left(\int_0^\delta \rho u w dy \right)}{\partial z} = \frac{\partial (p_\delta(\delta_p - \delta))}{\partial x} - p_\delta \frac{\partial \delta}{\partial x} + \frac{\mu_\delta}{Re} \left(\frac{\partial v}{\partial x} + \frac{\partial u}{\partial y} \right) \Big|_\delta - cf \frac{\rho_\delta u_\delta^2}{2} \\
& + \frac{1}{Re} \left(\frac{\partial}{\partial x} \left[\int_0^\delta \tau_{xx} dy \right] - \tau_{xx} \Big|_\delta \frac{\partial \delta}{\partial x} \right) + \frac{1}{Re} \left(\frac{\partial}{\partial z} \left[\int_0^\delta \tau_{xz} dy \right] - \tau_{xz} \Big|_\delta \frac{\partial \delta}{\partial z} \right)
\end{aligned} \tag{2.85}$$

At this point the first assumption is introduced, which considers negligible span wise variations $\partial/\partial z = 0$

$$\begin{aligned}
\rho_\delta(\delta - \delta^*) \left(\frac{\partial u_\delta}{\partial t} + u_\delta \frac{\partial u_\delta}{\partial x} \right) + u_\delta \frac{\partial \left(\rho_\delta(\delta_\rho - \delta^*) \right)}{\partial t} - \frac{\partial (\rho_\delta u_\delta^2 \theta)}{\partial x} &= \frac{\partial (p_\delta(\delta_p - \delta))}{\partial x} - p_\delta \frac{\partial \delta}{\partial x} + \\
& \frac{\mu_\delta}{Re} \left(\frac{\partial v}{\partial x} + \frac{\partial u}{\partial y} \right) \Big|_\delta - cf \frac{\rho_\delta u_\delta^2}{2} + \frac{1}{Re} \left(\frac{\partial}{\partial x} \left[\int_0^\delta \tau_{xx} dy \right] - \tau_{xx} \Big|_\delta \frac{\partial \delta}{\partial x} \right)
\end{aligned} \tag{2.86}$$

In an attempt to simplify the model and reduce the number of unknowns a change of variables is proposed:

$$\xi = \frac{u_{\delta,0} \bar{t}}{x} \tag{2.87}$$

$$\bar{t} = \left(t - \frac{L^* - x}{u} \right) \tag{2.88}$$

This change of variable assumes that there exists similarity in the solution at different axial locations. Presuming that the quantities of interest for the model will follow similar temporal evolution at the different normal planes along the plate. To account for the acoustic propagation of the acceleration across the domain a shifting in time is proposed. The temporal delay is proportional to the speed of the slowest characteristic, which carries out the changes of density. The feasibility of the change of variable is evaluated in Figure 2.33, where the temporal evolution of the free-stream velocity a), density b) and boundary layer momentum thickness c) are represented

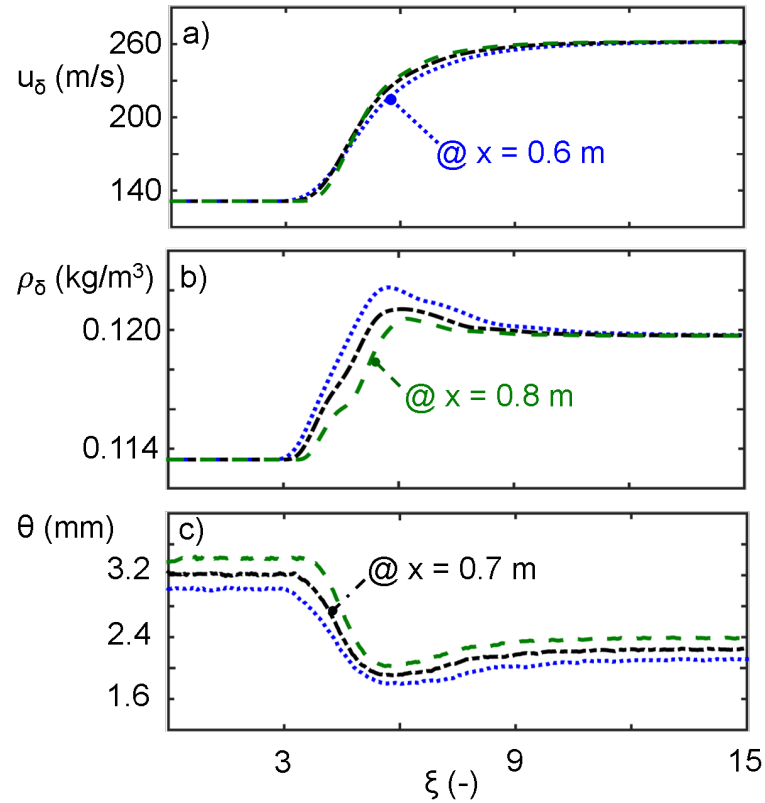


Fig. 2.33. Evaluation of similarity based on the URANS simulations at three different axial locations, $x=0.6$, $x=0.7$ and $x=0.8$; a) Stream-wise velocity, b) Flow density, c) Boundary layer momentum thickness

for three different axial locations in, $x=0.6$ m, $x=0.7$ m and $x=0.8$ m based on the URANS results.

Applying the change of variable the evolution of the free-stream axial velocity seems to collapse for the three different locations along the domain in Figure 2.33 a). Where only minimal differences on the acceleration are observed throughout the transient. In terms of mean flow density and boundary layer momentum thickness after implementing the change of variable the transient evolution at the three observation planes follows the same trends and depicts similar progression, verifying the validity of the change of variable to capture the transient influence. Introducing the change of variable and rearranging some terms equation 2.86 becomes:

$$\begin{aligned}
& \underbrace{\rho_\delta(\delta - \delta^*) \left(\frac{u_{\delta,0}}{x} - u_\delta \left(\frac{u_{\delta,0}\bar{t}}{x^2} \right) \right)}_a \frac{\partial u_\delta}{\partial \xi} + \underbrace{u_\delta \frac{\partial u_{\delta,0}}{\partial x} \frac{\partial(\rho_\delta(\delta_\rho - \delta^*))}{\partial \xi}}_b + \underbrace{\left(\frac{u_{\delta,0}\bar{t}}{x^2} \right) \frac{\rho_\delta u_\delta^2 \theta}{\partial \xi}}_c = \\
& - \underbrace{\left(\frac{u_{\delta,0}\bar{t}}{x^2} \right) \frac{\partial(p_\delta(\delta_p - \delta))}{\partial \xi}}_d + \underbrace{p_\delta \left(\frac{u_{\delta,0}\bar{t}}{x^2} \right) \frac{\partial \delta}{\partial \xi}}_e - \underbrace{\frac{\mu_\delta}{Re} \left(\left(\frac{u_{\delta,0}\bar{t}}{x^2} \right) \frac{\partial v}{\partial \xi} \right) |_\delta}_f + \underbrace{\frac{\mu_\delta}{Re} \left(\frac{\partial u}{\partial y} \right) |_\delta}_g - \underbrace{cf \frac{\rho_\delta u_\delta^2}{2}}_h - \\
& \underbrace{\frac{1}{Re} \left(\left(\frac{u_{\delta,0}\bar{t}}{x^2} \right) \frac{\partial}{\partial \xi} \left[\int_0^\delta \tau_{xx} dy \right] \right)}_i + \frac{1}{Re} \left(\left(\frac{u_{\delta,0}\bar{t}}{x^2} \right) \tau_{xx} |_\delta \frac{\partial \delta}{\partial \xi} \right)
\end{aligned} \tag{2.89}$$

Similar to the methodology proposed by Toubert and Sandham [42], the Direct Numerical Simulation results can be used to evaluate the magnitude of each one of the terms on equation 2.89 and identify the ones playing a more relevant role during the flow sudden acceleration. Figure 2.34 represents the evolution of term in equation 2.89. The first term of equation 2.89 is related to the evolution of the velocity change at the edge of the boundary layer seems to be relevant from the outset of the acceleration till its final phase. On the contrary, the second term including the relative change of the density boundary layer thickness to the displacement thickness seems to be of lower magnitude and hence expendable. The third term deals with evolution of the free stream velocity and density combined with the momentum thickness and it appears to have marginal relevance during the flow transient.

The fourth term on equation 2.89 considers the evolution of the pressure at the edge of the boundary layer and the difference between the pressure and boundary layer thicknesses. This parameter has strong positive magnitude throughout the initial phase of the acceleration and then shifts its sign for the latter stages of the transient. The term e) represents the progression of the boundary layer thickness along the sudden flow acceleration. Based on the results depicted in Figure 2.34 its trend is of considerable influence throughout the transient and its evolution is opposite to the term d), having an initial negative peak in the first instances and then shifting to a positive magnitude for the final flow settlement. The rest of the terms in equation 2.89

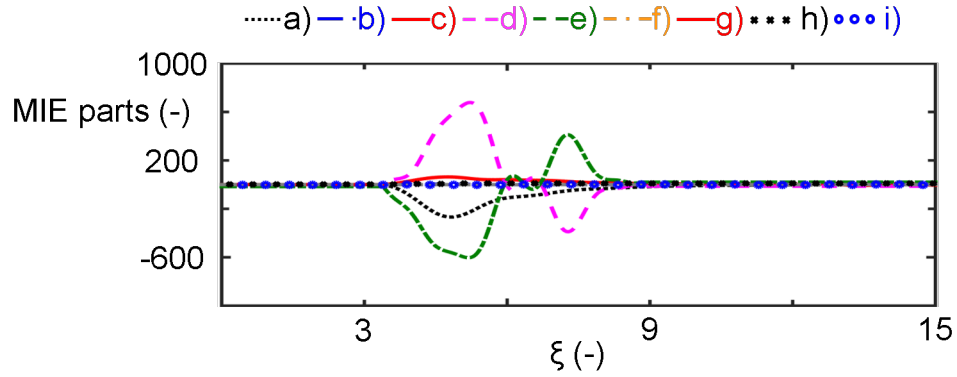


Fig. 2.34. Momentum Integral Equation terms order of magnitude evaluation

dealing with the viscous diffusion across the boundary layer of the normal and axial velocity components as well as the shear stress distribution appear to be unimportant along the acceleration process. Which reveals the dominance of the flow inertia and boundary layer thicknesses evolution over the diffusion and shear stresses distribution. Figure 2.35 represents the evolution of the Reynolds stresses integral value across the boundary layer thickness along the transient simulation. The $u'u'$ stress is the one of largest magnitude followed by $w'w'$, $v'v'$ and $u'v'$, being $u'w'$ the one of smallest magnitude. The integral value across the boundary layer height of all the Reynolds stresses linearly augments its magnitude from the initial flow condition to the final, without depicting any abrupt change driven by the acceleration rate.

Eliminating the aforementioned irrelevant terms and exploding the terms c) and d), equation 2.89 becomes:

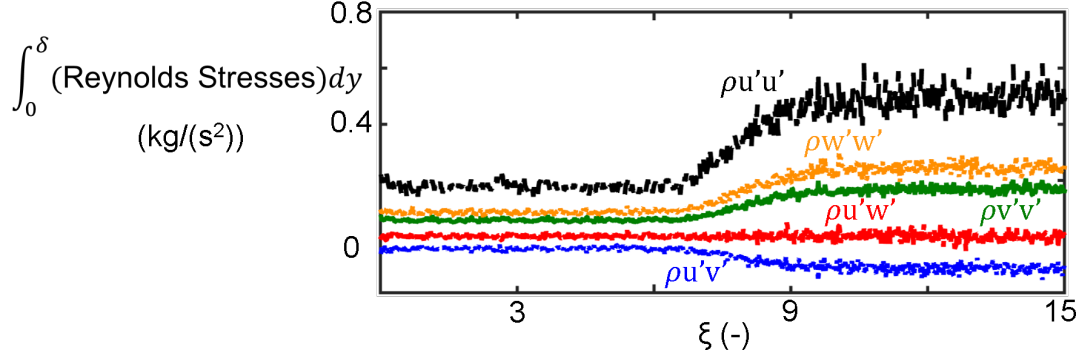


Fig. 2.35. Integral Reynolds Stress across the boundary layer during the sudden flow acceleration

$$\begin{aligned}
 & \underbrace{\rho_{\delta}(\delta - \delta^*) \left(\frac{u_{\delta,0}}{x} - u_{\delta} \left(\frac{u_{\delta,0}\bar{t}}{x^2} \right) \right) \frac{\partial u_{\delta}}{\partial \xi}}_a + \underbrace{u_{\delta}^2 \theta \left(\frac{u_{\delta,0}\bar{t}}{x^2} \right) \frac{\partial \rho_{\delta}}{\partial \xi}}_{c-1} + \underbrace{\theta \rho_{\delta} \left(\frac{u_{\delta,0}\bar{t}}{x^2} \right) \frac{\partial u_{\delta}^2}{\partial \xi}}_{c-2} \\
 & + \underbrace{\rho_{\delta} u_{\delta}^2 \left(\frac{u_{\delta,0}\bar{t}}{x^2} \right) \frac{\partial \theta}{\partial \xi}}_{c-3} = - \underbrace{p_{\delta} \left(\frac{u_{\delta,0}\bar{t}}{x^2} \right) \frac{\partial \delta_p}{\partial \xi}}_{d-1} + \underbrace{p_{\delta} \left(\frac{u_{\delta,0}\bar{t}}{x^2} \right) \frac{\partial \delta}{\partial \xi}}_{d-2} - \underbrace{\delta_p \left(\frac{u_{\delta,0}\bar{t}}{x^2} \right) \frac{\partial p_{\delta}}{\partial \xi}}_{d-3} + \quad (2.90) \\
 & \quad \quad \quad \underbrace{\delta \left(\frac{u_{\delta,0}\bar{t}}{x^2} \right) \frac{\partial p_{\delta}}{\partial \xi}}_{d-4} + \underbrace{p_{\delta} \left(\frac{u_{\delta,0}\bar{t}}{x^2} \right) \frac{\partial \delta}{\partial \xi}}_e
 \end{aligned}$$

Figure 2.36 represents the progression of each one of the terms in equation 2.90 along the transient. Revealing that the influence of the density boundary layer thickness, momentum boundary layer thickness and pressure boundary layer thickness are expendable when compared to the impact of the mean flow velocity, free-stream density and boundary layer thickness growth. Retaining only the terms with stronger influence on the sudden free-stream acceleration equation 2.90 becomes:

$$\rho_{\delta}(\delta - \delta^*) \left(\frac{u_{\delta,0}}{x} - u_{\delta} \xi \right) \frac{\partial u_{\delta}}{\partial \xi} + \theta \rho_{\delta} \xi \frac{\partial u_{\delta}^2}{\partial \xi} - \xi \delta \frac{\partial p_{\delta}}{\partial \xi} = 2 p_{\delta} \xi \frac{\partial \delta}{\partial \xi} \quad (2.91)$$

In order to transform the partial differential equation into an ordinary differential form, a similarity solution is proposed. In this case all the remaining boundary layer

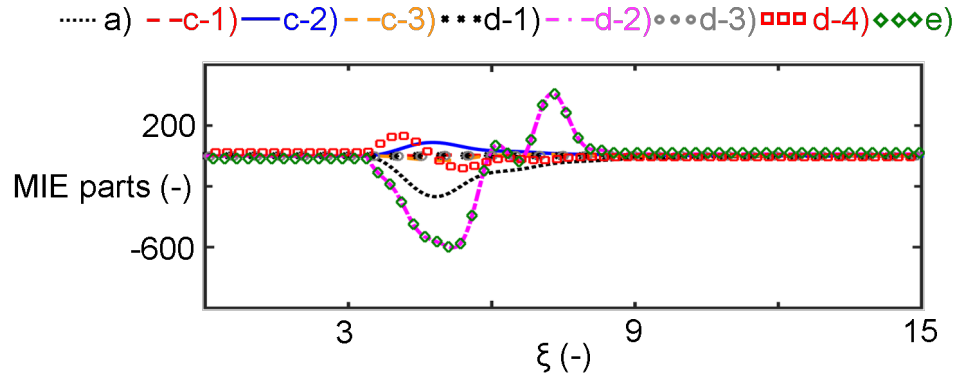


Fig. 2.36. Reduced Momentum Integral Equation terms order of magnitude evaluation

thicknesses in equation 2.91, δ, δ^* and θ are assumed to follow a comparable trend with a scaling factor.

$$\delta_i = F(\xi)\Delta_i \quad (2.92)$$

The feasibility of this assumption along the transient evolution is evaluated based on the Direct Numerical Simulation results. Figure 2.37 represents the ratios between the displacement and momentum boundary layer thickness to the boundary layer thickness.

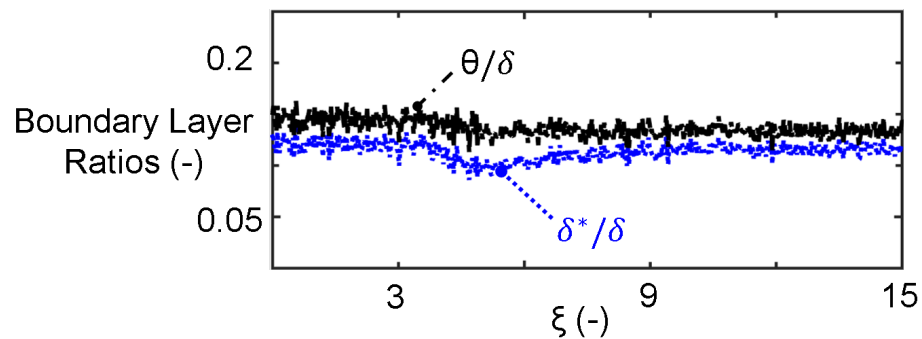


Fig. 2.37. Boundary layer ratios throughout the transient

The momentum boundary layer thickness ratio stays constant throughout the transient and the displacement thickness suffers only a 5% decay during the strongest acceleration phases. Consequently, the similarity solution can be applied and the ratios between the boundary layer, the momentum and displacement thicknesses are expressed as:

$$\frac{\Delta^*}{\Delta} = \frac{1}{9} \quad (2.93)$$

$$\frac{\Delta^\theta}{\Delta} = \frac{2}{15} \quad (2.94)$$

Introducing the similarity hypothesis and the ratios between the boundary layer thicknesses, equation 2.91 becomes the following expression:

$$\frac{\rho_\delta \left(1 - \frac{\Delta^*}{\Delta}\right) (u_{\delta,0} - u_\delta \xi) F(\xi) \frac{\partial u_\delta}{\partial \xi} + \frac{\rho_\delta \Delta^\theta}{\Delta} F(\xi) \xi \frac{\partial u_\delta^2}{\partial \xi} - A_p \xi F(\xi) \frac{\partial p_\delta}{\partial \xi}}{2p_\delta \xi} = \frac{\partial F(\xi)}{\partial \xi} \quad (2.95)$$

Which shows that the evolution of the boundary layer thickness is dictated by the progression of the free-stream velocity, the free-stream density and the static pressure at the edge of the boundary layer. Given the change of the free-stream velocity, density and pressure, as depicted in Figure 2.38 the boundary layer thickness evolution could be predicted solving the ordinary differential equation 2.95. The mean flow quantities evolution after the total pressure rise in the inlet can also be predictive with an inexpensive 1D Euler transient simulation. For the free stream velocity, density and pressure there exists a perfect matching between the DNS and Euler simulations.

Equation 2.95 is solved with Runge Kutta 4th order model and its results are represented in Figure 2.39 against the evolution of the boundary layer thickness along the DNS evaluation. In order to capture correctly the magnitude of the temporal evolution a constant parameter, A_p , is required. The constant boosts the influence of the density changes on the actual boundary layer evolution. Based on the DNS dataset of 10 ms the constant A_p is equal to 11.4.

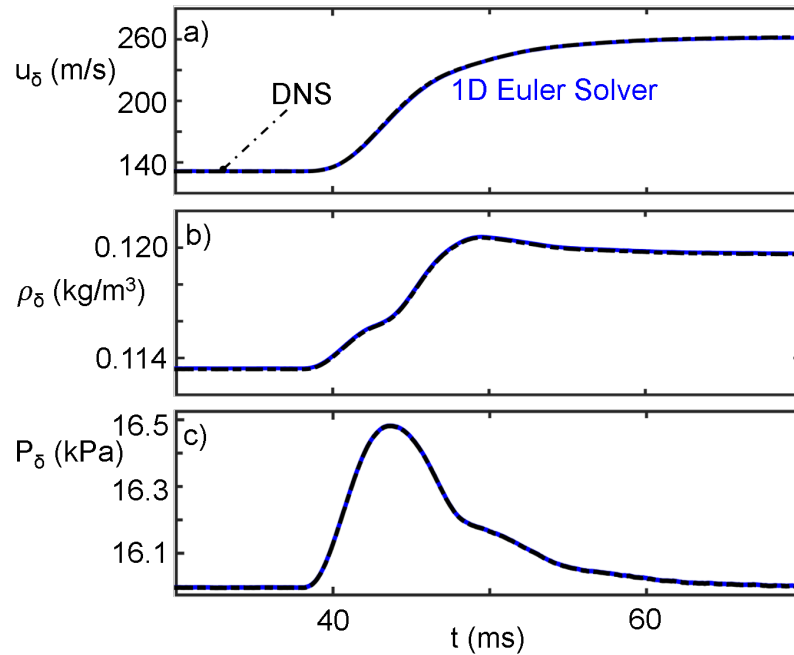


Fig. 2.38. Free-stream conditions input for simplified model evaluation; a) Stream-wise velocity, b) Gas density, c) Static Pressure

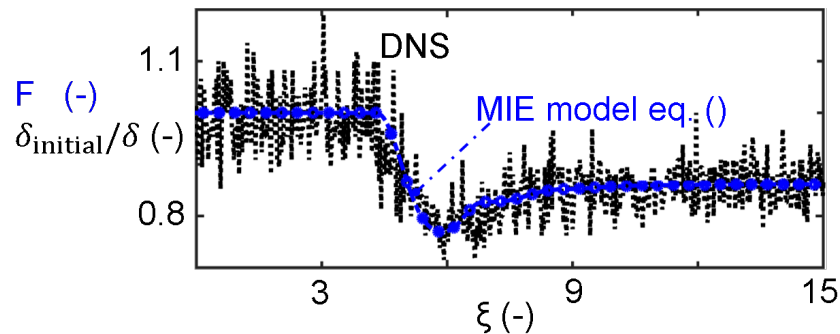


Fig. 2.39. Simplified model prediction of the boundary layer transient evolution 10 ms

To verify the performance of the model and guarantee the applicability of the constant to any other subsonic acceleration a second transient evolution is evaluated with the DNS solver. The initial and final status of the second acceleration are the same as for the first case but in this case the transient had a duration of 25 ms. Figure 2.40 represents the evolution of the boundary layer thickness and the

prediction achieved by the simplified model. A perfect agreement between the DNS results and the simplified model is achieved.

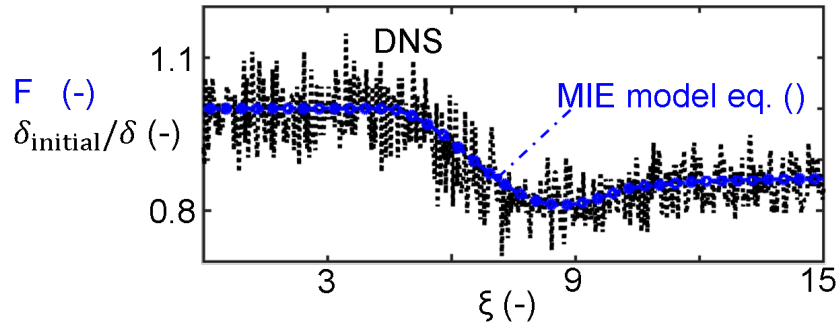


Fig. 2.40. Simplified model prediction of the boundary layer transient evolution 25 ms

Shear stress prediction along the transient evolution

Besides the pure boundary layer evolution, the progression of the wall fluxes through the transient is of major relevance on the design and early development phases of fluid machinery operating under transient mean flow conditions. Based on the evolution of the boundary layer a prediction of the shear stress and heat flux temporal growth is derived. The simplified integral transient boundary layer model 2.95 cannot be used to retrieve the shear stress since the skin friction coefficient influence was rejected based on the magnitude of its gradient. However, the outcome of the model can be used to predict the progression of the skin friction when combined with previous established wall shear stress correlations. In particular looking at the definition of the shear stress:

$$\tau = \mu \left. \frac{\partial u}{\partial y} \right|_{y=0} \quad (2.96)$$

Its evolution is dictated by the ratio between the free stream velocity and the boundary layer thickness

$$\tau \propto \frac{u_\infty}{\delta} \quad (2.97)$$

von Karman and Prandtl [84, 85] reported that the turbulent skin friction coefficient over a smooth plate can be predicted by expressions of the type:

$$cf = A(u\rho x/\mu)^{-1/5} \quad (2.98)$$

For instance, the Turbulent Boundary Layer Prandtl-Schlichting correlation:

$$cf = 0.0588(u\rho x/\mu)^{-1/5} \quad (2.99)$$

Where the skin friction evolves with $u^{-1/5}$. Consequently, based on the initial skin friction value, the impact of the free stream velocity change can be modeled as $(u/u_0)^{-1/5}$. The simplified transient boundary layer model 2.95 can then be used to reflect the influence on the boundary layer height change. Given the initial condition, $cf(0)$ and $u(0)$, the temporal evolution of the free stream velocity $u(\xi)$, and the transient development prediction of the boundary layer, the skin friction can be estimated:

$$cf(\xi) = cf(0)(u(\xi)/u(0))^{-1/5}F(\xi) \quad (2.100)$$

Figure 2.41 a) compares the skin friction evolution during the transient with the Turbulent Boundary Layer Prandtl-Schlichting correlation considering only the free stream velocity change $(cf(0)(u(\xi)/u(0))^{-1/5})$ and the prediction based on equation 2.100. When only considering the impact of the free stream velocity, the correlation lacks of capability to predict the magnitude change and fails on estimating the actual trend followed by the shear stress. However, when adding the influence of the boundary layer transient growth $(F(\xi))$, the model can then predict the actual change of magnitude and follow closely the trend. Figure 2.41 b) compares again the model developed in equation 2.100 with the results of the 25 ms transient, displaying again

a considerable agreement. Only some anticipation of the minimum skin friction value is predicted by the model when compared to the DNS outcome.

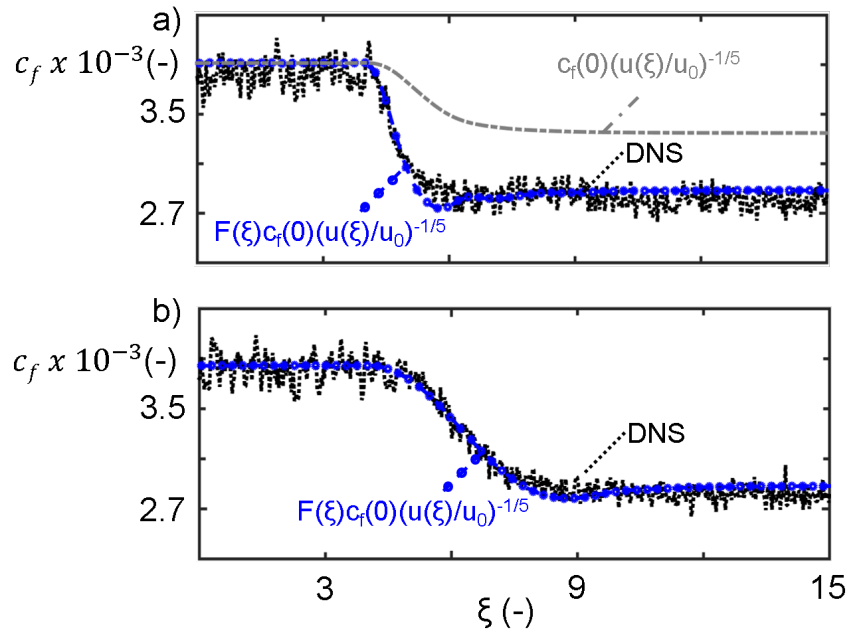


Fig. 2.41. Skin friction prediction correction based on boundary layer transient evolution, a) 10 ms transient, b) 25 ms transient

Once the skin friction evolution is retrieved the heat transfer coefficient (htc) can be then derived with the Reynolds analogy [86]:

$$htc = \frac{c_f}{2} Pr^{-2/3} \rho_\delta u_\delta c_p \quad (2.101)$$

where c_p is the gas specific heat and Pr is the Prandtl number.

$$htc = \frac{c_f(0)(u(\xi)/u(0))^{-1/5} F(\xi)}{2} Pr^{-2/3} \rho_\delta u_\delta c_p \quad (2.102)$$

Figure 2.42 represents the comparison of the heat transfer coefficient prediction based on the boundary layer development and the Reynolds analogy against the results from the Direct Numerical Simulations displaying an excellent agreement.

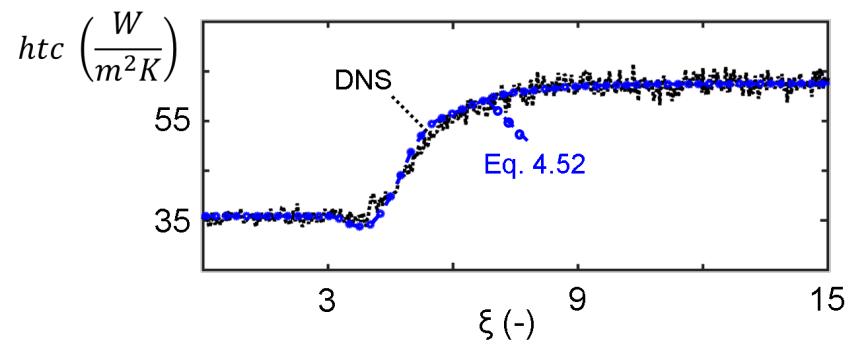


Fig. 2.42. Reynolds analogy application to find the transient evolution of the heat transfer coefficient after the sudden flow acceleration

3. TRANSIENT PERFORMANCE OF SEPARATED FLOWS

The aerothermal performance of the low pressure turbine in UAVs is significantly abated at high altitude, due to boundary layer separation. During past years different flow control strategies have been proposed to prevent boundary layer separation, such as dielectric barrier discharges, synthetic jets, vortex generators. However, the optimization of the control approach requires a better characterization of the separated regions at several frequencies. The present chapter analyzes the behavior of separated flows, and specifically reports the characterization of the inception, reattachment and separation length, that allows the development of more efficient methods to enhance or abate flow separation under non-temporally uniform inlet conditions. The development of separated flows under sudden flow accelerations or pulsating inlet conditions were investigated with series of numerical simulations including Unsteady Reynolds Average Navier Stokes and Large Eddy Simulations. The present research was performed on a wall mounted hump which imposes an adverse pressure gradient representative of the aft portion of the suction side of low pressure turbines. The use of a smooth wall curvature geometry rather than a backward facing step unlocks the separation inception. The heat transfer and wall shear stresses were fully documented, as well as the flow velocity and temperature profiles at different axial locations to characterize the near wall flow properties and the thermal boundary layer. Through a sudden flow acceleration the dynamic response of the shear layer detachment as it is modulated by the mean flow evolution is investigated. Similarly, the behavior of the recirculation bubble under periodic disturbances imposed by sinusoidal inlet total pressure signals at various frequencies ranging from 10 to 500 Hz is studied. During each period the Reynolds number oscillates between 40000 and 180000 (based on a characteristic length of 0.1 m).

The uprising use of UAVs and the breakthrough of the distributed thrust is promoting the design of ultra-compact and versatile gas turbine engines [87], [88]. The cruise operation of such power plants at high altitudes is narrowed because of the small Reynolds number through the low pressure turbine stages. At reduced Reynolds numbers < 100000 (based on blade axial cord) the rear part of the blade suction can suffer flow separation, which dramatically lowers the stage efficiency [89]. Due to the flow separation, the flow capacity of the low pressure turbine stage is significantly reduced while the viscous losses are boosted [90]. This burdensome performance prevents its operation at higher altitudes and reduces the overall air-frame range.

Many studies have been performed on the control of flow separation through passive and active techniques on the quest towards compact LPT stages integration [91]. Gurney flaps concepts were proposed by Byerley et al. [92] to control the laminar flow separation on turbine blades. The flaps mounted on the pressure surface near the trailing edge, turn and accelerate the flow through the passage directing it towards the suction side. Preventing the flow separation, by reducing the adverse pressure gradient at low Reynolds conditions. Lake et al. [93] introduced the use of surface dimples to reduce the size of the separated flow regions. While, Volino [94] studied the effect of rectangular bars on the suction side surface to promote the boundary layer transition and encourage the flow reattachment. However, the passive flow control devices alter the performance of the vanes at higher Reynolds numbers, reducing the overall stage efficiency at lower altitudes. Consequently, low Reynolds tailored vane designs might be non-suitable for takeoff, climbing or landing environments. Which leads towards the integration of active flow control approaches to mitigate the flow separation when needed.

Greenblatt and Wygnanski [95] documented the control of flow separation by periodic excitation through hydrodynamic excitation methods. Ranging from acoustic wave based approaches to flow suction or ingestion. The application of glow discharge plasma actuation on the boundary layer control has been experimentally [96] and

numerically [97] proven. Determining its effectiveness promoting the transition in the shear layer, enhancing a fast flow reattachment.

On the other hand, single dielectric barrier discharge plasma actuators, (DBD), have been widely used for the suppression of the flow separation [98] [99]. Huang et al. [100], used DBDs on a low Reynolds number environment in a linear cascade. Similarly, Gksel et al. [101] looked into the efficiency impact of pulsed plasma actuators at various Reynolds numbers. The lower the Reynolds number, the most effective the control because of the increasing momentum coefficient. Porter et al. [102] detailed the effectiveness of the DBD plasma actuators tripping the boundary layer transition, which could alleviate and avoid the flow separation regardless of the actuator orientation. Based on surface pressure measurements, Post and Corke [103] analyzed the influence of plasma induced streamwise vortices and 2D axial jets on the airfoil suction surface at stall conditions. The plasma actuation enhanced the flow reattachment, boosting the lift to drag ratio at points beyond airfoil stall. In a similar way, Gaitonde et al. [104], applied asymmetric dielectric-barrier-discharge on stalled NACA symmetric airfoils. Evidencing the effectiveness of the streamlined actuation on the generation of wall jets that avoid the flow separation. Dielectric barrier discharges were also used by Rethmel et al. [105]. Generating coherent spanwise vortices that relocate momentum from the free stream into the near wall region, energizing the per se low momentum flow and endorsing the flow reattachment.

Many others authors propose the use of pulsed jets for the control of flow-separated regions based on the injection of flow from a higher pressure environment. Volino [94] used oscillating jet vortex generators to control the flow separation in the rear suction side of a low pressure turbine blade. The jets were injected into the suction side through spanwise orifices. Its effectiveness was demonstrated at a variety of frequencies and amplitudes. Similarly, Bons et al. [87] and Sondegaard et al [106], assessed the efficient control of laminar flow separation based on pulsed jets. Where the maximum effective frequencies were limited by the settlement time of the boundary layer as it reattaches.

The presence of unsteady flow conditions on the low pressure turbine will affect the behavior of the flow separated regions and its reaction to any flow control approach. In this regard, Schobeiri et al. [107] provided experimental data describing the evolution of inception and separated flow region as a consequence of unsteady mean flow conditions. Where the wake passing had a strong influence on the recirculation bubble, modulating its extension. In a similar way, Wissink [108], numerically investigated the effect of incoming wakes on a low pressure turbine cascade with DNS simulations. Where also the influence of the incoming flow disturbances on the separated flow region was highlighted.

In this section, a numerical research on the dynamic response of flow separated regions and its control based on a wall mounted hump domain is presented. The use of a smooth wall curvature geometry unlocks the separation inception, which then becomes on a relevant variable to determine the most effective near wall flow control. Wall mounted humps have been previously used under such circumstances on wind tunnel experiments at high Reynolds numbers [109]. Similarly, turbulent flow separation control experiments over wall mounted humps using dielectric barrier discharge have been documented [110] [111] [112]. In fact, He et al. [110] compared the experimental results with URANS analysis validating the use of several turbulent models resolving such flow structures. Through URANS and LES simulations, the dynamic response of the flow separated regions to mean flow periodic excitation or sudden flow accelerations were studied. Which reveal the strong dependence of the recirculation bubble on the mean flow velocity variations.

Many flow operated devices are exposed to flow separation and reattachment in a variety of a geometrical locations. The flow separation may be induced by rear flow facing steps [113] [114], positive pressure gradients [115] [116] [117], shock boundary layer interaction [118] [119] [120] or induced by unsteady flow impingement [121] [108] [121]. Particularly, many industrial heat exchangers exploit the mixing induced in the separated shear layer to magnify the heat transfer rate. In quest towards the performance improvement on heat exchanger operation as well

as aerodynamically driven process a proper understanding of the flow separation is required. Many authors have proposed different techniques on the flow separation control with two coupled objectives: heat transfer enhancement and minimization of aerodynamic losses. [95] [109] [122] [100] [123] [124]. However, it is generally found that the flow control approaches rely on passive devices, random periodic excitation or pulsating frequencies only found after optimization analysis. Following this principles the energy required to perform the flow control may exceed the actual requirement for effective flow control. Aiming a performance increase not only in terms of heat transfer enhancement or aerodynamic footprint, but also on an efficient and effective flow control the dynamic scales of flow separation are investigated.

The flow over a backward facing step has been extensively documented in both empirical and numerical studies. [125] [126] [127]. The investigation of the turbulent shear layer over a backward facing step has been conducive to the reattached boundary layer flow characteristics as well as the features flow reattachment [128]. The flow features for different expansion ratios were disclosed by Biswas et al [129], where a strong two-dimensional behavior was recognized. Similarly the analyses of several Reynolds number was helpful to the understanding of the different separated region geometrical scales

The analysis on the unsteadiness and convective instabilities over a backward-facing step conducted by Kaiktsis et al. [130] revealed the details of the disturbances propagation. The small disturbances were transmitted downstream with significant amplification by the local convective speed. Additional excitation into the shear layer region were only altering the flow separation characteristics at high frequency rates. Which is a symptom of the magnitude of the dynamic scales which control the shear layer region.

Similarly, based on LES simulations the effects of periodic perturbations inside of the detached shear layer behind a rear facing step have been qualified. Where again, the Strouhal number has been proven to notoriously affect the interaction between the shear layers instabilities, [127] Based on DNS simulations, Kaiktsis et

al [130] indicated that the 3 dimensionality onset takes place in the thresholds between primary and secondary recirculated regions. Emphasizing the presence of secondary instabilities in the shear layers being triggered by the corner vortex.

Combined heat transfer and aerodynamic measurements performed by Vogel and Eaton [131] explained the heat flux distribution downstream of a backward-facing step and its coupled nature with the fluid dynamic structures. Where fluctuating momentum and thermal boundary layer profiles had a strong influence on the transient evolution of the heat transfer rate along the reattachment region. Hence, the efficient enhancement of the heat transfer rates could only be guaranteed by a deep understanding of the aerodynamic scales.

3.1 Methodology

The main objective in this analysis is to resolve the dynamic scales involved in the flow separation and how the mean flow transients alter the boundary layer detachment. Looking into the phenomena driving the flow separation and reattachment under transient inlet flow conditions. Our focus will be centered on pure aerodynamic features without the instability issues raised by abrupt geometrical changes. In this sense the analysis of flow over a backward step is not of our primary interest due to the clear influence of the corner on the shear layer instabilities, as supported by Kaiktsis et al [130]. The geometrical obstacle was designed making use of Bezier curves in order to guarantee the continuity of the curvature. Figure 3.1 a) depicts the wall surface determination based on the use of several control points. The ground level of the domain is set by an initial point at the leading edge. The control points located at the same height close to the obstacle rise guarantee the horizontality of the first segment. The distance between those control points dictates the curvature of the obstacle on the leading region, as displayed in Figure 3.1 b) and c). The normal distance to the wall of the three central points determines the height of the hump, where again their spacing determines the radius of curvature of the summit. The

points in the hump fall set the axial length of the obstacle. Where the presence of three points at the same height of the initial segments restores the parallel ground of the plate. Finally, the last point defines the trailing edge of the domain. ¹

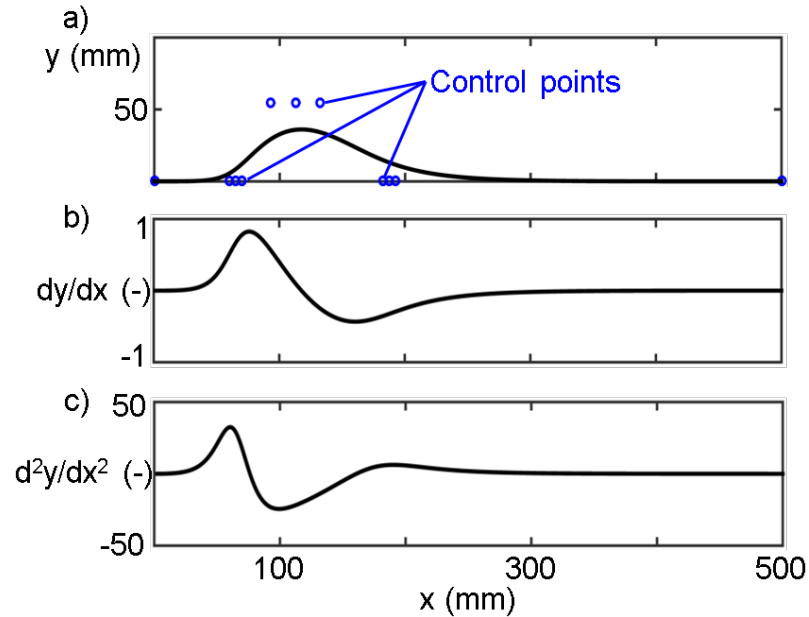


Fig. 3.1. Domain generation for flow separation dynamic scales analysis: a) Geometry definition based on Bezier curve; b) Slope distribution along the test article; c) Curvature distribution along the hump surface

The total length of the domain was set to 0.5 m to minimize the computational burden while guaranteeing enough axial distance for flow reattachment resolution under the examined flow conditions. Similarly, the maximum height of the channel is 170 mm. The use of a hump like obstacle, features as proposed by Seifert and Pack [109], generated with continuous curvature will be optimum for the analysis of the separation and reattachment flow. Exploring a domain suited to mimic the behavior of rear suction side of a low pressure turbine. Where massive flow separation can occur at low Reynolds conditions. While at high Reynolds number ($Re > 200000$)

¹Material Published on Transient Performance of Separated Flows: Characterization and Active Flow Control, J. Eng. Gas Turbine Power 141(1),2018

the flow could be fully attached. Where the Reynolds number is based on a 100mm cord length (L_{ref}).

$$Re = \rho u L_{ref} / \mu \quad (3.1)$$

Figure 3.2 introduces the numerical domain used for the flow separation dynamic analyses. The lower wall and upper walls of the domain, describing the obstacle characteristic, were modelled as an isothermal viscous surface at a constant temperature of 300K. The static pressure level was imposed by a pressure outlet boundary condition and the total pressure and temperature were dictated by the pressure inlet boundary condition. The domain was meshed making use of ANSYS ICEM. The proper geometrical discretization of each one of the proposed domains was ensured through a mesh sensitivity analysis following the approach outlined by Celik et al. [50]. Similarly, to enhance correct near wall flow prediction the y^+ was kept below 0.5 along the entire surface.

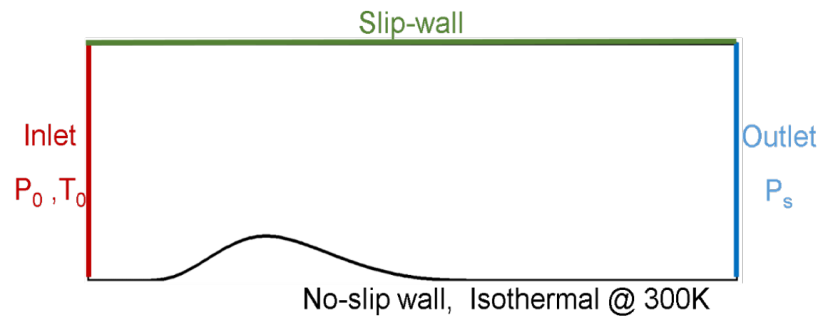


Fig. 3.2. 2D numerical domain for flow separation dynamics investigation

In the quest towards the optimum obstacle designs meeting our requirements a myriad of different hump like domains were explored. Some geometries are exposed in Figure 3.3. The use of the proposed domain was verified against another possible configurations, the details are presented in the Appendix 2, Domain Validation. In order to test the performance of the envisioned possible domains their aerodynamic

performance was assessed for a Reynolds/m of 8.9×10^5 . Which boundary conditions were set as described in the following table:

Table 3.1.
Boundary conditions for $Re/, 8.9 \times 10^5$

P_0	70.6	kPa
T_0	500	K
P	70	kPa
Inlet Turbulence Level	2.5	%
Wall Temperature	300	K
Inlet mean u_∞	49.5	m/s

For this numerical research the turbulence closure was achieved through the use of the transitional k- Shear Stress Transport developed by Menter [53] [54]. Further details about this scheme are provided in Section 2.

Due to the non-stationary flow behavior, and in order to resolve quantitatively the aerodynamic structures and the wall fluxes evolution, unsteady simulations were required. The time step and inner iterations set for the transient simulation were selected based on a benchmark analysis and considering a minimum frequency resolution of 40 kHz. Finally, as an outcome of the benchmark analysis the solver transient time step was set to $5 \times 10^{-7}s$ with up to 16 inner iterations. The unsteady convergence of the simulations for all the exciting frequencies was ensured prior to the data. The 2D axial velocity contour at Reynolds/m 8.9×10^5 are represented in Figure 3.3. In order to determine the performance at higher flow velocities with distinct heat transfer rates another evaluation was performed at a Reynolds/m of 2.9×10^6 which results are not displayed for brevity reasons.

Figure 3.4 a) and b) represent the free stream velocity and the acceleration parameter (k) along the flow separation domain. The acceleration parameter shows regions of acceleration in the front region of the mountain followed by a plateau of uniform

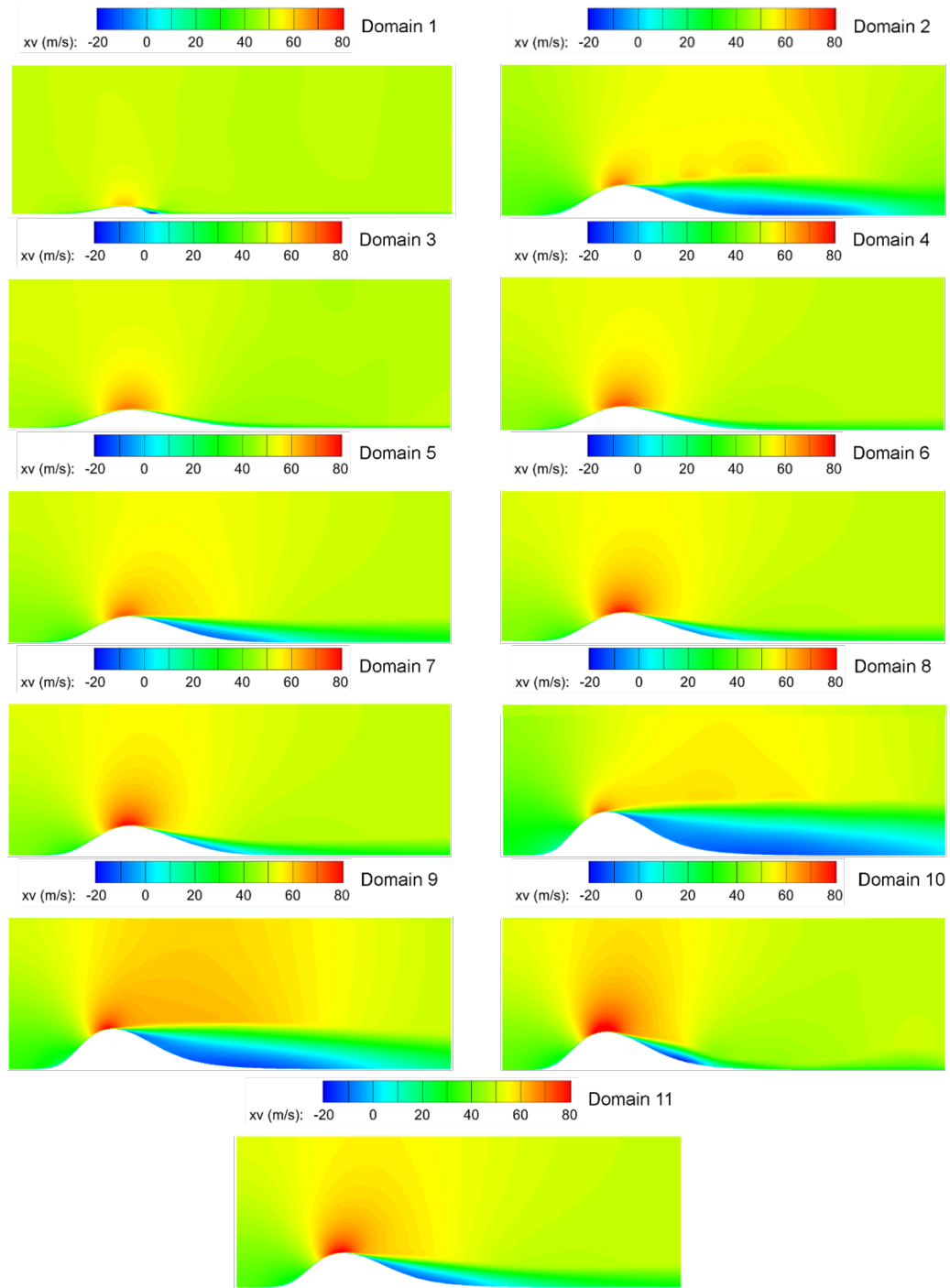


Fig. 3.3. Separation domains axial velocity contours at $Re/m 8.9 \times 10^5$

velocity in the obstacle summit. Later on, the flow suffers a deceleration through the obstacle decay. The deceleration is disrupted by the near wall flow detachment.

Finally, as the flow reattaches to the bottom wall surface the flow velocity slightly decays.

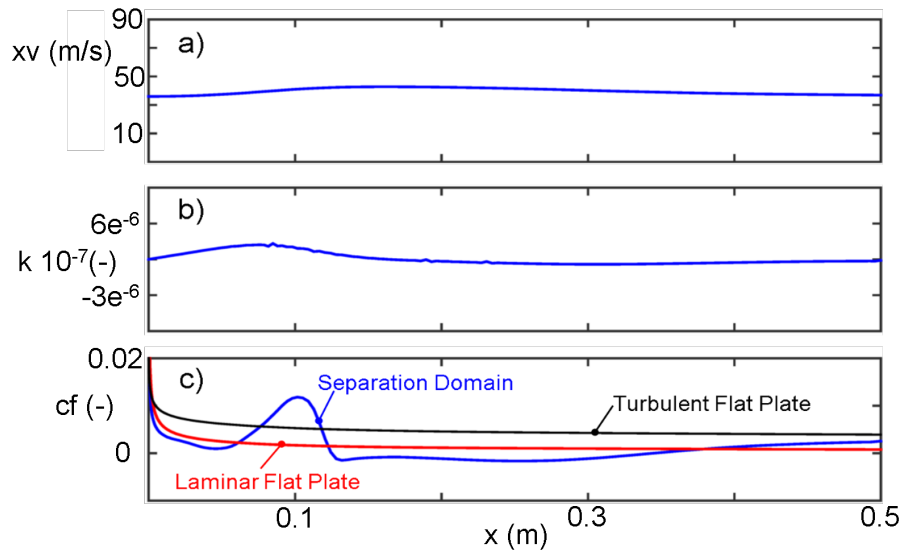


Fig. 3.4. Test article 11 performance at $Re/m 1.1 \times 10^6$ a) Free Stream Axial Velocity; b) Acceleration Parameter; c) Skin Friction coefficient along hump domain

Figure 3.4 c) represents the skin friction evolution along the hump profile for the entire domain compared with laminar and turbulent correlations for flat plates. The skin friction coefficient at the inlet of the domain although being fully turbulent flow depicts low skin friction coefficient. The reason for that behavior is the flow acceleration induced by the rise of the hump. In this sense, Figure 3.5 represents the axial velocity profile for several axial locations along the domain. Close to the leading edge of the plate (@ $x=0.05$) the boundary layer profile exhibits a final flow velocity smaller than the actual free stream velocity and the final accommodation of the boundary layer happens much further of the wall. Consequently, the resultant skin friction is substantially smaller than the expected at that mean flow Reynolds number.

During the rise of the hump the flow suffers acceleration, depicted by the boundary layer profile at $x=0.1$ m, which causes the peak on the skin friction coefficient in

Figure 3.4 c). As the flow detaches from the wall the recirculated region is generated driving towards negative skin friction coefficient (depicted in Figure 3.5 from $x=0.15$ to $x=0.3$). Further downstream the incipient reattachment of the flow could be observed at $x=0.35$ bringing the skin friction back to positive values. Right after the reattachment the boundary layer growths towards the domain trailing edge.

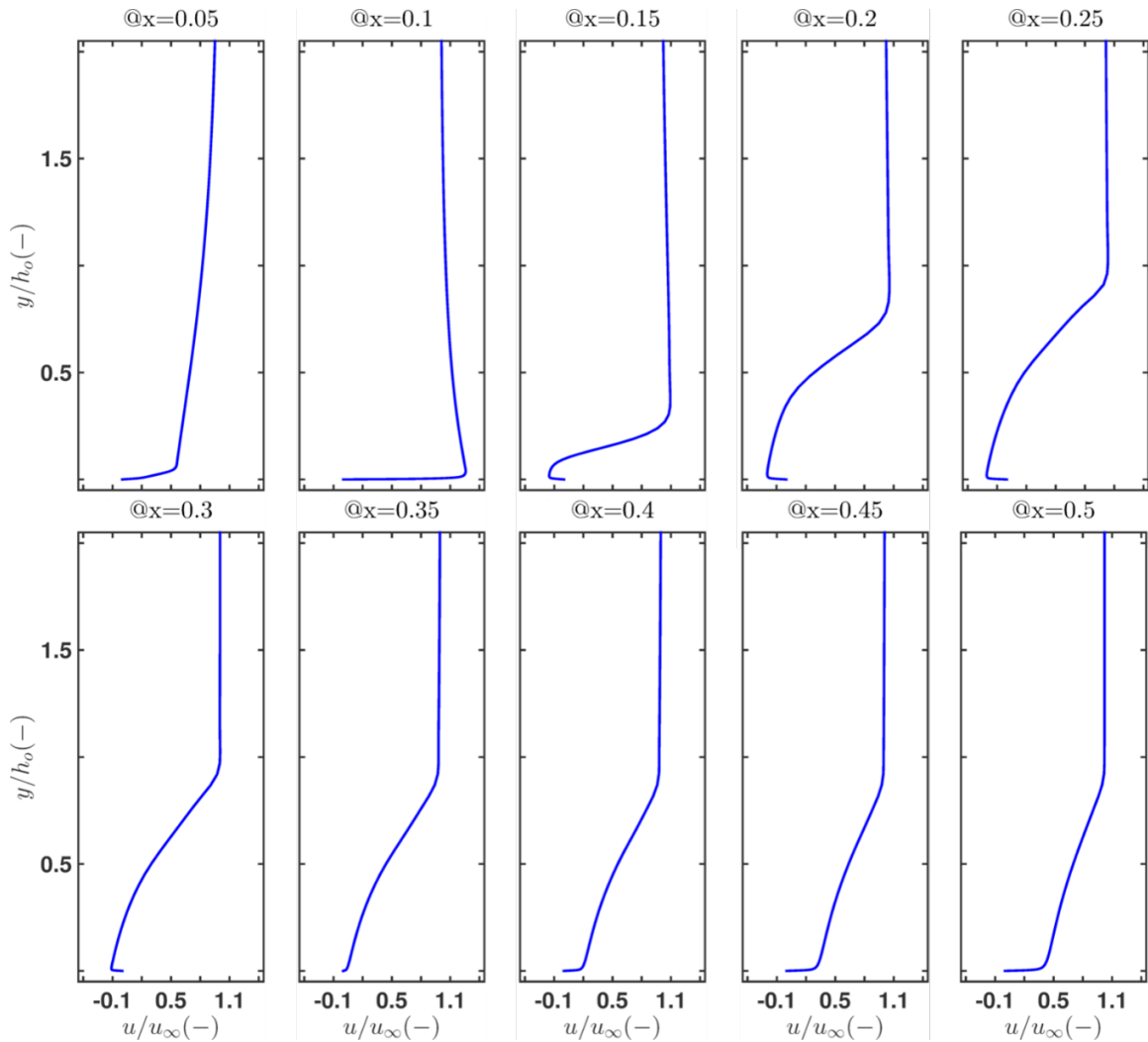


Fig. 3.5. Boundary layer profiles for different axial position along the flow separation domain

Figure 3.2 introduces the numerical domain used for the flow separation analyses. Aiming a reduction on the computational burden, the majority of the simulations were

performed in a 2D fashion. The upper and lower walls of the domain were modelled as isothermal viscous surfaces at 300K. The static pressure level was imposed by a pressure outlet boundary condition, mimicking the discharge to a constant pressure reservoir. Whereas, the total pressure and temperature were dictated by the inlet pressure boundary condition. The domain was meshed following a blocking strategy with ANSYS ICEM.

The proper geometrical discretization was ensured through a mesh sensitivity analysis. In order to enhance correct near wall flow prediction, the y^+ was kept below 0.5 along the walls for all the proposed meshes. Figure 3.7 a) depicts the grid convergence index of the various cases analyzed following the procedure outlined by Celik et al. [50]. Based on the convergence index, the grid of fifty thousand cells seems appropriate. However, looking at Figure 3.7 b) and c), which represent the axial velocity profiles and the wall shear stress evolution along the wall, there is a small mismatch on the 50 thousand cells case. In the axial velocity profiles at $x=0.3m$ there is a slight deviation of the lower resolution meshed compared to the 100 and 200 thousand cells. Similarly, the lower resolution grid displays smaller wall shear stress values when compared with the finer cases. Consequently, the grid of 100 thousand cells was selected for the rest of the numerical analysis. Which has 350 cells in the axial direction and 286 in the ground level normal direction.

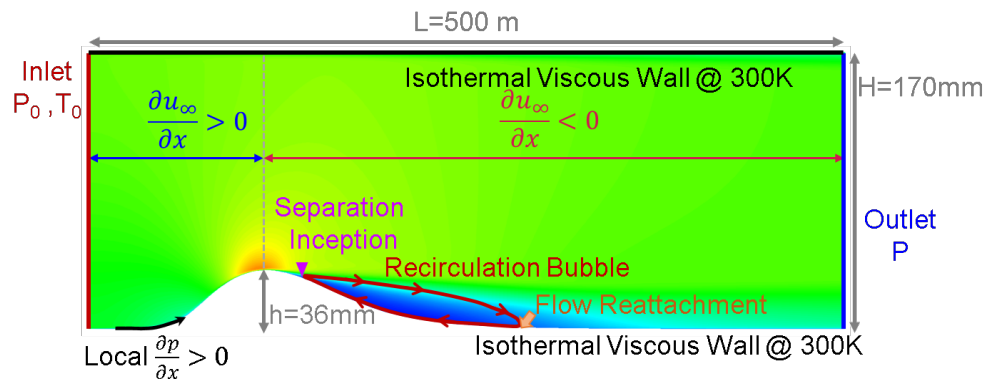


Fig. 3.6. 2D numerical domain for flow separation dynamics at $Re/m \ 1.1 \times 10^6$

The turbulence closure was achieved through the use of the Langtry-Menter 4 equation Transitional SST model [54] [51]. The transitional SST model takes the SST $k-\omega$ turbulence model and adds two other transport equations. The first one includes the intermittency while the second serves for the transition onset criteria. Further details on the turbulence closure scheme are described in Section 2.

The working fluid was air, modeled as an ideal gas. Which included the use of the Sutherland law to account for the temperature effect on the molecular viscosity. Second order upwind formulations were used for the flow and turbulent properties solution. The time step and inner iterations, $5 \cdot 10^{-7}$ s and 16 respectively, were selected based on a benchmark analysis. The transient advancement was promoted through second order bounded implicit formulations. The unsteady convergence of the simulations for all the excitation frequencies was ensured prior to the data acquisition based on the methodology outlined by Clark and Grover [65].

Vogel and Eatons combined heat transfer and aerodynamic measurements, [131], were used to verify the validity of the proposed 2D URANS methodology. They documented the heat flux distribution downstream of a backward-facing step and its coupled nature with the fluid dynamic structures. Figure 3.8 a) represents the numerical domain, which mimics Vogel and Eatons test section. Free stream velocity and total temperature were set in the inlet of the domain, 2.5 m upstream of the backward facing step. The static pressure was set in the outlet of the domain, a couple of meters downstream of the step. The upper and lower walls were modeled as viscous isothermal surfaces at 290 K. Figure 3.8 b) depicts the axial velocity contour on the backward facing step region. Where a separated flow region of about 3 times the step height is displayed.

Figure 3.8 c) shows the comparison of the Stanton number ($St = \frac{htc}{c_p \rho x v}$) for the numerical and experimental results. The agreement between both is notable along the recirculated region and the posterior reattached portion. There is only a small disagreement in the first measured location, which could be related to 3D flow phenomena not captured with the 2D numerical domain.

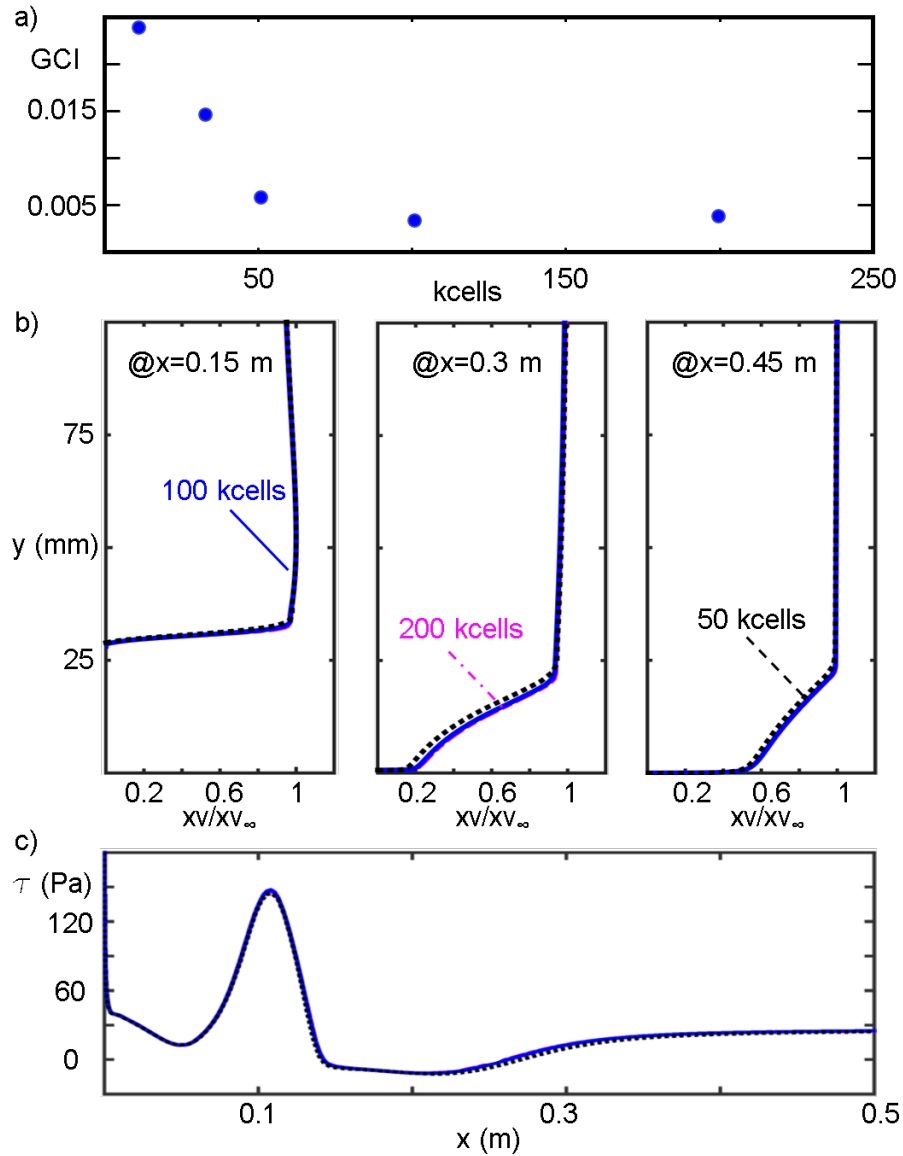


Fig. 3.7. Mesh sensitivity analysis: a) Grid convergence index, b) Momentum boundary layer profiles at various axial locations: 0.15, 0.3 and 0.45 m; c) Wall shear stress evolution along the hump surface

In addition to the 2D URANS simulations, LES simulations were carried out to verify the performance of the URANS models resolving the transient flow dynamics of the ongoing study. For this purpose, we selected the Smagorinsky Lilly subgrid scale model [132] [133]. The LES governing equations are obtained by filtering the

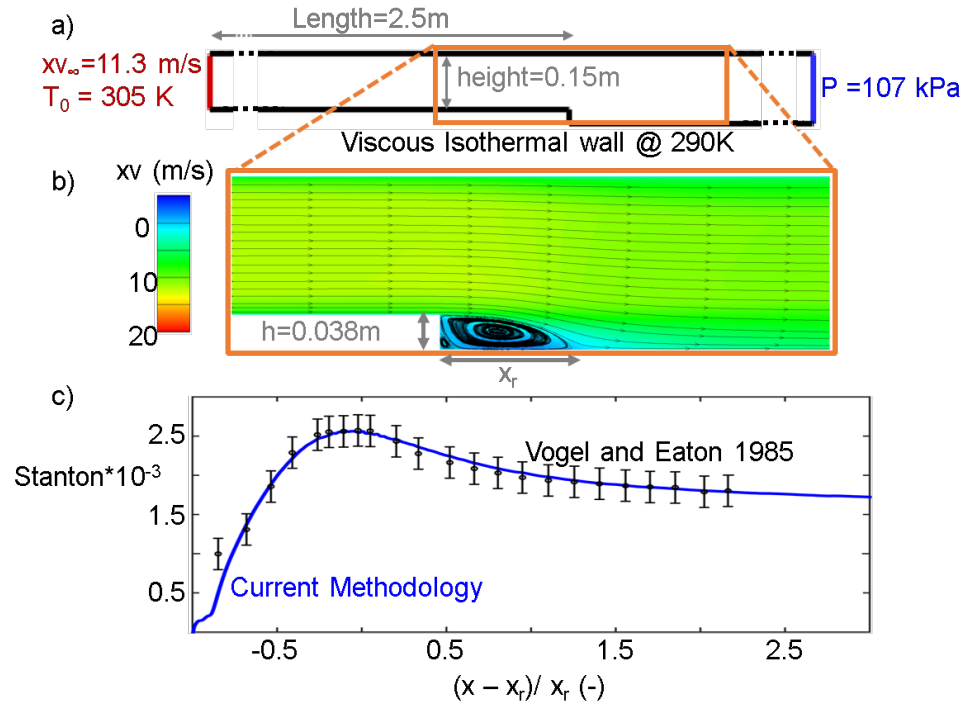


Fig. 3.8. Validation of the numerical methodology on separated flow aero-thermodynamics

time-dependent Navier-Stokes equations in either Fourier (wave-number) space or configuration (physical) space. Following this procedure, the eddies whose scales are smaller than the filter width or grid spacing used, are filtered out. Thus, the resulting equations only govern the dynamics of the large eddies. A filtered variable (denoted by an overbar) is defined by

$$\bar{\Phi}(x) = \int_D \Phi(x') G(x, x') dx' \quad (3.2)$$

Where D is the fluid domain and G is the filter function that determines the resolved scales. The finite volume discretization provides the filtering operation

$$\bar{\Phi}(x) = \frac{1}{V} \int_V \Phi(x') dx', x \in V \quad (3.3)$$

Where V is the volume of the cell. The filter function is defined as

$$G(x, x') = \begin{cases} \frac{1}{V}, x' \in V \\ 0, x' \text{ otherwise} \end{cases} \quad (3.4)$$

By filtering the Navier Stokes equations:

$$\frac{\partial \rho}{\partial t} + \frac{\partial}{\partial x_i}(\rho \bar{u}_i) = 0 \quad (3.5)$$

$$\frac{\partial \rho}{\partial t}(\rho \bar{u}_i) + \frac{\partial}{\partial x_i}(\rho \bar{u}_i)(\rho \bar{u}_i u_j) = \frac{\partial}{\partial x_j}(\mu \frac{\partial \sigma_{ij}}{\partial x_j} + \frac{\partial \bar{p}}{\partial x_i} - \frac{\partial \tau_{ij}}{\partial x_i}) \quad (3.6)$$

Where σ_{ij} is the stress tensor due to molecular viscosity:

$$\sigma_{ij} = \left[\mu \left(\frac{\partial \bar{u}_i}{\partial x_j} + \frac{\partial \bar{u}_j}{\partial x_i} \right) \right] - 2/3 \mu \frac{\partial \bar{u}_i}{\partial x_i} \delta_{ij} \quad (3.7)$$

and τ_{ij} denotes the subgrid-scale stress defined by

$$\tau_{ij} = \rho \overline{u_i u_j} - \rho \bar{u}_i \bar{u}_j \quad (3.8)$$

The subgrid-scale stress resulting from the filtering operation are unknown and require modeling. In order to model them the Boussinesq hypothesis [134] is applied, similar to the RANS models, computing subgrid-scale turbulent stresses from:

$$\tau_{ij} - 1/3 \tau_{kk} \delta_{ij} = 2 \mu_t \overline{S_{ij}} \quad (3.9)$$

Where μ_t is the subgrid-scale turbulent viscosity. The isotropic part of the stresses τ_{kk} is not modeled but added to the filtered static pressure term. $\overline{S_{ij}}$ represents the rate of the strain tensor for the resolves scale, defined by

$$\overline{S_{ij}} = 1/2 \left(\frac{\partial \bar{u}_i}{\partial x_j} + \frac{\partial \bar{u}_j}{\partial x_i} \right) \quad (3.10)$$

For compressible flows, the Favre or density-weighted filtering operator:

$$\overline{\Phi} = \frac{\rho \overline{\Phi}}{\bar{\rho}} \quad (3.11)$$

The compressible form of the subgrid stress tensor is defined as

$$T_{ij} = -\rho u_i u_j + \bar{\rho} u_i u_j \quad (3.12)$$

The term is divided into its isotropic and deviatoric part

$$T_{ij,deviatoric} = T_{ij} - 1/3 T_{ll} \delta_{ij}; \quad T_{ij,isotropic} = 1/3 T_{ll} \delta_{ij}$$

The deviatoric part of the subgrid scale stress tensor is modeled using the compressible form of the Smagorinsky model

$$T_{ij} - 1/3 T_{ll} \delta_{ij} = 2\mu_t (\delta_{ij} - 1/3 \delta_{ii} \delta_{ij}) \quad (3.13)$$

The term involving T_{ll} can be added to the filtered pressure or directly neglected [135]. Indeed, this term can be re-written as $T_{ll} = \gamma M_{sgs}^2 \bar{p}$ where M_{sgs} is the subgrid Mach number. This subgrid Mach number is expected to be small when the turbulent Mach number of the flow is small.

For the μ_t in this case the dynamic kinetic energy subgrid-scale model was used. Subgrid-scale turbulent flux of a scalar, Φ is modeled using a subgrid-scale turbulent Prandtl number by

$$q_j = \frac{\mu_t}{\sigma_t} \frac{\partial \Phi}{\partial x_j} \quad (3.14)$$

Where q_j sets the subgrid-scale flux. In the dynamic models, the subgrid-scale turbulent Prandtl number or Schmidt number is obtained by applying the dynamic procedure originally proposed by Germano [132] to the subgrid-scale flux.

The generally used Smagorinsky-Lilly models [136], [132], [133] are essentially algebraic models in which the sub scale stresses are parametrized using the resolved velocity scales. The underlying assumption is the local equilibrium between the transferred energy through the grid filter scale and the dissipation of the kinematic energy at smaller scales. Hence, in order to improve the accuracy of the predictions the transport of the subgrid-scale turbulent kinetic energy can also be accounted.

The dynamic subgrid-scale kinetic energy model used in this research takes advantage of the model proposed by Kim and Menon [137]. The subgrid-scale kinetic energy is defined as

$$k_{sgs} = \frac{1}{2}(\overline{u_k^2} - \overline{u_k}^2) \quad (3.15)$$

Which is obtained by contracting the subgrid-scale stress in the filtered Navier Stokes equation. The subgrid-scale eddy viscosity, μ_t is computed using k_{sgs} as

$$\mu_t = C_k k_{SGS}^{1/2} \Delta_f \quad (3.16)$$

Where Δ_f is the filter-size computed from $\Delta_f = V^{1/3}$. The subgrid-scale stress can be rewritten as

$$\tau_{ij} - 2/3 k_{sgs} \delta_{ij} = -2C_k k_{SGS}^{1/2} \Delta_f \overline{S_{ij}} \quad (3.17)$$

k_{sgs} is obtained by solving the transport equation

$$\frac{\partial \overline{k}_{sgs}}{\partial t} + \frac{\partial}{\partial x_i} (\overline{u_j k_{sgs}}) = -\tau_{ij} \frac{\partial \overline{u_i}}{\partial x_j} - C_s \frac{k_{sgs}^{3/2}}{\Delta_f} + \frac{\partial}{\partial x_j} \left(\frac{\mu_t}{\sigma_k} \frac{\partial k_{sgs}}{\partial x_j} \right) \quad (3.18)$$

In the above equations, the model constants C_k and C_ϵ determined dynamically [137] and σ_k is set to 0.7. The details of the implementation of the described model in Fluent and its validation are given by Kim [138].

Figure 3.9 depicts the numerical domain for the LES evaluation. The lateral walls were set as periodic translational boundary conditions. The static pressure was fixed in the outlet of the domain, while the total temperature and the temporal evolution of the total pressure were imposed in the inlet. Both, bottom and upper surfaces were modeled as viscous isothermal walls. The width of the domain was limited to 46 mm to reduce the numerical burden of the simulation. The geometrical discretization followed the guidelines established by Chapman, Choi and Moin [139] [140]. Where Δz^+ was set to 20, Δx^+ was fixed at 40 and at least 50 points per boundary layer thickness were discretized in the normal direction outside of the boundary layer. The

total cell count is 260 nodes in the normal direction, 900 elements in the axial direction and 125 across the width of the domain, with a grid of 29.25 million cells.

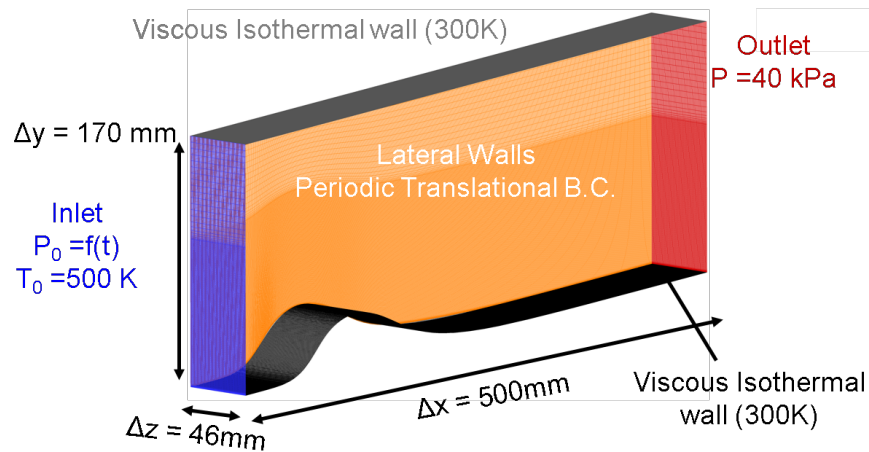


Fig. 3.9. Large Eddy Simulations numerical domain for separated flow dynamics analysis

3.2 Separated flow region reaction to sudden flow start-up

The behavior of the separated flow region after a sudden flow start-up was modeled to determine its effect on the performance of the recirculation bubble. The sudden flow discharge was set imposing a SmootherStep rise profile on the inlet total pressure. The initial pressure level $P_0(t_i0)$ was equal to 65 kPa. The overall pressure rise required 50 ms and the pressure was boosted up to $P_0(t_i0.5) = 65.516$ kPa, as depicted in Figure 3.10 a). Based on the dynamic pressure increment, the mean flow through the domain accelerates from stagnant conditions up to 47.61 m/s. The passage is initialized at room temperature, 300 K, just before the sudden flow is discharged at 500 K. During the flow start-up, the Reynolds number rises up to 80000. The wall fluxes and both momentum and thermal boundary layer were monitored at various axial locations along the hump. For comparison purposes, several steady state simulations were

carried along the total pressure rise, mimicking a quasi-steady evolution. For those evaluations, the inlet total pressure is maintained constant till convergence is achieved.

Figure 3.10 c) represents the massflow evolution at the outlet plane of the domain during the transient acceleration. Depicting a smooth rise of the massflow for the initial phase while the flow is set into motion. Then, about 50 ms later, there is a sudden massflow decay related with the arrival of the lower temperature flow. Afterwards, once the final flow velocity is established the massflow achieves a constant level.

Figure 3.10 d) represents the integrated drag coefficient along the lower wall of the domain. It steadily rises during the first instances of the acceleration. However, at about $t = 35$ ms there is a decay on the drag, which is related to the generation and growth of the separated flow region. It also suffers some sudden variation due to the thermal gradient convection across the domain, and finally achieves its final status at $t = 100$ ms.

Figure 3.11 a) represents the axial velocity at $x = 0.25$ m during the sudden flow release compared to the steady state simulations. The steady state simulations are represented at the time of the inlet total pressure conditions they correspond to. There is a noticeable time shift between the steady results and the actual conditions in the center of the domain during the transient. This temporal delay is a consequence of the mean flow establishment. Which is driven by the time that characteristics take to travel across the domain. When the flow is suddenly released, at the first instances of the total pressure rise, pressure waves are generated at the inlet. The pressure waves travel at the speed of sound plus the convective speed across the domain. Once they reach the outlet and phase the open-end boundary condition, the pressure waves are reflected as expansion waves. Which then travel backwards at the speed of sound the convective speed. Consequently, the free stream velocity correspondent to the inlet total pressure change does not take place until the expansion wave reaches that axial location. The temporal shift can be corrected based on the characteristic speeds and the particular axial location. Using this approach, the steady results in the following

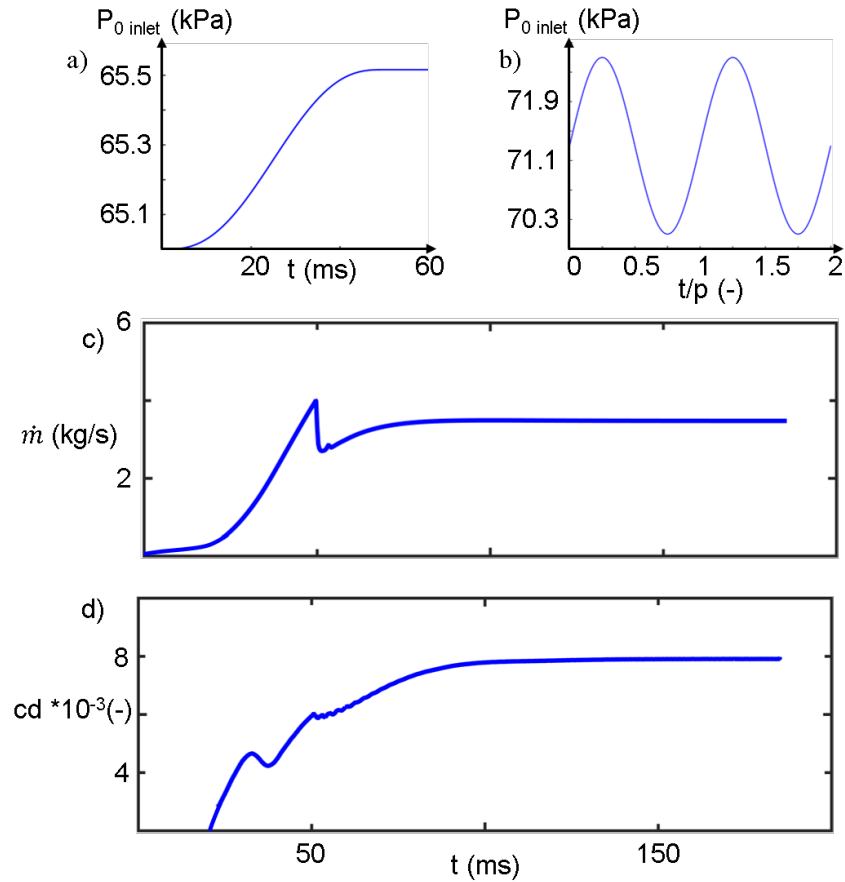


Fig. 3.10. a) Inlet boundary condition for sudden flow acceleration; b) Inlet boundary condition for periodic flow perturbation; c) Massflow through the domain and d) drag coefficient during the sudden flow acceleration

graphs of Figure 3.11 are temporally shifted to match the free stream conditions of the transient evolution.

Figure 3.11 b) depicts the evolution of the bubble length during the sudden flow start up compared to the steady state results. Likewise, Figure 3.11 c) represents the separation inception location. For the first instances of the acceleration, where the flow velocity is smaller and consequently the Reynolds number the lowest, the steady simulations depict early boundary separation and the longest separated flow region. Although, for the transient flow acceleration during the first 30 ms there is no

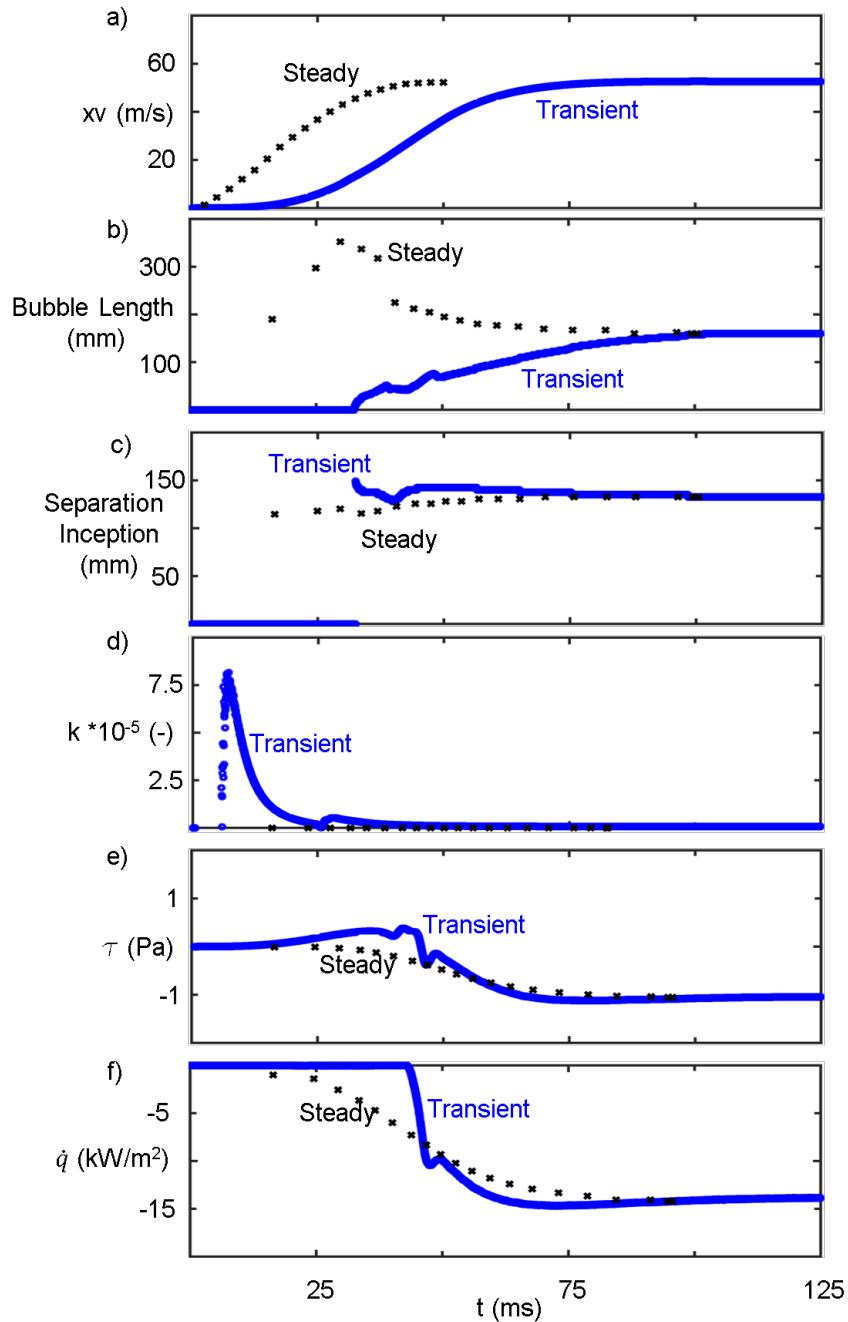


Fig. 3.11. Free stream, wall fluxes and separated region evolution during the sudden flow acceleration

separation at all. In a similar way, as opposed to the steady results the inception starts further downstream location and then gradually moves upstream. This is because of

the mean flow evolution effect on the near wall flow region. During the first instances of the sudden flow discharge there is a strong acceleration that energizes the near wall region, preventing the flow separation. As the acceleration dilutes, near the end of the total pressure rise, the scarcity of flow momentum in the boundary layer, together with the adverse pressure gradient triggers the flow separation and the bubble starts to grow up. Figure 3.11 d) represents the evolution of the acceleration parameter (k) right at the summit of the hump. For the first part of the acceleration ($t < 30$ ms) the acceleration parameter is above 10^{-7} . Denoting that during this period, the mean flow conditions are driving the narrowing of the boundary layer and preventing the flow separation. Once the flow approaches its final free stream velocity and the acceleration vanishes, the boundary layer smoothly recovers its status and becomes more prone to separation.

Figure 3.11 e) and f) represent the axial wall shear stress evolution and the heat flux footprint at the center of the domain. Because of the differences on the recirculation bubble size, the wall shear stress on the transient evolution stays positive till $t = 40$ ms while the steady results depict always negative values. In terms of heat flux, due to the initialization of the domain at room temperature, the heat flux during the initial phase of the acceleration is zero. Once the sudden discharged flow reaches the observation location through convection at $t = 45$ ms there is a sudden increase on the heat flux magnitude. Afterwards due to the smaller size of the bubble during the transient evaluation the heat flux level is higher. The smaller the bubble, the less isolation is provided between the wall and the warmer core flow.

This analysis proves how the dynamic pressure gradients; particularly the mean flow accelerations, has a strong influence modulating the flow separation. Being able to abate the separation at the lowest Reynolds numbers ($Re < 50000$) through the stimulation of the flow momentum inside of the boundary layer.

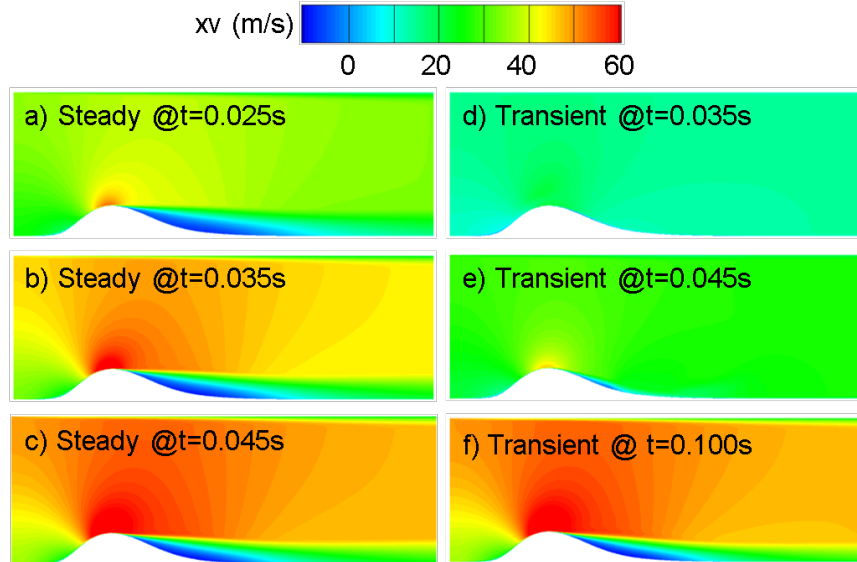


Fig. 3.12. Axial velocity contours at various instances during the blowdown compared to steady evaluations along the transient

3.3 Flow separation performance under fluctuating inlet conditions

For the analysis of the flow separation performance under fluctuating inlet conditions the same numerical domain was used. The inlet total pressure evolution followed a sinusoidal profile with a mean level of 71.3 kPa and an amplitude of 2.4 kPa, ($P_0 \in [70.1 \text{ } 72.5 \text{ kPa}]$), represented in Figure 3.10 b). The total temperature at the inlet of the domain was fixed at 500 K. With a minimum flow velocity of 20.24 m/s and a maximum of 100.1 m/s. Based on the flow temperature and its velocity, the Reynolds number during this inlet fluctuation spanned from 36000 up to 180000. The flow separation was explored at frequencies of 10, 20, 50, 100, 200, 400 and 1000 Hz. In addition, several steady state simulations were evaluated with various inlet flow conditions along the period.

Figure 3.13 a) represents the mean flow axial velocity for all the analyzed frequencies together with the steady evaluations at $x=0.25 \text{ m}$. As the excitation frequency approaches the domain frequency response, determined by the time that the characteristics take to travel across the domain ($f_{domain} = L/c$) the amplitude of the free

stream velocity is reduced. For low frequencies, 10 Hz, the peak-to-peak variations in the velocity are very similar to the ones present in the steady cases. However, as the frequency rises, since the domain does not have time to react to the inlet changes, the amplitude variations are limited. For high fluctuation rates, the free stream velocity tends to an average status. Although the mean level of the free stream velocity along the period keeps increasing as the excitation frequency intensifies. In this regard, Figure 3.13 b) represents the acceleration parameter at the hump summit. For the slower frequencies, the acceleration parameter displays its larger magnitude, over 1.5×10^{-6} . Once the frequency increases, the acceleration parameter is reduced due to the minimization of the flow velocity fluctuations. However, after the frequency exceeds 100 Hz the acceleration raises again. Although suffering small velocity magnitude fluctuations the changes at those frequencies happen so fast that flow acceleration is build up again. In this sense, Figure 3.14 represents the axial velocity profiles at $x = 0.25$ m for various instances during the periodic evolution.

For frequencies above 100 Hz the variations on the axial velocity profile are minimal. While for small frequencies, 10, 20 and 50 Hz the profiles suffer more distortion. In fact the 10 Hz profiles seem to follow closely the evolution dictated by the quasi-steady evolution.

Figure 3.13 c) and d) represent the bubble length and the separation onset respectively. It is remarkable how regardless of the fluctuation frequency, or even for the steady evaluations the separation inception remains locked in the same region for the wide range of Reynolds number explored, near $x = 140$ mm. In terms of bubble length, the 10 Hz case follows along some parts of the period the steady simulation evolution due to its similitude on the flow velocity. However as the acceleration parameter peaks (at $t/p = 0.8$), the bubble length is suddenly reduced. Reflecting again the strong influence of the mean flow temporal evolution on the separation onset.

For higher actuation frequencies, the amplitude of the bubble length variations is lessen due to the smaller velocity changes. At the highest analyzed frequencies, 200, 400 and 1000 Hz the bubble size variations are minimal and mainly driven by

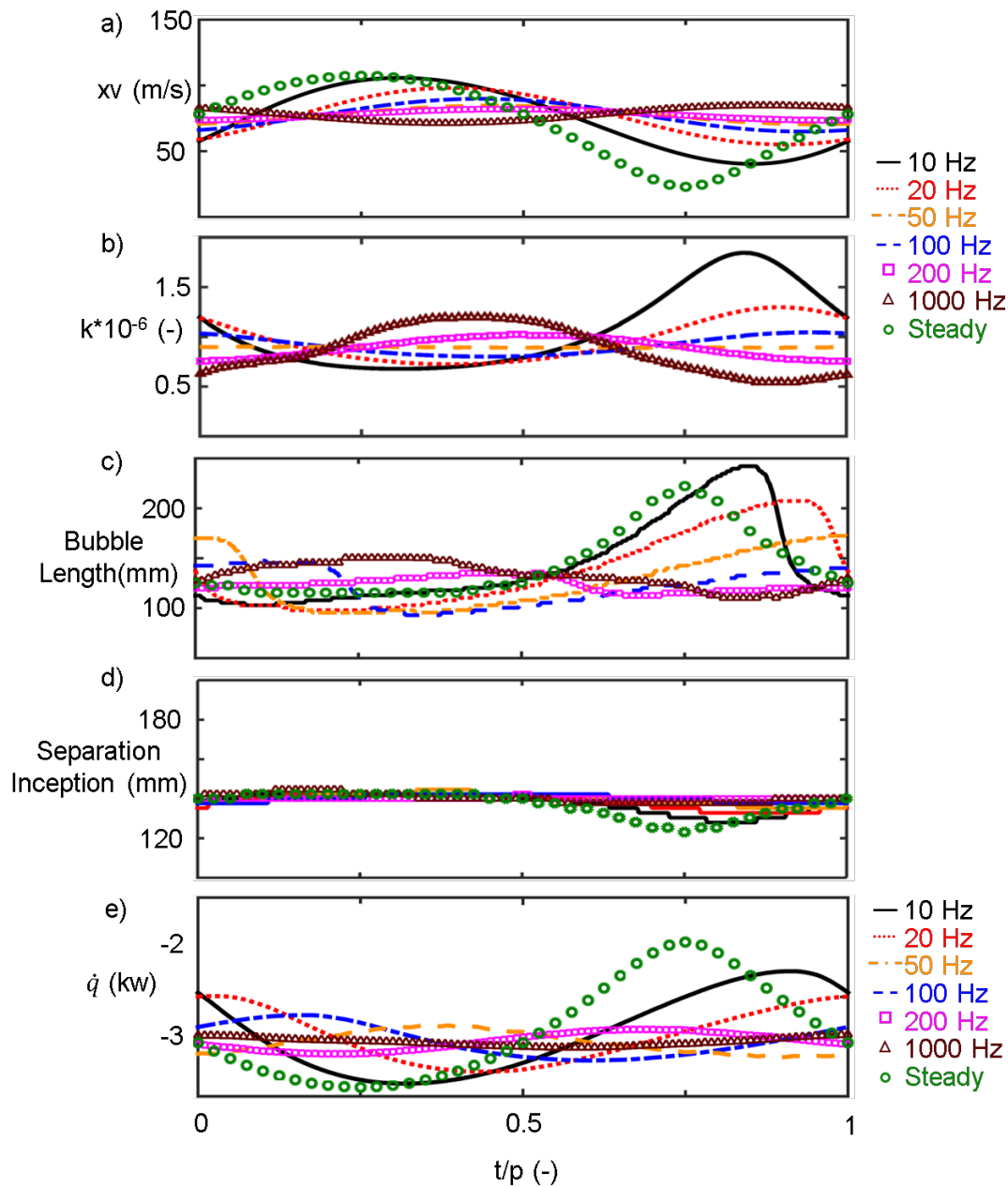


Fig. 3.13. Mean flow, separated region and wall fluxes evolution at various excitation frequencies

the dynamic flow acceleration. In particular, for the 200 Hz case the bubble length is locked at 125mm. In terms of heat transfer rates, Figure 3.13 e) depicts the heat

flux evolution at the center of the domain. The magnitude of the heat flux level is reduced when the frequency increases because of the smaller bubble sizes.

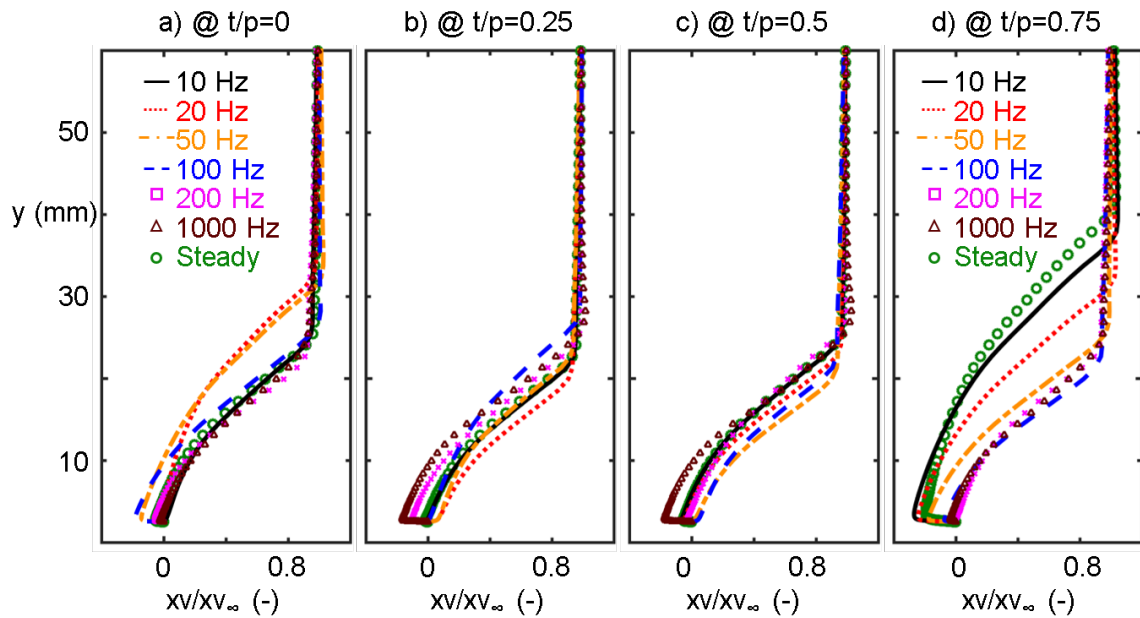


Fig. 3.14. Axial velocity profiles at various instances during the periodic disturbance at $x=0.25\text{m}$

Figure 3.15 represents the scaled drag coefficient a) along the wall mounted hump for the analyzed frequencies, together with their FFTs, b). For all the cases there are amplitude peaks at the excitation frequency and its correspondent harmonics. However, as the fluctuation rate increases, two more peaks show up at 1.4 kHz and 1.9 kHz. Those peaks correspond to the axial and normal frequency response of the domain.

An additional URANS simulation was performed to compare the results to an LES simulation with the same inlet properties. The purpose of this comparison is to verify the accuracy of the selected turbulence model resolving the dynamic performance of the flow-separated region. The fluctuation on the Reynolds number ranged 47000 up to 82000 to reduce the computational effort. Driven by a total pressure oscillation,

between 40.3 and 40.9 kPa, with a static pressure level of 40 kPa. Driven by the total pressure changes, the mean flow velocity oscillates between 40 and 80 m/s.

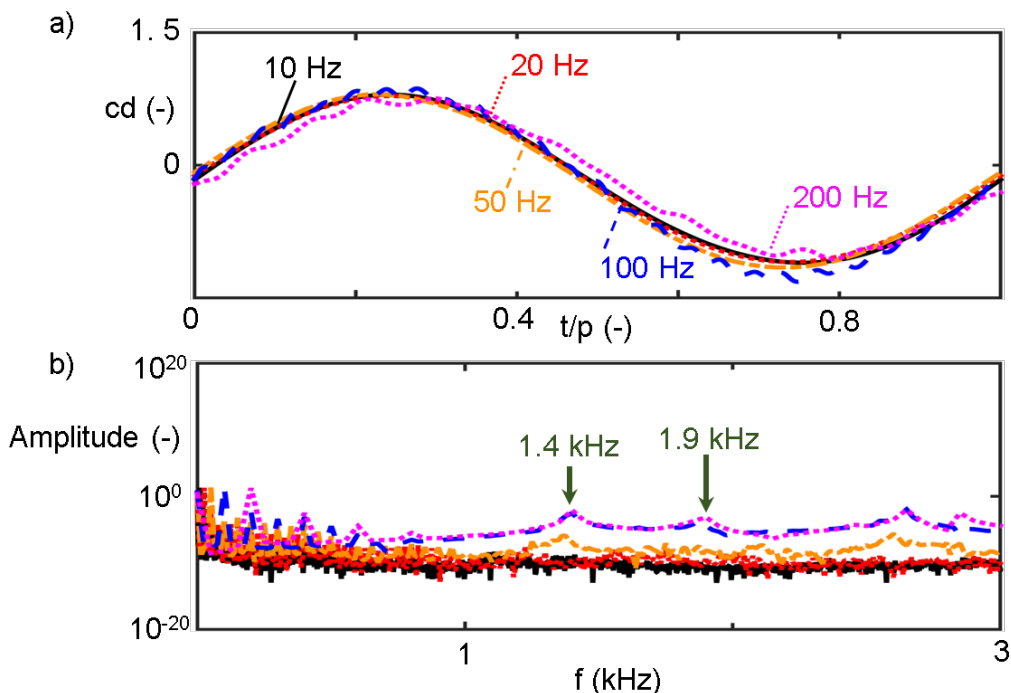


Fig. 3.15. Integral drag along the plate for various excitation frequencies, a) Drag signal after periodic convergence, b) FFT of the drag signal for 8 periods

The LES results are the phase locked average results of 18 cycles of the solution after convergence is ensured. This procedure is required to achieve an average solution comparable to Reynolds Averaged Navier-Stokes results. The number of cycles required to obtain a reasonable average was selected based on the results from a steady evaluation at the inlet total pressure mean level. Thirty different time steps were stored once the convergence was assessed. Figure 3.16 a) and b) represent the axial velocity and thermal profile at $x = 0.20$ m for various amounts of profiles averaged.

Each time step is first averaged across the width of the domain and then different time steps are averaged among each other. As the number of time steps considered increases, the silhouettes tend to match to a smoother profile. Figure 3.16 a) shows

how for less than 10 time steps averaged the mean profile deviates from the standard mean and misleading conclusions could be withdrawn if just a few periods were taken into account. Similarly, Figure 3.16 b), depicts how above 14 averaged periods the deviation from the true mean is minimal. In this sense, Figure 3.17 represents the Root Mean Square Deviation (RMSD) of the axial velocity and thermal profile for various amounts of periods averaged. The reference or true mean is assumed to be the one obtained with 30 time steps averaged. Once the amount of time steps considered is above 16 the root mean square deviation on the axial velocity and temperature are below 1.4 m/s and 1 K respectively.

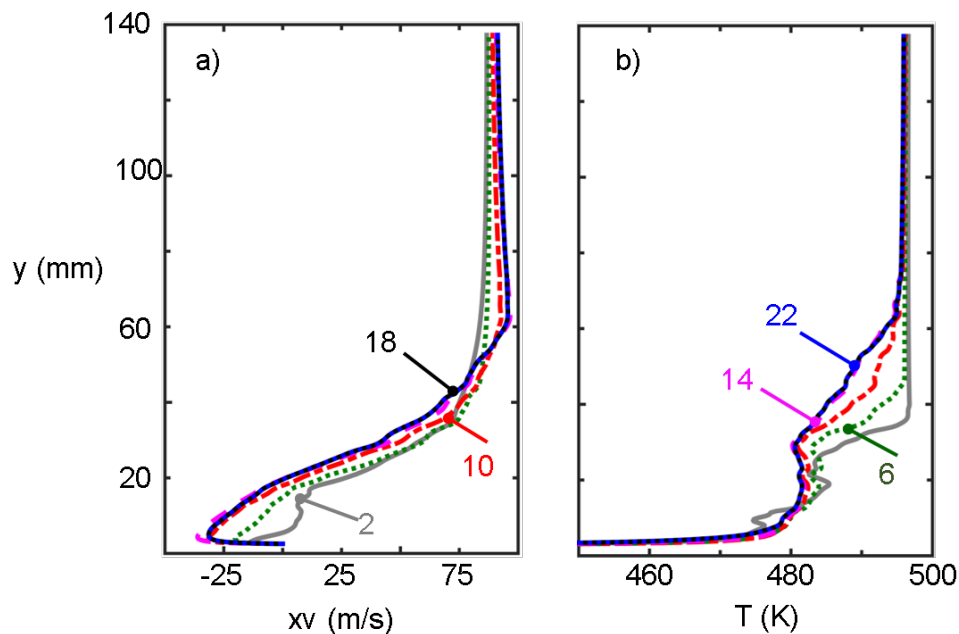


Fig. 3.16. Averaged axial velocity and thermal profiles for various # periods

Figure 3.18 a) represents the energy spectra of three different points in the domain. The first one is at the hump summit axial location and 4 cm above its pinnacle. The second one is at the same height at $x = 270$ mm. While the third one is at $x = 270$ mm and $y = 40$ mm. For all the points there is a peak corresponding to the inlet fluctuation frequency 25Hz. Points 1 and 2 follow the Kolmogorov -5/3 power law

energy decay. While the energy distribution at Point 3 is quite altered by the flow separation.

Figure 3.18 b) represents the axial flow velocity contour at 75% percent of the period for the 11th cycle. Displaying the flow separation present in the latter deceleration phase of the flow. In the bottom, there is a representation of various Q-criterion iso-surfaces. Providing an illustration of the vortical structures present in the flow.

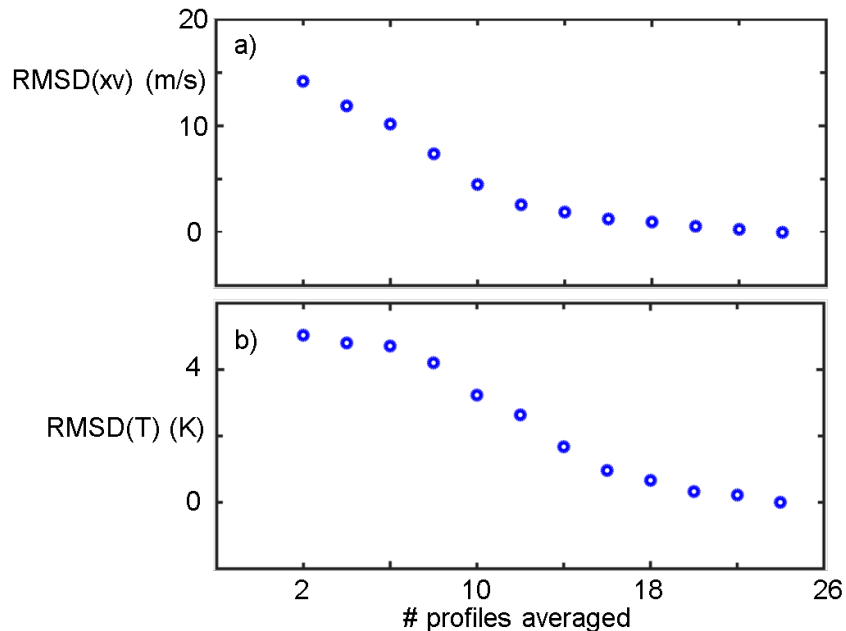


Fig. 3.17. Root mean square deviation of axial velocity and temperature along the normal plane for different # periods

Figure 3.19 represents the evaluation of the phase locked average LES results and the 2D URANS prediction with the transitional SST turbulence model. Figure 3.19 a) depicts the development of the bubble length throughout the period. The size of the separated region on the 2D URANS is over-predicting the LES results, as was already discussed in steady evaluations by Biswas et al. [129]. However, the evolution of the bubble length along the period, following the inlet total pressure fluctuations, is identical in both numerical approaches. Where only a constant offset along the period is present between the URANS and LES results. Which demonstrates the

capability of the 2D URANS simulations on predicting the dynamics of the separated flow region under transient mean flow conditions. In this way, Figure 3.19 b) represents the separation inception for the LES and URANS simulations. Displaying a perfect agreement between both numerical schemes with less than 5mm of discrepancy between them.

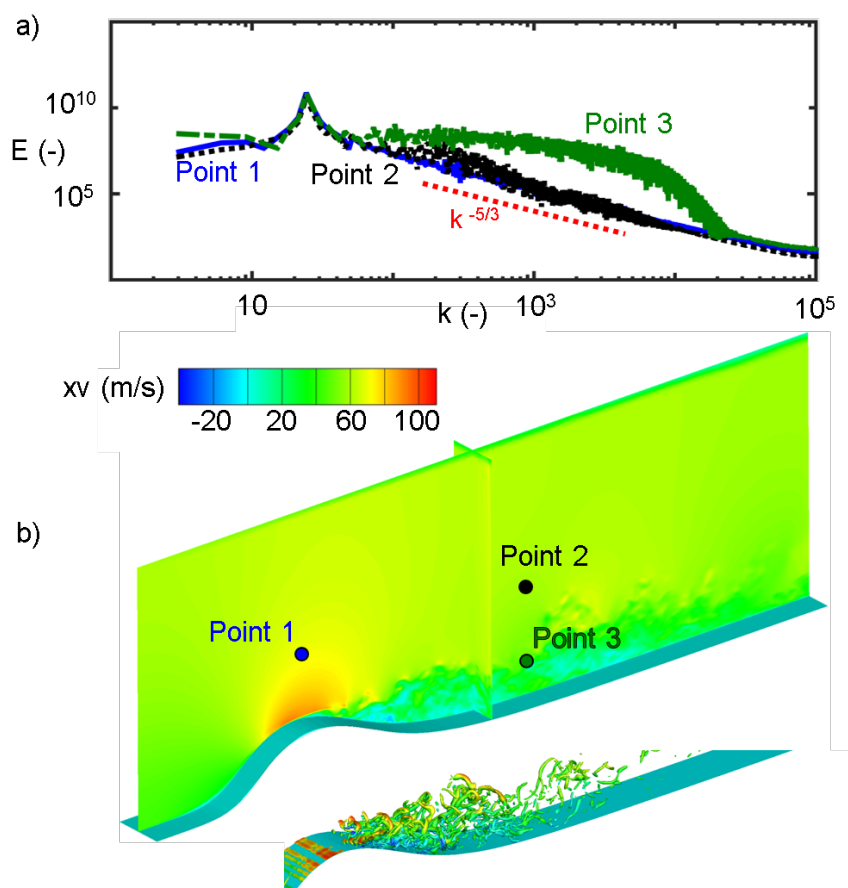


Fig. 3.18. a) Energy spectra on the domain at 3 given points b) Axial velocity contour at $t/p = 0.75$ with q -criterion iso-surfaces display

Additionally, Figure 3.19 c) represents the heat transfer coefficient evolution at $x=0.25$. Both cases follow similar evolution with variations in the magnitude driven by the differences on the recirculated flow region size.

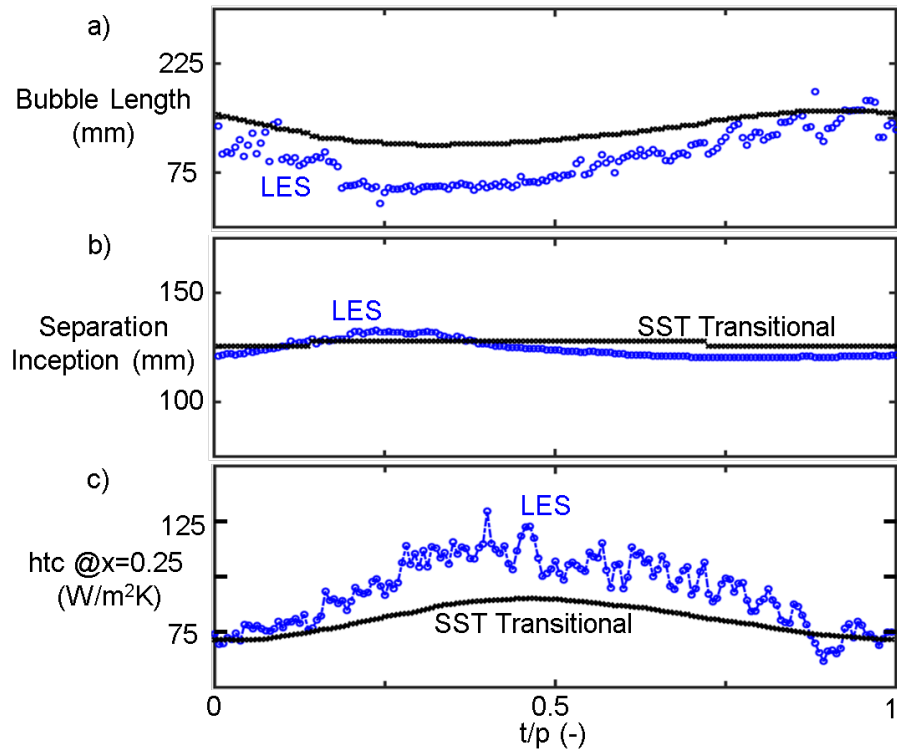


Fig. 3.19. Large Eddy Simulation vs 2D SST Transitional results, a) bubble length, b) separation inception, c) heat transfer coefficient at $x=0.25m$ during the periodic oscillation

4. EMPIRICAL ANALYSIS OF MEAN FLOW ACCELERATION IMPACT ON THE BOUNDARY LAYER DETACHMENT

A facility was designed for fundamental and applied research on detached and near wall attached flow aero-thermodynamics in a wide range of Reynolds and Mach numbers. It consists of a rectangular prism aimed for experimentation of Technology Readiness Level (TRL) 1 to 2. The facility was conceptually designed to broaden the range of Reynolds number and Mach number while guaranteeing a minimal flow conditions build up time. It is envisioned for full visual access, where the test section is defined by four different windows, as displayed in Figure 4.1 a) and b). Following this design there will not be any flow feature hidden and the corner vortices will also be visible through the working section sides.

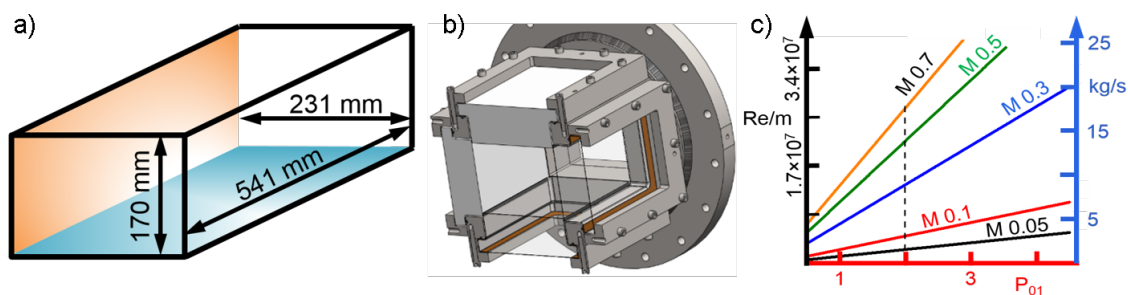


Fig. 4.1. Linear wind tunnel; a) Test section visual access dimensions; b) Test section assembly; c) Mach and Reynolds subsonic envelope

4.1 Wind tunnel design and operation

Wind tunnels are developed to replicate the actual operating conditions in a controlled environment, to measure with accuracy all the relevant fluid properties in

the test article [30, 141–145]. Generally, this matching is performed by replicating the relevant non-dimensional numbers for each application, two of the most significant non-dimensional numbers are Reynolds number and Mach number. The linear wind tunnel designed for this research is part of the Purdue Experimental Turbine Aerothermal Lab. Each one of the wind tunnels has an individual settling chamber specifically designed to set the proper conditions of velocity, temperature and turbulence of the flow before entering in the test section. The air supply of the two wind tunnels comprises the high pressure reservoir, admission valves, air heater, mixer, critical Venturi flow meter and two fast actuation valves before each one of the settling chambers. A schematic of the wind tunnel configuration is shown in Figure 4.2. The high pressure reservoir of 56 m³ contains 10000 kg of dry air at a pressure of 150bar. There are two admission valves located downstream of the high pressure reservoir that control the mass-flow through the facility. The first valve regulates the mass-flow going through the air heater, limited to 4 kg/s, and the other can provide up to 25 kg/s of dry air directly to the settling chamber. The mass-flow is measured by a Critical Flow Venturi (CFV) located just upstream of the fast actuating valves.

The pressure and the mass-flow are uncoupled in the test section thanks to the use of a sonic throat downstream of the test section. By reducing the area of this valve the total pressure in the test section is increased. The flow exiting the sonic valve will go to the atmosphere or to a vacuum tank of 283 m³, depending on the Reynolds number target of the experiment. In case of high and moderate Reynolds the air will be discharged to the atmosphere. Otherwise, for low Reynolds the air is vented to the vacuum tank, where the pressure can be brought down to 10 mbar in less than 5 hours. An additional line for purge is included in the schematic. This line is used during the starting of the facility. The flow will be directly vented to the atmosphere till steady operation is achieved in the heater and mass-flow control valves, guaranteeing steady state mean flow conditions.

The general operation of the wind tunnel follows the traditional performance of a blow-down facility. Once the admission valve opens, air starts flowing from the

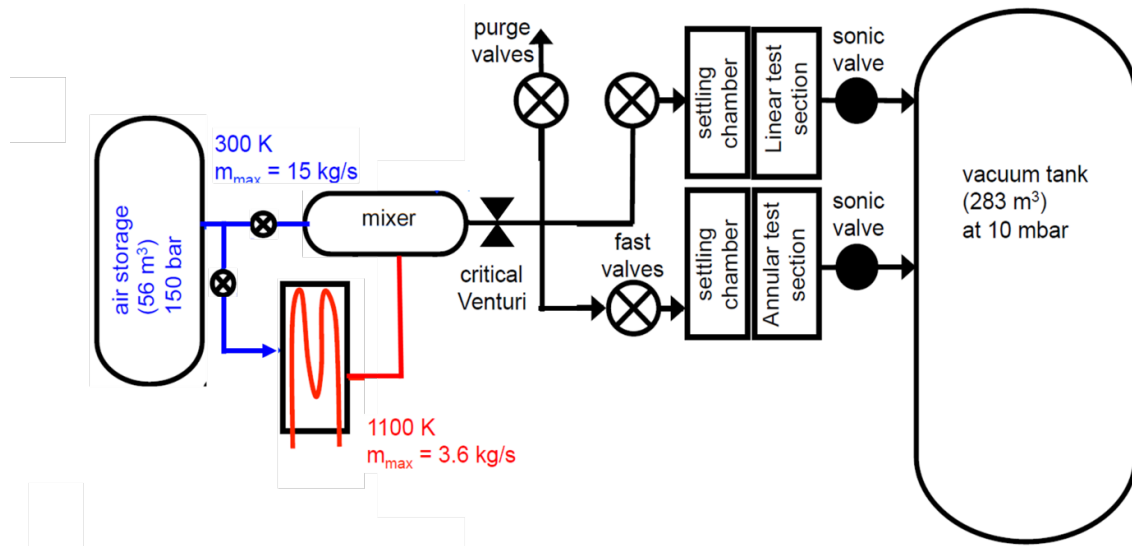


Fig. 4.2. Sketch of the Purdue Experimental Turbine Aerothermal Laboratory facility

high pressure reservoir. There are implemented two different admission valves: one to regulate the amount of air warmed up in the heater up to 1100K and the other one which regulates the cold mass-flow. The temperature is controlled by adjusting the relative position of these admission valves. The final temperature of the flow going through the facility is homogenized in a mixer, and right downstream the mass flow is measured by a critical flow Venturi with an uncertainty up to 0.15%. The fast acting valves can provide a sudden step in temperature and pressure in the test sections which allows the conduction of heat transfer experiments. The pressure in the test section is set by a manually adjusted sonic valve. Finally, the experiment finishes once the vacuum tank is filled up or whenever the high pressure reservoir is depleted (for the operation with atmospheric discharge).

The independent control of the admission valves, which accommodate temperature and total mass-flow, together with the sonic valve area, allows the independent adjustment of Mach and Reynolds number in the test section along the entire envelope, as indicated in Figure 4.3. The test section was structurally design with the following operational limits:

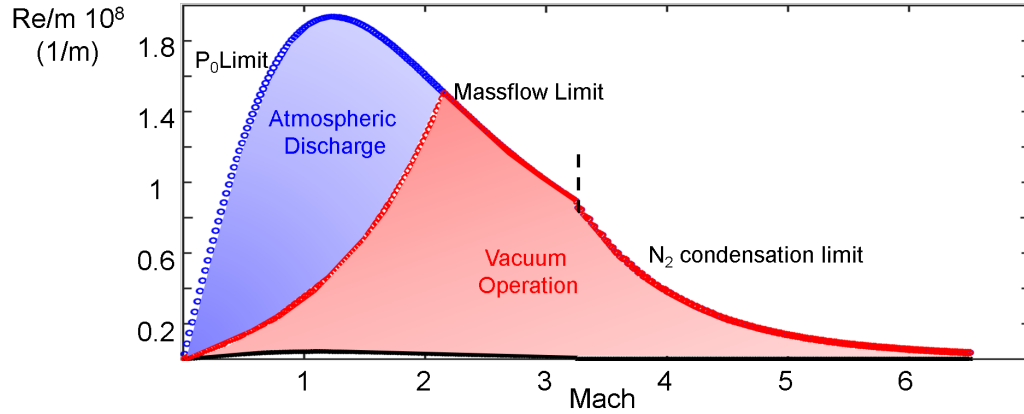


Fig. 4.3. Re/m and Mach number envelope of the linear test section

$$\begin{cases} P_0 : 0.1 - 6bar \\ T_0 : 220 - 700K \\ \dot{m} : 0.1 - 30kg/s \end{cases} \quad (4.1)$$

The maximal operational pressure was limited in order to reduce the profile thickness of the support structure and allow the use of thinner windows. While the limit on the flow temperature is set by the structural integrity of the settling chamber and its inner components. The mass-flow bandwidth is restricted by the air storage capabilities at Zucrow Laboratories and the size of the upstream piping. Figure 4.4 a) and b) represent the 3D model of the linear test section and the final hardware assembly in the laboratory. The sonic valve allows a careful adjustment of the back throat through the axial displacement of a wedge that slides inside of the test section cross sectional area.

4.2 Wind tunnel flow conditioning

Blow-down wind tunnels are cost-effective tools to study convective heat transfer and aerodynamics in high speed flows. The wind tunnel must replicate the actual

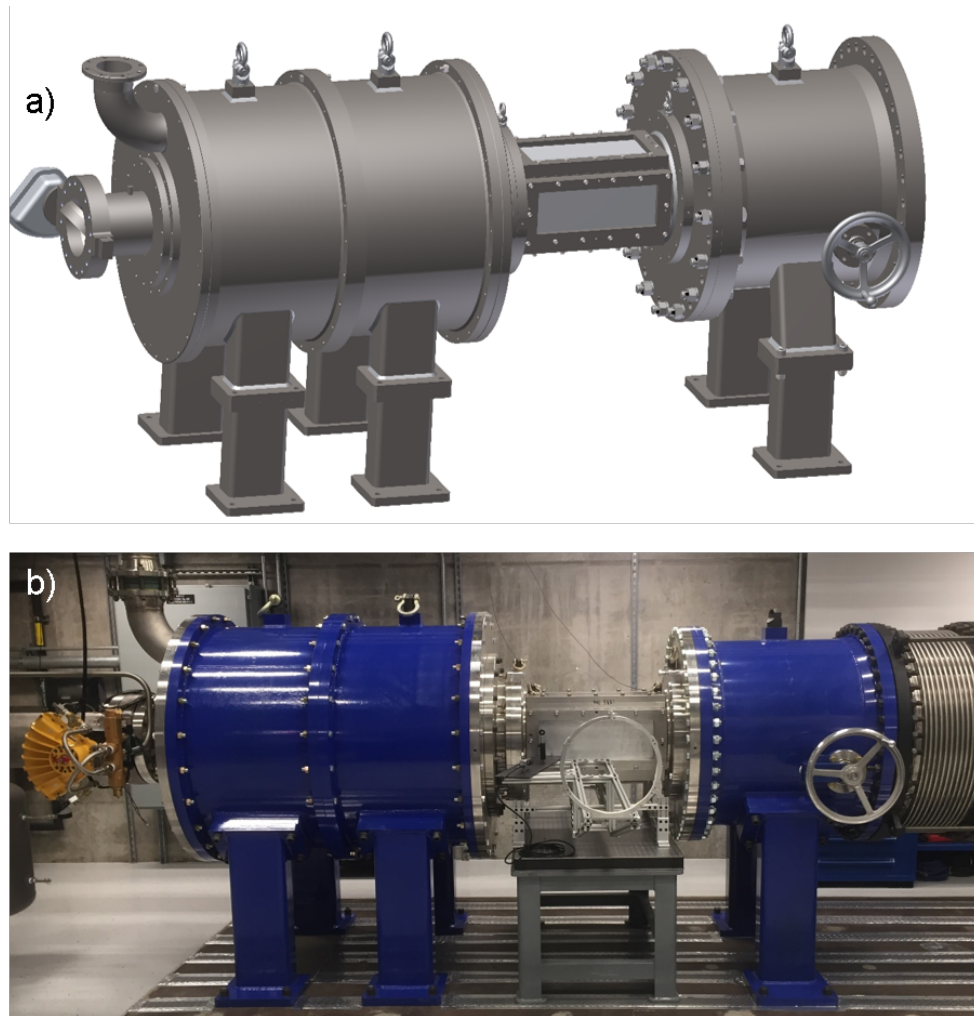


Fig. 4.4. Linear Wind tunnel design; a) CAD model, b) Wind tunnel installed at Zucrow Laboratories

running operation around the prototype, but additionally those conditions should be easy to reproduce multiple times. Consequently, the spatial and time dependent uniformity of the flow conditions around the test article should be assessed carefully. This section provides design rules and particular features of the components that guarantee adequate flow conditioning for blow-down wind tunnels suitable for subsonic and supersonic operation with mass-flow limits ranging from 1kg/s to 25 kg/s and Reynolds over meter all the way from 10^5 up to 4×10^7 . In terms of Mach numbers the described flow conditioning system will be suitable from 0.01 up to a

maximum of 7 if a convergent divergent nozzle is equipped prior to the test section. The performance was assessed using 2D and 3D Steady and Unsteady Reynolds Averaged Navier Stokes simulations. The quality of the flow conditioning was quantified in terms of total pressure loss and Root Mean Square-Deviation of the axial flow velocity inside of the test section.

Wind tunnels have been used for research and development since the Wright brothers first studied models of their planes in a wooden wind tunnel. As the requirement on performance of commercial aerospace and aeronautical transport continue to increase there is an unceasing need of understanding and clear description of the flow physics involved in each component. Due the continuous advancements and developments on Computational Fluid Dynamics the use of wind tunnels have been reduced. Nonetheless, wind tunnels remain being of primary need for many research areas, like turbomachinery, hypersonic flows or high speed convective heat transfer [143, 146–149], where the complex flow phenomena and the coupled structural, fluid-dynamics and thermal interactions are not accurately resolved yet by computational methods. Hence, in aerospace and generally in engineering, the use of wind tunnels in experimental approaches results fundamental for the ulterior advance of science and technology [150–152].

In a blow-down wind tunnel, Figure 4.5, the test section is located in between two reservoirs: the upstream high pressure tank and the downstream pressure reservoir, which could be a vacuum tank for low pressure levels or the atmosphere. A fast actuated control valve is located at the exit of the high pressure reservoir. Once the valve opens the air flows naturally towards the low pressure chamber through the test section. Just upstream of the test section the settling chamber is the element that smooths the flow and mitigates the flow fluctuations providing constant and uniform flow conditions to the test section. Turbulence, temperature, flow velocity magnitude and direction must be properly modulated upstream of the test article. In subsonic operation Mach and Reynolds number are controlled by the upstream conditions and a sonic throat located downstream of the test section. For a constant total pressure in

the high pressure reservoirs the opening of the upstream valve will set the mass-flow, assuming it gets choked. Then the position of the downstream valve will establish the experimental back pressure. By closing the throttle valve even beyond the choking limit, the static pressure in the test section will increase. Based on the downstream valve throat area once it gets choked, the Mach number through the test section is adjusted following the prescribed area ratio between the throat and the test section area. In addition, by changing the flow total temperature the Reynolds number is modulated.

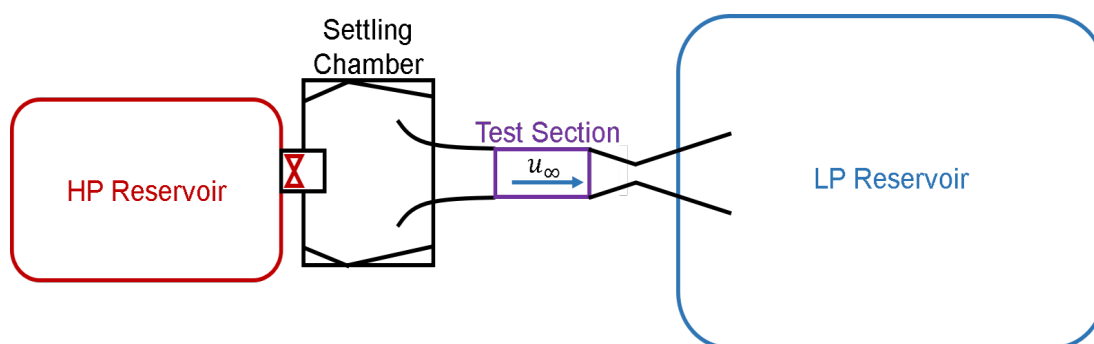


Fig. 4.5. Blow-down wind tunnel layout

The operation of a blow-down wind tunnel is normally constrained by a limited test time determined by the volume of the reservoirs and the test conditions. Due to the finite temporal window availability, the uniformity on the test conditions must be promptly guaranteed. To achieve uniform and stable flow conditions through the test article, the settling chamber and the contraction area are used to smooth and standardize the flow [153]. The settling chamber is the volume upstream of the contraction where the flow is discharged from the high pressure reservoir. Inside of the stilling section the flow must be distributed as uniformly as possible. Similarly, its velocity is reduced to alleviate the energetic disturbances that the stream may entrain while travelling through the system, eliminating swirl and unsteadiness. Inside of the settling chamber several combinations of honeycombs and screens are placed to modulate the turbulence level and mitigate upstream disturbances.

The contraction area is one of the most critical elements of a wind tunnel, its main purpose is to further homogenize the flow and guide the flow from the settling chamber to the final test cross sectional configuration. A defective design of the contraction area may cause flow separation just upstream of the test section and perturb the experimental capabilities of the wind tunnel. The design of the contraction area has been heavily researched including, 2D, 3D and axi-symmetric shapes with disparate cross sectional profiles [154–157]. In this sense, numerical modeling tools have been previously used to assess the performance of wind tunnel contractions [158].

The targeted performance envelope of this flow conditioning systems ranges from low Reynolds and mass-flows around 10^5 Reynolds/m and 1 kg/s up to 4×10^7 Reynolds/m and 25 kg/s respectively. In terms of Mach numbers this design should provide uniform conditions for various test section Mach numbers all the way from 0.01 up to hypersonic conditions Mach 7. Additionally, the maximum operational pressure of the settling chamber is fixed at 1 MPa. On top of that, in order to guarantee enough flow uniformity during the complete envelope, the flow velocity should be homogeneous in both time and space. The design requirements consist on a maximum temporal variation of the flow velocity of 2% while geometrically expecting deviations below 2.5% in the core section. Geometrically, aiming the minimization of the overall wind tunnel dimensions, trying to keep both the length and the diameter of the conditioning system as small as possible. In order to design such system Unsteady Reynolds-Averaged Navier-Stokes simulations are carried out to characterize the performance of several type of contractions and qualify the 3D flow features on radially discharged subsonic blow-down wind tunnel operation.

4.2.1 Flow discharge into the settling chamber

The flow discharge in the settling chamber is a fundamental element in the design of a wind tunnel. It becomes a critical component for blow-down or short duration facilities. Once the fast actuated valves or membranes open, there is a sudden discharge

of pressurized flow into the settling chamber. The pressure wave that is generated during this first instances is considerably powerful being able to damage, bend or destroy the honeycomb and flow straighteners that may find in its path. Consequently, the flow release into the stilling section must be done in such way that the integrity of the settling chamber is kept, minimizing the pressure losses while maintaining a reasonable volume. In Figure 4.6 there are represented four different flow discharge configurations.

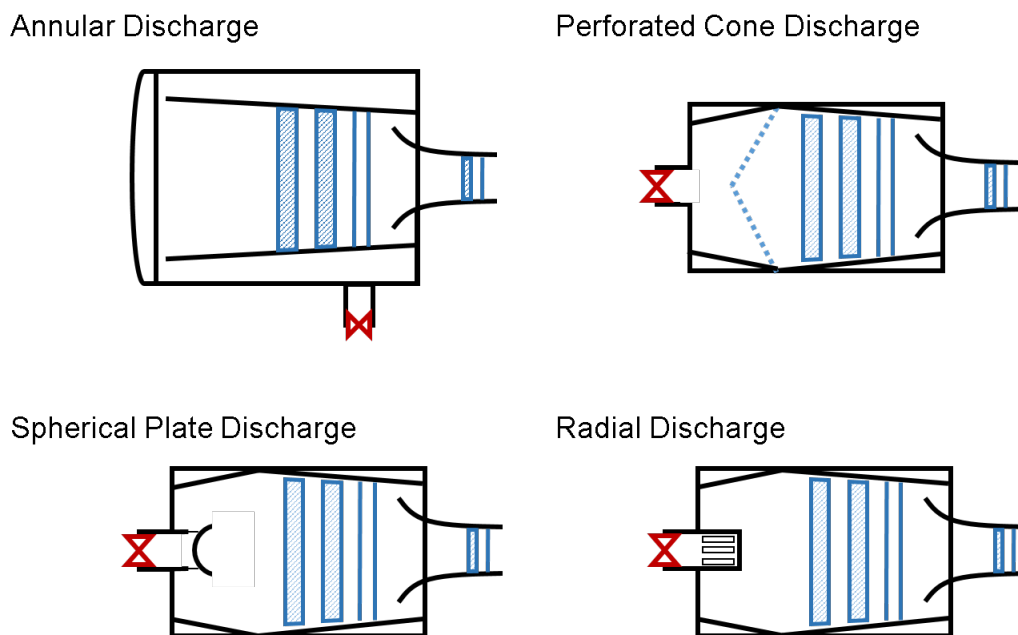


Fig. 4.6. Flow discharge topologies

- a) Annular discharge; In this case the flow is radially discharged into a cylindrical channel conformed in between the external wall and the wall of the settling chamber. The flow is guided towards the front wall of the external cylinder and then diverted into the open end of the settling chamber inner wall. From then on the flow goes through the honeycombs and screen till the contraction area. This type of flow discharge guarantees the settling chamber integrity. However, this solution requires a larger diameter in order to accommodate the cylindrical volume of the discharge. During the first instances of sudden flow

discharges there could be flow accumulation in the settling chambers of short duration wind tunnels. Due to the abrupt opening of the discharge valves large amounts of high pressure air are vented into the chamber till the back pressure information acoustically travels backward and the mass-flow levels are adjusted. Those mass-flow accumulations cause compression phenomena that leads to local temperature increase, as exposed by Andreoli et al. [159]. In order to reduce the initial temperature peaks, which endanger the system integrity, the settling chamber volume must be minimized. Consequently, to maintain the settling chamber reliability this option is not the preferred one.

- b) Discharge into a perforated cone. In this design the flow is axially discharged in the settling chamber volume and diverted to the honeycombs through a perforated cone. This option guarantees a homogeneous discharge into the honeycomb cross sectional area. Although, during the first instances of the blow-down operation the cone must hold the strong pressure gradients harming the structural integrity. This topology of flow discharge is better suited for continuous wind tunnels. However its application is not optimum for blow down neither for short duration facilities.
- c) Discharge into a spherical plate. In this case, the discharge of the jet is done against a spherical plate that distributes the flow radially into the settling chamber.
- d) Radial discharge into the settling chamber volume. In this configuration the flow is radially distributed providing uniform flow released towards the lateral walls of the settling chamber volume avoiding direct discharge of the jets to the honeycombs.

4.2.2 Stilling section

The stilling section is the element designed to provide uniform and stable flow to the downstream elements of the wind tunnel, mitigating the flow disturbances generated upstream. To increase the flow quality and alleviate energetic structures in the flow it contains the largest cross sectional area of the wind tunnel. Ideally the flow must be slowed down as close as possible to stagnant conditions and later on smoothly accelerated in a uniform manner [160]. To develop good quality flow, several devices like screens and honeycombs are placed through the settling chamber, reducing the turbulence levels. The length of the settling chamber before the honeycomb must guarantee the flow alignment with the wind tunnel axis, reducing the incidence angle through the honeycomb cells. The total length of the settling chamber could be about 0.5 to 3 stilling section hydraulic diameters. Extreme short settling chambers may be unable to properly modulate the flow turbulence. On the contrary, excessive length could cause harsh mass-flow accumulation issues, as explained earlier in the discharge topology discussion, leading to temperature peaks and an oversize of the wind tunnel. Similarly, considering the boundary layer growth on the wall of the settling chamber the length should be minimized. The turbulence intensity and length scale of the flow delivered to the contraction area can be moderated through the honeycombs and screen series located along the settling chamber. By modifying the cell sizes and the distances between the honeycombs and screens both, turbulence intensity and length scales can be controlled.

4.2.3 Honeycomb

The honeycombs placed with its cells aligned to the flow direction will ease the transversal velocity fluctuations with a minimal effect on the stream wise velocity. They are the most efficient devices to lessen the flow swirl and lateral velocity variations [151, 161]. The honeycomb cells can be of various shapes: circular, squared or hexagonal, as displayed in Figure 4.7(a,b,c). Among these, the most usual choice is

the hexagonal cross sectional shape due to its lower pressure drop coefficient [162], Table 4.1.

Table 4.1.
Pressure loss coefficient of different honeycomb cross sectional configurations

Honeycomb type	Circular	Rectangular	Hexagonal
Loss coefficient (K_l)	0.3	0.33	0.2

There are some characteristic parameters that describe the honeycomb cell geometry (Figure 4.7 d): the honeycomb length, L_h , the side height d_h , the metal sheet thickness t_h , the hydraulic cell diameter Φ_h , and the porosity β_h .

The honeycomb porosity is defined as the ratio between flow area and the total area

$$\beta_h = \frac{flow_{area}}{total_{area}} = \left(1 - \frac{\Phi_h}{\Phi_{SC}}\right)^2 \quad (4.2)$$

Where Φ_{SC} is the settling chamber diameter at the honeycomb location.

To maximize the honeycomb performance, the cell size should be smaller than the scale of the incoming cross-sectional velocity fluctuations. However, extremely small cell sizes should be avoided to prevent the clogging risks. Similarly, to guarantee the structural integrity of the honeycomb, they should have sufficient rigidity to support the applied forces, avoiding deformation. To maintain the force load in a minimum level and improve the honeycomb performance the flow velocity through the cells must be as low as possible. Likewise, to maximize the turbulence mitigation to generation ratio, the porosity of the honeycomb (β_h) should always be larger than 0.8 [163].

The length of the honeycomb should be contained between 6 to 10 cell hydraulic diameters [151]. Extremely short cells will not mitigate the flow swirl, whereas excessive long passages will generate unnecessary total pressure decay due to the boundary layer growth [164]. To guarantee the proper operation of the honeycomb the flow yaw and pitch angle should not be larger than 10 degrees, avoiding stall in the honeycomb

cells, which will increase the overall pressure drop and generate non-uniformities. In case of larger swirl and flow angles, screen meshes could be placed before honeycomb to reduce the flow incidence. Taking this into the consideration, the first honeycomb should be placed in a location of the settling chamber where the flow is already axial. The spacing between the successive honeycombs results fundamental for two different reasons. Firstly, in order to guarantee the proper operation of the later honeycomb, the distance between adjacent flow straighteners should be enough to allow the complete recovery from the pressure perturbation caused by the prior one. On the other hand, in order to correctly dissipate the flow disturbances the distance should be smaller than the larger eddies contained in the flow. Based on this requirements two different design rules could be adjusted: the distance between consecutive honeycombs should be at most about 0.2 settling chamber diameters as proposed by Mehta and Bradshaw [165], or equivalently, the spacing between them should be between 5 and 10 times the honeycomb length [162].

The honeycombs reduce the lateral turbulence as the air flows through its narrowed cells, however they introduce longitudinal turbulence scaled with the cell hydraulic diameter. In order to mitigate the longitudinal flow fluctuations screens are introduced [166]. Screens disband large eddies into smaller scales which are decomposed faster thanks to dissipation, causing a significantly decay of turbulence. The flow is homogenized by imposing a static pressure drop proportional to the squared of the flow velocity travelling through the screen. The space between them should be of the order of the largest energy content eddies in order to stabilize the static pressure. As for the honeycomb, the screen porosity can be defined as

$$\beta_s = \frac{flow_{area}}{total_{area}} = \left(1 - \frac{d_s}{\Phi_{SC}}\right)^2 \quad (4.3)$$

To be efficient reducing the incoming flow turbulence the screen must have a porosity in the range from 60 to 80%. Screen porosity below 60% will lead to flow instabilities as a consequence of the formation of small vortices [167]. Distributing the screens with various porosities with the coarsest screen upstream and the finest screen

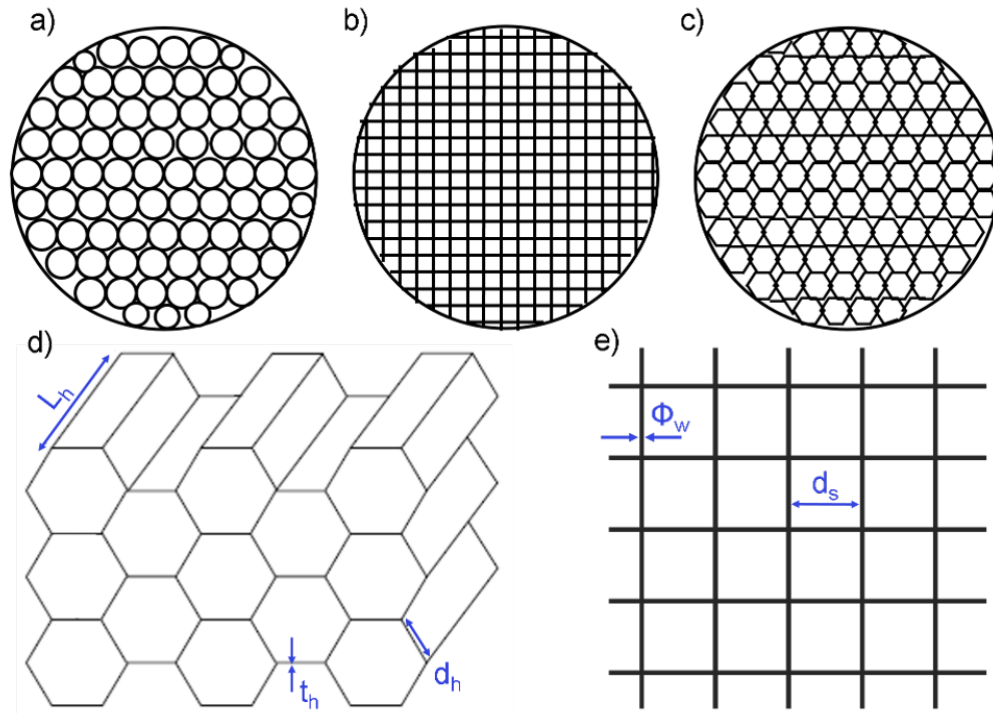


Fig. 4.7. Flow straightener a,b,c) Available cell configurations; d) cell structure; e) Rectangular screen configuration

close to the contraction area will further lessen the turbulence levels. The spacing between successive screens is adjusted following the same principles that apply for flow straighteners. Besides the screen porosity, Schubauer et al. [168] dictated that the Reynolds number based on the screen wire diameter (Re_s) should be kept below 60 to avoid supplementary turbulence generation due to vortex shedding.

$$Re_s = \frac{u\Phi_w}{\nu} \quad (4.4)$$

To ensure a proper modulation of the flow turbulence characteristics a combination of honeycombs and screens is recommended. A compromise between the turbulence control and the number of honeycombs and screens installed must be achieved to avoid over-sizing of the settling chamber and reduce the total pressure drop before the area contraction. In this sense, the optimum combination of honeycombs and screens is

very much dependent on the applications. Their combination must be adjusted in function of the final turbulent level desired in the test section.

The selection of the honeycomb and its location is also influenced by the discharge topology. We should keep in mind that in order to provide correct flow conditioning the honeycombs must perceive a maximum flow angle of 10 degrees. In this sense, for instance with the discharge with a perforated cone proposed in Figure 4.6 b), the first honeycomb could be placed close to the discharge outlet due to the low swirling introduced by this release methodology. On the contrary, for the other proposed topologies, a,c and d on Figure 4.6, there will be swirling flow with variable tangential velocity that impedes the placement of the honeycombs nearby the discharge. Hence, the honeycomb must be located downstream of the largest cross sectional area where the flow velocity is minimum and the tangential components of the velocity have been minimized. To prevent local stall in the first honeycomb, a screen could be placed in front of it, damping the radial or tangential variations under such discharge conditions.

4.2.4 Contraction area

The contraction area plays the most critical role in the flow conditioning of a wind tunnel. Its main purpose is to homogenize and guide the flow towards the working section. It must accelerate the incoming flow to the desired test section velocity and reduce the tangential and radial velocity fluctuations, while maintaining the flow uniformity both in space and time. Through the contraction area the axial flow oscillations are further mitigated by the stretching of the vortex filaments, driven by the flow acceleration. In a similar way, the contraction helps reducing the temporal variations of the flow velocity and reduces the boundary layer thickness along its walls. A contraction ratio $N = A_{inlet}/A_{outlet}$ between 6 and 15 is generally recommended [165,169], small contractions ratios will not cause much mitigation of the longitudinal flow disturbances, however excessive values will unreasonably increase the settling

chamber diameter. On the other hand, for extremely low turbulence levels in the test section, below 0.5%, the use of contraction ratios above 14 is generally adopted. For a fixed flow velocity in the test section, the use of the larger area ratios will further diminish the flow velocity through the settling chamber. In such sense again the use of larger area ratios benefits the entire flow conditioning system. However, considering the minimum length and volume objective that was stated for this research the use of area ratios in the order of 9 is selected. As disclosed by Morel [169], for larger contraction ratios the optimum length over diameter of the contraction decreases but still larger contraction ratios imply longer designs to maintain the flow uniformity.

Several types and shapes of flow contractions have been studied through the wind tunnel development history. The size and the shape of the contractions dispose the final flow quality and turbulence level in the test section [170]. Morel [169] suggested a simple analytical method of matched polynomials. While Su [158] recommended the use of a cubic polynomial at the contraction entrance matched with a higher-order polynomial for the rear part of the contraction. Similarly, the Bell and Mehtas Fifth-Order Contraction Polynomial [165] has been widely used in the design of aerospace wind tunnels:

$$y(x) = H_i - (H_i - H_e) \left[6 \left(\frac{x}{L_c} \right)^5 - 15 \left(\frac{x}{L_c} \right)^4 + 10 \left(\frac{x}{L_c} \right)^3 \right] \quad (4.5)$$

Where H_i the contraction height at inlet, H_e the contraction height at exit, y is the height of the contraction, x is the axial coordinate, and L_c the contraction length.

The use of Bezier curves to determine the shape of the contraction given the area ratio and the contraction length is recommended. The use of Bezier curves will guarantee the curvature continuity while still giving the designer the freedom to select the particular pattern of the contraction. The Bezier curve is generated from several control points, as displayed in Figure 4.10 left. This technique eases the future implementation of optimization routines on the wind tunnel contraction design.

Regarding the local wall changes, in general, large radius of curvature are preferred to reduce the over accelerations and avoid the boundary layer separation. Similarly,

the walls should be as smooth as possible and both inlet and outlet slopes must be parallel to the sections they are associated to. Along the length of the settling chamber and particularly after the last set of screens or honeycombs a boundary layer is developed in the lateral walls, which height and topology will depend on the overall dimensions of the settling chamber. To avoid the ingestion of such boundary layer and its detrimental effects, reducing the practical cross sectional area of the test section, the use of a cantilever contraction is pursued, as displayed in Figure 4.10 right. Following this procedure, a new boundary layer is formed in the lips of the contraction and the height of the boundary layer entering in the test section is mitigated, as also proposed by Bottini et al. [171].

In terms of cross sectional topologies, the contractions are also the elements in charge of guiding the flow from the settling chamber down the test section nature. They could be conical (circular to circular contraction), rectangular (rectangular to rectangular cross section contraction) or hybrid contractions (circular to rectangular cross sections or vice versa). The same design rules in terms of contraction ratio properties apply to the three different types. However, some practical design rules must be taken into consideration for hybrid contractions. In general the contractions should maintain the cross section similarity to prevent the radial or tangential flow distortions. In this line, Abbott et al. [172] presented a test section aspect ratio to contraction length/ Δ height ratio design limit to avoid corner flow separations, presented in Figure 4.8 right. In this case for the 2D contraction research assuming a rectangular design. However, in the 3D simulations will take advantage of an hybrid contraction from circular to rectangular cross section as the one depicted in Figure 4.8 left.

In order to determine the performance of some of the proposed contractions types and prove the validity of the use of Bezier curves CFD analysis of several contractions types were evaluated. Unsteady Reynolds Averaged Navier Stokes simulations were run to analyze the subsonic and supersonic performance of each configuration. The numerical simulations were carried out with the software ANSYS Fluent. To reduce

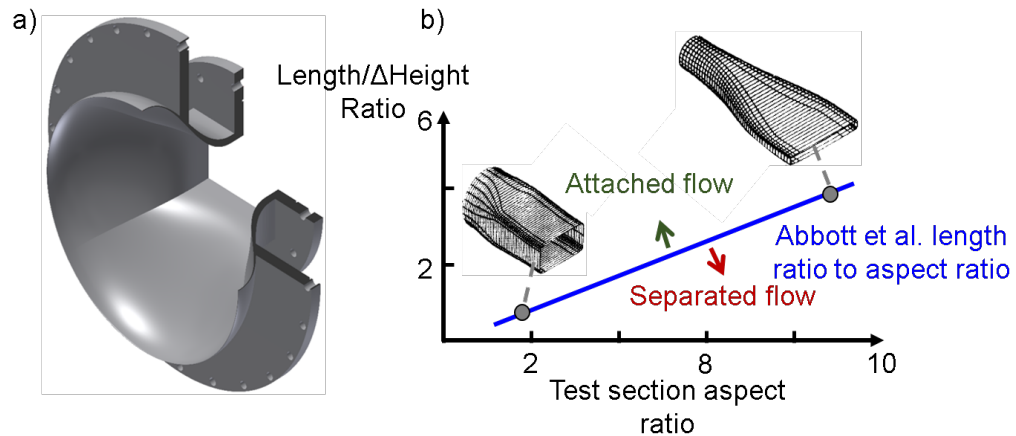


Fig. 4.8. a) 3D Contraction Area, circular to rectangular cross section
 b) Abbot et al. [172] length to aspect ratio design limits

the computational burden, some of the simulations were performed in 2D geometries. The domain, Figure 4.10 right, was meshed making use of ANSYS ICEM. While the k-SST turbulence model developed by Menter [173] was chosen for the turbulence closure. Due to the non-stationary flow behavior, in order to resolve quantitatively the aerodynamic structures, unsteady simulations were required.

The time step and inner iterations set for the transient simulation were selected based on a benchmark analysis and considering the required frequency resolution. Likewise, mesh sensitivity analysis to ensure the independence of the results were carried out, following the guidelines of Celik et al. [50]. Six different mesh sizes ($N_{c1}=7000$, $N_{c2}=12500$, $N_{c3}=25000$, $N_{c4}=50000$, $N_{c5}=100000$, $N_{c6}=200000$) were used. Figure 4.9 depicts the mass flow averaged axial velocity in the outlet plane for the different mesh configurations. The root mean square deviation (RMS-D) of the axial velocity results lower than 1.4 % for meshes like N4 or larger. The grid convergence index for the mesh of fifty thousand cells is 0.12%. Consequently, due to its proven performance the mesh N4 was selected for the study.

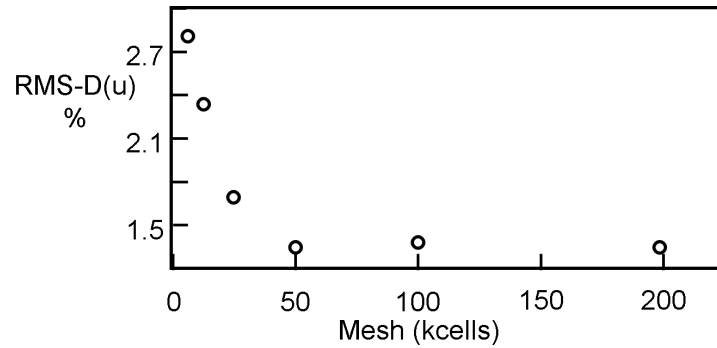


Fig. 4.9. Mesh sensitivity analysis: RMS-Deviation of axial flow velocity in the outlet plane for different meshes

Regarding the boundary layer resolution the y^+ was always kept below 0.5. The unsteady convergence of the simulations was assessed making use of the criteria published by Clark and Grover [65].

To compare the simplest contraction geometry and common design procedures with the proposed Bezier design four different configurations were evaluated, presented in Figure 4.11. Two different Bezier geometries are proposed, the first one, v1, has the inflection point close to the end of the contraction. While the second proposal, v2, has the change of curvature closer to the contraction start. Also a flat design is compared, being the cheapest solution reducing the budget of the wind tunnel. In a similar way, to evaluate the performance of the Bezier design with geometries previously employed also looking at the Bell Mehta 5th order Polynomial design. For all of them the contraction area to length ratio was kept constant. Figure 4.12 top represents the wall curvature of all the domains downstream of the lip. In this case, being a rectangular contraction, the contraction area is 14 and the length over height variation ratio is 2.25.

For all the analyzed contractions, except for the flat case, the design of the contraction lip was the same. The baseline flow conditions were kept constant: inlet P_0 104kPa, inlet T_0 500 K and a test section ideal axial velocity of 106 m/s. At the inlet the total pressure is imposed uniformly over the entire height promoting a uniform

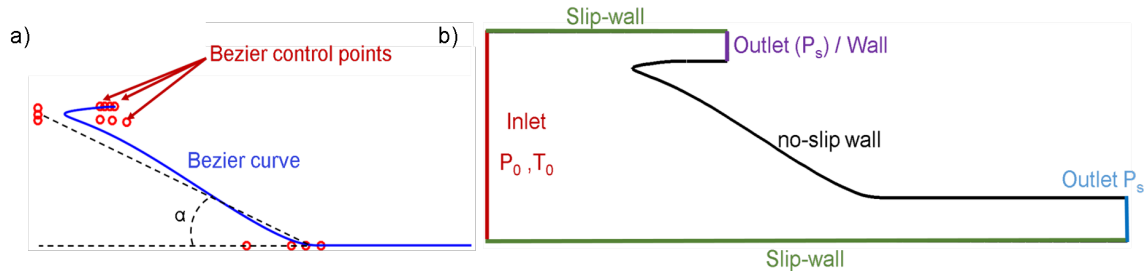


Fig. 4.10. Numerical domain for contraction area design, a) Design based on Bezier curve, b) Numerical domain for 2D URANS analysis

velocity distribution and a free stream turbulence of 3% was isotropically enforced. The static pressure of the simulation was set at the outlet, which was located 0.5 m downstream of the contraction end. In this simulation aspiration of the flow over the contraction area was performed by modelling the upper normal segment, in purple in Figure 4.10 right, as a pressure outlet.

Table 4.2.
Contractions shape performance

Type	\bar{u} (m/s)	RMSD(u)	P_0 loss
Flat Design	105.15	2.1%	0.4 %
Bell Mehta Polynomial	106.14	1.6%	0.25 %
Bezier Design v1	106.16	1.3%	0.21 %
Bezier Design v2	106.15	1.35%	0.22 %

Based on the flow velocity profile (Figure 4.11 Right) and the Root Mean Square Deviation of the axial velocity (Table 4.2) the flat design shows the worse performance. Both Bezier design have shown similar performance capabilities compared to the Bell Mehta 5th order polynomial, enabling the use of this sort of curves to assess the flow quality while not constraining the shape and length of the contraction.

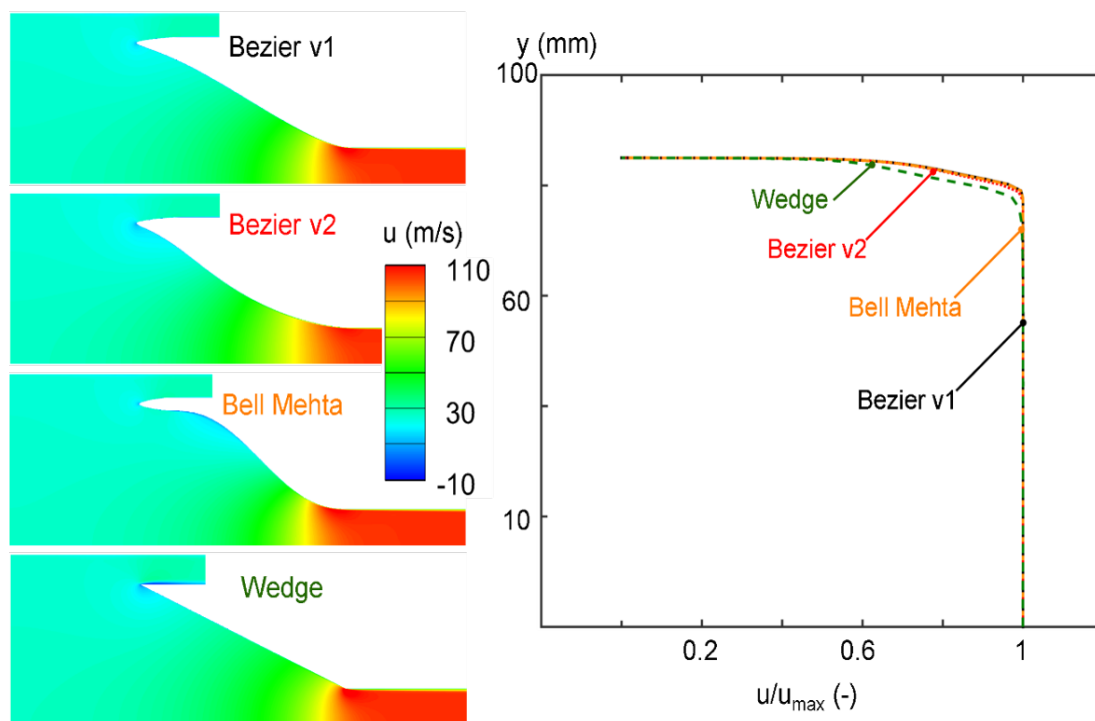


Fig. 4.11. Left) Axial velocity contour of the analyzed contraction types, Right) Flow velocity profiles at the outlet plane of the domain

Figure 4.12 bottom represents the wall pressure distribution for all the cases. In such representation we can appreciate the effect of the inflection point location and its consequences on the local wall pressure variations. Extreme adverse pressure gradients could promote the separation of the boundary layer, although from the analyzed geometries the only configuration that generates a relatively large negative pressure gradient is the flat one. In such sense the second proposed Bezier geometry has the smallest pressure gradient. Based on the axial flow velocity deviations from the root mean square value, we will focus on the Bezier design v1 for the following sections of the analysis. In this regard, the performance of the 2D Bezier v1 contraction area for several Reynolds is summarized in Table 4.3.

Table 4.3.
Contractions shape performance

Re	P_0 (kPa)	P (kPa)	T_0 (K)	\bar{u} (m/s)	RMSD(u)	P_0 loss
$4e^6$	123.05	100	400	212.32	1.1%	0.397 %
$2e^6$	110	100	500	161.69	1.4%	0.21 %
$1e^6$	92.475	90	500	88.48	2.1%	0.068 %
$5e^5$	80.675	80	500	48.08	2.9%	0.024 %
$2.5e^5$	70.192	70	500	27.38	4.2%	0.008 %

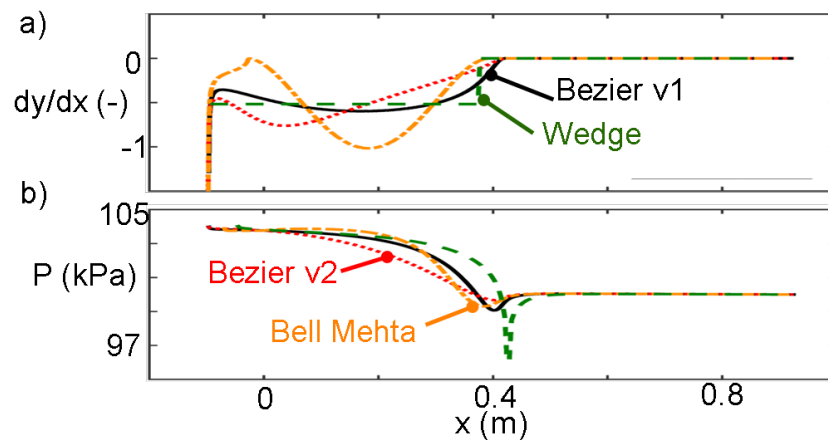


Fig. 4.12. a) Curvature of contraction shapes; b) Static pressure distribution along the contraction wall

Angle of the contraction

In order to minimize the dimensions of the flow conditioning system and abate the boundary layer growth along the contraction, the length of the contraction must be reduced. However, excessive contraction area to length ratio should be lessened to avoid adverse pressure gradients along the contraction. Instead of referring to such property as the length over height change the equivalent contraction angle will be used. Which is defined as the arctangent of the height change over the length of the

domain. Contraction angles of 10, 20, 30, 40 and 50 degrees were analyzed in the quest for the optimum contraction area to length ratio.

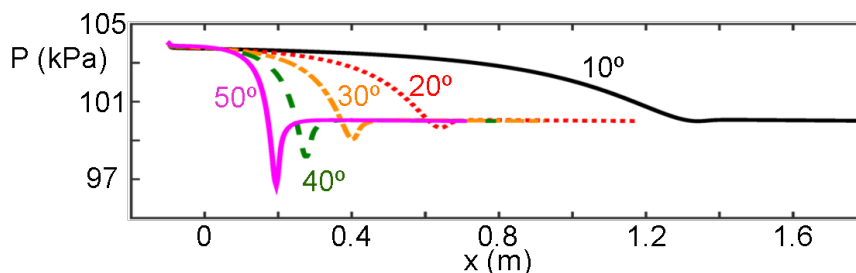


Fig. 4.13. Wall pressure distribution along the contraction for various design angles

Figure 4.14 depicts the 2D axial velocity contour of the contraction angles explored. Figure 4.15 Left and Right represent the axial velocity profile and the Root Mean Square-Deviation of the axial velocity in a plane 0.2 m downstream of the contraction end. As expected, the smaller contraction angles lead to disproportionate boundary layer growth, reducing the available test section area and increasing the blockage issues. However, as reflected in Figure 4.15 right, contractions angles above 30 degrees lead to larger deviations of the axial velocity due to over-accelerations in the contraction corner. In fact, Figure 4.13 represents the wall pressure distribution along the contractions for the explored options. The shortest contraction displays the largest adverse pressure gradient due to the reduced wall curvature. While for longer domains the pressure gradient is gradually mitigated. In order to reduce the flow conditioning dimensions and minimize the boundary layer thickness along the lateral walls of the test section the use of 30 degrees contractions is proposed.

The equivalent optimum design angles based on the propose rules of Mikhail [174] and Bell and Mehta [161] are displayed also in Figure 4.15. Based on the optimum flow uniformity avoiding separation Bell and Mehta recommended a ratio of length to height of 1.6 which is equivalent to an angle of 32 degrees. Similarly, Mikhail for the contraction ratio of our design recommends an equivalent angle of 35 degrees.

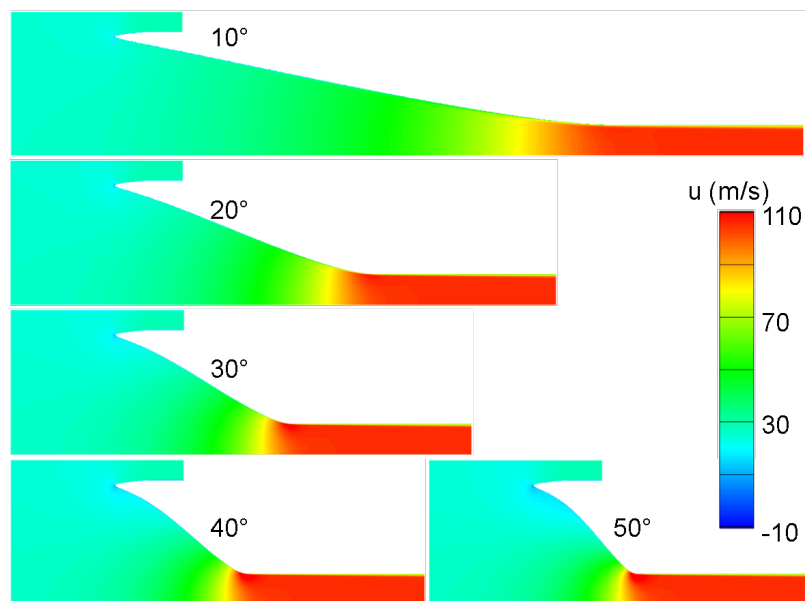


Fig. 4.14. 2D Contours of axial velocity of different contraction angles

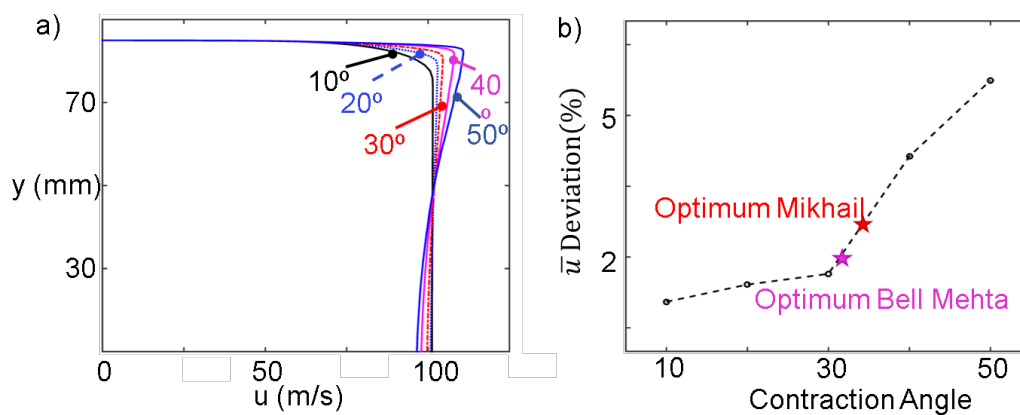


Fig. 4.15. a) Axial velocity profile; b) RMS-D (u) of different contraction angles at a plane 0.0 5m downstream of the contraction outlet

4.2.5 Detailed analysis of the 3D flow features

Simulations of the complete settling chambers volumes including the flow discharge and the contraction area were carried out to analyze the 3D flow features present in the flow conditioning system. In this case looking into radial flow dis-

charge characteristics based on the nature of the targeted wind tunnel and the objective of minimizing the flow conditioning system dimensions. Similarly, for this analysis a hybrid contraction guiding the flow from a circular cross section down to a rectangular test section configuration was introduced. The area ratio for this 3D contraction is 8.75. Based on the design recommendation in the 2D contraction analysis, a 30 degrees contraction shape was used for the top and bottom test section surfaces for optimum flow homogenization. Which entails a 27 degrees contraction for the lateral walls, keeping the length to height change ratio close to the optimum design conditions for both dimensions. Figure 4.16 depicts the modelled numerical domains of the 3D settling chamber. In order to characterize the pure aerodynamic effects of the settling chamber topology and shape, the numerical simulations did not include the flow straighteners. The use of different type of flow straighteners and their distribution along the settling chamber will modulate differently the final flow uniformity and turbulence levels. However, the purpose of this analysis is just to look at the global aerodynamic properties and the flow conditioning capabilities of only the proposed flow conditioning system which will serve as a common general source for different honeycomb and grid sets. Similarly, through the numerical simulations without straighteners the optimum location to place the honeycombs can be found looking at the distribution of the flow velocity and swirl.

To determine the effect of the flow distribution through the radial discharge two different discharge geometries were researched. Figure 4.17 represents the velocity magnitude and the flow stream-traces of a discharge with four slots, top images. Each one of the slots generate a jet that directly impinges in the settling chamber end wall. The interaction of the jets and the contoured wall creates 8 vortical structures that merge along the settling chamber. To minimize the strength of the discharged jets and achieve a more uniform radial distribution of the flow, the number of slots is doubled, bottom images of Figure 4.17. The total discharge surface in both configurations is the same, hence the jet velocity is maintained. The use of a more distributed discharge reduces the energy of each jet minimizing the strength of the induced vortices.

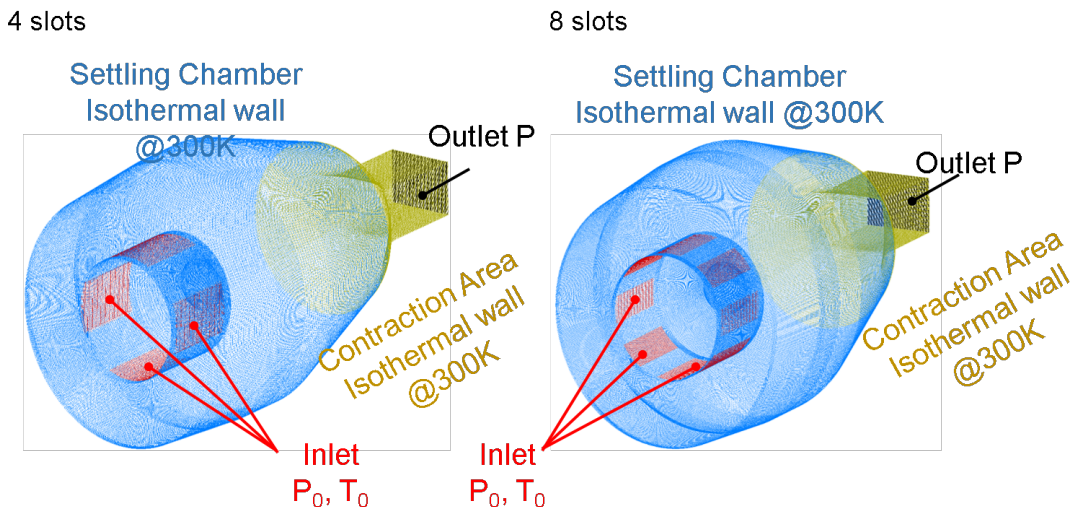


Fig. 4.16. 3D Numerical domain for complete settling chamber URANS simulations

Comparing the results of the 4 slots to the case of 8 slots it becomes apparent how the formed vortices in the tangential planes are stronger. In this sense, in the 4 slots configuration the vortices do not seem to be dispersed till almost the start of the contraction. However, for the 8 slots configuration the vortical structures dissipate much earlier, about half way through the settling chamber. In fact, in both cases at the outlet of the numerical domain, 0.5m downstream of the contraction area the flow is completely axial and there isn't any evidence of swirl. The velocity magnitude contour reveals the presence of faster flow spots near the lateral wall of the settling chamber before the divergence section starts. While in the 8 slots discharge the flow seems to decelerate more smoothly down to values around 5 m/s in the largest cross sectional area and then accelerated through the convergent segment of the settling chamber. Based on this analysis, in order to reduce the velocity of the discharge jets the discharge area must be maximized. Similarly, a more uniform discharge through multiple injection slots will prevent the generation of energetic vortical structures and promote the flow standardization as the air flows through the settling chamber.

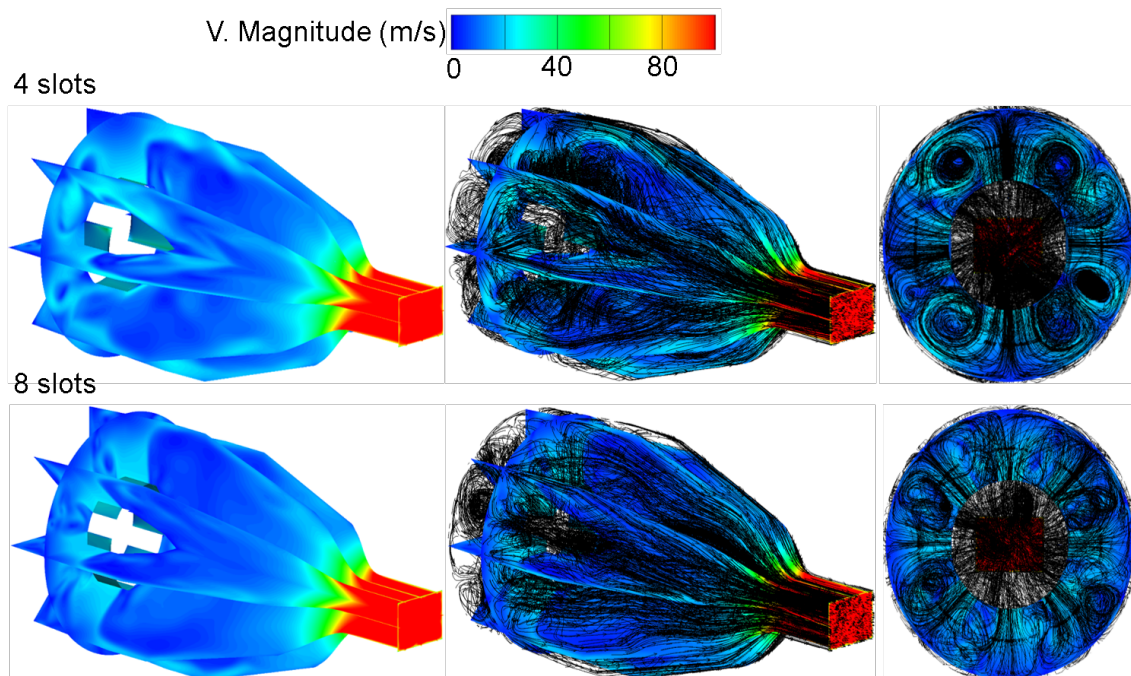


Fig. 4.17. 3D Velocity contours with streamlines comparing 4 and 8 radial discharge slots

A transient blow-down simulation was performed to assess the dynamic response of the settling chamber. The pressure in the inlet was raised from 100 kPa up to 104 kPa in 50 ms following a smoother-step transient profile, simulating the aperture of a fast actuated valve. The inlet turbulence level was kept at 3% and the turbulent viscosity ratio at 10. Which are representative values of flow through several large diameter pipelines, elbows and various valve types. The outlet pressure was kept constant for the entire simulation at 100 kPa. The discharged flow has a total temperature of 500 K. While prior to the discharge, the still air inside of the settling chamber is assumed at room temperature, 300 K. The walls through the settling chamber and the contraction were modelled as isothermal viscous surfaces at a temperature of 300 K.

Figure 4.18 a) represents the evolution of the mass-flow averaged total pressure in the outlet plane during the blow-down simulation. For the first instances of the blow-down it follows the imposed inlet profile with a delay equivalent to the charac-

teristics propagation through the settling chamber. A plateau in the total pressure is maintained till approximately $t=0.2$ s where some fluctuations are perceived and then after $t=0.3$ s the total pressure remains constant for the rest of the simulation. Figure 4.18 b) displays the evolution of the total temperature throughout the blow-down simulation. The pressure information across the domain travels at the speed of sound plus the convective speed but the temperature is only transmitted through convection and consequently a much longer delay is perceived till the total temperature starts to raise in the outlet of the domain. In this case it takes about 180 ms for the warm flow to travel 0.5 m downstream of the area contraction outlet. The total temperature rise follows the pattern dictated by the transient mixing of the stagnant flow in the settling chamber and the discharged hotter flow. That process stabilizes approximately at $t = 0.38$ s where the total temperature reaches its final value and remains constant. Finally, Figure 4.18 c) depicts the axial flow velocity during the simulation. For the first instances it follows the trend of the total pressure reaching a plateau at $t=0.07$ s and then as a consequence of the total temperature variations steeply increasing between $t=0.18$ and 0.22 s. It finally stabilizes at $t = 0.27$ s at a value of 102 m/s.

Figure 4.19 depicts the 3D temperature contour of the settling chamber at different time steps during the discharge, displaying the convection of the warmer flow released during the start-up of the blow-down. While Figure 4.20 represents the 3D velocity magnitude contour at the same snapshots of the blow-down. At $t = 0.05$ s large vortical structures are formed as a consequence of the radial flow discharge, which are revealed in both temperature and velocity magnitude contours. Those eddies promote the mixing of the hotter released flow and the stagnant flow displayed in the temperature contours for $t = 0.075$ and $t = 0.100$ s.

The response of the flow conditioning system in terms of pressure and flow velocity takes about 60 ms while for the temperature takes approximately 300 ms more due to its lower propagation characteristics. In such sense, the velocity contours remain unaltered from $t = 0.075$ s to $t = 0.38$ s, once the total temperature rise is completed

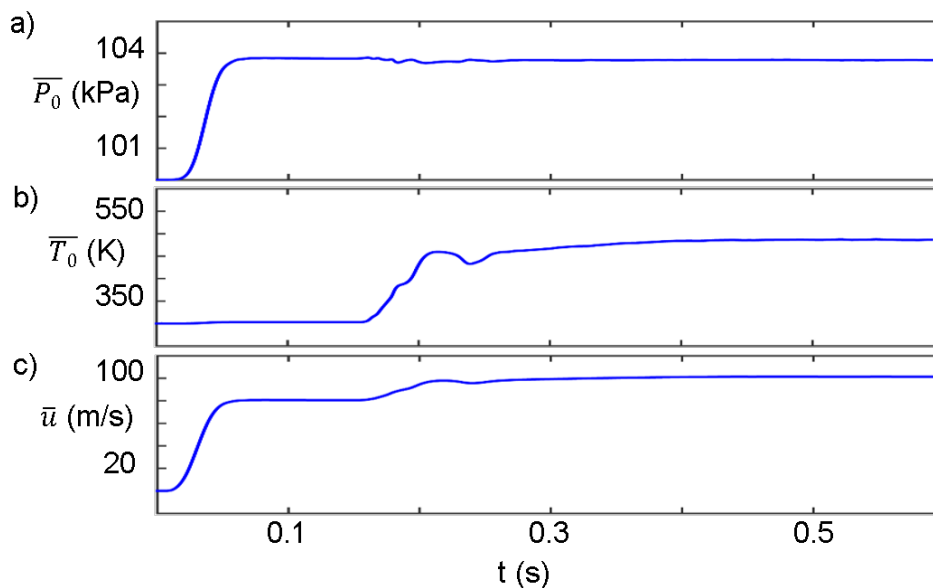


Fig. 4.18. Evolution of mass-flow averaged axial velocity, temperature, pressure and total pressure during blow-down operation at the outlet plane of the settling chamber

the final flow velocity is set. In fact, the temperature contour at $t = 0.150$ reveals how the mixed temperature flow is gradually convected through the settling chamber nucleus downstream of the larger cross sectional area. Finally, both temperature and velocity magnitude contours at $t = 0.5$ s reveal the nominal operation of the designed flow conditioning system. At design conditions the geometrical root mean square deviations for the flow velocity and temperature without considering the boundary layer are 1.2 and 1.6 % respectively.

Figure 4.21 a) depicts the deviation from the Root Mean Square of the mass-flow averaged total pressure signal in the outlet plane, which is about 0.5m downstream of the test section inlet. In this case the Root Mean Square value is computed once the flow is established, after $t = 0.38$ s. The temporal oscillations in the total pressure remain lower than 30 Pa which is about 0.03 % of the nominal total pressure. Similarly, Figure 4.21 b) represents the deviation from the Root Mean Square of the mass-flow averaged total temperature. Prior to the complete settlement of the

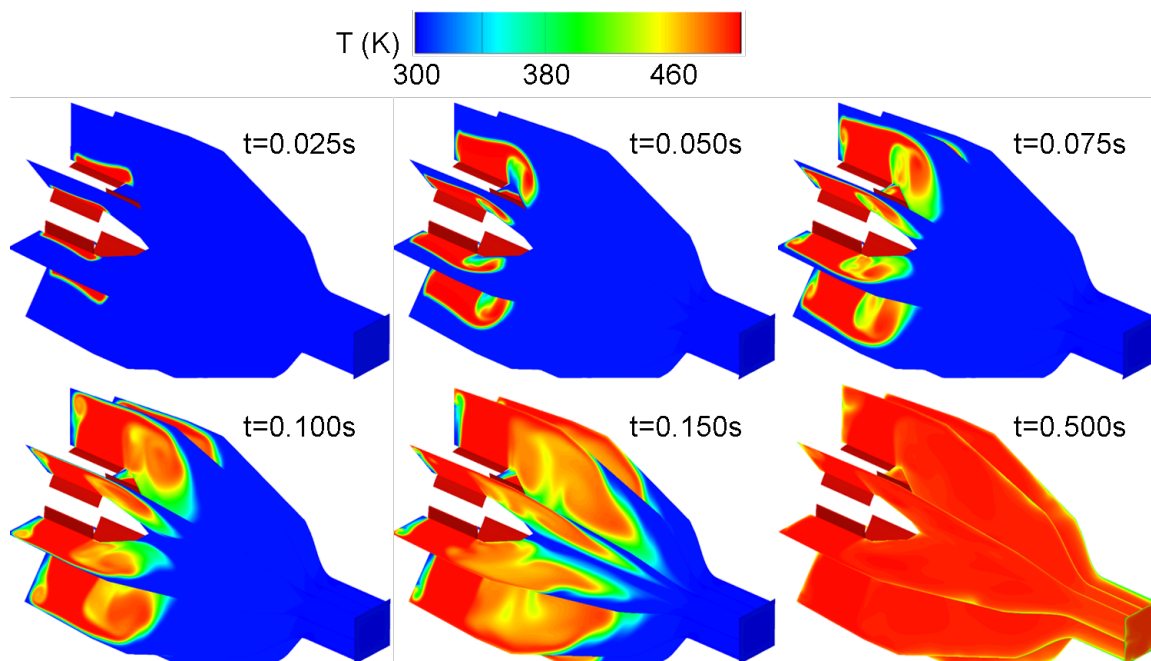


Fig. 4.19. 3D Static Temperature contour during sudden flow discharge numerical experiment

flow conditions the total temperature is still raising but after it reaches its nominal value, the maximum temporal deviation is 4 K, which represents 0.8% of total flow temperature.

In this sense, Figure 4.21 b) displays the deviation from the Root Mean Square of the mass-flow averaged axial velocity. The velocity follows slightly the trend depicted by the temperature and stabilizes at $t = 0.38s$. After that point the oscillations remain below 1 m/s.

In order to proof the robustness of the domain and investigate the harmful consequences of the blockage of one of the discharge slots an additional simulation where one of the injections slot is constrained and modelled as a wall was evaluated. Under such conditions the swirling of the flow might increase and the entire flow in the settling chamber may travel in a rotation fashion. Figure 4.22 a, and c represent the flow velocity magnitude and the stream traces for the 8 slots radial discharge configuration. While Figure 4.22 b and d represent the same domain blocking the upper

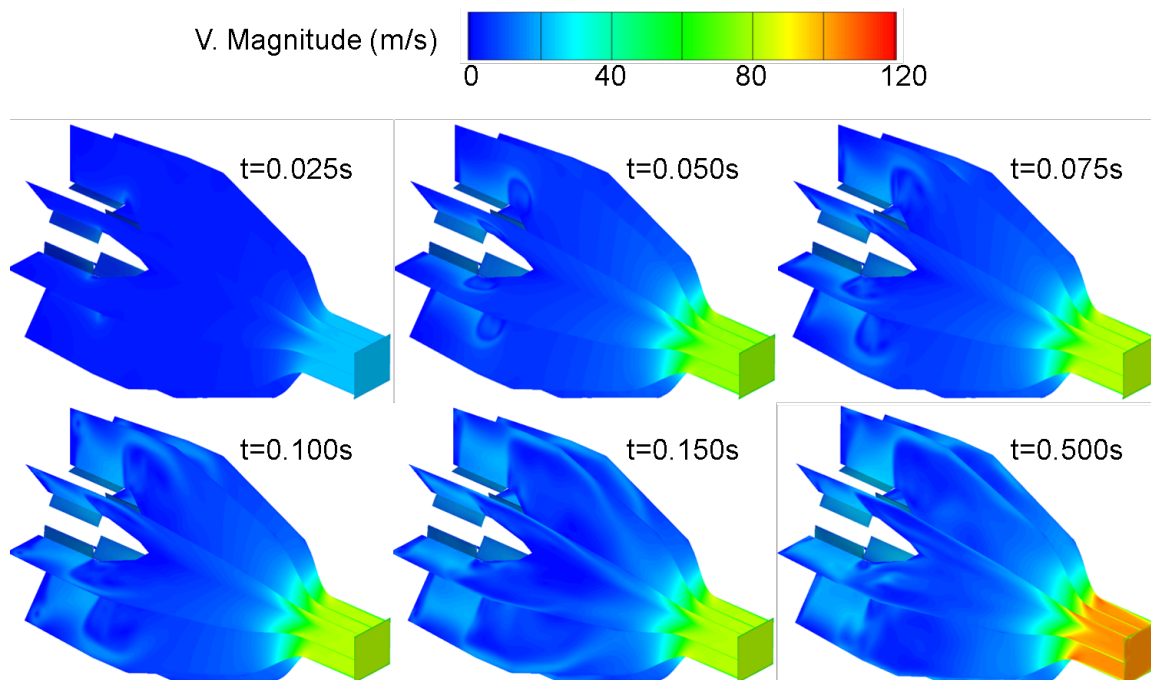


Fig. 4.20. Velocity Magnitude contour during blow-down numerical experiment

injection slot, as the flow velocity in Figure 4.22 b reveals. Due to the slot blockage there is indeed more swirling in the flow and a larger vortex is created in the upper region of the settling chamber. As a consequence, the tangential and radial components of the flow inside of the settling chamber are maintained for a longer portion in the settling chamber, as perceived by comparing Figure 4.22 c and d. However, regardless of the slot blockage the flow in the contraction outlet is purely axial and similar flow qualities are observed for both conditions.

This analysis was a useful guide to design and iterate on the design on the flow conditioning system of the linear wind tunnel. Guaranteeing sufficient flow uniformity for short duration operation and ensuring adequate flow conditioning for the testing of prototypes running mass-flow rates from 1 up to 25 kg/s. In high-speed blow-down wind tunnels it is fundamental to ensure the structural integrity of the flow straighteners, while allowing fast step-wise evolution in the flow properties for heat transfer research. Similarly, verifying the applicability of contraction designs

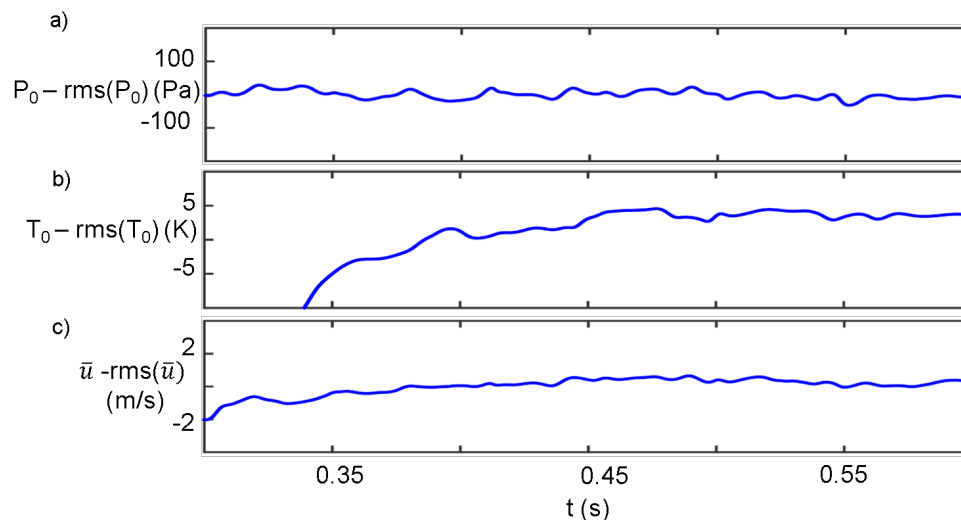


Fig. 4.21. Total pressure, total temperature and stream-wise velocity temporal evolution at the outlet plane during the sudden flow discharge transient simulation

taking advantage of Bezier polynomials to preserve continuity on the wall curvature. Also exploring the optimum length to contraction area ratio for such designs and recommended the use of 30 degrees equivalent angle contractions.

4.2.6 Experimental assessment of the facility flow conditioning

Upon commissioning of the facility several traverses and long exposure experiments were carried out to assess the performance of the flow conditioning system.

Pressure, Temperature and hotwire temporal stability

Figure 4.23 represents the static pressure measured upstream of the critical flow Venturi and the mass-flow stability for various Reynolds number operation. The mass-flow stability was assessed at different levels ranging from 0.6 kg/s up to 4 kg/s. Further details on the flow conditions for each one of the Reynolds number displayed are provided in Table 4.8.

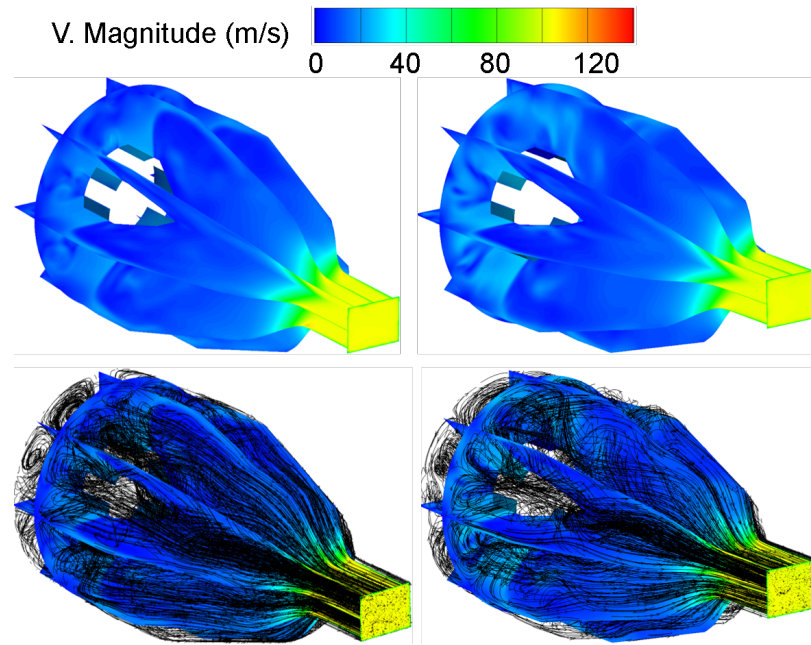


Fig. 4.22. Settling chamber velocity magnitude contours at normal operation compared to a case when one of radial discharge slots is obstructed, robustness analysis

Regardless of the mass-flow level the upstream control valve is able to guarantee an uniform and stable operation at the targeted experimental condition. As the total pressure decays in the upstream high pressure reservoir the mass-flow control valve gradually adjusts its aperture to assess constant mass-flow operation.

Figure 4.24 represents the temporal stability of total pressure, P_0 , total temperature, T_0 and stream-wise velocity for the operation at various Reynolds number. The flow conditioning system guarantees the uniformity of the total temperature and total pressure throughout the entire span of the experiment. Ensuring constant static temperature and axial flow velocity along the test section as long as the mass-flow and the downstream static pressure are constant.

Figure 4.24 represents the temporal uniformity of the total temperature evolution during an experiment with the heat exchanger in operation. Once the flow is released to the linear wind tunnel, $t = 75$ s, there is a sudden increase on the total flow temperature as the hot flow is convected through the test section. There exists

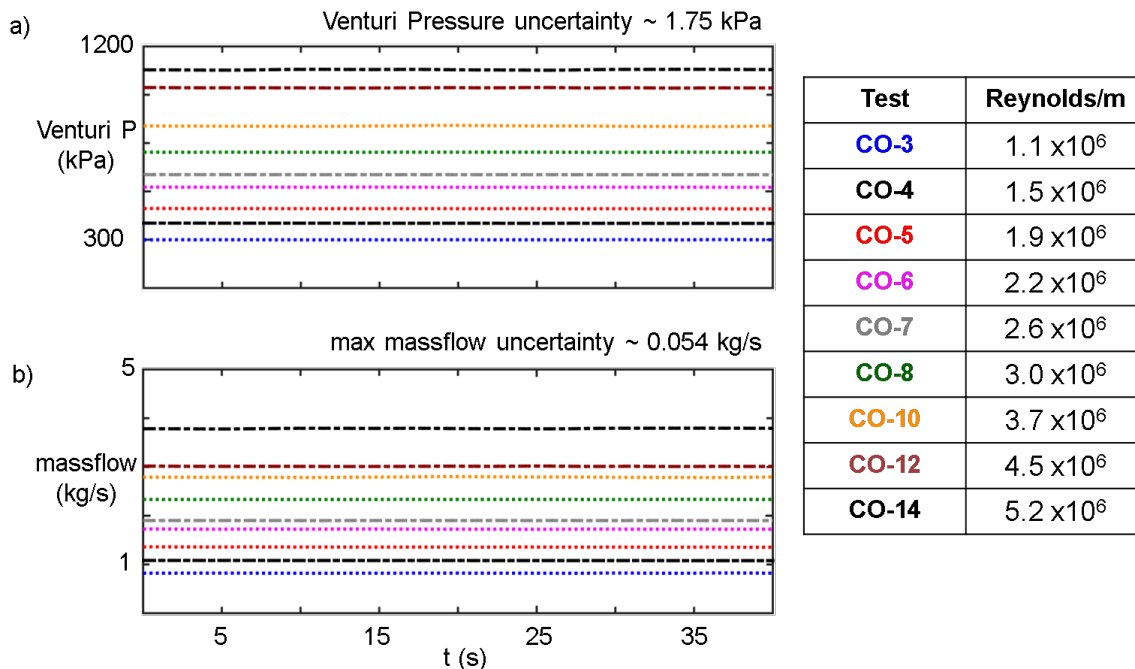


Fig. 4.23. Facility mass-flow stability

conduction heat loss as the flow travels through the settling chamber and contraction area, consequently, as the hardware warms up large total temperatures are achieved in the test section. After six minutes of operation the slope of the total temperature rise is reduced and only 1 K of total temperature increase are perceived through windows of 20 s.

Figure 4.26 top left represents the readings of the Constant Temperature Anemometer for the operation at various Re/m conditions. The mono-dimensional hotwire probe displayed on the right corner was used to characterized the temporal stability of the stream-wise velocity component, the turbulence intensity and length scales present in the wind tunnel test section. After applying the calibration of the hotwire (procedure described in Appendix D.2), Figure 4.26 bottom right depicts the temporal evolution of the stream wise velocity component in the test section. The flow conditioning system guarantees the temporal uniformity of the axial velocity as depicted in the mean value of the stream-wise velocity at a variety of Reynolds numbers.

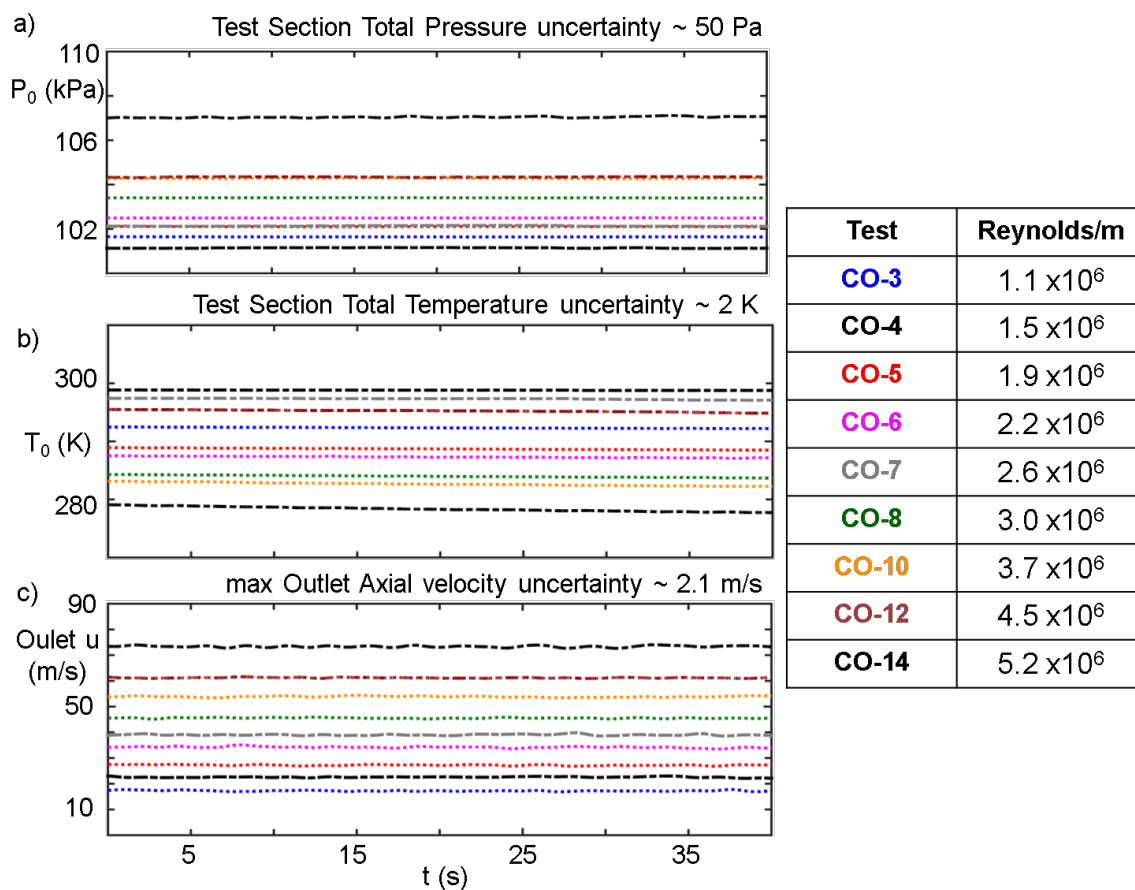


Fig. 4.24. Flow Conditioning performance, temporal uniformity of main quantities in the test section

Table 4.4 summarizes the turbulence properties during operation at 8 different Reynolds numbers, with flow velocities ranging from 10 m/s up to 120 m/s in the test section. The turbulence intensity has a slight tendency to raise with the flow velocity, from Reynolds 1.09×10^6 at 10 m/s up to 3.26×10^6 at 120 m/s the turbulence intensity grows from 3.19 % to 4.03 %. The larger Reynolds numbers are achieved with smaller flow velocities but larger static pressures and the turbulence intensity decays to 3.78 %. The integral length scale and dissipative length scale increase quasi-linearly with the Reynolds number. The integral length scale stays within 1 and 6 times the length scale of the flow straighteners cell size. The average turbulence

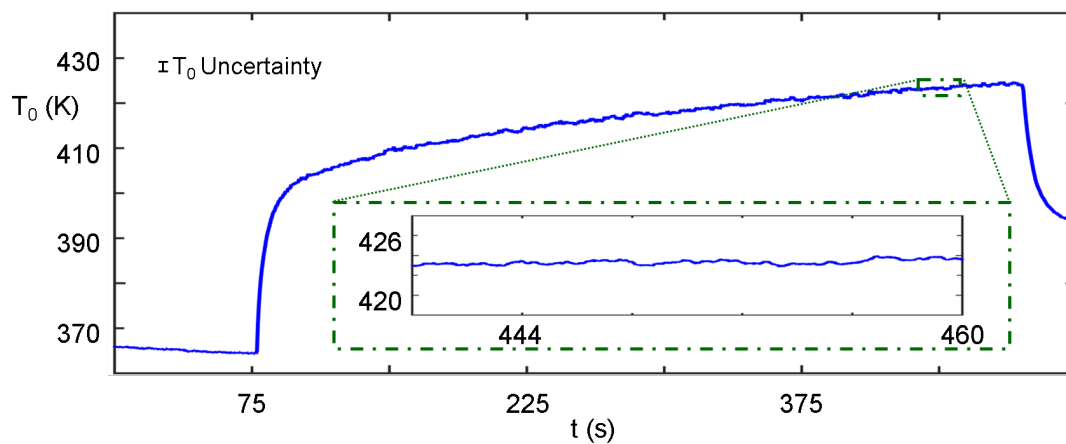


Fig. 4.25. Total flow temperature stability measured along the centerline of the test section

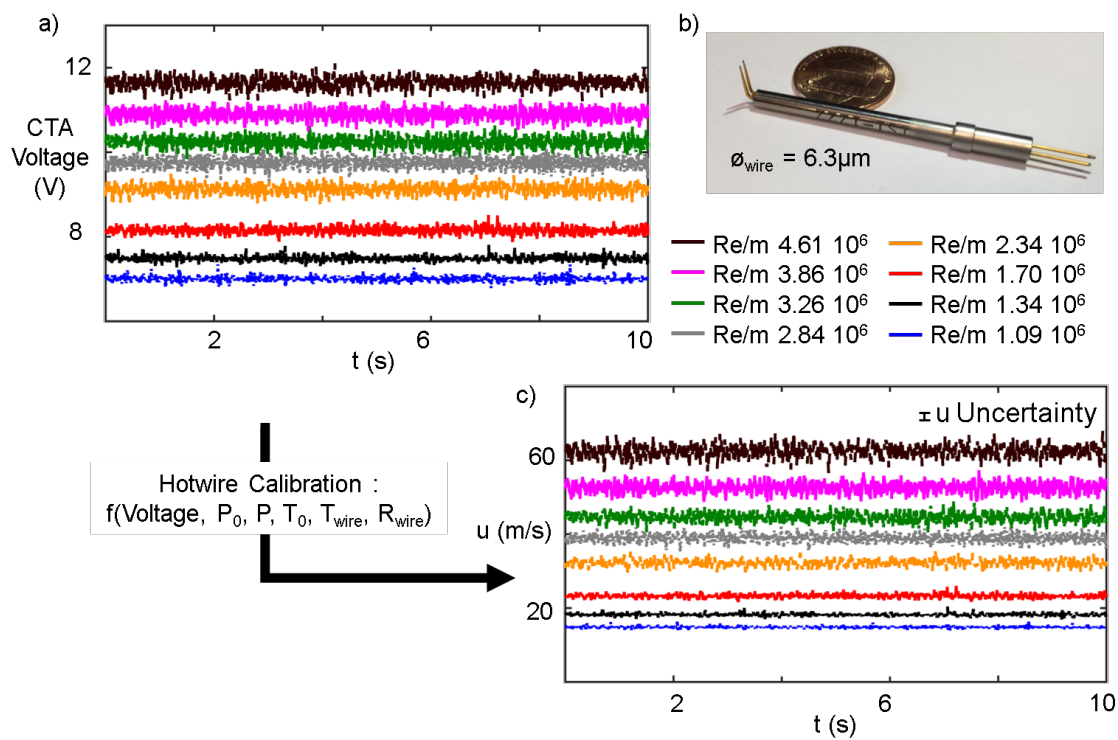


Fig. 4.26. Hot Wire temporal stability at several conditions

intensity is 3.74 % while the the averaged integral length scale and the averaged dissipative length scale are 0.02 m and 0.0059m respectively.

Table 4.4.
Turbulence, integral length scale and dissipative length scale at various Reynolds

Re/m	Tu %	Integral Length Scale, Λ_x (m)	Dissipative Length Scale, λ_x (m)
1.09×10^6	3.19	0.0065	0.0036
1.34×10^6	3.29	0.0135	0.0038
1.70×10^6	3.46	0.0135	0.0046
2.34×10^6	4.01	0.0142	0.0065
2.84×10^6	3.99	0.0225	0.0067
3.26×10^6	4.03	0.0259	0.0069
3.86×10^6	3.91	0.0322	0.0072
4.61×10^6	3.78	0.0379	0.0082

Pressure, temperature and hotwire traverses

In order to assess the spatial homogeneity of the flow delivered by the flow conditioning system hotwire, thermocouple and total pressure traverses were performed in the center plane of the test section, 0.3 m downstream of the contraction area outlet. Figure 4.27 a) represents the stream-wise velocity distribution across the height of the test section for two different conditions. The static pressure and flow total temperature were kept constant during both conditions at 101 kPa and 296 K respectively. The immersion height of the probe was adjusted for each measurement and the data acquired at each height was averaged during windows of at least 10 s duration. The velocity profile at both operational regimes is quite uniform and the deviations remain within the hotwire uncertainty. Only a small decay on the stream-wise velocity is observed for the lower mass-flow case, which could be an indication of the boundary layer size at that Reynolds number. Figure 4.27 b) depicts the Root Mean Square Deviation of the stream-wise velocity component for each normal location

along the traverse. The impact of the boundary layer height is reflected in the Root Mean Square Deviation representation near the test section boundaries. Similarly, the larger flow velocity condition depicts larger deviations from the mean during the exposure time at each height, symptoms of the hotwire uncertainty and the larger turbulence intensity at higher velocities.

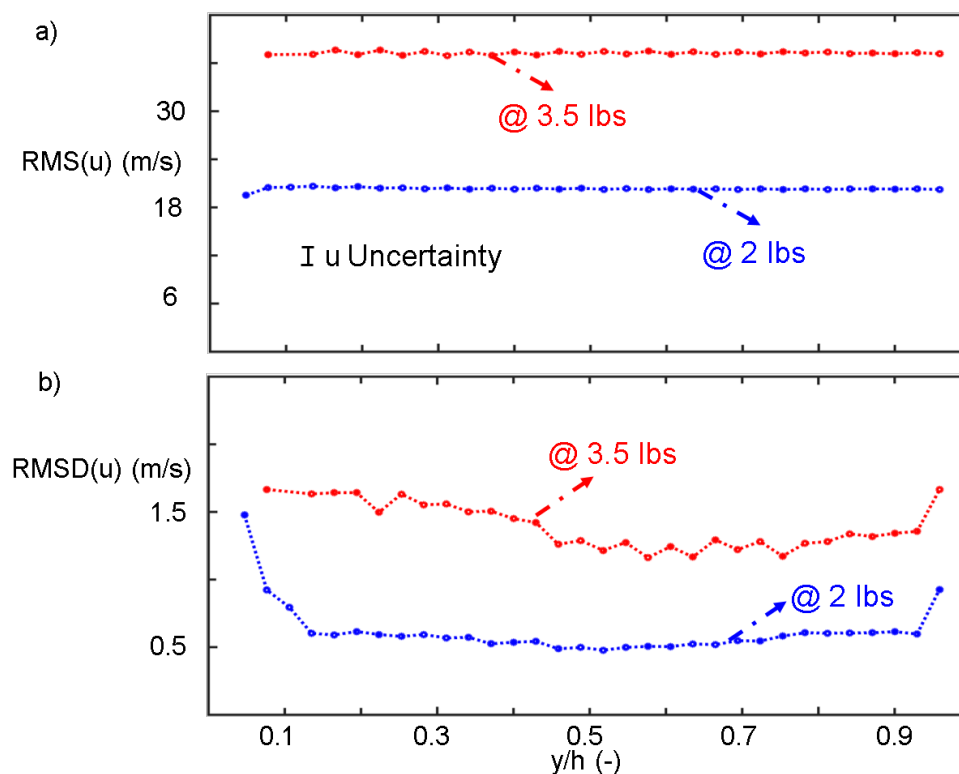


Fig. 4.27. a) Stream wise velocity profile across the height of the test section and b) Root Mean Square Deviation profile of the axial velocity component

Figure 4.28 a) depicts the total flow temperature profile across the test section height obtained with thermocouple traverses at 3 different Reynolds numbers. The operation at two different total temperature was explored: 450 K and 370 K. The operation at moderate Reynolds number, $Re/m 1.3 \times 10^6$, displays the larger thermal boundary layer profiles, with up to 10% of the test section height on each side of the test section. On the other hand, the cases at larger Reynolds numbers display smaller

thermal boundary layer thickness with less than 5% at each extreme. The temperature profile across the core of the test section remains unaltered with oscillations within the thermocouple uncertainty, indicating the correct performance of the flow conditioning system. Providing uniform total temperature across the test section height. The total temperature profiles displayed are the result of averaging 4 different sensors distributed across the span of the test section during exposure times of more than 20 seconds. In this regard, Figure 4.28 b) depicts the Root Mean Square Deviation of the total temperature across the height of the test section. Peaks of root mean square deviation are present for the three different Reynolds near to the thermal boundary layer edges. While the deviation from the mean across the core of the test section stays within the thermocouple uncertainty.

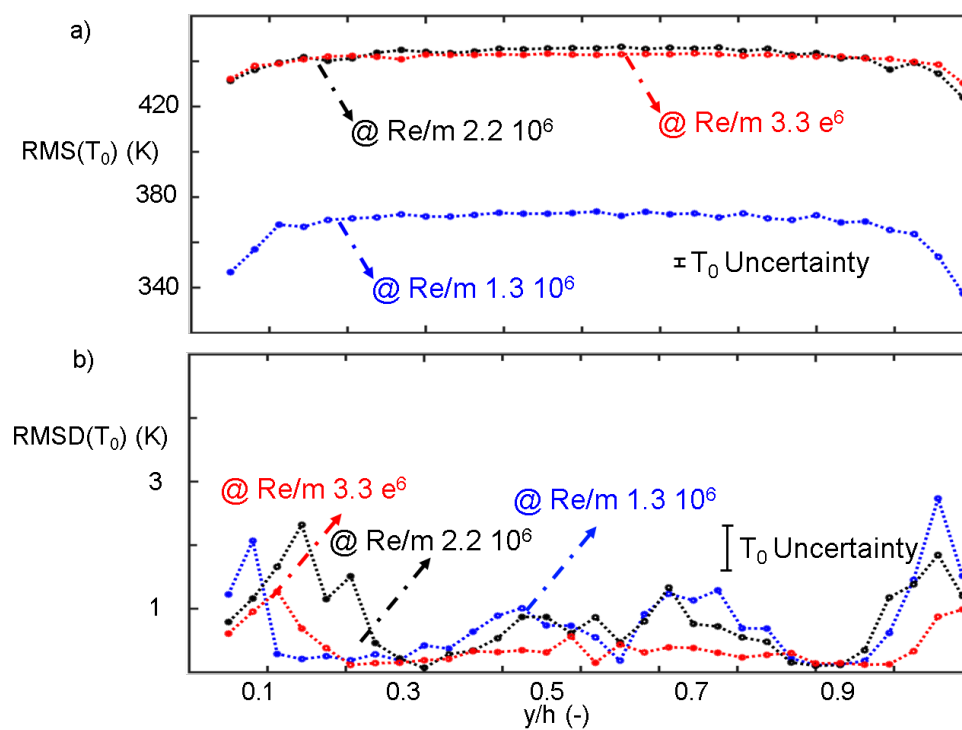


Fig. 4.28. a) Total temperature and b) Total Temperature Root Mean Square Deviation profiles across the test section height

Figure 4.29 and Figure 4.30 represent the total pressure and Root Mean Square Deviation of the total pressure distribution across the test section height operating at two different regimes. Figure 4.29 depicts the total pressure profile at two different span locations, 36 % and 64 % of the test section span respectively. The static pressure in this condition was 101 kPa while the total temperature was 296 K. The mass-flow was set to 2.2 lb/s leading to 0.06 Mach number in the test section and Reynolds 1.5×10^5 . The perfect matching between both span locations depicts the total pressure uniformity across the test section span. In a similar way, the profile evolution through the core of the test section height illustrates the spatial homogeneity of the total pressure thanks to the flow conditioning system. The root mean square deviation of the total pressure for exposure times over a minute remain below sensor uncertainty.

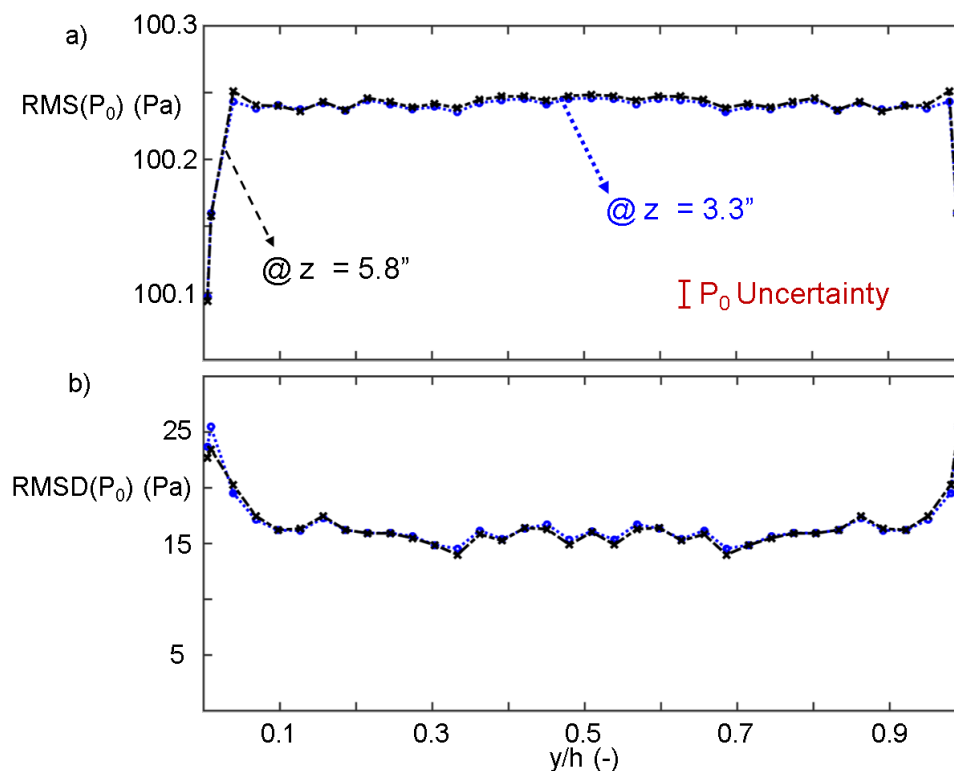


Fig. 4.29. a) Total Pressure and b) Total Pressure Root Mean Square Deviation profiles along the test section height at Reynolds 1.5×10^5

Figure 4.30 represents the total pressure spatial uniformity across the test section center plane when operating at Mach 0.13 with a mass-flow of 5 lb/s and a Reynolds number of 3.4×10^5 . Both span locations reflect again the same behaviour while thinner boundary heights are depicted in the normal total pressure distribution, in agreement with the larger Reynolds number operation.

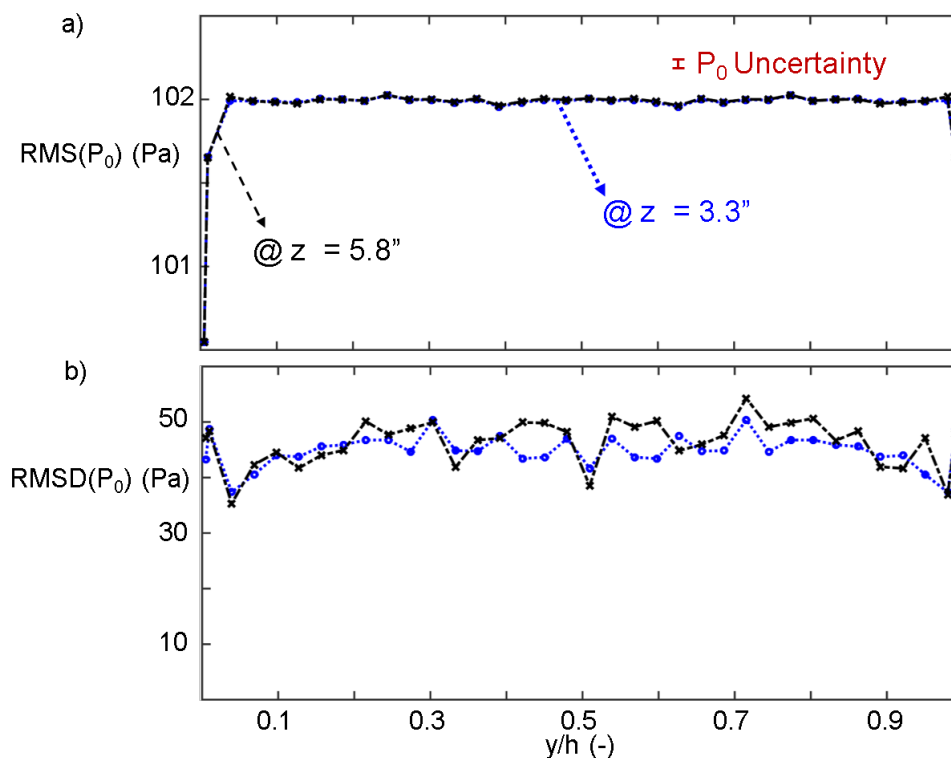


Fig. 4.30. a) Total Pressure and b) Total Pressure Root Mean Square Deviation profiles along the test section height at Reynolds 3.4×10^5

Sudden flow discharge and valve oscillation

Regarding the dynamic performance of the flow conditioning system and its ability to promptly deliver uniform flow conditions, Figure 4.31 represents the stream-wise velocity in the center of the test section during sudden flow discharge experiments and cyclic upstream valve actuation.

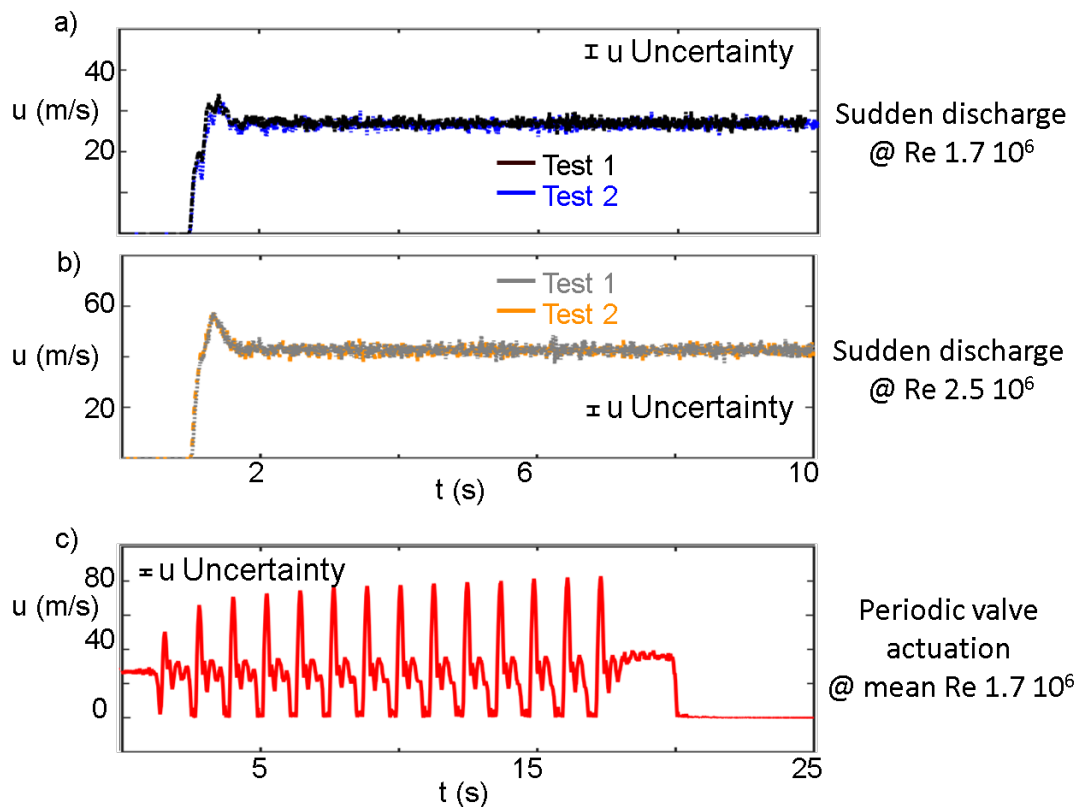


Fig. 4.31. Dynamic response and replicability characterization of the flow conditioning system, Sudden flow discharge and valve cyclic actuation experiments.

Figure 4.31 a) depicts the axial flow velocity during two similar sudden flow discharge experiments performed on consecutive days. These experiments were run at constant inlet total temperature of 300 K and atmospheric flow discharge. At time $t = 1$ s the butterfly valve upstream of the linear settling chamber is actuated and in about 50 ms it reaches the fully open position. To maintain the integrity of the wind tunnel and prevent any over-pressure in the pipeline the purge line is kept open during the aperture of the linear valve. Once the linear wind tunnel valve is open the purge line is closed. When operating at low mass-flows environments and discharging to the vacuum tank through the linear test section the purge line operates at sub-atmospheric conditions and it aspirates flow from the atmosphere. As

a consequence there is a slight increase on the experimental mass-flow during those instances. The hotwire sensor perceives the arrival of the pressure wave about 100 ms after the aperture of the linear butterfly valve. Delay associated with the propagation time of the characteristics through the flow conditioning system till its arrival to the center plane of the test section. There is a peak of maximum flow velocity associated with the mass-flow aspiration while the purge valve remains open and then the flow velocity drops to its nominal value. The entire process to settle the actual operating conditions takes around 400 ms and then the mean stream-wise velocity is maintained stable throughout the rest of the experiment. The signal from both tests at the same Reynolds conditions identifies the replicability of the experiments thanks to the performance of the flow conditioning system.

Figure 4.31 b) represents the flow start-up in the center of the test section for two sudden discharge experiments at a larger Reynolds number. In this case the static pressure was maintained also at atmospheric conditions but the mass-flow level was increased, leading to larger flow velocities. The signal from both experiments illustrates again the replicability of the test conditions. The establishment time of the mean flow conditions happens earlier for this test case driven by the larger flow velocity across the settling chamber and test section, which promotes the propagation of the characteristics.

Figure 4.31 c) depicts the stream-wise velocity temporal evolution during a test where the butterfly upstream of the test section is cycled. When oscillating the aperture and closure of the butterfly valve, the reaction time of the actuator decays and the valve can only cycle at 4 Hz. The initial cycles produce flow velocity oscillations between 0 and 40 m/s, as the pressure is stabilized in the upstream pipeline segments, the flow velocity oscillates between 0 and 80 m/s with a frequency of 1.5 Hz. In this case the flow conditioning system acts as a damper and reduces the frequency of the flow oscillation. Still even when reducing the frequency of the cycle, the dynamic performance of the settling chamber design allows the performance of sudden flow discharge experiments and periodic flow oscillations guaranteeing the spatial unifor-

mity of the flow conditions. The uncertainty calculations associated with each one of the measurements exposed in this section are summarized in Annex D.5.

4.3 Facility Calibration

The calibration of wind tunnels is normally performed when the facility is new or after an important change in their configuration, even though it is recommended to perform a calibration before each experimental campaign [175]. The high cost and the difficulty of designing an efficient strategy of calibration, as well as time constraints in most of the cases, limits the calibration phase which would help reducing uncertainties in the measurements. This section presents the experimental characterization of the aerodynamic behavior that will be used for the uncertainty analysis of future experimental campaigns at the linear wind tunnel of the Purdue Experimental Aerothermal Laboratory [149].

The linear test section is calibrated in order to explore the wind tunnel response in terms of pressure and the mass flow under different conditions, controlling the Reynolds and Mach number in the test section at each operational point. There are two variables to control, the pressure in the test section and the mass flow through the wind tunnel, which are regulated by the variable sonic throat downstream of the test section and the admission valve downstream of the high pressure reservoir respectively. The selection of the number of points and its location inside of the envelope was performed using a combination between an isentropic model of the facility and a Kriging interpolation meta-model [176] coupled with a Genetic Algorithm optimizer [177].

The calibration was performed using pressure taps, pitot probes and Resistance Temperature Detectors (RTD) to monitor pressure velocity and temperature respectively. The experiments were performed limiting the design space to the subsonic range of operation and taking into account the constraints in mass-flow and pressure set by the valves. The number of points used to calibrate and analyze the uncertainty

and sensitivity of the facility was minimized using a Kriging methodology and the results were analyzed using a statistic program suitable for the determination of the effect of the different variables. The calibration of the linear test section is performed operating in blow-down mode discharging directly to the atmosphere and with a constant inlet total temperature of 286 K. Additionally, for practical safety reasons the maximum operative mass-flow used during this wind tunnel characterization is 15kg/s and the maximum pressure targeted in the test section was 5 bar.

An isentropic model was built to predict the performance of the wind tunnel. The inputs for the model were the area of the sonic throat, the upstream massflow and the atmospheric pressure. If the throat will be choked for the conditions evaluated, from the massflow and the area the static flow quantities are derived at the throat. Then knowing the unity Mach number the total flow quantities are derived. Finally, considering isentropic evolution throughout the nozzle the flow quantities upstream of the sonic valve are retrieved.

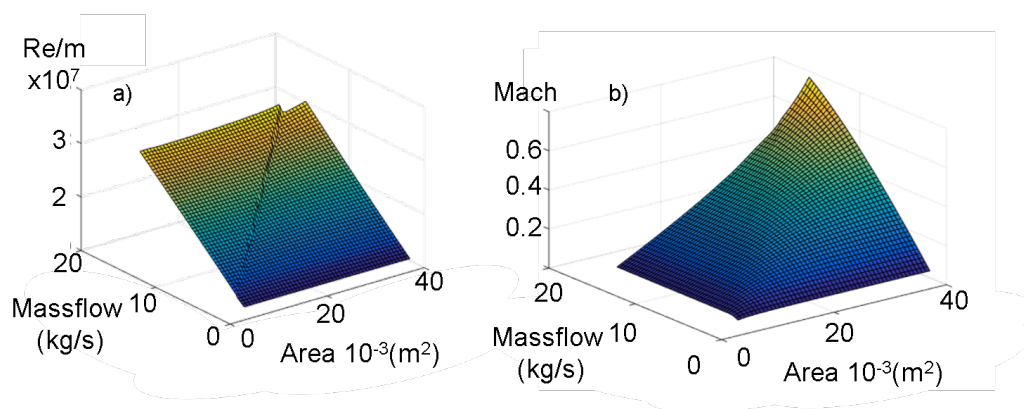


Fig. 4.32. a) Reynolds/m b) Mach number maps achieved in the linear test section

On the other hand, if the throat is unchoked for the mass-flow and sonic valve area settings, using continuity and the isentropic relations the test section conditions were derived. Afterwards considering the static flow quantities in the test section, the Reynolds/m and the Mach number in the working section were derived. Figure 4.32 represents the envelope of Reynolds/m and Mach number for the range of

mass-flows and upstream pressures considered. The discontinuity that appears in the Reynolds/m envelope represents the condition at which the isolation throat passes from choked or sonic conditions to unchoked status.

4.3.1 Calibration methodology

The calibration is performed by checking different non-dimensional quantities: Reynolds and Mach number. The purpose of the calibration is to characterize the response of the facility to the control parameters and be able to reach accurately each one of the points inside the envelope by setting the correct mass-flow and sonic throat of the wind tunnel.

The calibration has three successive steps. First, the selection of the number of points to test, providing a reasonable uncertainty in the prediction of the complete envelope. Then, a total number of experimental points is chosen based on the shape of the Mach and Reynolds maps considering a second order model. Once the number of points is decided, a Kriging interpolation method is developed and coupled with a Genetic Algorithm optimizer in order to choose the location of the testing points inside of the envelope, minimizing the Root Mean Squared Error (RMSE) of every point inside the envelope. The cloud of the testing points obtained with this optimization is assessed and compared with a structured array of the same number of points. Finally, the points are tested in the experimental facility and compared to the analytic results.

The selection of the calibration points is carried out taking into account the model used to predict the behavior of the wind tunnel [178, 179]. The number of points needed to build a d th-order model is directly related with the number of independent variables, the tolerance for interference errors and the uncertainty of the estimated values [175]. The minimum number of points for a specified tolerance is defined by N_p .

$$N_p = \frac{(d + kn)!}{d!kn!} (t_\alpha + t_\beta)^2 \frac{\sigma^2}{\gamma^2} \quad (4.6)$$

In this equation, d represents the order of the model, kn is the number of independent variables, t_α and t_β are the t-statistics related with the Type I and Type II errors, σ is the estimated standard deviation of the measurements and γ is the precision requirement. Therefore, in order to facilitate the feasibility of the experimental calibration a balance between the desired precision and the limited number of points must be achieved.

Assuming a 2nd order model, with $kn=2$ variables, the mass-flow through the test section and the sonic valve area the previous formulation can be evaluated. The t-statistics type I and type II (t_α and t_β) are extracted from Tables of the t-student distribution with a probability of error of 0.02 and 0.05, respectively. The standard deviation of the data taking into account the accuracy of the measurements is estimated around 9×10^4 for the Reynolds number per meter and 0.011 for the Mach number. Doubling the precision requirement of the measurements accuracy, the number of experiments is about 40 for both non-dimensional numbers. Since both, Reynolds and Mach envelopes are irregular due to the status of the sonic valve, a meta-model based using a Kriging interpolation was implemented to compute the different quantities [180].

The Kriging fitting tool is a model with an infinite number of degrees, which implies that the obtained precision in the different quantities is highly dependent on the location of the points inside of the surface. As a consequence, the input provided by the equation for nk can only be considered an approximation. The purpose of the Genetic Algorithm coupled with the Kriging interpolation is to minimize the error (RMSE) of the surfaces with respect to the meta-model created with the determined number of points. After choosing the amount of points, their location inside of the design space is optimized using a Kriging methodology developed in Matlab. In this case, the objective is to find the optimum location of the points to generate an accurate Kriging model that matches the isentropic model that minimizes the error of interpolation. Then those points will be tested in the linear wind tunnel and with them obtain a Kriging model of the actual performance of the test section. By using

the points that derived the most accurate representation of the isentropic model a more accurate actual performance is expected.

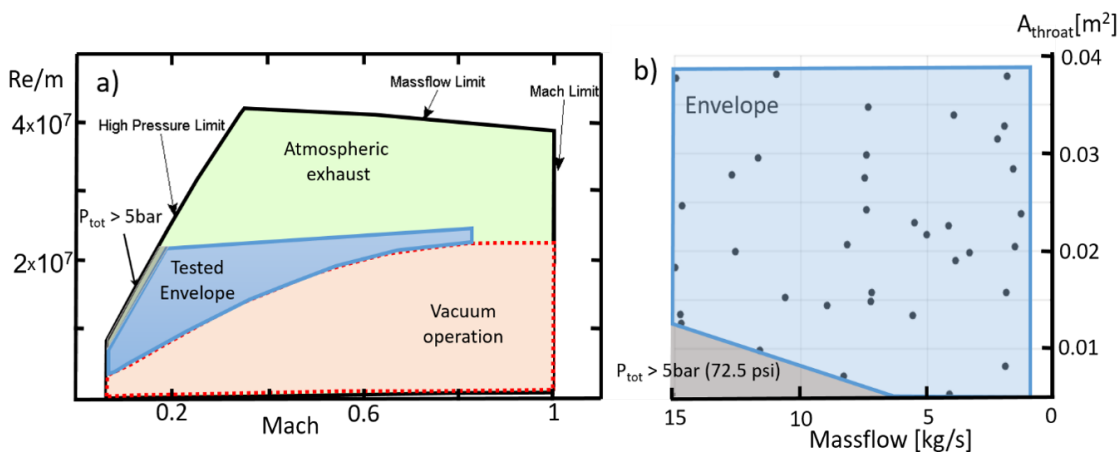


Fig. 4.33. a) Complete envelope of Re/m and Mach numbers of the linear test section compared with the envelope tested in the experiments. b) Tested envelope in function of the two control variables: the area of the throat and the mass-flow through the test section.

The envelope of operation shown in Figure 4.3a) was reduced to perform the experiments in safe conditions. The studied envelope is represented in Figure 4.33 b), where the maximum mass-flow was limited to 15kg/s and the flow was directly discharged to the atmosphere, the blue region represents the limits of this analysis. Figure 4.33 a) shows the envelope represented in function of the Mach and Re/m numbers and Figure 4.33 b) shows the tested envelope in function of the two control variables (b)). The location of the 36 experimental points, which location was optimized, is also represented in the same plot.

Even though the results of the optimization look randomly distributed there are some patterns on its collocation along the envelope. There is a cluster of points at very low mass-flow at different areas of the throat forming a vertical line in the plot. Additionally, in order to minimize the error around the test section maximum pressure threshold, there are 4 points around that limit.

The selection of the number of points was based in the equation 4.6 to give a statistical sense assuming a second order function. Similarly to a grid sensitivity evaluation, the RMSE between all the points of the real model and the Kriging meta-model for Mach number and Reynolds number was assessed for 20, 36 and 50 points of measurement. Figure 4.34 c) depicts the evolution of the error for both quantities, and shows the targeted errors tolerance, 0.015 for the Mach and 5×10^5 for the Reynolds number. There is a trade-off between the number of points that can be tested and the admitted error, therefore 36 experiments were selected for which the Mach number is well below the error limit and for the Reynolds it is close enough. Figure 4.34 a) and b) represents the comparison between the surface generated by the isentropic model of the facility (in color) and the surface generated by the Kriging interpolation method (in white mesh) for the Reynolds number per unit length and the Mach number respectively. The agreement between model and meta-model is accurate for the selection of the points of the optimization, introducing a larger difference outside of the testing envelope where the pressure is higher than 5 bar.

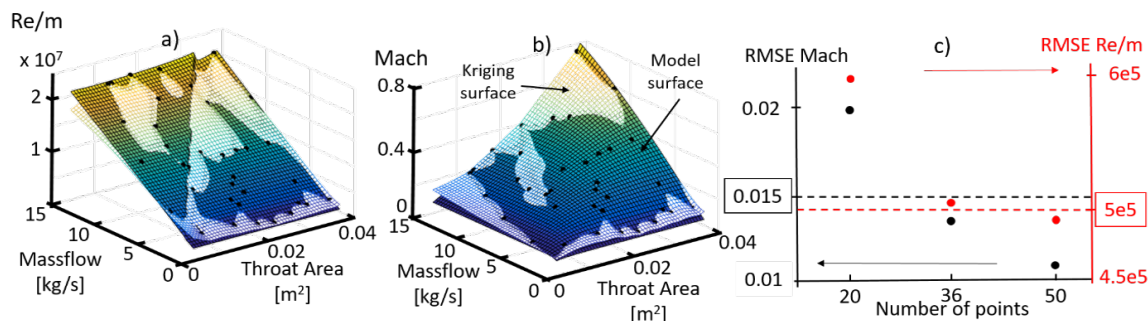


Fig. 4.34. a) Comparison between the Re/m map and the Kriging meta-model in function of the massflow and the throat area with the representation of the points resulted from the optimization methodology. b) Comparison between the Mach number map and the Kriging meta-model in function of the massflow and the throat area with the representation of the points resulted from the optimization methodology. c) Root mean squared error of the Mach number and Re/m number using 20, 36 and 50 points in the Kriging interpolation optimization methodology. pressure amplitude effect on the separated flow region and thermal isolation

Once the optimization is performed and the results numerical results have been verified, the next step consists in the experimental characterization of the facility using the optimized points.

4.3.2 Experimental characterization of the performance envelope

A simplified schematic of the wind tunnel layout and the hardware for the calibration is presented in Figure 4.2 and 4.4 b). The flow admission was regulated by two different valves. The first one is a safety ball valve which isolates the facility from the high pressure reservoir. The second one is as Flowserve Starpac valve that allows the mass-flow control through a DC signal. For the wind tunnel calibration campaign all the windows were metallic and the upper one was machined to place instrumentation inserts.

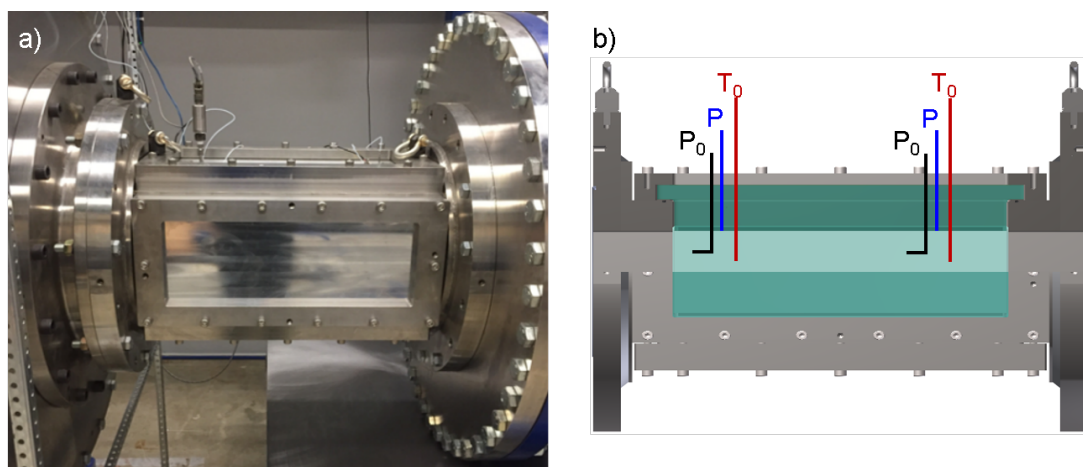


Fig. 4.35. a) PETAL Linear Test Section; b) Instrumentation location for facility envelope characterization

Total temperature, total and static pressure were acquired at two different axial locations in the wind tunnel. Both total pressure and temperature were measured at different test section heights for each one of the axial locations. The total pressure was monitored through interchangeable Pitot probes connected to a Scanivalve DSA3217 pressure scanner with an acquisition rate of 500 Hz. Similarly, pressure tapings were

installed in the same axial locations to monitor the static pressure evolution with the same pressure scanner.

Through the Pitot probes and the wall pressure readings the Mach number at each one of the locations was obtained and their result was averaged to obtain the mean test section performance. The total temperature in the test section was acquired with two 1/8 in k-type thermocouples sampled at 10 Hz. Combining the Mach number and the total temperature, the static temperature together with the Reynolds number were derived.

4.3.3 Experimental envelope comparison to isentropic performance model

Figure 4.36 represents the performance envelope for both Mach and Reynolds numbers obtained with the isentropic model compared against the experimental values. The experimental points are represented together with their associated uncertainty. Figure 4.36 a) and b) display the envelope of Mach number from two different perspectives for a better representation of the results over the entire facility envelope. For low mass-flows the deviation of the experimental points from the isentropic evaluation results negligible. However, at larger mass-flows the experimental points slightly deviate from the modelled envelope, where more non isentropic flow behaviors are present along the test section.

Regarding the Reynolds number, Figure 4.36 c) and d) depict the Reynolds/m from two different perspectives for a clearer comparison of the results over all the regimes. As described for the Mach number, the experimental points fall within the uncertainty inside of the isentropic envelope and the numerical model. However, for larger mass flows associated with larger Mach numbers, the experimental points deviate from numerical predictions.

As an example of the experimental conditions, Figure 4.37 a) represents the mass-flow during the test. The mass-flow is acquired at the upstream flow control valve. At approximately $t = 50$ s the mass-flow stabilizes at its nominal value, 3.8 kg/s.

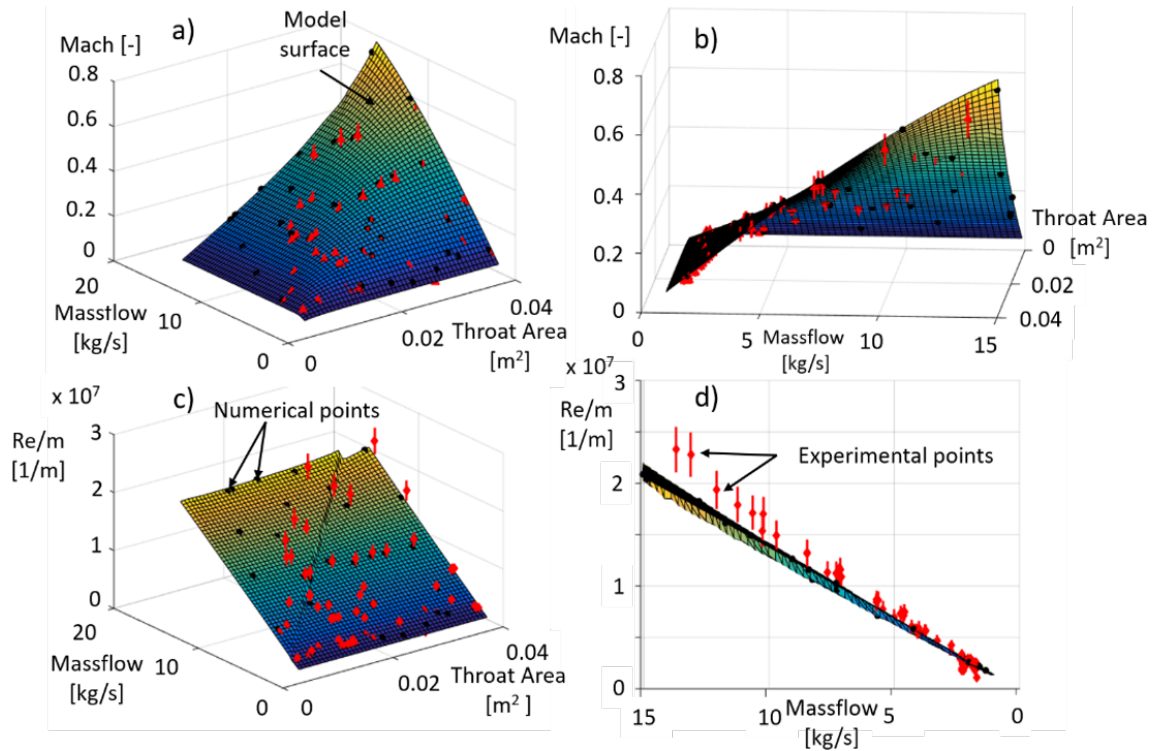


Fig. 4.36. a) Comparison of the isentropic model with the experimental data; a)Mach number map (front view). b) Mach number map (rear view). c) Re/m number map (front view). d) Re/m number at several mass-flow levels.

The upstream valve automatically adjusts the aperture of the valve to maintain a constant mass-flow level while the upstream pressure tanks deplete. The total and static pressure recorded at the test section during this run are represented in Figure 4.37 b). Similarly, Figure 4.37 c) represents the Mach and Reynolds/m evolution during the experiment.

4.3.4 Uncertainty Analysis

In order to quantify the uncertainty of both Mach and Reynolds number results several factors must be taken into account. The main sources of uncertainty in the calibration experimental methodology are the total and static pressure together with the total temperature measurement. Table 4.5 presents the absolute uncertainty of

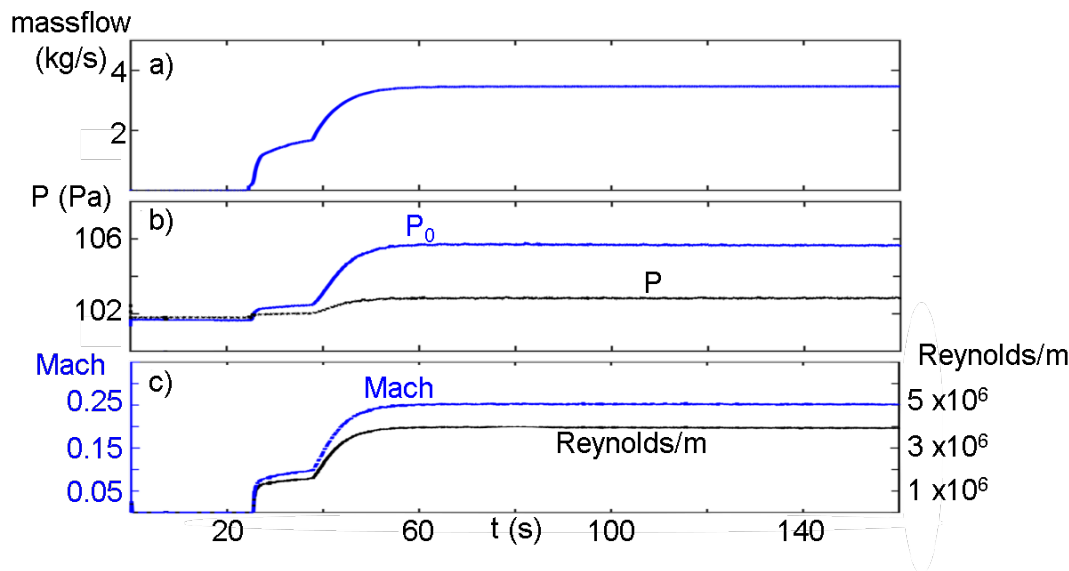


Fig. 4.37. Mass-flow, Total and static pressure, Mach and Reynolds/m number evolution during a performance characterization experiment

the prime variables considered in this analysis. Where all the error evaluations are given at 95% confidence level.

Table 4.5.
Facility performance envelope calibration sensors absolute uncertainty

	Absolute Uncertainty	Units
massflow	0.1	kg/s
P_0	100	Pa
P	100	Pa
T_0	3	K
$Area$	0.0009775	m^2

The Mach number is computed based on the total to static pressure difference taking advantage of the isentropic flow relations. However, its value is also affected by the total temperature by means of the heat capacity ratio. Table 4.5 presents the

uncertainty analysis for the Mach number, where both total and static pressure play a relevant role as highlighted by the sensitivity of the Mach number to its uncertainty. Based on our analysis the uncertainty in the obtained Mach number is 3.55 %.

Table 4.6.
Mach number uncertainty during facility calibration experiments

	Mean		Abs.	Uncertainty	M (with	ΔM	
	Value	Units	uncer.	% Mean	uncertainty)	%	Sensitivity
P_0	105000	Pa	100	0.0952	0.17	2.45	2574
P	103000	Pa	100	0.0971	0.1617	2.56	2640
T_0	265	K	3	1.1321	0.1659	0.002	0.1426
Mean					Mach		
Mach	0.165				Uncertainty	3.55	

Similarly, Table 4.7 presents the uncertainty analysis for the Reynolds number. Where again the pressure levels play a major role. Although in this case the sensitivity of the Reynolds number to the temperature is 3 orders of magnitude larger than for the Mach number. For this particular case and with the prime variables absolute uncertainties the uncertainty on the Reynolds number is 3.79 %.

The facility calibration provided a good understanding on the behavior of the facility under different mass-flow set points and sonic valve position. The objective of the calibrations was to quantify the relevant non-dimensional numbers of the experiment as a function of the control parameters. The model built during this calibration will be useful to select the experimental conditions of the latter experimental campaigns. A reliable isentropic behavior model has been built, describing the behavior of the complete facility at any possible condition with the objective of reducing the calibration procedures.

Table 4.7.
Reynolds uncertainty during facility calibration experiments

	Mean		Abs.	Uncertainty	Re (with	ΔM	
	Value	Units	uncer.	% Mean	uncertainty)	%	Sensitivity
P_0	105000	Pa	100	0.0952	$4.5e^6$	2.46	2590
P	103000	Pa	100	0.0971	$4.e^6$	2.48	2556
T_0	265	K	3	1.1321	$4.3e^6$	1.65	249
Mean					Re		
Re	$4.3e^6$				Uncertainty	3.79	

4.4 Test article design and instrumentation

4.4.1 Test article design

In order to verify the numerical findings and expand the effort on the analysis of the dynamic scales present on the flow separation and reattachment, the ad-hoc designed wall mounted hump will be tested in the linear wind tunnel. The first step in this process is the design of the actual test article. The numerical simulations assumed 2D flow behavior, hence the same physics are targeted in the experimental approach. As a first attempt a straight extrusion of the domain is conceived. Where the hump takes place across the entire width of the test section, as the numerical domain in Figure 4.38 a) represents. In order to test the feasibility of the designed test section, 3D URANS simulations were performed taking advantage of the transitional $k\omega$ SST turbulence closure.

Figure 4.39 a) and b) represent the bubble length and separation inception of the 3D extruded domain compared to the 2D URANS. The results of the extruded domain reflect an unsteady behavior of the flow separation, where the inception oscillates between 20 and 360 mm. Also the actual bubble length in the center of the domain is much smaller than the one identified in the 2D case. In this sense, Figure 4.39

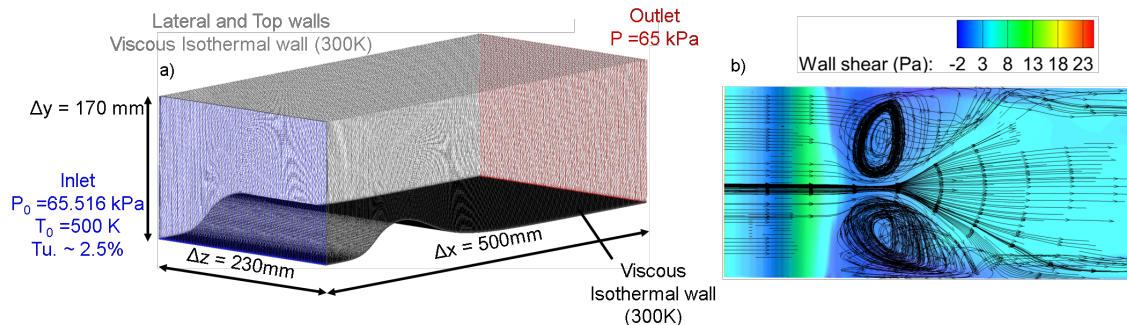


Fig. 4.38. Extruded 3D Domain for Experimental analysis; a) Numerical domain replication for performance assessment analysis b) Wall shear stress contour for operation at $Re/m \ 2 \times 10^6$

c) compares the axial velocity contours of the 2D against the center plane in the 3D extruded domain. A negligible bubble is found in the 3D case, which contrasts with the 150mm bubble length predicted in the 2D simulation. The main reason for this behavior is the effect of the lateral wall boundary layers near the corners of the domain. Figure 4.38 b) depicts the wall shear stress distribution along the hump together with some stream-traces illustrating the behavior of the flow at a given time step. Along the test article corners, where the boundary layer over the hump surface and the lateral wall meet, there is massive flow separation that modifies the effective cross sectional area. The presence of the massive lateral flow separation actually imposes an acceleration along the hump in the center line. Which mitigates the adverse pressure gradient and prevents the use of such geometry for the experimental campaign.

To alleviate this issue several approaches have been considered in the past. One approach could be the isolation of the test article center by installing isolation fins, [181, 182], or include slots on the side of the test article to disengage the test article from the later walls of the wind tunnel. The latter approach was selected, smoothly reducing the hump towards the side walls of the domain. Following this procedure, the hump is imposed across approximately 3/5 of the domain. Figure 4.40 a) represents

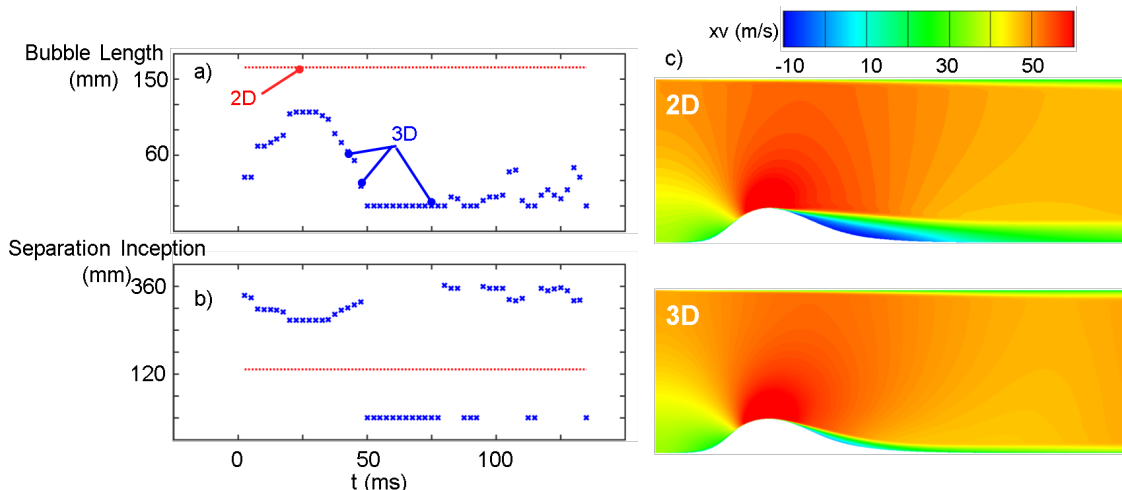


Fig. 4.39. Comparison of 3D extruded domain against 2D numerical analysis

the numerical domain for the analysis of this design with identical numerical settings to the extruded case.

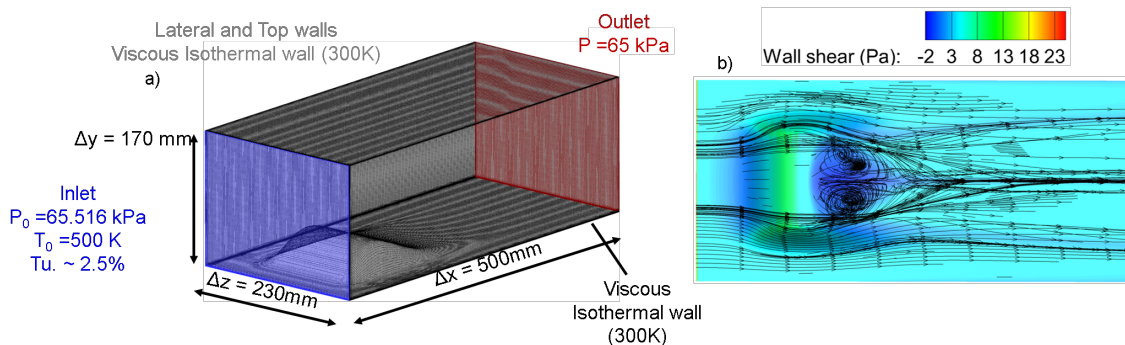


Fig. 4.40. Contoured 3D Domain for Experimental analysis; a) Numerical domain , b) Wall shear stress contour for operation $Re/m \ 2 \times 10^6$

Figure 4.41 a) and b) depict the bubble length and separation inception of the 3D contoured domain compared to the 2D URANS. After convergence is achieved, $t > 25 \text{ ms}$, the separation inception in the center of the domain takes place in the same location than for the 2D case. In terms of bubble length still the contoured domain reflects smaller recirculated flow regions. Figure 4.41 c) displays two different

stream-wise velocity contours of the 2D and 3D contoured domain in the center plane. The shape of the separated flow regions in both cases is different. Although the separation phenomena that occurs in this geometry follows a 2D behaviour, the flow reattachment is inevitably affected by 3D flow features. Such as the entrainment of the air flowing on the sides of the hump towards the test article center. The recirculated flow region aspirates flow from the test article sides. Which generates the lift off of the separated flow and enhances the flow attachment.

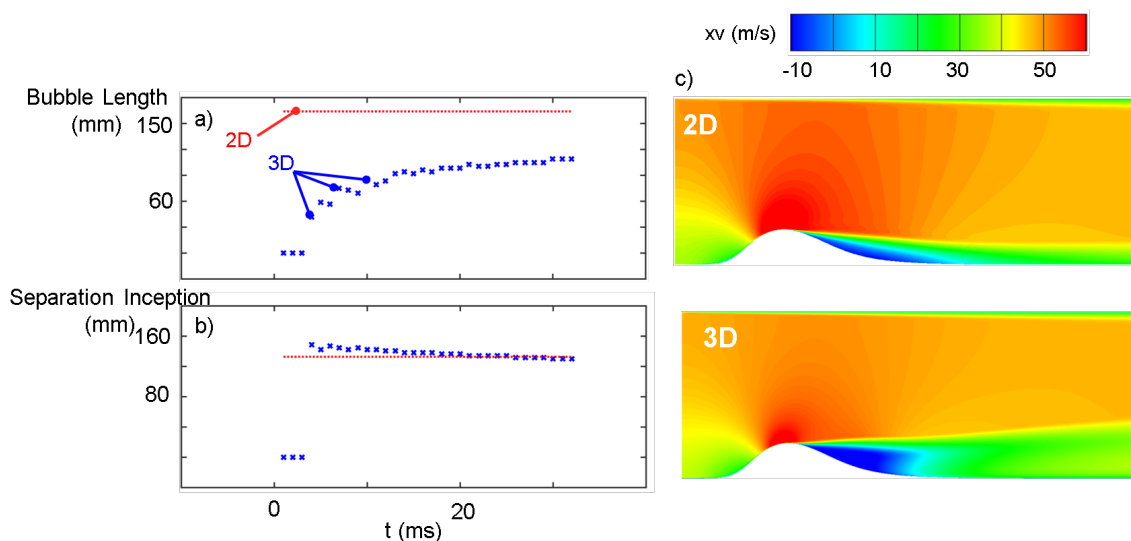


Fig. 4.41. Comparison of 3D contoured domain against 2D URANS analysis

Figure 4.40 b) represents the wall shear stress distribution along the hump together with some stream-traces depicting the behavior of the flow at a given time step. In this case, the massive sidewalls flow separation is prevented, but there is flow circulation from the near lateral wall region to the center of the domain that again modulates the geometrically imposed pressure gradient. The best approach to prevent massive impact of the sidewall flow entrainment in the core is to increase the hump extension across the span, however a trade-off must be found to prevent the side wall boundary layer detachment. The final 3D geometry has the hump extruded through 4/5 of the test section span with a rapid decay towards the borders. Figure 4.42 represents the

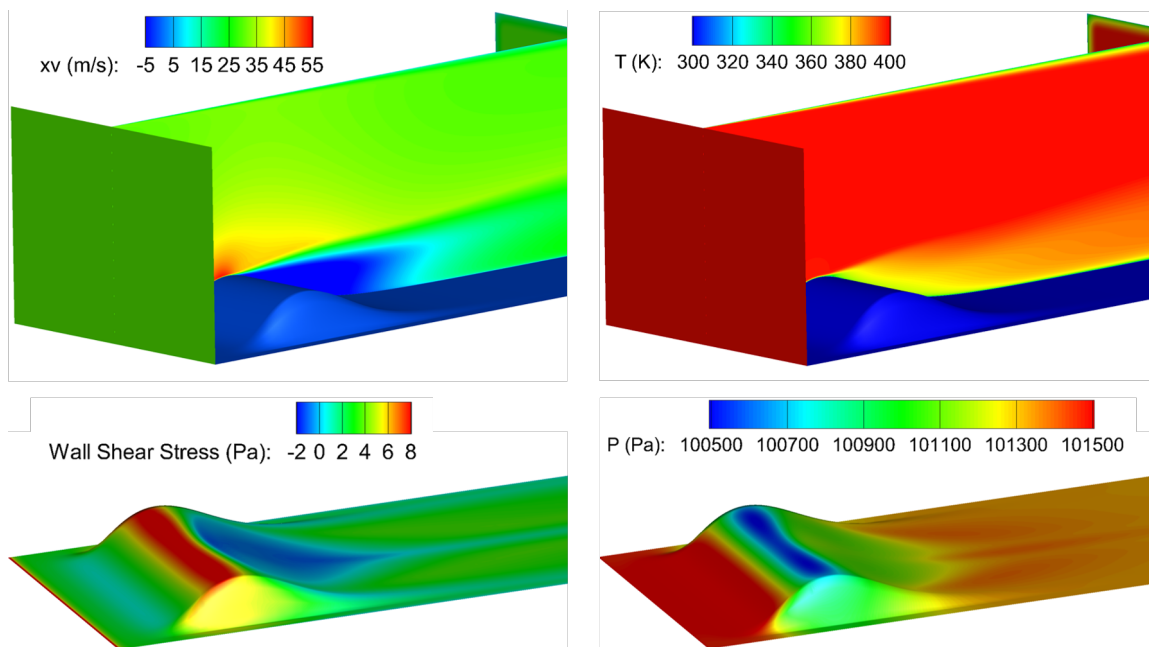


Fig. 4.42. 3D Flow Separation Domain Performance assuming boundary layer development from the test section inlet

axial free stream velocity and static temperature contours in the inlet and center-plane of the domain. The wall shear stress and static pressure distribution along the hump surface are also presented. However, this simulation does not consider the incoming boundary layer development along the contraction area of the settling chamber, as represented in Figure 4.43. Starting at the lip of the cantilever contraction, a new boundary layer will be developed along the walls of the contraction and once the flow is delivered to the test section there will be a developed boundary layer.

In order to assess the impact of such incoming boundary layer in the performance of the test article and determine if the size of the slot will be sufficient a new 3D URANS simulation was performed. In this case, a 4 mm height momentum boundary layer was imposed in the inlet of the test section. In a similar way, based on the Prandtl number and the Crocco relation, a thicker thermal boundary layer was prescribed. The core flow conditions, total pressure and total temperature are identical to the previous test cases. Figure 4.44 represents the axial velocity and static

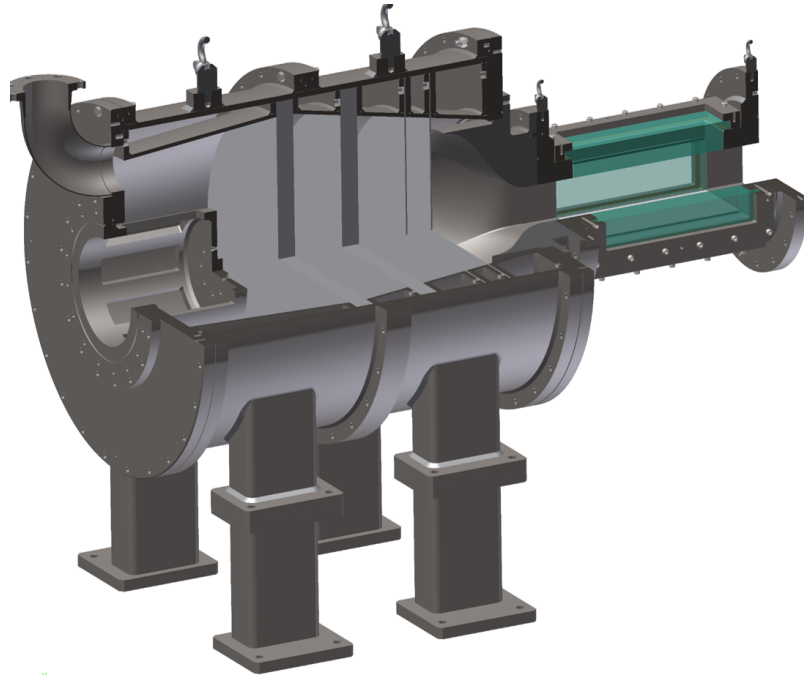


Fig. 4.43. Test section geometry integration in the flow conditioning system

temperature contours at the inlet and center-plane of the domain. The contours at the inlet of the domain reflect the height of the incoming momentum and thermal boundary layers. The impact of the developed boundary layer on the boundary layer detachment and reattachment phenomena seems minimal. The boundary layer developed along the contraction on the lateral walls is stretched as the flow approaches the hump due to the flow acceleration. In this sense, the lateral slots of the flow separation domain result sufficient to accommodate the thicker boundary layer profiles. There are not appreciable differences on the flow detachment and reattachment phenomena, where the only remarkable factor is the shortly earlier detachment of the flow due to the thicker boundary layer.

Figure 4.45 depicts a contoured 3D wall mounted hump integrated in the PETAL linear wind tunnel. The bottom window is replaced by the test article and still visual access is granted through the lateral walls and the upper window. The lateral plates will be replaced by fused quartz windows to carry out optical measurements. While

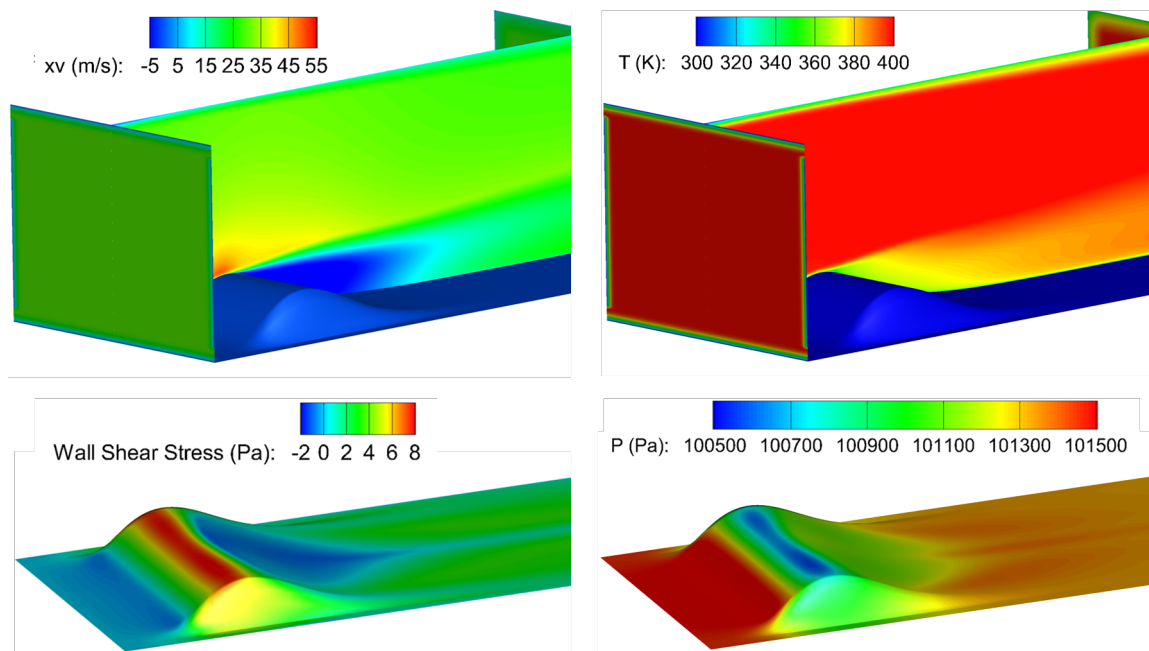


Fig. 4.44. 3D Flow Separation Domain performance with prescribed inlet momentum and thermal boundary layer profiles

the top plate will be changed by multiple inserts to introduce probes and rakes in the test section.

Figure 4.46 a) depicts the Flow Separation Domain upon its delivery. The test article was machined out a slab of aluminum 600 mm long, 200 mm height and 250 mm wide. To minimize the light and laser reflection from the test article the surface was coated with Cerakote red ceramic paint. Figure 4.46 b) shows the coated test article integrated in the test section. For simple flow visualization cotton tufts were installed over the hump rise, fall and side slots.

4.4.2 Test article assembly and instrumentation

Figure 4.47 depicts the test article installed in the PETAL Linear Wind tunnel and the distribution of the total pressure and temperature probes. Similarly the location of the pressure taps and wall temperature thermocouples is illustrated. A total pressure rake with 5 heads and two total pressure Kiel probes were used to monitor free

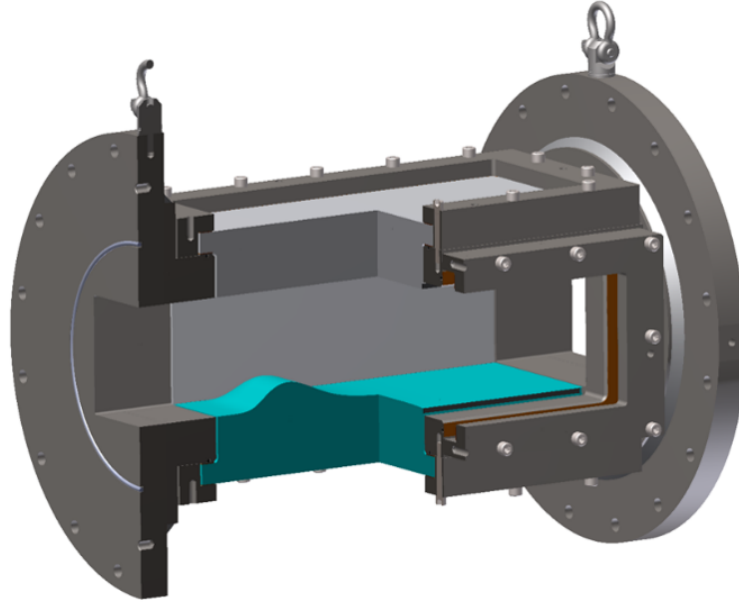


Fig. 4.45. Flow Separation Domain Test Article integration in the PETAL Linear Wind Tunnel

stream evolution during the experimental campaign. The total pressure readings were monitored with a Scanivalve MPS pressure scanner at a sampling frequency of 850 Hz. 1/16th pressure tubing connections of 0.15 m length were used to guide the pressure signal till the pressure scanner. Several exposed k-type thermocouples were distributed along the test section center-line to identify the distribution of the total temperature along the working section.

Similarly, 15 wall mounted thermocouples were distributed along the flow separation domain. While 5 thermocouples were mounted on the back of the test article to monitor its temperature evolution and provide the back reference temperature for heat flux derivation. The sensing element is glued with kapton tape to the surface. The entire unsteady surface-temperature data acquisition was done at a sampling frequency of 1 kHz. The calibration procedure for the thermocouples is presented in Appendix D.3.

A total of 78 pressure taps were perforated along the test article to monitor the evolution of the wall pressure during the experiments. The surface taps were dis-



Fig. 4.46. Flow Separation Domain test article

tributed in 4 different regions. A cluster of 4 points identified by the indicator I-# was installed near the centerline of the domain on the leading edge of the test article. 6 taps were installed near the left boundary identified with the indicator L-# while 7 taps were perforated near the right boundary of the hump, R-#. Finally, 61 surface taps were distributed in three different groups near the center of the domain. 28 pressure taps were dispersed from the hump summit till the trailing edge of the domain at half span of the test article. The rest of the surface taps were collocated 5% of the span away from the center and covering the gaps of the ones distributed along the center. Additionally, 10 wall pressure readings were installed on the upper side of the domain scattered among the instrumentation inserts to monitor the evolution of the static pressure on the opposite surface. The wall pressure was monitored with a scanivalve MPS unit with a 15 psi range. The surface taps were connected to the

pressure scanner through 1/16" nylon tubing of 0.1 length. The pressure taps were scanned with a sampling frequency of 850 Hz. However, for the transient performance experiments only the center line pressure taps were monitored and they were sampled at a frequency of 2.5 kHz.

In addition to the pressure and temperature measurements, the stream-wise velocity component was also monitored with a mono-dimensional hotwire, wire diameter of $6.3 \mu\text{m}$.

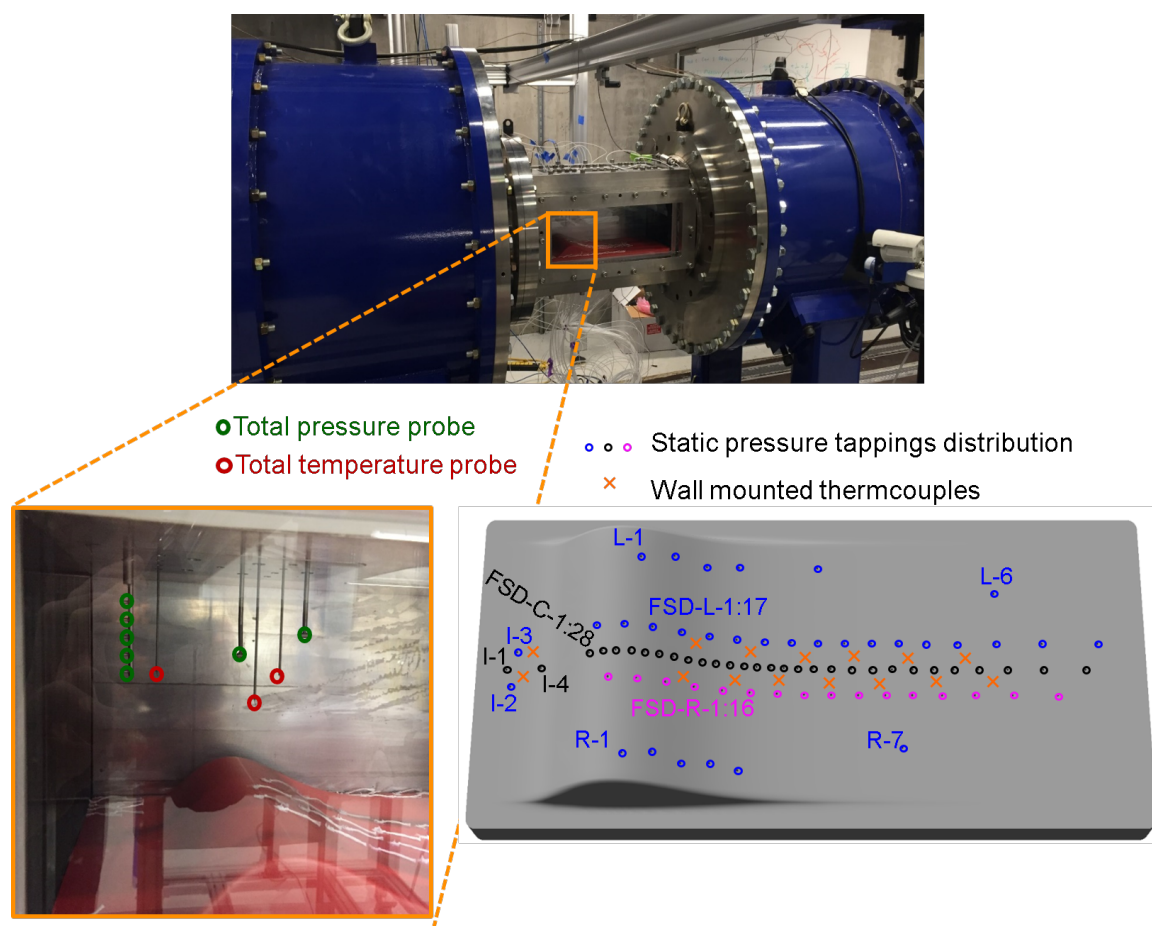


Fig. 4.47. Test article instrumentation distribution for separated flow dynamic response experimental campaign

The experimental assessment of the flow separation performance under mean flow unsteadiness is divided in two phases. During the first part of the campaign only

steady conditions were measured aiming the characterization of the domain at different flow conditions.

The second phase of the experimental campaign was focused on the effect of mean flow transients on the performance of separated flow regions. The mean flow variations were imposed by the fast acting valve located upstream of the settling chamber. The actuator of the valve have been boosted to guarantee a fast opening and closing of about 50 ms each. Allowing the generation of sudden flow discharge into the settling chamber.

4.5 Steady State Performance of Flow Separation Domain

Figure 4.48 a) represents the static pressure distribution along the Flow Separation Domain for multiple Reynolds/m, ranging from 1.1×10^6 up to 5.2×10^6 . Table 4.8 presents a summary of the mean flow properties of each Re/m operational point: critical flow Venturi total pressure, dynamic pressure at the test section inlet, total temperature, Mach number, axial flow velocity and mass-flow through the test section. The flow downstream of the test section was directly discharged to atmospheric conditions, hence the static pressure was atmospheric for all the cases, $\sim 101325 Pa$.

Figure 4.48 b) depicts the reattachment location over the range of explored Reynolds numbers. The reattachment location was identified by the end of the plateau on the wall pressure distribution. The uncertainty associated to its measurement is the maximum distance to the nearest surface tap either in the upstream or downstream direction. There is a quasi-linear trend on the reduction of the reattachment location as the Reynolds number increases.

Figure 4.49 a) and b) represent the mass-flow and axial free stream velocity temporal evolution during 4 different experiments replicating the same operating conditions. Figure 4.49 c) represents the performance of the test article during each one of those experiments displaying a perfect agreement on the static pressure distribution and

Table 4.8.
Reported Experimental points

Test	P_0 Venturi (kPa)	Inlet Dyn. P (Pa)	T_0 Test S. (K)	Mach	xv (m/s)	massflow (kg/s)	Re/m
CO-3	313.2	140.8	290	0.045	14.67	0.75	1.1×10^6
CO-4	417.6	250	290	0.059	19.54	1.00	1.5×10^6
CO-5	521.9	390	290	0.074	24.39	1.25	1.9×10^6
CO-6	626.3	560	290	0.089	29.22	1.50	2.2×10^6
CO-7	730.7	765	290	0.104	34.12	1.75	2.6×10^6
CO-8	835.1	1000	290	0.119	38.99	2.00	3.0×10^6
CO-10	1043.8	1570	290	0.148	48.76	2.50	3.7×10^6
CO-12	1252.6	2260	290	0.178	58.38	3.00	4.5×10^6
CO-14	1461.4	3070	290	0.207	67.87	3.50	5.2×10^6
CO-20	1875.2	6000	290	0.289	94.04	4.90	7.4×10^6
HO-4	596.6	465	365	0.081	36.24	1.00	9.4×10^5
HO-7	1045.8	1420	365	0.141	63.14	1.75	1.7×10^6

confirming the test to test replicability promoted by the flow conditioning system of the facility.

Figure 4.50 a) represents the pressure coefficient (c_p) distribution along the test article for an attached flow condition, CO-20. 3D URANS numerical results are compared against the experimental results. Where the reference pressure, P_{ref} , is the outlet static pressure. In case of attached flow conditions there is an excellent agreement between the numerical and experimental results. Figure 4.50 b) depicts the pressure coefficient variation along the hump. The shape of the domain imposes an expansion with a gradient of up to 65% at the pinnacle of the domain while the maximum diffusion during the hump fall is near 40% .

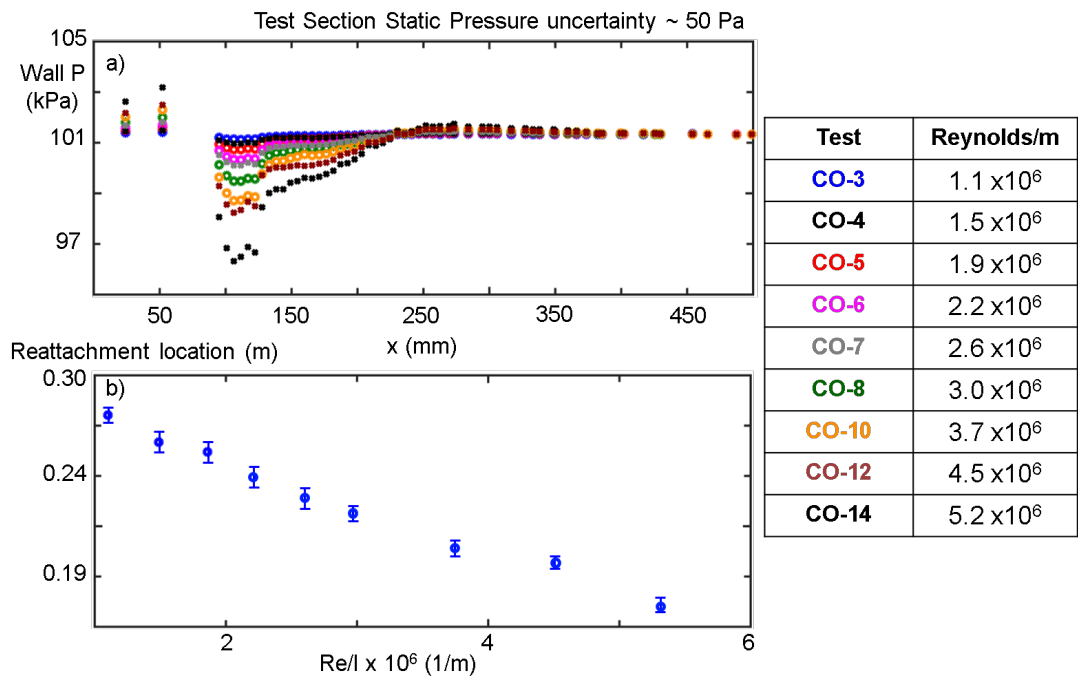


Fig. 4.48. Flow Separation Domain wall pressure distribution and reattachment location at several Reynolds numbers

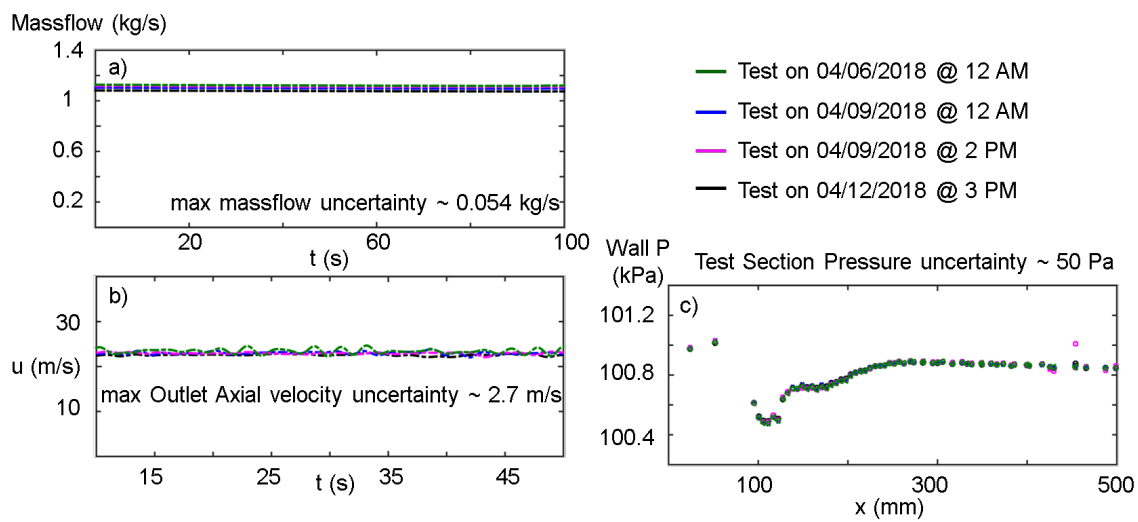


Fig. 4.49. Test conditions repeatability

Figure 4.51 a) represents the static pressure contour over the flow separation domain test article under CO-7 operation. As the flow accelerates through the hump

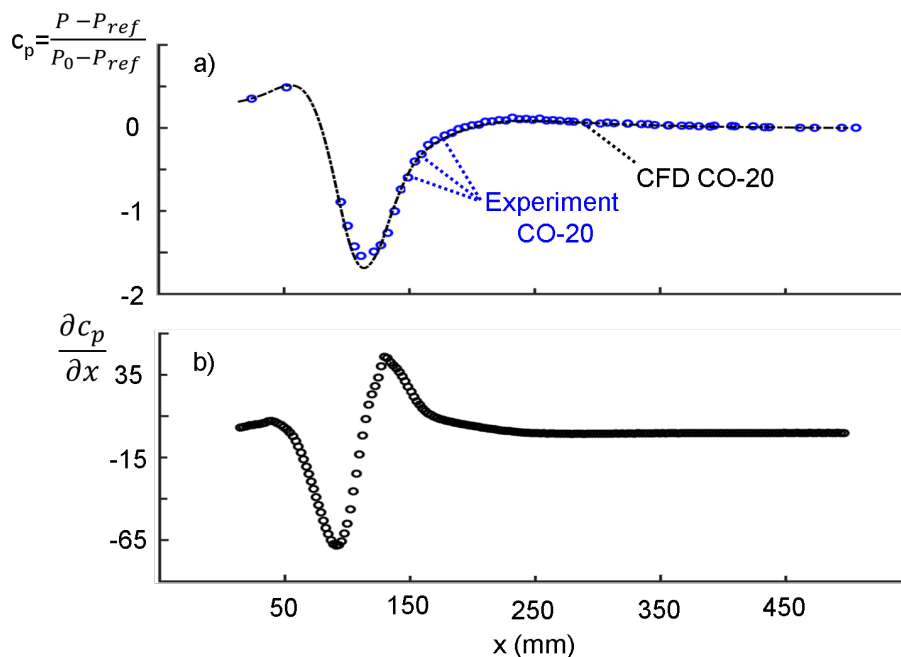


Fig. 4.50. Test article performance at high Reynolds Environments, CO-20

rise, the static pressure decays reaching minimum over the hump summit. The recirculated flow region extends across 50 % of the span of the test section displaying a constant level of static pressure and then its size is gradually strained to the center as the flow from the sides is entrained by the pressure gradient. The flow reattachment process is driven by 3D flow features including the absorption of the flow near the lateral walls and the lift-up of the recirculated flow. However the flow separation process follows the expected 2D flow separation behavior. Figure 4.51 b) represents the static pressure distribution along the wall mounted hump at three different span locations, 45 %, 50% and 55%. The agreement among the three distributions depicts the uniformity of the test article performance across the center of the domain.

Figure 4.52 represents the static pressure distribution along the wall mounted hump operating at $Re/m 1.5 \times 10^6$. The experimental results are compared to 2D and 3D Unsteady Reynolds Averaged Navier Stokes Simulations with the $k\omega$ SST Transitional turbulent model. The URANS model both 2D and 3D are able to capture

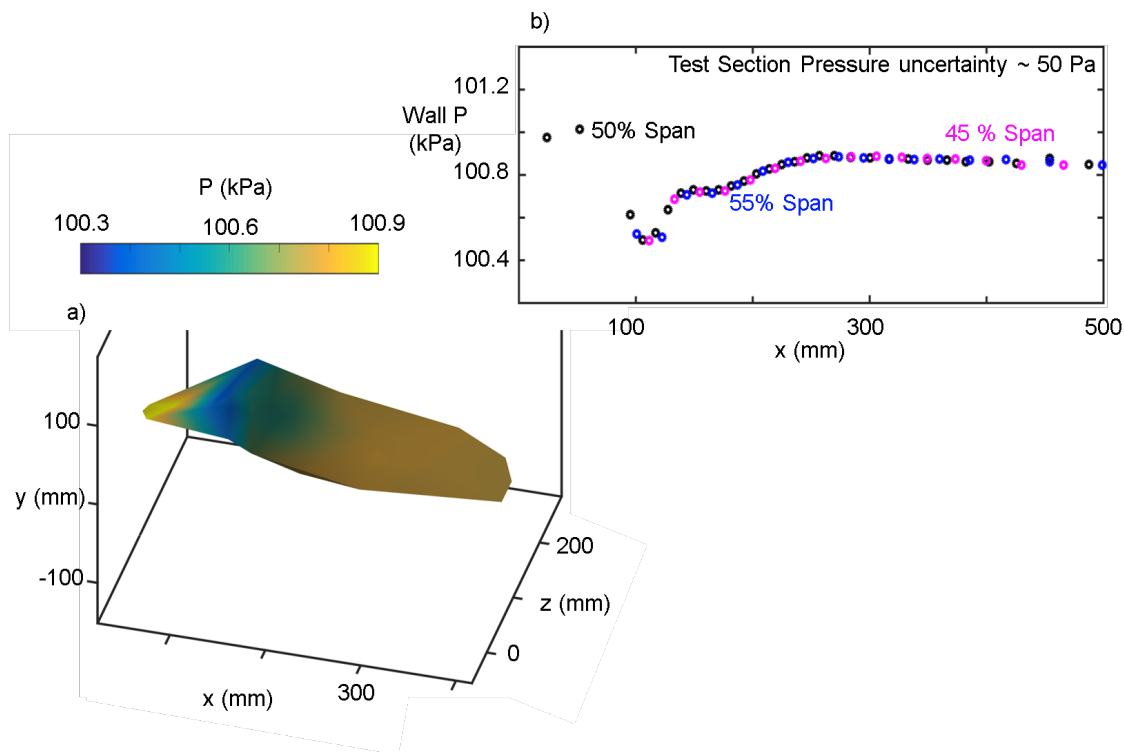


Fig. 4.51. 3D Flow behaviour at CO-7, a) Static pressure contour, b) Static pressure distribution along the test article at various span locations

correctly the detachment inception of the boundary layer over the diffusion section of the hump. The origin on the pressure plateau on both CFD predictions matches the experimental results. However, the two numerical models over-predict the extension of the recirculated flow region. In this line, the 3D case predicts an earlier reattachment compared to the 2D evaluation thanks to the influence of the 3D flow features, such as the lateral flow entrainment.

Figure 4.53 and Figure 4.54 represent the hotwire traverses for conditions CO4 and CO7 respectively. Figure 4.53 a) depicts the stream-wise velocity profile in the center of the domain 210 mm downstream of the leading edge of the test article. The experimental results are compared against the 3D-URANS simulations velocity profile at the same axial location. Figure 4.53 b) represents the turbulence intensity at each one of the interrogated heights compared to the Turbulent Kinetic Energy

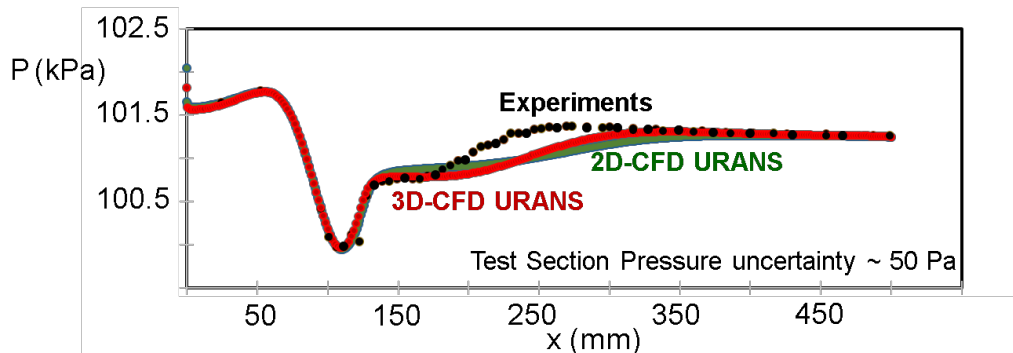


Fig. 4.52. Unsteady Reynolds Average Navier Stokes prediction of separated flow regions compared against experimental results operating at CO-4

numerical profile. The CFD prediction matches within the experimental uncertainty the velocity profile across the upper segment of the test section. However, there is a mismatch on the axial velocity profile near the recirculated flow region prediction. The mono-dimensional hotwire sensor traversed across the test section height can't accurately determine the flow velocity along the recirculated flow region. However, the turbulence intensity profile can also be a good indicator for the flow behaviour under detached flow conditions. In this sense, based on the turbulence intensity profile when compared to the turbulent kinetic energy distribution, the current computational simulation over-predicts the extension of the recirculated flow region. The peak of maximum turbulence intensity identifies the trace of the detached shear layer and its convection downstream. In this line, the numerical solver predicts a similar trend, however the extension of separated flow region is larger than the experimental one.

Similarly, Figure 4.54 compare the hotwire axial velocity measurement and turbulence intensity to the numerical prediction based on the $k\omega$ transitional SST turbulence model. As described for the operation at CO4 conditions, the agreement between experimental and numerical results in the free stream flow is excellent. However, based on the extension of the recirculated flow region, the numerical model again predicts a higher distortion on the axial velocity distribution due to the bound-

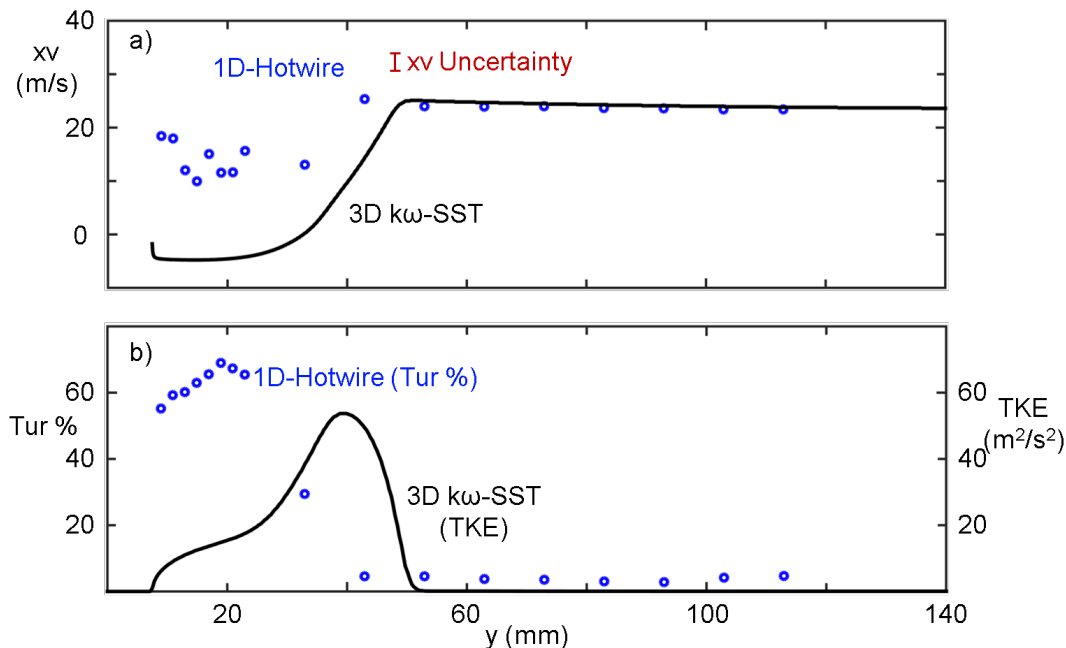


Fig. 4.53. CO-4 Hotwire Traverse

ary layer separation. Although there is a mismatch on the actual extension of the recirculated flow region the trend predicted by the numerical approach matches the experimental turbulence intensity distribution.

Hot flow conditions operation

In order to compare the prediction of heat transfer distribution along separated flow regions experiments with larger gradients between the free-stream flow and the test article were performed, HO-4 and HO-7. Figure 4.55 represents the temporal evolution of the total pressure, total temperature and free stream velocity during both experiments. Driven by the flow aspiration while purge and linear butterfly valves are simultaneously open during the start-up and shut-down of the experiment, there are peaks on the total pressure and axial flow velocity. However, during the core of the experiment the total pressure and axial free stream velocity depict steady mean flow operation. On the other hand, caused by the wind tunnel hardware warm-up,

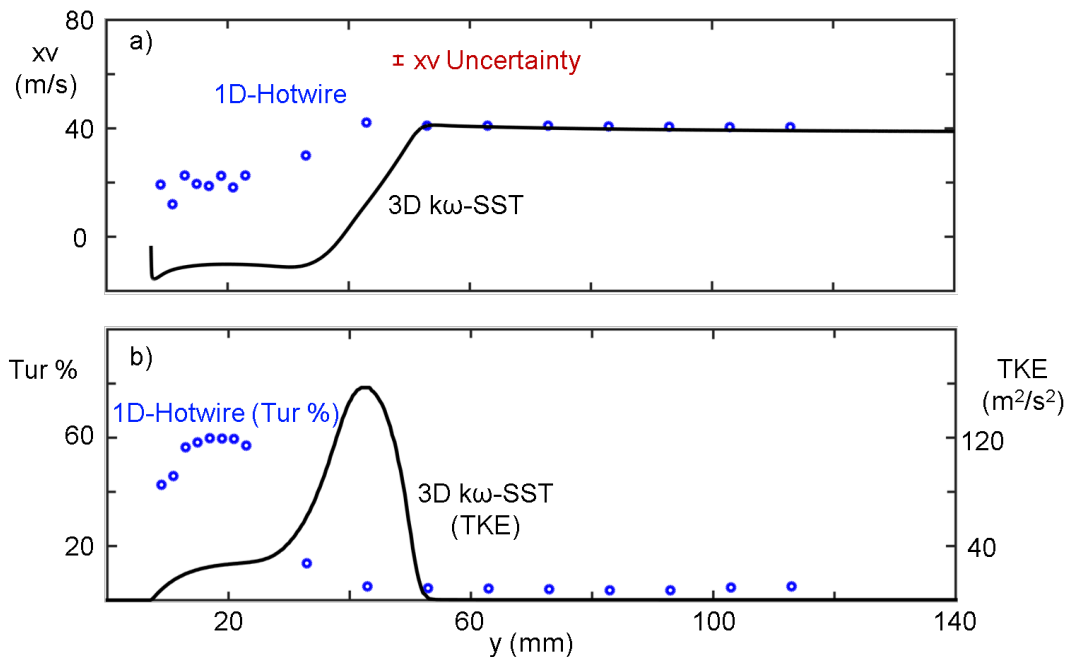


Fig. 4.54. CO-7 Hotwire Traverse

the total temperature in the test section is continuously rising. Only after 1 minute of flow the slope of the temperature seems to decay and more stable conditions are achieved, at $t = 60$ s for HO-4 and at $t = 85$ s for HO-7.

Figure 4.56 a) and b) represent the temporal evolution of three of the wall mounted thermocouples over the hump surface for HO-4 and HO-7 operation respectively. Thermocouple FSD T_w 3 is installed near the leading edge, while thermocouple FSD T_w 1 is installed 0.1 m downstream of the hump pinnacle and FSD T_w 10 is installed 0.2 m downstream of the hump summit. The thermocouple FSD T_w 3 displays the larger temperature rise driven by the smaller boundary layer thickness at its axial location, while FSD T_w 1 is within the recirculated flow region and FSD T_w 10 is downstream of the reattachment point.

Taking advantage of the temporal evolution of the wall temperature readings at the hump surface and following the procedure indicated in the Appendix D.4, the

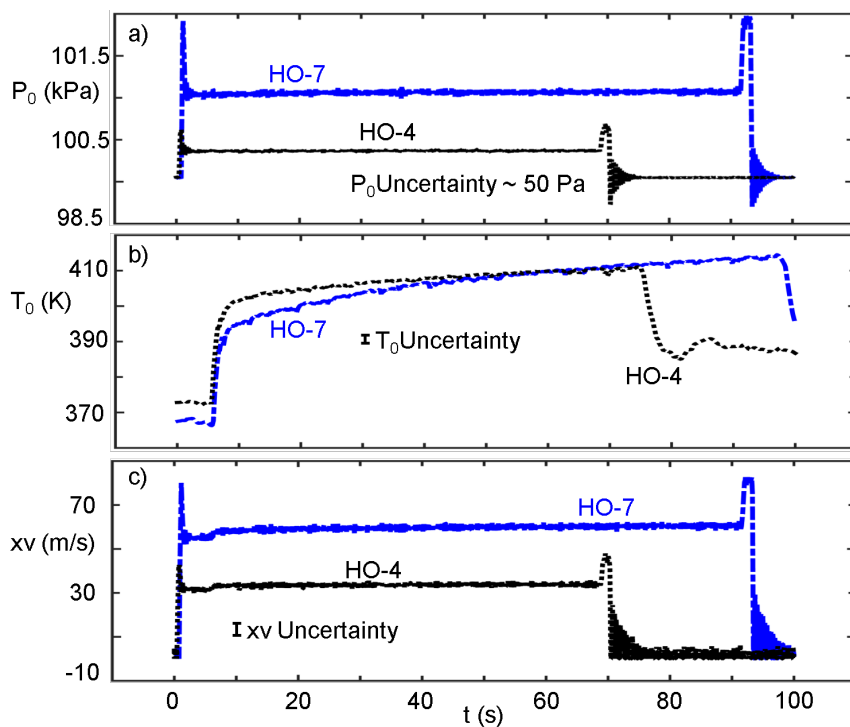


Fig. 4.55. Hot flow experiments mean flow Conditions

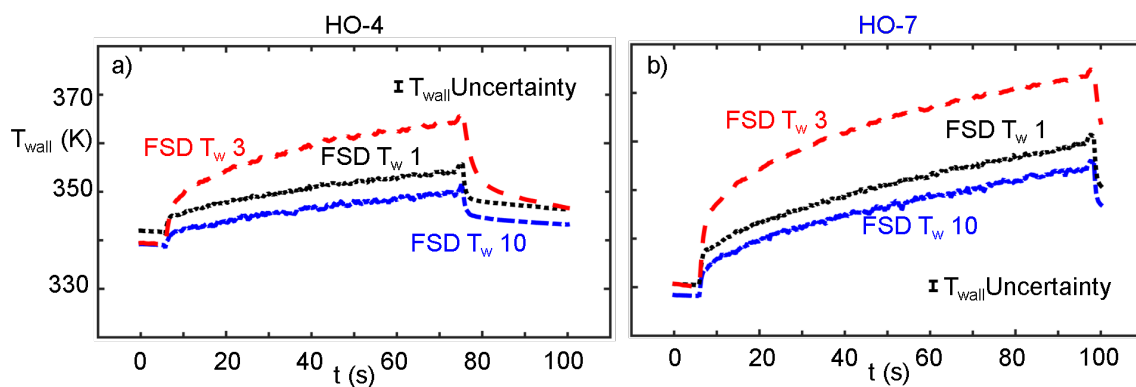


Fig. 4.56. Wall temperature evolution at different axial locations along the hump surface for hot flow conditions

heat transfer coefficient distribution along the Flow Separation Domain is derived for the described operating conditions.

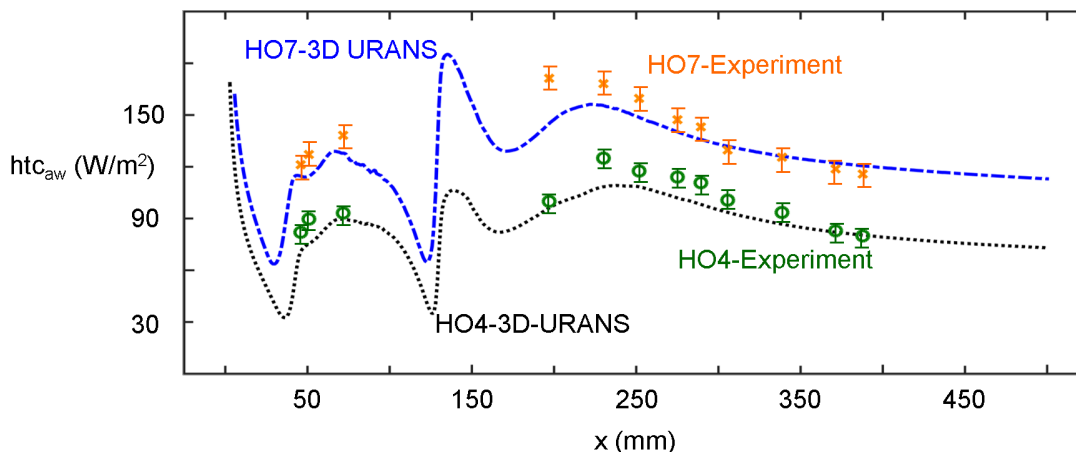


Fig. 4.57. Heat Transfer Coefficient distribution along the hump surface during operation at two different Reynolds numbers, comparison between experimental and numerical results

Figure 4.57 represents the heat transfer coefficient evolution along the test article centerline for both operational conditions and its comparison against 3D Unsteady Reynolds Average Simulations ($k\omega$ transitional SST). Throughout the initial attached flow region the CFD simulations predicted slightly smaller heat transfer coefficient than compared to the experimental results with the exact same trend. The numerical evaluations were performed assuming the development of the boundary layers from the leading edge of the domain and with an inlet turbulence level of 3.8%, matching the wind tunnel turbulence level of the facility. The predicted heat transfer coefficient throughout the hump fall also under-estimates the experimental heat transfer coefficient. Where again the over-prediction of the recirculated flow region extension is reflected on the axial distance difference between the peaks of maximum heat transfer downstream of the hump summit. Closely upstream of the reattachment location there is a peak of heat transfer as a consequence of the reattached flow impingement, [131]. The experimental trend at HO-4 operation shows a reattachment location $x \in [210 - 235]$ mm while the numerical simulation predicts the reattachment around x 245 mm. Similarly, for operation at HO-7 conditions the reattachment hap-

pens nearby $x = 200$ mm or even further upstream, while the URANS reattachment prediction is at $x = 230$ mm.

4.6 Flow separation performance under sudden flow discharge

After characterizing the performance of the test article under steady state operational conditions the next sections will explore the impact of sudden mean flow changes on the boundary layer detachment.

Sudden Flow discharge for operation at $Re/m \ 1.9 \times 10^6$

Figure 4.58 represents the evolution of the mean flow properties during sudden flow discharge at CO-5 conditions. The air stream was vented through the purge line till the total pressure upstream of the Venturi was uniform and the critical flow Venturi reached stable operation. At $t = 0$ s, the butterfly valve was actuated and the flow was discharged to the linear wind tunnel settling chamber. Figure 4.58 b) and c) represent the total pressure evolution at the test section inlet for the experiment. The signal of the local Kiel probe and the average of total pressure rake heads, black and blue respectively, represent the evolution of the total pressure in the test section through the experiment. The local Kiel probe has a much faster response time, promoted by the reduced distance between the probe and the pressure scanner, representing the arrival of the compression wave sort after the aperture of the linear butterfly valve, ($\Delta t < 100ms$). However, this probe displays acoustic reflection within the pressure tubing and once the flow is established the monitored pressure oscillates around the mean value with a frequency of 10 Hz. The averaged pressure reading from the total pressure rake has a much slower response and displays a total pressure mean value of 101.150 kPa. Figure 4.58 d) depicts the transient evolution of the total flow temperature during the experiment. Characterized by the sudden temperature drop once the flow is discharged into the test section. Similarly, Figure 4.58 e) represents the stream-wise velocity evolution at the inlet of the test section, derived from the

local total pressure probe and static pressure readings in the upper wall of the test section.

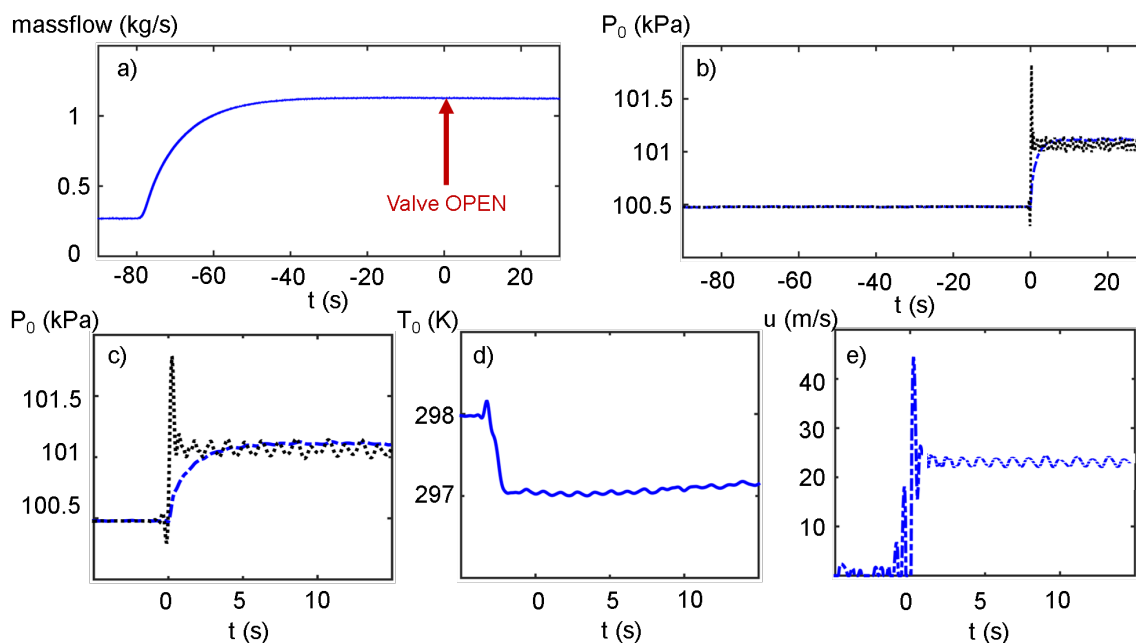


Fig. 4.58. Sudden flow discharge experiment CO-5 conditions, mass-flow, total pressure, total temperature and axial free stream velocity evolution

Figure 4.59 represents the wall pressure distribution along the hump centerline for several time steps along the transient evolution. The pressure was monitored at 2.5 kHz and then a low pass filter at 400 Hz was applied to the transient signal at each axial location. Prior to the valve aperture, $t = -0.07$ s, the entire test section has stagnant flow and the surface taps display the atmospheric pressure. Once the valve is open the passage of the initial compression waves is felt as a local rise of the static pressure along the test article axis, $t = 0.03$ s. Once the main pressure wave has travelled through the settling chamber and arrived to the test section, the flow is set into motion, $t = 0.13$ s. As the inlet flow velocity increases, the pressure distribution exerted by the hump geometry appears, reducing the static pressure towards the hump pinnacle followed by the diffusion along the fall. The dynamic pressure at

the domain inlet gradually increases as the mean flow approaches the nominal flow velocity, driving stronger expansion and diffusion across the centerline, $t = 0.18s$ and $t = 0.23s$. For later time steps, $t \approx 0.28s$ the mean flow conditions have already achieved their nominal values and a pressure plateau appears through the diffusion segment of the hump, illustrating the boundary layer detachment and the generation of the recirculated flow region. Following the boundary layer initial detachment, the recirculated flow region grows, $t = 0.33s$, till it achieves its final extension, $t = 0.38s$ and $t = 0.58s$. During the first instances of the sudden flow release although the hump is already imposing the diffusion through its fall, the boundary layer does not detach. The near wall region receives a momentum boost in terms of boundary layer height reduction driven by the flow inertia. Under such circumstances the near wall flow region is able to overcome the adverse pressure gradient. Once the acceleration rate of the flow decays and the momentum boost vanishes the boundary layer detaches from the wall and the recirculated flow region is generated.

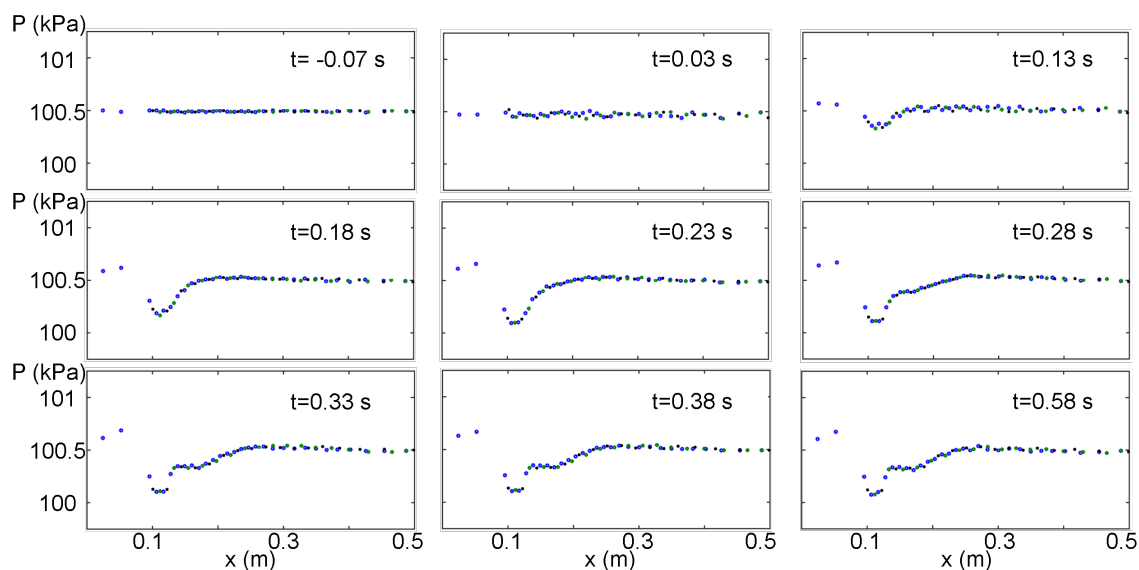


Fig. 4.59. Surface pressure evolution during CO-5 sudden discharge experiment

Figure 4.60 represents the temporal evolution of the stream-wise velocity component at various normal distances from the wall, 210 mm downstream of the test article

inlet and 80 mm downstream of the hump summit. The profiles above the recirculated flow region, ($y = 72.9, 92.9$ and 112.9 mm) follow the same trend, depicting the evolution of the mean flow velocity during the sudden discharge experiment. Following the arrival of the initial compression wave the flow velocity suddenly increases. Then it reaches a uniform value at $t = 0.140$ s to suffer a second increase towards the final flow velocity. The flow acceleration trend is promoted by the passage of the latest compression wave and the arrival of the expansion waves from the test section outlet. The measurements were obtained with a mono-dimensional hotwire probe. Hence the magnitude of the axial velocity component within the recirculated flow region ($y < 35$ mm) does not reflect only the stream-wise velocity component but also the influence of the transversal components. However, relevant information can be extracted from the transient trends about the development of the recirculated flow region by looking at the local flow unsteadiness.

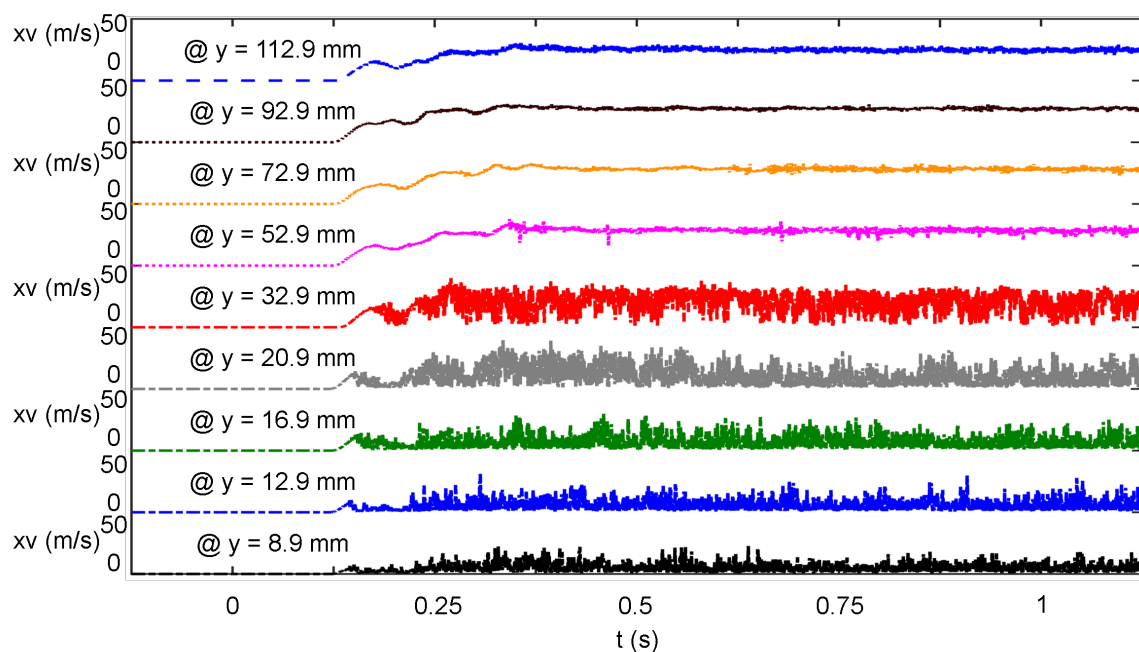


Fig. 4.60. Stream-wise velocity transient evolution during CO-5 sudden flow discharge at different wall distances.

Figure 4.61 represents the stream-wise velocity component deviation from the average local velocity. The averaged local velocity is obtained applying a low pass filter of 20 Hz to the transient signal. This indicator is a measure of the temporal evolution of the local unsteadiness or flow turbulence at each normal location. For mean flow conditions, 92.9 mm, the local stream-wise unsteadiness remains within the wind tunnel inlet turbulence level, 4 %. However, this indicator displays larger magnitudes for the profiles nearer to the wall due to the flow recirculation. Interestingly, during the initial phases of the sudden flow discharge the local unsteadiness is one order of magnitude smaller than for the nominal flow operation, which is in agreement with wall pressure distribution transient evolution. Revealing the abatement of the boundary layer detachment during the transient acceleration phase.

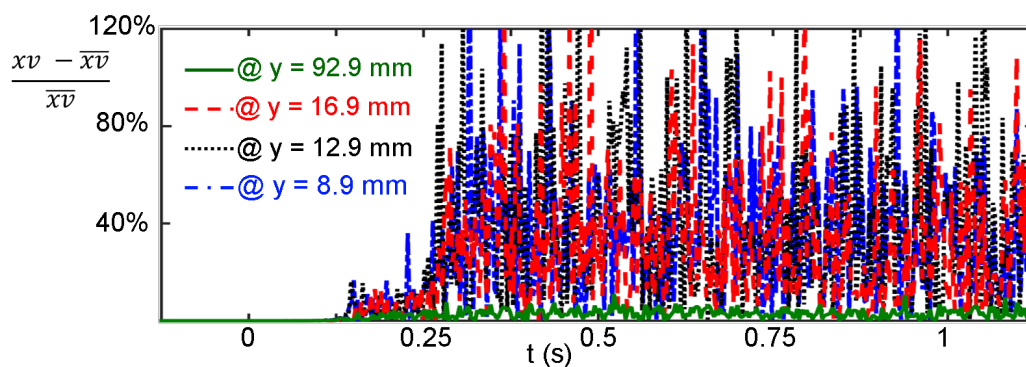


Fig. 4.61. Local stream-wise velocity unsteadiness during CO-5 Sudden Flow Discharge Experiment

Sudden Flow discharge for operation at $Re/m \ 3 \times 10^6$

Figure 4.62 represents the evolution of the mean flow properties during sudden flow discharge under operation at CO-8. The air stream was exhausted to the atmosphere through the purge while the critical flow Venturi reached stable operation. At $t = 0$ s, the linear wind tunnel butterfly valve was open and the flow was discharged to the

linear wind tunnel settling chamber. Figure 4.62 b) and c) represent the total pressure evolution at the test section inlet for the experiment. The signal of the local Kiel probe and the average of total pressure rake heads, black and blue respectively, represent the evolution of the total pressure in the test section through the experiment. The local Kiel probe represents the arrival of the compression wave sort after the aperture of the linear butterfly valve, ($\Delta t < 100ms$). Figure 4.58 d) shows the temporal evolution of the total flow temperature during the experiment, characterized by the sudden temperature drop once the flow is discharged in the test section. Similarly, Figure 4.58 e) depicts the stream-wise velocity evolution at the inlet of the test section, derived from the local total pressure probe and static pressure readings in the upper wall of the test section.

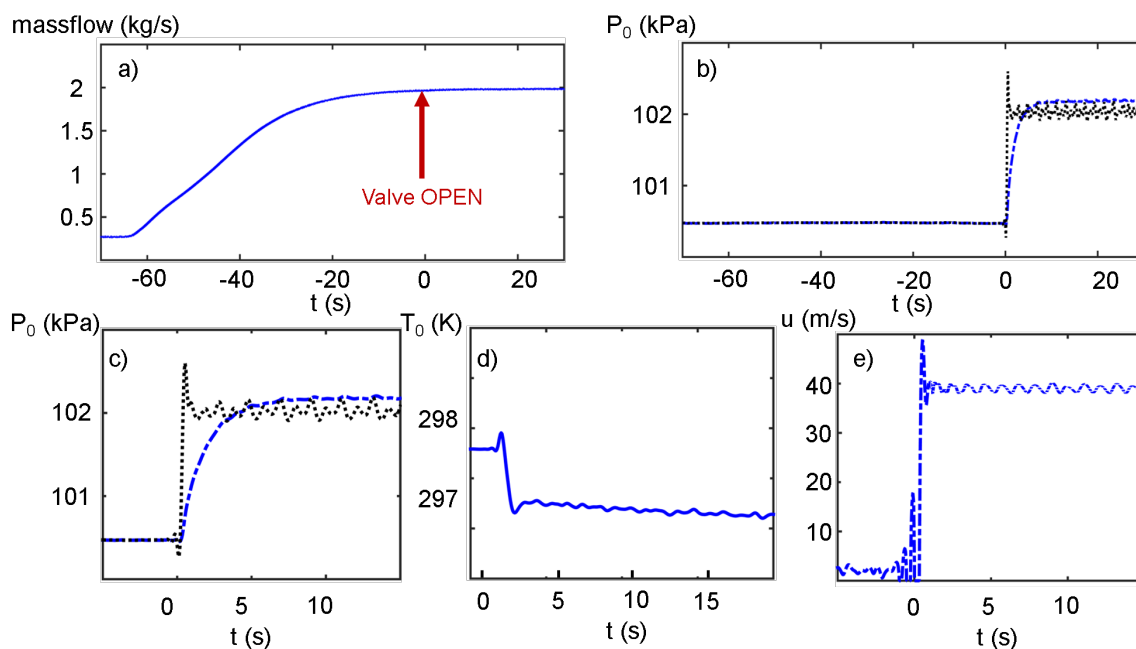


Fig. 4.62. Sudden flow discharge experiment at CO-8 Conditions, mass-flow, total pressure, total temperature and axial free stream velocity evolution

Figure 4.63 represents the wall pressure distribution along the hump centerline for several time steps along the condition start-up. Similar to the performance at

Re/m 1.9×10^6 , as the flow is set into motion, $t > 0.1s$, the hump imposes the flow expansion and diffusion across the centerline of the domain. Which is illustrated by the progressive reduction of static pressure towards the hump pinnacle. Driven by the sudden flow discharge the boundary layer is able to overcome the adverse pressure gradient and there is no presence of flow separation during the start-up, $t \leq 0.3$. As the acceleration rate dilutes the boundary layer detaches and a plateau on the pressure evolution is noticed for $t \geq 0.35$. The recirculated flow region gradually increases its extension up to its establishment, $t \geq 0.4$.

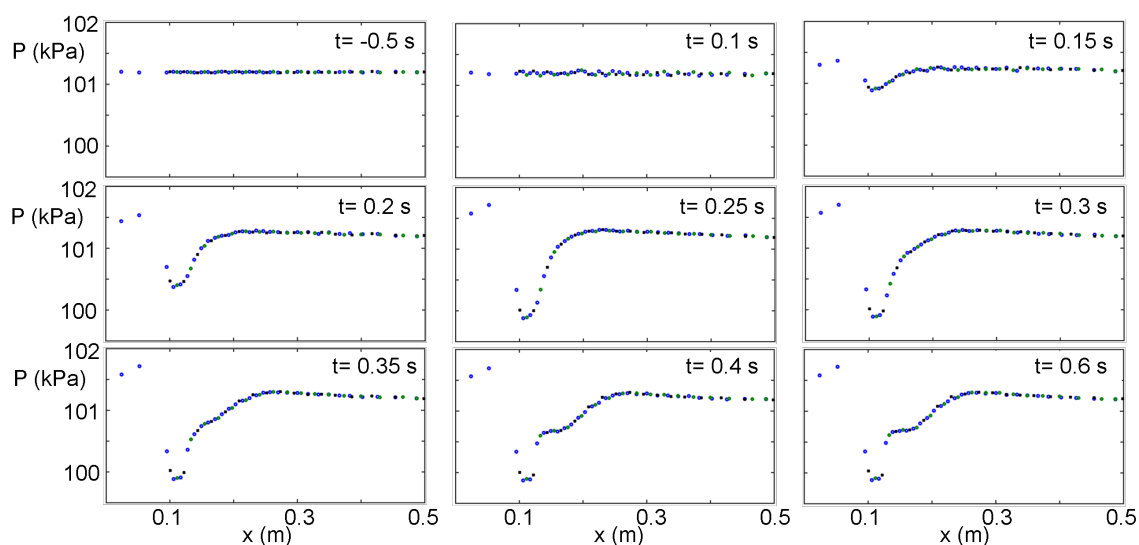


Fig. 4.63. Surface pressure evolution during CO-8 sudden discharge experiment

Figure 4.64 represents the transient evolution of the stream-wise velocity component at various normal distances from the wall, 60 mm downstream of the hump summit. The mean flow profiles ($y \geq 52.9$ mm) display identical evolution, the flow accelerates following the arrival of the compression waves till $t = 0.3$ s, where it reaches a maximum value and then gradually adjusts to the nominal operating condition, $t \geq 0.4s$.

Figure 4.64 illustrates the stream-wise velocity component deviation from the average local velocity. The transient local unsteadiness above the recirculated flow

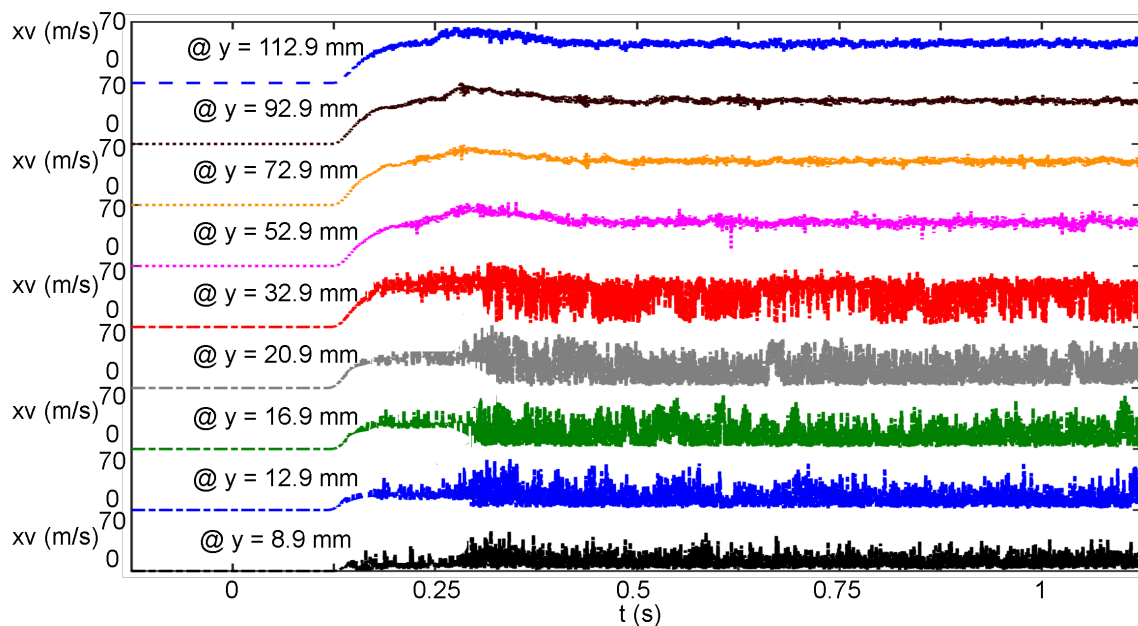


Fig. 4.64. Stream-wise velocity transient evolution during CO-8 sudden flow discharge at different wall distances.

region depicts values in agreement with inlet turbulence level. Along the recirculated region when operating at nominal conditions the mean local unsteadiness is around 50 %, in agreement with the values obtained for the steady traverses under operation at CO-4 and CO-7. However, during the initial phases of the sudden discharge, $t \leq 0.3$ s the local unsteadiness remains below 6 %. Revealing the absence of massive flow separation along the diffusion section of the hump. Which evidences the momentum boost received by the near wall flow region through the mean flow acceleration.

Finally, 4.66 represents the stream-wise velocity profile across the height of the test section 80 mm downstream of the hump summit for several time steps along the transient. The experimental velocity profile is compared against the results of a 3D URANS blow-down simulation with the $k\omega$ Transitional SST turbulence model. The sudden flow discharge in the numerical simulation was imposed with a smoother-step profile evolution that mimicked the pressure rise over 100 ms. The use of a smoother

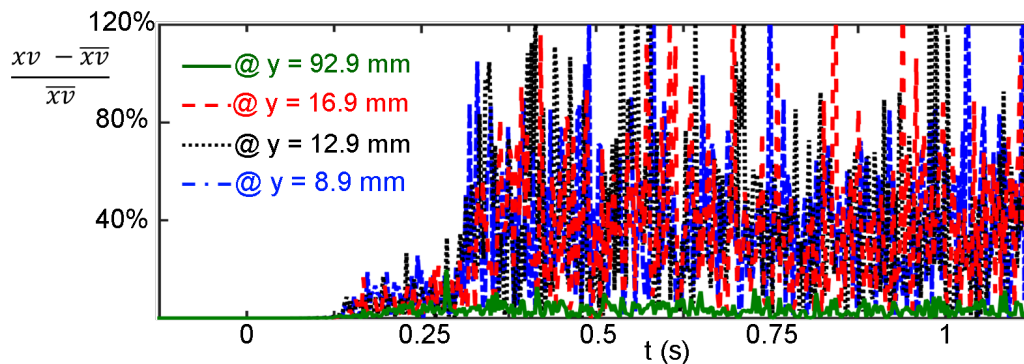


Fig. 4.65. Local stream-wise velocity unsteadiness during CO-8 Sudden Flow Discharge Experiment

step profile enhances the numerical stability of the simulation although it generates some disagreements on the initial release of pressure waves at the inlet.

Following the arrival of the initial pressure waves the flow is set into motion $t = 0.124s$. The numerical profile follows behind the initial flow acceleration, $t \leq 0.186$, due to the differences on the inlet total pressure prescription. However, for $t \geq 0.186$ the core flow velocity evolution is almost identical to the experimental evolution. The numerical blow down simulation reflects attached flow performance for $t \leq 0.272$ at the probe axial location. Similarly, the local unsteadiness in the experimental profile remains at moderate levels up to that point. Afterwards, for $t \geq 0.27$ there is a portion of the velocity profile that reveals reversed flow performance in the numerical simulations and larger profile deviations in the experimental results. The growth of the reversed flow region extends above the region of larger unsteadiness and lower velocity magnitude monitored by the hotwire, as already illustrated for steady state performance in Figures 4.53 and 4.54.

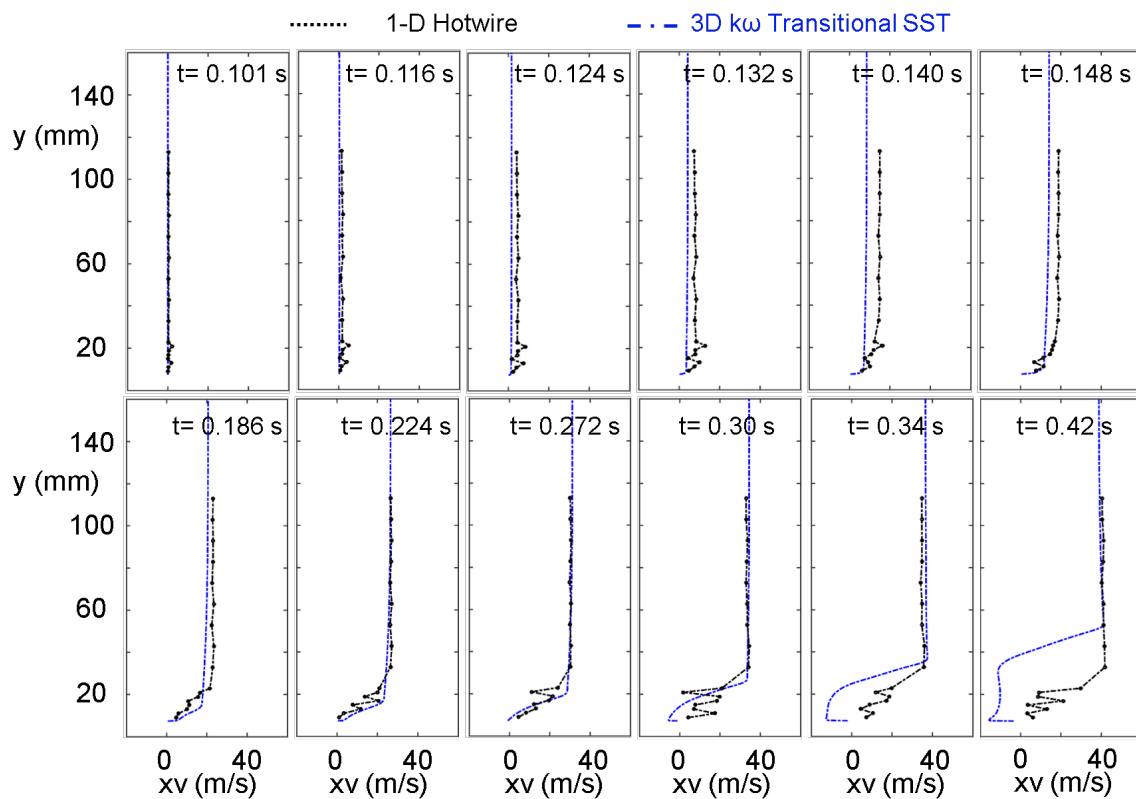


Fig. 4.66. Stream-wise velocity profile at several time-steps along the sudden flow discharge, experimental profiles (1-D Hotwire) vs. URANS numerical prediction

5. FLOW SEPARATION CONTROL THROUGH TRANSIENT SUCTION AND INJECTION

The key element driving the flow separation is the momentum inside the boundary layer. If it is too low, the boundary layer will not be able to withstand an adverse pressure gradient and will then detach from the wall. However if this near wall flow is either re-energized or absorbed, the flow separation will be abated. To illustrate this phenomena four different cases were studied with a constant Reynolds number but various flow and wall conditions. The first case considers an isothermal wall with a temperature at 300K. The inlet total pressure and temperature were 72.5 kPa and 500K respectively. While the static pressure was set in the outlet with a value of 70 kPa. For the second case all the fluid boundary conditions are kept but the wall is considered adiabatic. In the third case the total flow temperature is reduced to 300K. In order to maintain the same Reynolds number the total pressure was reduced to 71.5 kPa while maintaining the same static pressure level, reducing the mean flow velocity. Finally, in the last case the total flow temperature is also set at 300K and in this occasion the static pressure level is reduced to 41.6 kPa and the total pressure is set to a level that will guarantee the same mean flow velocity than in the first 2 cases. Figure 5.1 depicts the axial flow velocity, thermal and density profile at $x = 0.120$ m. While Table 5.1 summarizes the separation inception and the bubble length for each one of the cases. In the same table the flow momentum inside of the boundary layer and the flow angle in the near wall region are displayed.

Considering that all the cases share the same mean Reynolds number, they are exposed to equivalent flow conditions. However, the key parameter driving the flow separation is the flow momentum inside of the boundary layer or equivalently, by the momentum thickness Reynolds number, as presented by Eaton and Johnston [183]. The first case, which consisted on an isothermal wall at 300K depicts the smaller

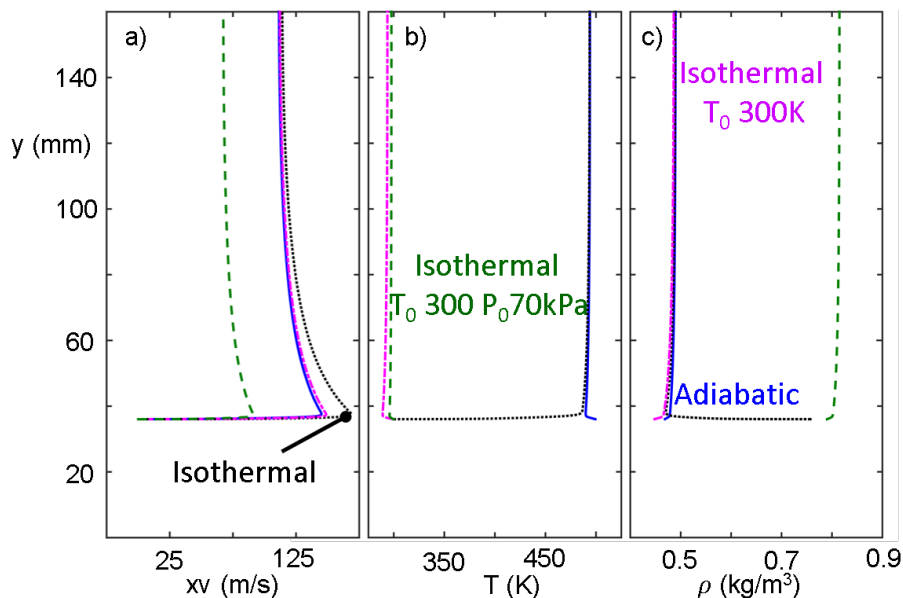


Fig. 5.1. Flow momentum deficit driving the flow detachment

bubble length with the separation inception located further downstream. This case has the larger Reynolds number based on the momentum thickness. Which implies it is the one with larger flow momentum in the near wall region. As the flow momentum inside of the boundary layer is reduced, the detachment takes place further upstream and the length of the recirculated flow region increases.

Through the previous analysis on the wall-mounted hump, section 3, the separation inception was found to occur in the same region for a wide range of Reynolds number, from 50000 up to 180000, where the same set of boundary conditions were kept. Hence, a point closely upstream of that location will be an ideal candidate for flow control approaches. In this regard, a slot 1.5 cm upstream of the separation onset was introduced. Either ingesting the boundary layer or injecting some flow to boost the flow momentum in the near wall region, the flow separation could be modulated. The domain modification is displayed in Figure 5.2. Where in case of flow injection, the flow angle (α), is set to 0. For this analysis, the mean flow through the domain was steady with a Reynolds number of 80000. The inlet total pressure and

Table 5.1.
Flow momentum deficit driving the flow detachment

	Isothermal	Adiabatic	T_0 300 K P_0 70 kPa	T_0 300 K P_0 70 kPa
Separation Inception x(m)	142.35	125.48	130.4	127.9
Bubble Length (mm)	115.38	222.15	194.8	217.2
Flow Momentum Inside of BL $kg/(ms^2)$ @ x=0.12m	278×10^3	142×10^3	167×10^3	153×10^3
Avg. Flow Momentum Inside of BL $kg/(ms^2)$ @ x=0.12m	4145	2116	2662	2315
Momentum thickness, θ	1.46×10^{-5}	1.35×10^{-4}	1.25×10^{-4}	1.14×10^{-4}
Re_θ	635.6	348.18	467.68	450.98

temperature were 65516 Pa and 500 K respectively. Where the pressure was fixed in the outlet at 65 kPa.

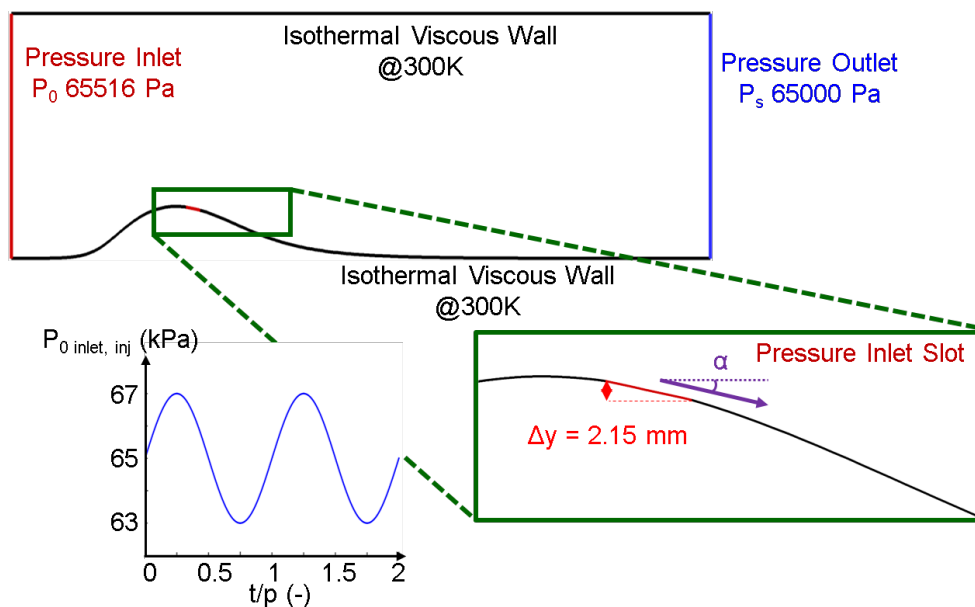


Fig. 5.2. Numerical domain for flow control analysis

Several simulations were evaluated with the total pressure in the slot ranging from 62.5 kPa up to 68.5 kPa. Exploring the amount of flow ingestion or injection required to prevent the flow separation. For cooling purposes the total temperature of the injected flow through the slot was fixed at 300 K. Figure 5.3 a) and b) represent the length of the separated region and the mass-flow through the slot. For pressures below the static pressure in that portion of the hump, there is flow ingestion (mass-flow < 0). While for pressures above it, there is flow ejection into the domain (mass-flow > 0). If there is enough portion of the boundary layer absorbed through the slot, the separation is prevented, as displayed in Figure 5.3 a) for slot pressures below 64 kPa. However, if there is not enough flow ingestion the separation onset is not modified and there is flow detachment, where only a reduction on the bubble length appears.

On the other hand, if enough flow is injected in the domain, mass-flow > 0.07 kg/s ($P_0 > 65.7$ kPa) the boundary layer momentum is boosted and it prevents the separation. The total mass-flow through the domain under these flow conditions without actuation is 3.5 kg/s. Which implies that to prevent flow separation, only 2% of the mass-flow will be required. For lower mass-flow injections, the amount of added energy results insufficient to prevent flow detachment. In the axial velocity contours at various injection pressures the differences between mass-flow ingestion and injection are perceived. After the boundary layer is drained from the slot, the size of the boundary layer is much smaller and the flow detachment is dwindled. On the contrary, for relevant mass-flow injection, the flow velocity in the near wall region is even larger than the free stream one. Hence the separation is lessened through boundary layer flow momentum boost. ¹

Upon disclosure of the pressure range that effectively modulate the separated bubble size and prevent the separation, a periodic flow actuation is proposed. Where the pressure in the slot ranges from 63 up to 67 kPa, as depicted in Figure 5.2. Several frequencies were explored spanning from 10 Hz up to 500 Hz. Figure 5.4 a) represents

¹Material Published on Transient Performance of Separated Flows: Characterization and Active Flow Control, J. Eng. Gas Turbine Power 141(1),2018

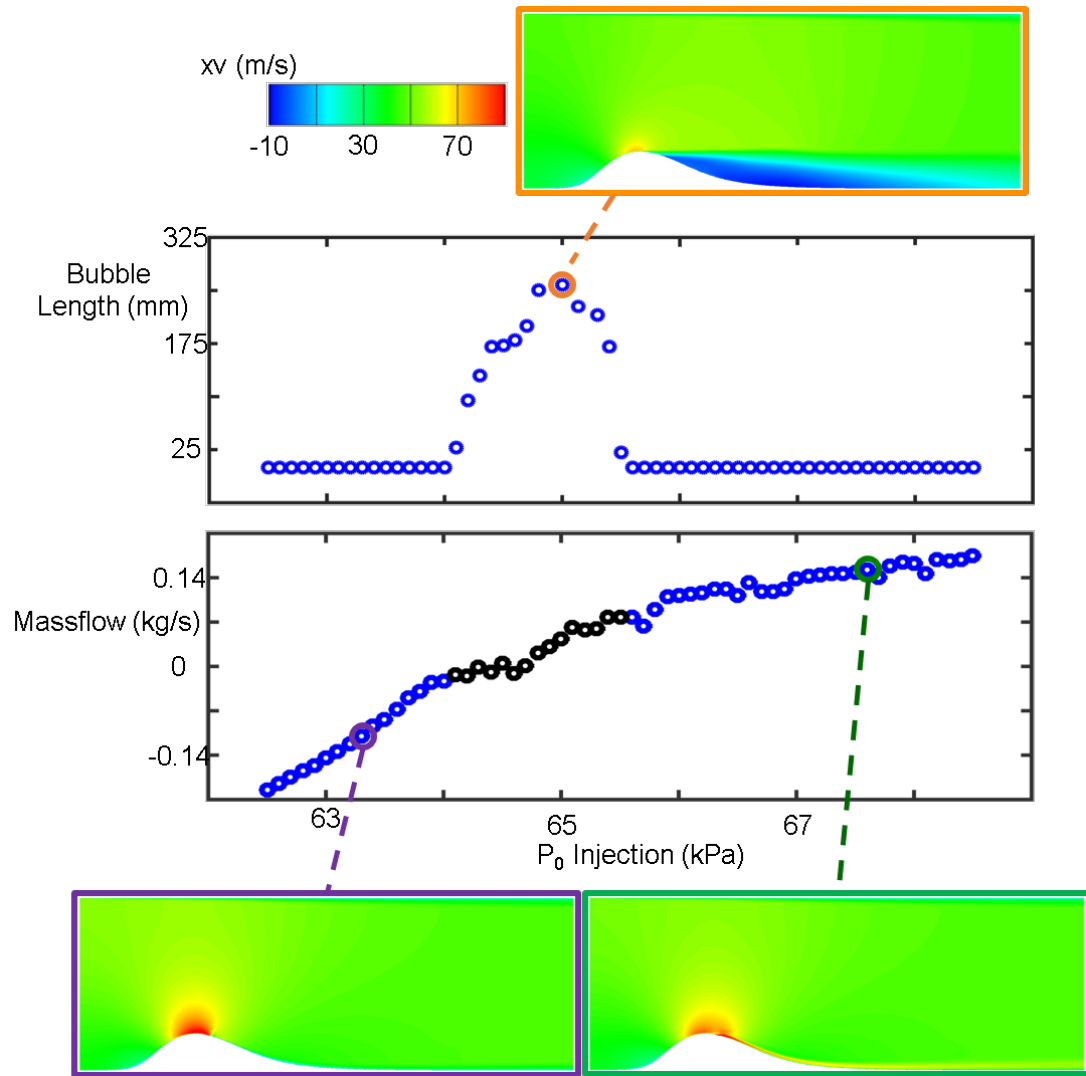


Fig. 5.3. Flow separation control envelope for different slot pressures

Table 5.2.

Dynamic pressure loss for various inlet frequencies

	No inj.	10 Hz	20 Hz	50 Hz	100 Hz	200 Hz	500 Hz
$\frac{P_{0loss}}{P_{dyn}}$	6.06%	2.64%	2.57%	2.28%	2.14%	1.99%	2.02%

the mass-flow ingestion/injection through the slot for the frequencies under scrutiny.

Regardless of the excitation frequency, all the cases present minimal variations with respect to each other on the mass-flow through the aperture.

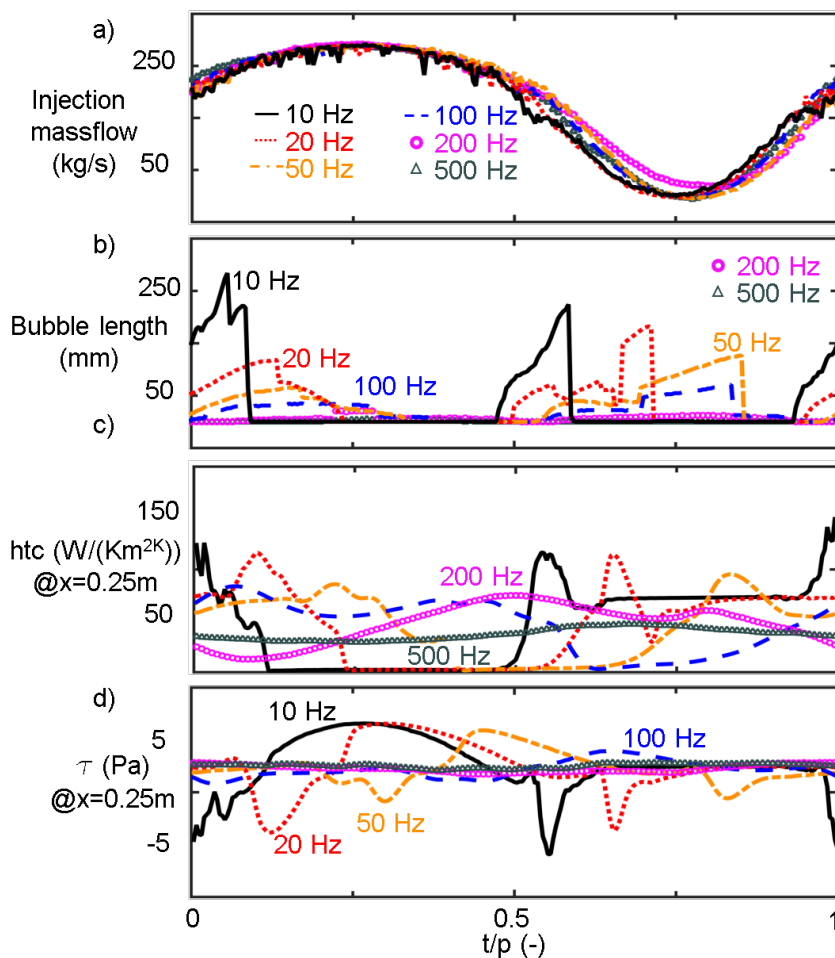


Fig. 5.4. Slot pressure fluctuation effect on the separated flow region with an actuation amplitude of 4 kPa

Figure 5.4 b) depicts the bubble size along the period of actuation for all the different cases. For the lowest frequency, 10 Hz, the maximum magnitude of the separated flow region is still comparable to the size of the case without injection. When the pressure through the slot stays in the range of the static pressure above the hump, there is a large separated flow region. Once the frequency rises, the maximum length of the recirculation bubble is reduced. For frequencies above 100 Hz the separation is almost fully tapered. In this regard, Table 5.2 represents the total

pressure loss referenced to the dynamic pressure at the inlet of the domain. The total pressure loss for the periodic injection cases is mass-flow averaged along the domain height at $x = 0.48$, and then averaged along the period. In absence of actuation, the dynamic pressure loss is about 6%. Once there is some flow injection and ingestion, even at low frequencies, the loss decays to 2.6 %. The minimum losses happen for the frequency of 200 Hz, where the level of pressure loss is comparable to the one experienced on a straight channel.

In fact, considering the bubble length for this Reynolds number without any flow actuation and the injection frequency, the Strouhal number will be:

$$St_{BubbleLength} = \frac{BubbleLength \times f_{exc}}{xv_{\infty}} = 0.87 \quad (5.1)$$

Which is close to the optimum excitation frequency as defined by Huang et al. [100]. Whose recommendation was to use excitation frequencies that will lead to a unity Strouhal number based on the bubble length.

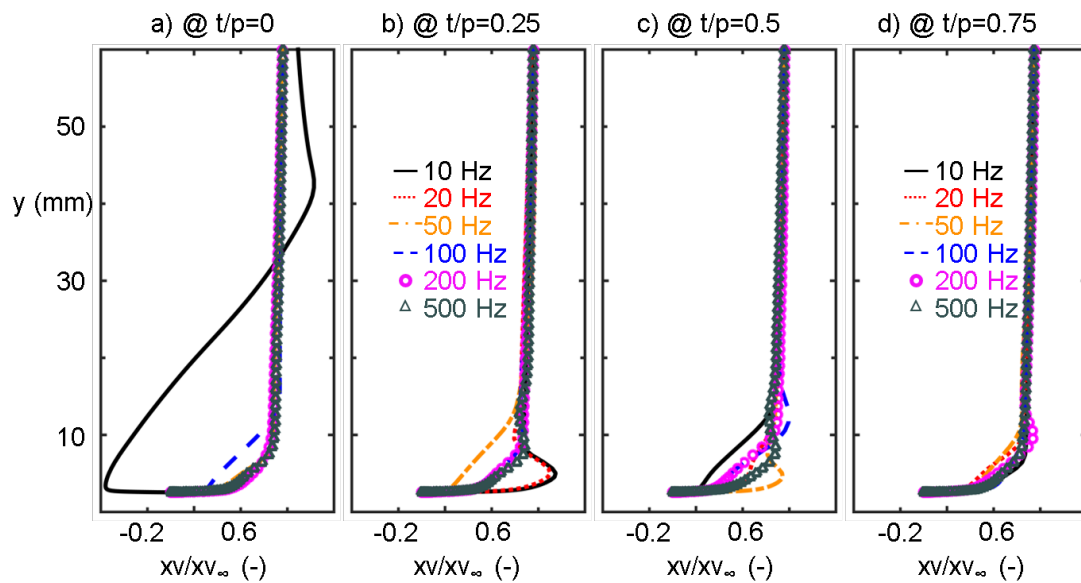


Fig. 5.5. Momentum boundary layer profiles at $x=0.25$ m for various injection frequencies

Regarding the wall shear stress evolution, Figure 5.4 c) represents its evolution along the actuation at $x = 0.25$ m. In a similar way, Figure 5.5 represents the axial velocity profile at the same location. For the initial phase of the period, the actuation at 10 Hz is insufficient and there is recirculated flow at this location, leading to a negative wall shear stress footprint. At a latter phase of the actuation $t/p = 0.25$, when the injection pressure is maximum, the low frequency cases depict an energized boundary layer and the flow velocity near the wall region exceeds the free stream axial velocity, which prevents the flow detachment. For faster actuation rates, the axial velocity profiles stay at an almost steady averaged condition, where the effect of the various injection pressures on the flow acceleration and deceleration on the near wall region is minimized.

In terms of heat flux, Figure 5.4 d) depicts the heat transfer coefficient evolution along the period at $x = 0.25$ m. As occurred for the shear stress, the cases of lower actuation frequency had the larger temporal deviations of heat transfer. Whereas, for higher frequencies they tend to an averaged status. In this regard, Figure 5.6 represents the thermal boundary layer profiles at the same axial location for various instances along the period. At the mean injection pressure level, the low frequency cases suffer flow separation, which alters the temperature profile downstream of the hump, as depicted at $t/p=0$ for the 10Hz case. If the boundary layer is completely aspirated, at the lowest pressure levels of the aperture ($t/p = 0.75$), there is almost no insulation from the core flow and the heat transfer coefficient increments. On the contrary, for the largest slot pressure, the flow injection generates a small layer of colder flow that isolates the wall from the hotter free stream conditions ($t/p = 0.25$). However, when averaging the heat transfer coefficient along the period, the cases that depict the lower heat transfer rates are the higher frequency ones. Consequently, based on the ranges of frequencies explored, the larger the injection frequency the lower the heat transfer is.

Two additional analysis of periodic actuation were performed in the quest towards an optimum flow control. Minimizing the flow separation with the slowest amount

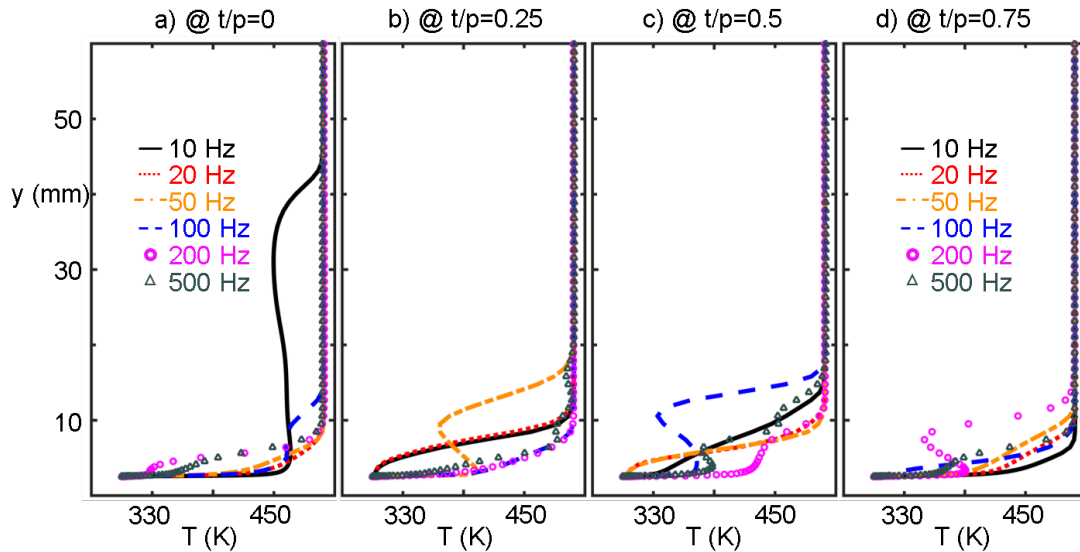


Fig. 5.6. Thermal boundary layer profiles at $x=0.25$ m for various injection frequencies

of mass-flow injection. In these cases, the frequency of the actuation was fixed at 200 Hz, but the amplitude of the slot pressure fluctuations was modified. In the first analysis, the maximum total pressure was fixed for all the cases and the amplitude of the variations was reduced, ranging from 4 kPa (the original case at 200Hz) down to 1kPa, as represented in Figure 5.7 a). Figure 5.7 b) depicts the mass-flow injection through the hump aperture. Once the amplitude is below 2.5 kPa there is no flow absorption and all the control is achieved through mass-flow injection.

Figure 5.7 c) displays the bubble length along the period. The original actuation amplitude prevents the bubble formation throughout the period. However, as the maximum ingestion rate is minimized, the absorption part of the period is ineffective and the flow detaches from the wall. Once the minimum pressure in the aperture is equal to the static pressure level in the back of the domain, the length of the separated bubble is limited to 40 mm. For lower pressure fluctuation, $\min(P_{0,inj}) > 65.5$, the flow separation is prevented along the entire period. In this regard, Table 5.3 summarizes the dynamic pressure loss for the various amplitudes under analysis.

Table 5.3.
Dynamic pressure loss for various injection total pressure amplitudes
keeping a constant upper level

	63-67	64-67	64.5-67	65-67	65.5-67	66-67
$\frac{P_{0,loss}}{P_{dyn}}$	1.99 %	2.58%	2.29%	2.5%	1.3%	0.95%

For the cases with relative ingestion, $63.5 < \min(P_{0,inj}) < 65.5$, the pressure losses are increased compared to the larger pressure range. Once, there is only flow injection through the slot, the pressure loss keeps decaying when the amplitude is minimized. Which is also influenced by the increment on the mass-flow injection through the slot throughout the period.

In terms of cooling, all the lower amplitude cases outperform the original case. Figure 5.7 d) represents the heat transfer coefficient evolution at $x = 0.25$ throughout an entire actuation period. At first, the reduction on the near wall ingestion increases the boundary layer size at the observation location, expanding the isolation layer between the wall and the core flow. As the amplitude rises and the injection from the slot increases, a near wall cold flow jet is formed. This near wall jet completely isolates the hump valley, lessening the heat transfer from the free stream flow to the wall.

Shifting gears, Figure 5.8 represents the total pressure inlet in the slot for the second amplitude analysis. In this case, the minimum pressure level is kept constant, matching the static pressure in the outlet of the domain. Figure 5.8 b) represents the mass-flow injection for the analyzed amplitudes. The maximum mass-flow injection for the amplitude of 2 kPa is about 0.14 kg/s, which is 4% of the core main flow. The reduced slot pressure amplitudes imply less mass-flow injected in the domain. In terms of flow separation control, as the mass-flow injected through the slot gets reduced, the momentum boost in the boundary layer is minimized and the bubble lengths rises. In this sense, Figure 5.8 represents the bubble length for the different

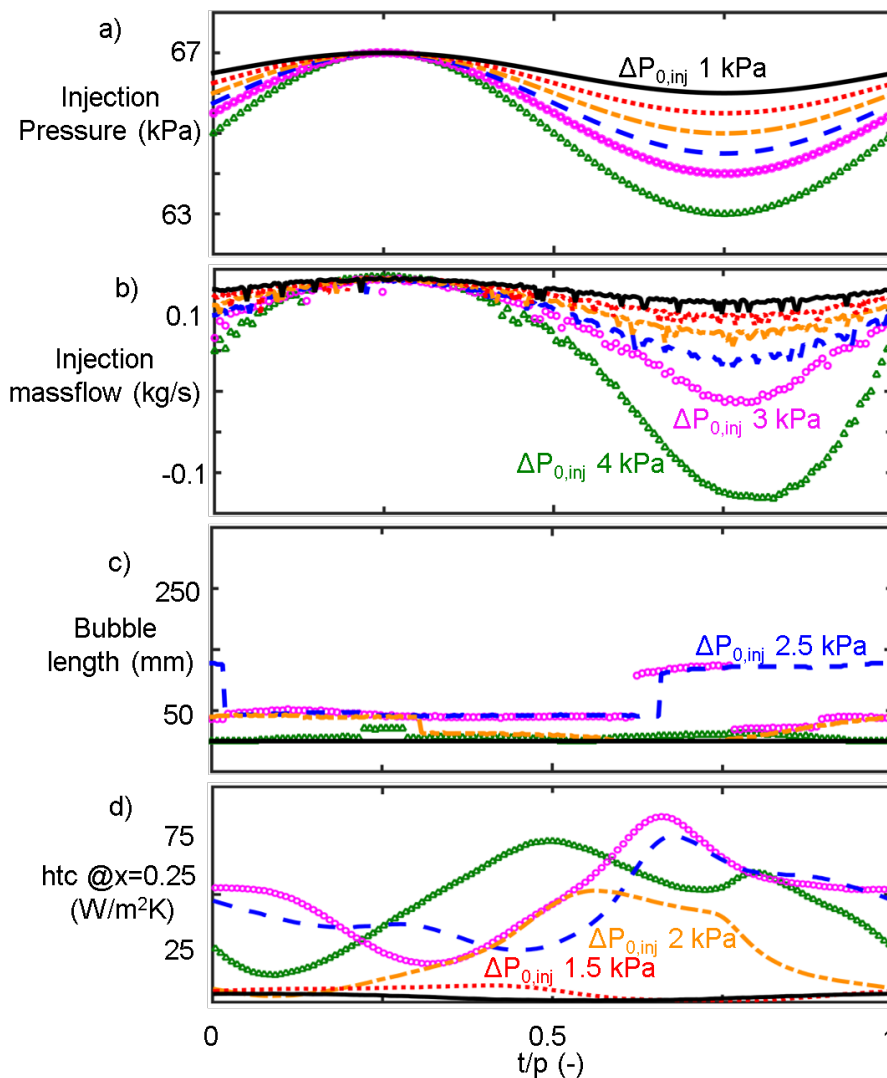


Fig. 5.7. Injection pressure amplitude effect on the separated flow region and thermal isolation

inlet pressure collections. For ranges below 1.5 kPa, where the peak pressure is under 66.5 kPa, there is not enough energy addition to avoid the separation burst, nor to keep the bubble length at a moderate level.

Table 5.4 compares the dynamic pressure loss for the different pressure ranges under scrutiny. For injection pressures below 66 kPa the pressure losses along the domain exceed the one experienced in the case without actuation. Suggesting that

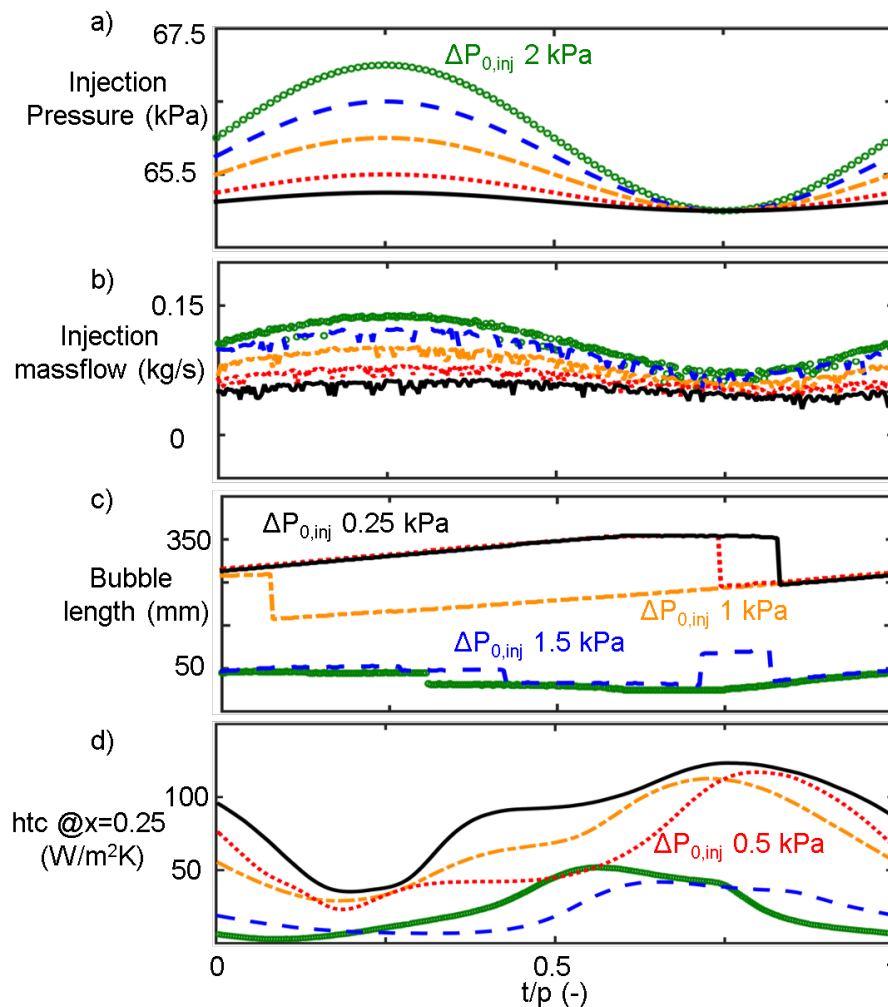


Fig. 5.8. Injection pressure amplitude effect on the separated flow region and thermal insulation

low flow momentum injection will further enhance the boundary layer detachment rather than preventing its separation.

Low frequency actuation effectively abates the flow separation near the extremes of the injection and ingestion. However, they fail to prevent separation at mean pressure levels. As the frequency of actuation increases, they effectively prevent the separation onset. In addition, the thermal and axial velocity profiles tend to an average status, which minimizes the heat transfer rate from the core flow to the wall.

Table 5.4.
Dynamic pressure loss for various injection total pressure amplitudes
keeping a constant upper level

	65-67	65-66.5	65-66	65-65.5	65.5-65.25
$\frac{P_{0loss}}{P_{dyn}}$	2.00 %	2.75%	4.09%	7.39%	9.61%

To reduce the total pressure loss, the excitation frequency was the one closer to the Strouhal = 1 (St referenced to the recirculated flow bubble length). Finally, in the quest towards the most efficient flow control, various injection pressures were analyzed at the optimum actuation frequency. Revealing that the most effective control takes place when the momentum of the flow being injected exceeds the one of the flow outside of the boundary layer.

The boundary layer detachment phenomena is abated thanks to the addition of momentum to the boundary layer or through the ingestion of the near wall flow. In case of laminar flow separation the flow ingestion or injection can promote the transition of the flow to turbulent status, which could further prevent the boundary layer detachment. However, to have an efficient control over the boundary layer detachment through active transition the actuator should be placed further upstream, allowing enough time for the boundary layer to reach full turbulent status. To assess the effectiveness of the slot promoting transition and its implication on the boundary layer detachment abatement, Figure 5.9 and figure 5.10 compare the performance of the injection for turbulent flow separation and laminar/transitional boundary layer separation.

Figure 5.9 a) compares the massflow averaged axial velocity at a plane 0.25 m downstream of the inlet for the transitional and the fully turbulent case. While Figure 5.9 b) compares the skin friction during a complete period of the slot actuation for both cases at 200 Hz and with 4 kPa amplitude. The comparison assess whether the injection affects the separation through the promotion of the transition or its

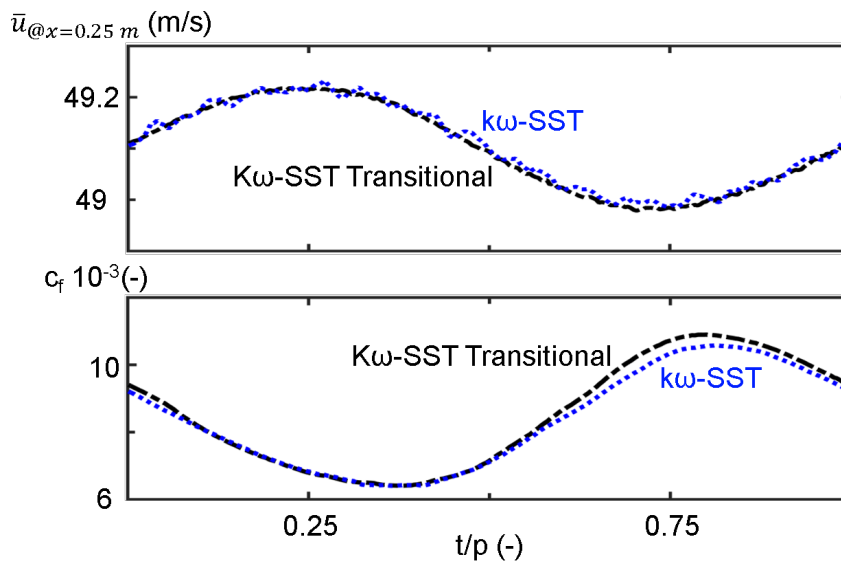


Fig. 5.9. Mass-flow averaged axial velocity and skin friction evolution at plane $x = 0.25$ m for transitional and full turbulent periodic injection

purely due to the injection of momentum. The difference on the separated length axial length throughout the period is negligible, depicting how even if being able to promote the transition to turbulent state in case of laminar separation, its impact will be minimal when compared to the momentum addition or ingestion.

Figure 5.10 compares the periodically averaged 2D contour of turbulent kinetic energy for both cases, transitional and fully turbulent, left and right respectively. In the transitional case the influence on the local adverse pressure gradient upfront of the hump is perceived on the local rise of the turbulent kinetic energy. However as the flow accelerates that local boost is diluted and the turbulent kinetic energy at the slot origin is minimal. The flow ingestion/injection at the slot triggers the transition and a increase on turbulent kinetic energy over the fall of the hump is observed. In regards to the fully turbulent case, already high values of turbulent kinetic energy at the slot onset are observed, depicting the turbulence status of the flow even at the hump pinnacle.

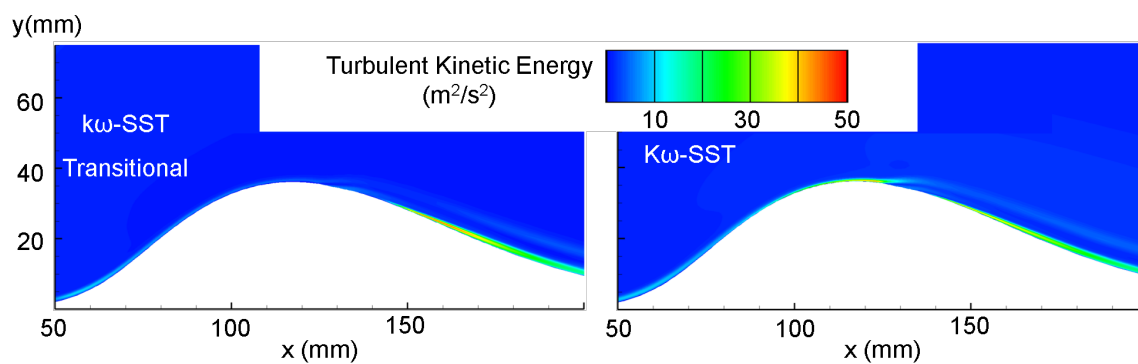


Fig. 5.10. Averaged 2D contour of Turbulent Kinetic Energy for transitional and fully turbulent case with flow aspiration and injection

6. CONCLUSION

Transient flow behavior impacts momentum and thermal boundary layer development in all fluid-mechanic machinery. The near wall region can suffer from inertia, turbulence mitigation, or turbulence enhancement driven by sudden changes or oscillatory behavior of the free-stream conditions. This phenomenon is of particular relevance for short duration wind tunnels where the flow is set into motion by shock waves and only a few milliseconds of testing are available. In a similar way, the confined flow inside of turbomachinery passages or heat exchangers suffers from mean flow oscillations driven by upstream components. Free-stream flow changes, in particular sudden flow accelerations affect the development of the boundary layer and impact the evolution of the wall fluxes.

The dynamic response of the boundary layer is characterized based on detailed Unsteady Reynolds Averaged Navier-Stokes (URANS) simulations, the wall heat flux response to periodic or sudden flow velocity changes was explored. Driven by the flow acceleration, the boundary layer is first stretched, rapidly boosting the wall shear stress. Later on, delayed by the viscous diffusion across the boundary layer height, the low momentum flow adjusts to the new free-stream conditions. The behavior of the boundary layer at low frequency is similar to the response to an individual deceleration followed by an acceleration. However, at higher frequencies the mean flow topology is completely altered. One would expect that higher acceleration rates would cause a further stretching of the boundary layer and boosting the wall shear stresses and heat fluxes. However, the opposite is observed; the amplitude of the skin friction coefficient is abated, while the peak level is an order of magnitude smaller than at low frequencies. The heat flux and wall shear stress depict a slower response as a consequence of the propagation delay across the boundary layer height. The mean flow quantities are transferred through convection

(T) and acoustic propagation (P) along the domain. However, the transmittance of the information across the boundary layer happens in a diffusive manner. The diffusion transmissivity is much slower than the convective one and consequently there exists a perceptible delay on the reaction of the wall fluxes.

When the boundary layer is under periodic flow perturbations there are two distinct behaviors depending on the actuation to response rate of the domain. For lower Strouhal numbers there are large fluctuations on the wall heat fluxes. The skin friction coefficient greatly exceeds the turbulent prediction due to the flow inertia right after the acceleration, while the turbulent delay during the flow deceleration drives smaller shear stresses. In terms of heat flux, due to the slower thermal diffusion across the boundary layer, the heat transfer rates do not exceed the turbulent predictions. For moderate Strouhal numbers the amplitude of the heat flux and wall shear stress variations are mitigated. However, at large excitation frequencies the mean flow sudden variations can impact the nature of the boundary layer through the promotion of reverse transition. Which has a direct impact on the wall fluxes distribution.

The time-characterization of the momentum boundary layer development in transient turbulent compressible air flows was further explored based on Direct Numerical Simulations. The simulations analyzed the development of the boundary layer over a flat plate after accelerating from Mach 0.3 up to 0.6 in 10 milliseconds. Based on data from numerical experiments and a simplification of the integral boundary layer momentum equation, a reduced-order model to predict the evolution of the boundary layer under mean flow transients was developed. Given the initial boundary layer height, the temporal evolution of the free-stream pressure, velocity, and density, the model can accurately predict the development of the boundary layer thickness. Once the transient evolution of the boundary layer is captured, the temporal progression of the skin friction and heat transfer coefficient can be tracked taking advantage of standard shear stress correlations and the Reynolds analogy.

During transient flow conditions or periodic flow perturbations, the flow momentum near the wall region can be benefited from the unsteady flow behavior and delay

or prevent the boundary layer detachment. The flow separation is induced by the lack of momentum on the near wall region when exposed to adverse pressure gradients. This dissertation analyzed the behavior of separated flows, reporting the inception and separation length, under non-temporally uniform inlet conditions through Unsteady Reynolds average NavierStokes (URANS), large Eddy simulations (LES) and experiments in a linear wind tunnel. The investigation is focused on ad-hoc wall mounted hump that mimics the performance of a low pressure turbine airfoil. Where the flow is attached for high Reynolds number but the boundary layer detaches for low Reynolds conditions. Through sudden flow accelerations, the dynamic response of the shear layer detachment was also assessed. While based on periodic inlet total pressure fluctuations the performance of flow separation under continuous flow oscillations was explored.

Based on the sudden flow discharge analysis, at similar Reynolds conditions, **the presence of flow acceleration energizes the near wall flow preventing the flow separation. On the contrary, in case of mean flow deceleration, the boundary layer is more predisposed to detach and the length of the separated region increases.** In this line, the strong influence of the mean flow temporal evolution on the separation onset was remarked. Under periodic disturbances, once the excitation rates approach the domain frequency response, the mean flow quantities tend to an average condition. However, the boundary layer flow can perceive the influence of the pressure and expansion waves propagating across the domain, modulating its reaction when exposed to adverse pressure gradients.

To assess experimentally the impact of mean flow transients on the flow detachment and reattachment process a modular wind tunnel tailored to fundamental and low technology readiness level, 1-2, was designed and commissioned. The working section, 70x230 mm cross section and 550 mm long, has full visual access and can operate in sub-atmospheric and over-pressure conditions. The test section is defined by windows, allowing complete imaging resolution and enabling the use of a myriad of optical techniques to characterize the near wall region.

The test conditions in the working section can vary from Reynolds/m $\in [1 \times 10^5 - 1.9 \times 10^8]$ and Mach $\in [0.005 - 6.5]$. The design of the flow conditioning system was optimized with 3D Unsteady Reynolds Average Simulations to guarantee its performance. Delivering uniform flow conditions with a minimal response time to the upstream flow changes. Taking advantage of this facility, aero-thermodynamic measurements over the designed wall mounted hump were carried out to monitor the temporal evolution of boundary layer detachment and reattachment. The inlet flow conditions to the test article were interrogated with total pressure, total temperature and hotwire traverses. The transient growth of the recirculated flow region under the mean flow transients was monitored by means of wall pressure readings and hotwire traverses. Driven by the sudden flow release, the near wall region can overcome the adverse pressure gradient. As the flow acceleration dilutes, the boundary layer detaches and the separated flow region grows. The experimental results are compared to 2D and 3D transient Computational Fluid Dynamic simulations. Which proof the capability of Unsteady Reynolds Average Navier-Stokes models predicting the dynamics of this phenomena although over-predicting the extension of the separation.

Once the boundary layer detachment phenomena under mean flow transients was characterized, **flow control strategies based on flow injection and absorption were analyzed.** To investigate the impact of flow control on the flow separation dynamic response a slot was included in the geometry. Allowing the exploration of the recirculated flow region behavior under flow aspiration and injection. Low-frequency excitation effectively abates the flow separation near the actuation extremes. However, it fails to prevent separation along the mean levels of the actuation envelope. As the frequency of actuation increases, the cyclic injection-ingestion effectively prevents the separation onset throughout the entire period. In addition, the thermal and axial velocity profiles tend to an average status, which reduces the heat transfer rate from the core flow to the wall. **The actuation performance is boosted when the actuator frequency matches the frequency response of the separated region.**

REFERENCES

REFERENCES

- [1] K. t. Stewartson, “On the impulsive motion of a flat plate in a viscous fluid,” *The Quarterly Journal of Mechanics and Applied Mathematics*, vol. 4, no. 2, pp. 182–198, 1951.
- [2] K. Stewartson, “The theory of unsteady laminar boundary layers,” *Advances in Applied Mechanics*, vol. 6, pp. 1–37, 1960.
- [3] H. Schlichting and K. Gersten, *Boundary-layer theory*. Springer, 2016.
- [4] H. Blasius, *Grenzschichten in Flüssigkeiten mit kleiner Reibung*. Druck von BG Teubner, 1907.
- [5] S. Ostrach, “An analysis of laminar free-convection flow and heat transfer about a flat plate parallel to the direction of the generating body force,” National Aeronautics and Space Administration Cleveland, OH, Lewis Research Center, Tech. Rep., 1952.
- [6] C. E. Smith, “The starting process in a hypersonic nozzle,” *Journal of Fluid Mechanics*, vol. 24, no. 4, pp. 625–640, 1966.
- [7] H.-S. Huang and W.-J. Yang, “Unsteady compressible laminar boundary-layer flow over a flat plate,” *AIAA Journal*, vol. 7, no. 1, pp. 100–105, 1969.
- [8] J. Watson, “A solution of the navier–stokes equations illustrating the response of a laminar boundary layer to a given change in the external stream velocity,” *The Quarterly Journal of Mechanics and Applied Mathematics*, vol. 11, no. 3, pp. 302–325, 1958.
- [9] W. Davies and L. Bernstein, “Heat transfer and transition to turbulence in the shock-induced boundary layer on a semi-infinite flat plate,” *Journal of Fluid Mechanics*, vol. 36, no. 1, pp. 87–112, 1969.
- [10] M. J. Lighthill and M. H. A. Newman, “On boundary layers and upstream influence. i. a comparison between subsonic and supersonic flows,” *Proc. R. Soc. Lond. A*, vol. 217, no. 1130, pp. 344–357, 1953.
- [11] M. J. Lighthill, “On sound generated aerodynamically ii. turbulence as a source of sound,” *Proc. R. Soc. Lond. A*, vol. 222, no. 1148, pp. 1–32, 1954.
- [12] —, “Contributions to the theory of heat transfer through a laminar boundary layer,” *Proc. R. Soc. Lond. A*, vol. 202, no. 1070, pp. 359–377, 1950.
- [13] H. Mirels, “Boundary layer behind shock or thin expansion wave moving into stationary fluid,” National Advisory Committee for Aeronautics. Lewis Flight Propulsion Lab.; Cleveland, OH, United States, Tech. Rep., 1956.

- [14] M. S. Holden, "Establishment time of laminar separated flows," *AIAA journal*, vol. 9, no. 11, pp. 2296–2298, 1971.
- [15] J.-Y. Lee and M. J. Lewis, "Numerical study of the flow establishment time in hypersonic shock tunnels," *Journal of Spacecraft and Rockets*, vol. 30, no. 2, pp. 152–163, 1993.
- [16] P. Jacobs, R. Rogers, E. Weidner, and R. Bittner, "Flow establishment in a generic scramjet combustor," *Journal of Propulsion and Power*, vol. 8, no. 4, pp. 890–899, 1992.
- [17] H. Li and M. R. Nalim, "Thermal-boundary-layer response to convected far-field fluid temperature changes," *Journal of Heat transfer*, vol. 130, no. 10, p. 101001, 2008.
- [18] S. Szymko, R. Martinez-Botas, and K. Pullen, "Experimental evaluation of turbocharger turbine performance under pulsating flow conditions," in *ASME Turbo Expo 2005: Power for Land, Sea, and Air*. American Society of Mechanical Engineers, 2005, pp. 1447–1457.
- [19] D. Palfreyman and R. Martinez-Botas, "The pulsating flow field in a mixed flow turbocharger turbine: an experimental and computational study," in *ASME Turbo Expo 2004: Power for Land, Sea, and Air*. American Society of Mechanical Engineers, 2004, pp. 697–708.
- [20] J. Galindo, P. Fajardo, R. Navarro, and L. García-Cuevas, "Characterization of a radial turbocharger turbine in pulsating flow by means of cfd and its application to engine modeling," *Applied Energy*, vol. 103, pp. 116–127, 2013.
- [21] S. Rajoo and R. Martinez-Botas, "Unsteady effect in a nozzled turbocharger turbine," in *ASME Turbo Expo 2007: Power for Land, Sea, and Air*. American Society of Mechanical Engineers, 2007, pp. 1159–1170.
- [22] V. De Bellis, S. Marelli, F. Bozza, and M. Capobianco, "1d simulation and experimental analysis of a turbocharger turbine for automotive engines under steady and unsteady flow conditions," *Energy Procedia*, vol. 45, pp. 909–918, 2014.
- [23] M. Padzillah, S. Rajoo, and R. Martinez-Botas, "Influence of speed and frequency towards the automotive turbocharger turbine performance under pulsating flow conditions," *Energy Conversion and Management*, vol. 80, pp. 416–428, 2014.
- [24] A. Binder, W. Forster, H. Kruse, and H. Rogge, "An experimental investigation into the effect of wakes on the unsteady turbine rotor flow," *Journal of Engineering for Gas Turbines and Power*, vol. 107, no. 2, pp. 458–465, 1985.
- [25] N. Arndt, "Blade row interaction in a multistage low-pressure turbine," in *ASME 1991 International Gas Turbine and Aeroengine Congress and Exposition*. American Society of Mechanical Engineers, 1991, pp. V001T01A091–V001T01A091.
- [26] M. B. Giles, "Calculation of unsteady wake/rotor interaction," *Journal of Propulsion and Power*, vol. 4, no. 4, pp. 356–362, 1988.

- [27] V. P. Chaluvadi, A. Kalfas, M. Baniaghbal, H. Hodson, and J. Denton, "Blade-row interaction in a high-pressure turbine," *Journal of Propulsion and Power*, vol. 17, no. 4, pp. 892–901, 2001.
- [28] R. W. Moss, R. W. Ainsworth, and T. Garside, "Effects of rotation on blade surface heat transfer: An experimental investigation," in *ASME 1997 International Gas Turbine and Aeroengine Congress and Exhibition*. American Society of Mechanical Engineers, 1997, pp. V003T09A034–V003T09A034.
- [29] J. Braun, B. H. Saracoglu, and G. Paniagua, "Unsteady performance of rotating detonation engines with different exhaust nozzles," *Journal of Propulsion and Power*, pp. 121–130, 2016.
- [30] G. Paniagua, M. Iorio, N. Vinha, and J. Sousa, "Design and analysis of pioneering high supersonic axial turbines," *International Journal of Mechanical Sciences*, vol. 89, pp. 65–77, 2014.
- [31] A. Grönman, T. Turunen-Saaresti, A. Jaatinen, and J. Backman, "Numerical modelling of a supersonic axial turbine stator," *Journal of Thermal Science*, vol. 19, no. 3, pp. 211–217, 2010.
- [32] J. Sousa, G. Paniagua, and J. Saavedra, "Aerodynamic response of internal passages to pulsating inlet supersonic conditions," *Computers & Fluids*, vol. 149, pp. 31–40, 2017.
- [33] A. T. Hasan, "Characteristics of overexpanded nozzle flows in imposed oscillating condition," *International Journal of Heat and Fluid Flow*, vol. 46, pp. 70–83, 2014.
- [34] J. Braun, J. Saavedra Garcia, and G. Paniagua, "Evaluation of the unsteadiness across nozzles downstream of rotating detonation combustors," in *55th AIAA Aerospace Sciences Meeting*, 2017, p. 1063.
- [35] N. Rott, "Theory of time-dependent laminar flows," p. 421, 1964.
- [36] F. K. Moore, "Unsteady laminar boundary-layer flow," National Aeronautics and Space Administration, Washington, DC, Tech. Rep., 1951.
- [37] J. Schetz and S. K. Oh, "Approximate analysis of transient laminar boundary-layer development," *Journal of Heat Transfer*, vol. 90, no. 4, pp. 452–456, 1968.
- [38] H. Mirels, "The wall boundary layer behind a moving shock wave," in *Grenzschichtforschung/Boundary Layer Research*. Springer, 1958, pp. 283–293.
- [39] M. Holden, "Shock wave-turbulent boundary layer interaction in hypersonic flow," in *15th Aerospace Sciences Meeting*, 1972, p. 45.
- [40] S.-H. Lam and L. Crocco, *Shock induced unsteady laminar compressible boundary layers on a semi-infinite flat plate*. Princeton University, 1958.
- [41] J. Horlock and R. Evans, "The momentum-integral equation for a boundary layer with turbulence or ordered unsteadiness in the free stream," *Journal of Fluids Engineering*, vol. 97, no. 1, pp. 126–129, 1975.

- [42] E. Toubert and N. D. Sandham, “Low-order stochastic modelling of low-frequency motions in reflected shock-wave/boundary-layer interactions,” *Journal of Fluid Mechanics*, vol. 671, pp. 417–465, 2011.
- [43] J. Saavedra, G. Paniagua, and S. Lavagnoli, “On the transient response of the turbulent boundary layer inception in compressible flows,” *Journal of Fluid Mechanics*, vol. 850, pp. 1117–1141, 2018.
- [44] S. Uchida, “The pulsating viscous flow superposed on the steady laminar motion of incompressible fluid in a circular pipe,” *Zeitschrift für angewandte Mathematik und Physik ZAMP*, vol. 7, no. 5, pp. 403–422, 1956.
- [45] T. Mizushima, T. MARUYAMA, and Y. Shiozaki, “Pulsating turbulent flow in a tube,” *Journal of Chemical Engineering of Japan*, vol. 6, no. 6, pp. 487–494, 1974.
- [46] L. Shemer, I. Wygnanski, and E. Kit, “Pulsating flow in a pipe,” *Journal of Fluid Mechanics*, vol. 153, pp. 313–337, 1985.
- [47] T. Moschandrea and M. Zamir, “Heat transfer in a tube with pulsating flow and constant heat flux,” *International journal of heat and mass transfer*, vol. 40, no. 10, pp. 2461–2466, 1997.
- [48] J. Saavedra, S. Lavagnoli, and G. Paniagua, “Implications of boundary layer establishment on convective heat transfer experiments,” in *53rd AIAA Aerospace Sciences Meeting*, 2015, p. 0258.
- [49] O. Reynolds, “On the dynamical theory of incompressible viscous fluids and the determination of the criterion,” *Philosophical Transactions of the Royal Society of London. A*, vol. 186, pp. 123–164, 1895.
- [50] I. B. Celik, U. Ghia, P. J. Roache *et al.*, “Procedure for estimation and reporting of uncertainty due to discretization in {CFD} applications,” *Journal of fluids {Engineering-Transactions} of the {ASME}*, vol. 130, no. 7, 2008.
- [51] F. Menter, R. Langtry, and S. Völker, “Transition modelling for general purpose cfd codes,” *Flow, turbulence and combustion*, vol. 77, no. 1-4, pp. 277–303, 2006.
- [52] R. B. Langtry and F. R. Menter, “Correlation-based transition modeling for unstructured parallelized computational fluid dynamics codes,” *AIAA journal*, vol. 47, no. 12, pp. 2894–2906, 2009.
- [53] F. Menter, “Zonal two equation kw turbulence models for aerodynamic flows,” in *23rd fluid dynamics, plasmadynamics, and lasers conference*, 1993, p. 2906.
- [54] F. R. Menter, “Two-equation eddy-viscosity turbulence models for engineering applications,” *AIAA journal*, vol. 32, no. 8, pp. 1598–1605, 1994.
- [55] G. Palau Salvador and S. Frankel, “Numerical modeling of cavitation using fluent: validation and parametric studies,” in *34th AIAA Fluid Dynamics Conference and Exhibit*, 2004, p. 2642.
- [56] J. Badra, A. Masri, M. Freeman, and M. Fitch, “Enhanced heat transfer from arrays of jets impinging on plates,” in *16th Australasian Fluid Mechanics Conference (AFMC)*. School of Engineering, The University of Queensland, 2007, pp. 1187–1192.

- [57] J. Boussinesq, “Essa sur latheories des eaux courantes. memoires presentes par divers savants a lacademic des sciences de l’institut national de france,” *Tome XXIII*, no. 1, 1877.
- [58] F. G. Schmitt, “About boussinesq’s turbulent viscosity hypothesis: historical remarks and a direct evaluation of its validity,” *Comptes Rendus Mécanique*, vol. 335, no. 9-10, pp. 617–627, 2007.
- [59] W. L. M. Nyborg, “Acoustic streaming,” in *Physical acoustics*. Elsevier, 1965, vol. 2, pp. 265–331.
- [60] J. Lighthill and M. Lighthill, *Waves in fluids*. Cambridge university press, 2001.
- [61] B. Baldwin and T. Barth, “A one-equation turbulence transport model for high reynolds number wall-bounded flows,” in *29th Aerospace Sciences Meeting*, 1991, p. 610.
- [62] P. Spalart and S. Allmaras, “A one-equation turbulence model for aerodynamic flows,” in *30th aerospace sciences meeting and exhibit*, 1992, p. 439.
- [63] B. E. Launder and B. Sharma, “Application of the energy-dissipation model of turbulence to the calculation of flow near a spinning disc,” *Letters in heat and mass transfer*, vol. 1, no. 2, pp. 131–137, 1974.
- [64] D. C. Wilcox *et al.*, *Turbulence modeling for CFD*. DCW industries La Canada, CA, 1998, vol. 2.
- [65] J. Clark and E. Grover, “Assessing convergence in predictions of periodic-unsteady flowfields,” *Journal of Turbomachinery*, vol. 129, no. 4, pp. 740–749, 2007.
- [66] B. E. Launder and W. P. Jones, *On the prediction of laminarisation*. HM Stationery Office, 1969.
- [67] P. R. Spalart, “Numerical simulation of boundary layers. part 3: Turbulence and relaminarization in sink flows,” National Advisory Committee for Aeronautics. Lewis Flight Propulsion Lab.; Cleveland, OH, United States, Tech. Rep., 1986.
- [68] R. Narasimha and K. Sreenivasan, “Relaminarization in highly accelerated turbulent boundary layers,” *Journal of Fluid Mechanics*, vol. 61, no. 3, pp. 417–447, 1973.
- [69] H. Blasius, “Nthe boundary layers in fluids with little friction,” National Advisory Committee for Aeronautics. Lewis Flight Propulsion Lab.; Cleveland, OH, United States, Tech. Rep., 1950.
- [70] P. Bader, M. Pschernig, W. Sanz, J. Woisetschläger, F. Heitmeir, W. Meile, and G. Brenn, “Flat-plate boundary layers in accelerated flow,” in *ASME Turbo Expo 2016: Turbomachinery Technical Conference and Exposition*. American Society of Mechanical Engineers, 2016, pp. V02BT38A003–V02BT38A003.
- [71] J. Poggie, N. J. Bisek, and R. Gosse, “Resolution effects in compressible, turbulent boundary layer simulations,” *Computers & Fluids*, vol. 120, pp. 57–69, 2015.

- [72] J. Poggie and T. Leger, “Large-scale unsteadiness in a compressible, turbulent reattaching shear layer,” *Experiments in Fluids*, vol. 56, no. 11, p. 205, 2015.
- [73] D. S. Ebert, F. K. Musgrave, D. Peachey, K. Perlin, and S. Worley, *Texturing & modeling: a procedural approach*. Morgan Kaufmann, 2003.
- [74] N. Mullenix, D. Gaitonde, and M. Visbal, “A plasma-actuator-based method to generate a supersonic turbulent boundary layer inflow condition for numerical simulations,” in *20th AIAA Computational Fluid Dynamics Conference*, 2011, p. 3556.
- [75] N. J. Bisek, D. P. Rizzetta, and J. Poggie, “Plasma control of a turbulent shock boundary-layer interaction,” *AIAA journal*, vol. 51, no. 8, pp. 1789–1804, 2013.
- [76] F. M. White and I. Corfield, *Viscous fluid flow*. McGraw-Hill New York, 2006, vol. 3.
- [77] M. Elena and J.-P. Lacharme, “Experimental study of a supersonic turbulent boundary layer using a laser doppler anemometer,” *Journal de mécanique théorique et appliquée*, vol. 7, no. 2, pp. 175–190, 1988.
- [78] A. E. Alving, “Boundary layer relaxation from convex curvature,” *Ph.D. Thesis Princeton Univ.*, 1988.
- [79] W. Konrad, “A three-dimensional supersonic turbulent boundary layer generated by an isentropic compression,” *Ph. D. Thesis, Princeton University*, 1993.
- [80] I. Marusic, P. Brandner, and B. Pearce, “The logarithmic region of wall turbulence: universality, structure and interactions,” in *Proceedings of 18th Australasian Fluid Mechanics Conference, 3rd–7th December*, 2012.
- [81] I. Marusic, J. P. Monty, M. Hultmark, and A. J. Smits, “On the logarithmic region in wall turbulence,” *Journal of Fluid Mechanics*, vol. 716, 2013.
- [82] L. Rayleigh, “Lxxxii. on the motion of solid bodies through viscous liquid,” *The London, Edinburgh, and Dublin Philosophical Magazine and Journal of Science*, vol. 21, no. 126, pp. 697–711, 1911.
- [83] L. Howarth, “Rayleigh’s problem for a semi-infinite plate,” in *Mathematical Proceedings of the Cambridge Philosophical Society*, vol. 46, no. 1. Cambridge University Press, 1950, pp. 127–140.
- [84] T. V. Karman, “Turbulence and skin friction,” *Journal of the Aeronautical Sciences*, vol. 1, no. 1, pp. 1–20, 1934.
- [85] W. Tollmien, H. Schlichting, H. Görtler, and F. Riegels, “Bericht über untersuchungen zur ausgebildeten turbulenz,” in *Ludwig Prandtl Gesammelte Abhandlungen*. Springer, 1961, pp. 714–718.
- [86] R. G. Bradley, “Approximate solutions for compressible turbulent boundary layers in three-dimensional flow,” *AIAA Journal*, vol. 6, no. 5, pp. 859–864, 1968.

- [87] J. P. Bons, R. Sondergaard, and R. B. Rivir, "The fluid dynamics of lpt blade separation control using pulsed jets," in *ASME Turbo Expo 2001: Power for Land, Sea, and Air*. American Society of Mechanical Engineers, 2001, pp. V003T01A064–V003T01A064.
- [88] C. Goldberg, D. Nalianda, P. Pilidis, D. MacManus, and J. Felder, "Installed performance assessment of a boundary layer ingesting distributed propulsion system at design point," in *52nd AIAA/SAE/ASEE Joint Propulsion Conference*, 2016, p. 4800.
- [89] O. Sharma, G. Pickett, and R. Ni, "Assessment of unsteady flows in turbines," in *ASME 1990 International Gas Turbine and Aeroengine Congress and Exposition*. American Society of Mechanical Engineers, 1990, pp. V005T16A007–V005T16A007.
- [90] H. S. Hura, J. Joseph, and D. E. Halstead, "Reynolds number effects in a low pressure turbine," in *ASME Turbo Expo 2012: Turbine Technical Conference and Exposition*. American Society of Mechanical Engineers, 2012, pp. 1121–1130.
- [91] M. Gad-el Hak, "Modern developments in flow control," *Applied Mechanics Reviews*, vol. 49, no. 7, pp. 365–379, 1996.
- [92] A. R. Byerley, O. Strmer, J. W. Baughn, T. W. Simon, K. W. Van Treuren, and J. List, "Using gurney flaps to control laminar separation on linear cascade blades," in *ASME Turbo Expo 2002: Power for Land, Sea, and Air*. American Society of Mechanical Engineers, 2002, pp. 1191–1199.
- [93] J. Lake, P. King, and R. Rivir, "Reduction of separation losses on a turbine blade with low reynolds numbers," in *37th Aerospace Sciences Meeting and Exhibit*, 1999, p. 242.
- [94] R. J. Volino, "Separation control on low-pressure turbine airfoils using synthetic vortex generator jets," in *ASME Turbo Expo 2003, collocated with the 2003 International Joint Power Generation Conference*. American Society of Mechanical Engineers, 2003, pp. 845–859.
- [95] D. Greenblatt and I. J. Wygnanski, "The control of flow separation by periodic excitation," *Progress in aerospace Sciences*, vol. 36, no. 7, pp. 487–545, 2000.
- [96] L. Hultgren and D. Ashpis, "Demonstration of separation delay with glow discharge plasma actuators," in *41st Aerospace Sciences Meeting and Exhibit*, 2003, p. 1025.
- [97] J. Poggie, "Dc glow discharges: a computational study for flow control applications," in *36th AIAA Plasmadynamics and Lasers Conference*, 2005, p. 5303.
- [98] S. Roy and D. Gaitonde, "Multidimensional collisional dielectric barrier discharge for flow separation control at atmospheric pressures," in *35th AIAA Fluid Dynamics Conference and Exhibit*, 2005, p. 4631.
- [99] E. Moreau, "Airflow control by non-thermal plasma actuators," *Journal of physics D: applied physics*, vol. 40, no. 3, p. 605, 2007.

- [100] J. Huang, T. C. Corke, and F. O. Thomas, “Unsteady plasma actuators for separation control of low-pressure turbine blades,” *AIAA journal*, vol. 44, no. 7, pp. 1477–1487, 2006.
- [101] B. Göksel, D. Greenblatt, I. Rechenberg, Y. Singh, C. Nayeri, and C. Paschereit, “Pulsed plasma actuators for separation flow control,” *momentum*, vol. 10, p. 11, 2006.
- [102] C. Porter, T. McLaughlin, C. Enloe, G. Font, J. Roney, and J. Baughn, “Boundary layer control using a dbd plasma actuator,” in *45th AIAA Aerospace Sciences Meeting and Exhibit*, 2007, p. 786.
- [103] M. L. Post and T. C. Corke, “Separation control on high angle of attack airfoil using plasma actuators,” *AIAA journal*, vol. 42, no. 11, pp. 2177–2184, 2004.
- [104] D. Gaitonde, M. Visbal, and S. Roy, “Control of flow past a wing section with plasma-based body forces,” in *36th AIAA Plasmadynamics and lasers conference*, 2005, p. 5302.
- [105] C. Rethmel, J. Little, K. Takashima, A. Sinha, I. Adamovich, and M. Samimy, “Flow separation control over an airfoil with nanosecond pulse driven dbd plasma actuators,” in *49th AIAA Aerospace Sciences Meeting including the New Horizons Forum and Aerospace Exposition*, 2011, p. 487.
- [106] R. Sondergaard, R. B. Rivir, and J. P. Bons, “Control of low-pressure turbine separation using vortex-generator jets,” *Journal of propulsion and power*, vol. 18, no. 4, pp. 889–895, 2002.
- [107] M. T. Schobeiri, B. Ozturk, and D. E. Ashpis, “On the physics of the flow separation along a low pressure turbine blade under unsteady flow conditions,” in *ASME Turbo Expo 2003, collocated with the 2003 International Joint Power Generation Conference*. American Society of Mechanical Engineers, 2003, pp. 1063–1079.
- [108] J. Wissink, “Dns of separating, low reynolds number flow in a turbine cascade with incoming wakes,” *International Journal of Heat and Fluid Flow*, vol. 24, no. 4, pp. 626–635, 2003.
- [109] A. Seifert and L. G. Pack, “Active flow separation control on wall-mounted hump at high reynolds numbers,” *AIAA journal*, vol. 40, no. 7, pp. 1363–1372, 2002.
- [110] C. He, T. Corke, and M. Patel, “Numerical and experimental analysis of plasma flow control over a hump model,” in *45th AIAA Aerospace Sciences Meeting and Exhibit*, 2007, p. 935.
- [111] E. Pescini, F. Marra, M. De Giorgi, L. Francioso, and A. Ficarella, “Investigation of the boundary layer characteristics for assessing the dbd plasma actuator control of the separated flow at low reynolds numbers,” *Experimental Thermal and Fluid Science*, vol. 81, pp. 482–498, 2017.
- [112] D. Martínez, E. Pescini, F. Marra, M. De Giorgi, and A. Ficarella, “Analysis of the performance of plasma actuators under low-pressure turbine conditions based on experiments and urans simulations,” in *ASME Turbo Expo 2017: Turbomachinery Technical Conference and Exposition*. American Society of Mechanical Engineers, 2017, pp. V02AT40A034–V02AT40A034.

- [113] L. Kaiktsis, G. E. Karniadakis, and S. A. Orszag, "Onset of three-dimensionality, equilibria, and early transition in flow over a backward-facing step," *Journal of Fluid Mechanics*, vol. 231, pp. 501–528, 1991.
- [114] D. Barkley, M. G. M. Gomes, and R. D. Henderson, "Three-dimensional instability in flow over a backward-facing step," *Journal of Fluid Mechanics*, vol. 473, pp. 167–190, 2002.
- [115] V. Michelassi, J. Wissink, J. Fr-Ograve, hlich, and W. Rodi, "Large-eddy simulation of flow around low-pressure turbine blade with incoming wakes," *AIAA journal*, vol. 41, no. 11, pp. 2143–2156, 2003.
- [116] E. Curtis, H. Hodson, M. Banieghbal, J. Denton, R. Howell, and N. Harvey, "Development of blade profiles for low-pressure turbine applications," *Journal of Turbomachinery*, vol. 119, no. 3, pp. 531–538, 1997.
- [117] R. Howell, O. Ramesh, H. Hodson, N. Harvey, and V. Schulte, "High lift and aft loaded profiles for low pressure turbines," in *ASME Turbo Expo 2000: Power for Land, Sea, and Air*. American Society of Mechanical Engineers, 2000, pp. V003T01A066–V003T01A066.
- [118] D. S. Dolling, "Fifty years of shock-wave/boundary-layer interaction research: what next?" *AIAA journal*, vol. 39, no. 8, pp. 1517–1531, 2001.
- [119] B. Ganapathisubramani, N. Clemens, and D. Dolling, "Effects of upstream boundary layer on the unsteadiness of shock-induced separation," *Journal of Fluid Mechanics*, vol. 585, pp. 369–394, 2007.
- [120] J.-P. Dussauge, P. Dupont, and J.-F. Debiève, "Unsteadiness in shock wave boundary layer interactions with separation," *Aerospace Science and Technology*, vol. 10, no. 2, pp. 85–91, 2006.
- [121] M. Schobeiri and B. Ozturk, "Experimental study of the effect of periodic unsteady wake flow on boundary layer development, separation, and re-attachment along the surface of a low pressure turbine blade," in *ASME Turbo Expo 2004: Power for Land, Sea, and Air*. American Society of Mechanical Engineers, 2004, pp. 247–265.
- [122] J. P. Johnston and M. Nishi, "Vortex generator jets-means for flow separation control," *AIAA journal*, vol. 28, no. 6, pp. 989–994, 1990.
- [123] A. M. Kuethe, "Boundary layer control of flow separation and heat exchange," May 11 1971, uS Patent 3,578,264.
- [124] K.-B. Chun and H. J. Sung, "Control of turbulent separated flow over a backward-facing step by local forcing," *Experiments in fluids*, vol. 21, no. 6, pp. 417–426, 1996.
- [125] S. Jovic and D. Driver, "Reynolds number effect on the skin friction in separated flows behind a backward-facing step," *Experiments in Fluids*, vol. 18, no. 6, pp. 464–467, 1995.
- [126] K. Abe, T. Kondoh, and Y. Nagano, "A new turbulence model for predicting fluid flow and heat transfer in separating and reattaching flowsi. flow field calculations," *International journal of heat and mass transfer*, vol. 37, no. 1, pp. 139–151, 1994.

- [127] A. Dejoan and M. Leschziner, “Large eddy simulation of periodically perturbed separated flow over a backward-facing step,” *International Journal of Heat and Fluid Flow*, vol. 25, no. 4, pp. 581–592, 2004.
- [128] J. Kim, S. Kline, and J. Johnston, “Investigation of a reattaching turbulent shear layer: flow over a backward-facing step,” *Journal of Fluids Engineering*, vol. 102, no. 3, pp. 302–308, 1980.
- [129] G. Biswas, M. Breuer, and F. Durst, “Backward-facing step flows for various expansion ratios at low and moderate reynolds numbers,” *Journal of fluids engineering*, vol. 126, no. 3, pp. 362–374, 2004.
- [130] L. Kaiktsis, G. E. Karniadakis, and S. A. Orszag, “Unsteadiness and convective instabilities in two-dimensional flow over a backward-facing step,” *Journal of Fluid Mechanics*, vol. 321, pp. 157–187, 1996.
- [131] J. Vogel and J. Eaton, “Combined heat transfer and fluid dynamic measurements downstream of a backward-facing step,” *Journal of heat transfer*, vol. 107, no. 4, pp. 922–929, 1985.
- [132] M. Germano, U. Piomelli, P. Moin, and W. H. Cabot, “A dynamic subgrid-scale eddy viscosity model,” *Physics of Fluids A: Fluid Dynamics*, vol. 3, no. 7, pp. 1760–1765, 1991.
- [133] D. K. Lilly, “A proposed modification of the germano subgrid-scale closure method,” *Physics of Fluids A: Fluid Dynamics*, vol. 4, no. 3, pp. 633–635, 1992.
- [134] J. Hinze, “0. 1975 turbulence,” 1976.
- [135] G. Erlebacher, M. Y. Hussaini, C. G. Speziale, and T. A. Zang, “Toward the large-eddy simulation of compressible turbulent flows,” *Journal of fluid mechanics*, vol. 238, pp. 155–185, 1992.
- [136] J. Smagorinsky, “General circulation experiments with the primitive equations: I. the basic experiment,” *Monthly weather review*, vol. 91, no. 3, pp. 99–164, 1963.
- [137] W.-W. Kim, S. Menon, W.-W. Kim, and S. Menon, “Application of the localized dynamic subgrid-scale model to turbulent wall-bounded flows,” in *35th aerospace sciences meeting and exhibit*, 1997, p. 210.
- [138] S.-E. Kim *et al.*, “Large eddy simulation using unstructured meshes and dynamic subgrid-scale turbulence models,” *AIAA paper*, vol. 2548, p. 2004, 2004.
- [139] H. Choi and P. Moin, “Grid-point requirements for large eddy simulation: Chappans estimates revisited,” *Physics of fluids*, vol. 24, no. 1, p. 011702, 2012.
- [140] D. R. Chapman, “Computational aerodynamics development and outlook,” *AIAA journal*, vol. 17, no. 12, pp. 1293–1313, 1979.
- [141] K. Chana, D. Cardwell, and T. Jones, “A review of the oxford turbine research facility,” in *ASME Turbo Expo 2013: Turbine Technical Conference and Exposition*. American Society of Mechanical Engineers, 2013, pp. V03CT14A026–V03CT14A026.

- [142] M. Dunn and R. Mathison, "History of short-duration measurement programs related to gas turbine heat transfer, aerodynamics, and aeroperformance at calspan and the ohio state university," *Journal of Turbomachinery*, vol. 136, no. 4, p. 041004, 2014.
- [143] R. J. Anthony and J. P. Clark, "A review of the afrl turbine research facility," in *ASME Turbo Expo 2013: Turbine Technical Conference and Exposition*. American Society of Mechanical Engineers, 2013, pp. V03CT14A010–V03CT14A010.
- [144] A. Pope and K. L. Goin, *High-speed wind tunnel testing*. Wiley, 1965.
- [145] A. Epstein, G. Guenette, and R. Norton, "The mit blowdown turbine facility," in *ASME 1984 International Gas Turbine Conference and Exhibit*. American Society of Mechanical Engineers, 1984, pp. V004T09A011–V004T09A011.
- [146] R. Ainsworth, D. Schultz, M. Davies, C. Forth, M. Hilditch, M. Oldfield, and A. Sheard, "A transient flow facility for the study of the thermofluid-dynamics of a full stage turbine under engine representative conditions," in *ASME 1988 International Gas Turbine and Aeroengine Congress and Exposition*. American Society of Mechanical Engineers, 1988, pp. V004T09A022–V004T09A022.
- [147] I. BECKWITH, F.-J. Chen, and T. CREEL, JR, "Design requirements for the nasa langley supersonic low-disturbance wind tunnel," in *14th Aerodynamic Testing Conference*, 1986, p. 763.
- [148] K. Casper, S. Beresh, J. Henfling, R. Spillers, B. Pruett, and S. Schneider, "Hypersonic wind-tunnel measurements of boundary-layer pressure fluctuations," in *39th AIAA Fluid Dynamics Conference*, 2009, p. 4054.
- [149] G. Paniagua, D. Cuadrado, J. Saavedra, V. Andreoli, T. Meyer, J. P. Solano, R. Herrero, S. Meyer, and D. Lawrence, "Design of the purdue experimental turbine aerothermal laboratory for optical and surface aerothermal measurements," *Journal of Engineering for Gas Turbines and Power*, vol. 141, no. 1, p. 012601, 2019.
- [150] R. D. Marshall, *Performance requirements and preliminary design of a boundary layer wind tunnel facility*. US Department of Commerce, National Bureau of Standards, 1985.
- [151] M. Boyle, "Low speed wind tunnel testing," in *Semiconductor Thermal and Temperature Measurement Symposium, 1988. SEMI-THERM IV., Fourth Annual IEEE*. IEEE, 1988, pp. 31–39.
- [152] L. Cattafesta, C. Bahr, and J. Mathew, "Fundamentals of wind-tunnel design," *Encyclopedia of Aerospace Engineering*, pp. 1–10, 2010.
- [153] J. Lukasiewicz, "Some problems in design and operation of blowdown wind tunnels," *Zeitschrift für angewandte Mathematik und Physik ZAMP*, vol. 9, no. 5-6, pp. 422–437, 1958.
- [154] H. Nagib, A. Marion, and J. Tan-Atichat, "On the design of contractions and settling chambers for optimal turbulence manipulations in wind tunnels," in *22nd Aerospace Sciences Meeting*, 1984, p. 536.

- [155] H.-S. Tsien, "On the design of the contraction cone for a wind tunnel," *Journal of the Aeronautical Sciences*, vol. 10, no. 2, pp. 68–70, 1943.
- [156] J. H. Watmuff, "Wind tunnel contraction design," in *9th Australasian Fluid Mechanics Conference*, 1987, pp. 472–475.
- [157] J. Sargison, G. Walker, and R. Rossi, "Design and calibration of a wind tunnel with a two dimensional contraction," in *15th Australasian Fluid Mechanics Conference*. University of Tasmania, 2004.
- [158] Y.-x. Su, "Flow analysis and design of three-dimensional wind tunnel contractions," *AIAA journal*, vol. 29, no. 11, pp. 1912–1920, 1991.
- [159] V. Andreoli, S. Lavagnoli, G. Paniagua, and V. F. Villace, "Robust model of a transient wind tunnel for off-design aerothermal testing of turbomachinery," *Measurement*, vol. 82, pp. 323–333, 2016.
- [160] H. L. Dryden, "Reduction of turbulence in wind tunnels," National Bureau of Standards; Washington, DC, United States, Tech. Rep., 1931.
- [161] R. D. Mehta and P. Bradshaw, "Design rules for small low speed wind tunnels," *The Aeronautical Journal*, vol. 83, no. 827, pp. 443–453, 1979.
- [162] R. Loehrke and H. Nagib, "Control of free-stream turbulence by means of honeycombs: a balance between suppression and generation," *Journal of Fluids Engineering*, vol. 98, no. 3, pp. 342–351, 1976.
- [163] R. Loehrke and H. M. Nagib, "Experiments on management of free-stream turbulence," Illinois Institute of Technology, Chicago, Tech. Rep., 1972.
- [164] E. Laws and J. Livesey, "Flow through screens," *Annual Review of Fluid Mechanics*, vol. 10, no. 1, pp. 247–266, 1978.
- [165] J. H. Bell and R. D. Mehta, "Contraction design for small low-speed wind tunnels," *NASA TN*, 1988.
- [166] J. Scheiman, "Considerations for the installation of honeycomb and screens to reduce wind-tunnel turbulence," *NASA TM*, 1981.
- [167] J. H. Watmuff, "Detrimental effects of almost immeasurably small freestream nonuniformities generated by wind-tunnel screens," *AIAA journal*, vol. 36, no. 3, pp. 379–386, 1998.
- [168] G. B. Schubauer, W. G. Spangenberg, and P. Klebanoff, "Aerodynamic characteristics of damping screens," *NACA TN*, 1950.
- [169] T. Morel, "Comprehensive design of axisymmetric wind tunnel contractions," *Journal of Fluids Engineering*, vol. 97, no. 2, pp. 225–233, 1975.
- [170] G. Derbunovich, A. Zemskaya, E. Repik, and Y. P. Sosedko, "Effect of flow contraction on the level of turbulence," *Fluid Dynamics*, vol. 22, no. 2, pp. 289–294, 1987.

- [171] H. Bottini, G. Paniagua, P. Schreivogel, A. Sonda, and S. de las Heras, "Design and qualification of a supersonic wind tunnel for induced boundary layer transition research," *Proceedings of the Institution of Mechanical Engineers, Part G: Journal of Aerospace Engineering*, vol. 229, no. 3, pp. 562–578, 2015.
- [172] J. R. Scott and J. M. Abbott, "Inlets, ducts, and nozzles," in *In its Aeropropulsion 1991 27 p (SEE N91-20086 12-07)*, 1991.
- [173] F. R. Menter, M. Kuntz, and R. Langtry, "Ten years of industrial experience with the sst turbulence model," *Turbulence, heat and mass transfer*, vol. 4, no. 1, pp. 625–632, 2003.
- [174] M. Mikhail, "Optimum design of wind tunnel contractions," *AIAA journal*, vol. 17, no. 5, pp. 471–477, 1979.
- [175] M. Rhode and R. DeLoach, "Hypersonic wind tunnel calibration using the modern design of experiments," in *41st AIAA/ASME/SAE/ASEE Joint Propulsion Conference & Exhibit*, 2005, p. 4274.
- [176] J. P. Kleijnen, "Kriging metamodeling in simulation: A review," *European journal of operational research*, vol. 192, no. 3, pp. 707–716, 2009.
- [177] A. Chipperfield and P. Fleming, "The matlab genetic algorithm toolbox," *Parallel computing*, 1995.
- [178] R. DeLoach, "Tailoring wind tunnel data volume requirements through the formal design of experiments," in *20th AIAA Advanced Measurement and Ground Testing Technology Conference*, 1998, p. 2884.
- [179] M. Kammeyer, "Wind tunnel facility calibrations and experimental uncertainty," in *20th AIAA Advanced Measurement and Ground Testing Technology Conference*, 1998, p. 2715.
- [180] D. C. Montgomery, *Design and analysis of experiments*. John wiley & sons, 2017.
- [181] H. Babinsky, J. Oorebeek, and T. Cottingham, "Corner effects in reflecting oblique shock-wave/boundary-layer interactions," in *51st AIAA Aerospace Sciences Meeting including the New Horizons Forum and Aerospace Exposition*, 2013, p. 859.
- [182] P. K. Bruce and H. Babinsky, "Experimental study into the flow physics of three-dimensional shock control bumps," *Journal of Aircraft*, vol. 49, no. 5, pp. 1222–1233, 2012.
- [183] J. Eaton and J. Johnston, "A review of research on subsonic turbulent flow reattachment," *AIAA journal*, vol. 19, no. 9, pp. 1093–1100, 1981.
- [184] G. Paniagua, T. Yasa, A. D. La Loma, L. Castillon, and T. Coton, "Unsteady strong shock interactions in a transonic turbine: experimental and numerical analysis," *Journal of Propulsion and Power*, vol. 24, no. 4, pp. 722–731, 2008.
- [185] G. A. Sod, "A numerical study of a converging cylindrical shock," *Journal of Fluid Mechanics*, vol. 83, no. 4, pp. 785–794, 1977.

- [186] J. M. Martí and E. Müller, “The analytical solution of the riemann problem in relativistic hydrodynamics,” *Journal of Fluid Mechanics*, vol. 258, pp. 317–333, 1994.
- [187] G. A. Sod, “A survey of several finite difference methods for systems of nonlinear hyperbolic conservation laws,” *Journal of computational physics*, vol. 27, no. 1, pp. 1–31, 1978.
- [188] E. F. Toro, M. Spruce, and W. Speares, “Restoration of the contact surface in the hll-riemann solver,” *Shock waves*, vol. 4, no. 1, pp. 25–34, 1994.
- [189] T. Saito and K. Takayama, “Numerical simulations of nozzle starting process,” *Shock Waves*, vol. 9, no. 2, pp. 73–79, 1999.
- [190] C. L. Rumsey, “Apparent transition behavior of widely-used turbulence models,” *International Journal of Heat and Fluid Flow*, vol. 28, no. 6, pp. 1460–1471, 2007.
- [191] T. Yasa, G. Paniagua, and R. Dénos, “Application of hot-wire anemometry in a blow-down turbine facility,” *Journal of engineering for gas turbines and power*, vol. 129, no. 2, pp. 420–427, 2007.
- [192] J. Doorly and M. Oldfield, “The theory of advanced multi-layer thin film heat transfer gauges,” *International journal of heat and mass transfer*, vol. 30, no. 6, pp. 1159–1168, 1987.
- [193] —, “New heat transfer gages for use on multilayered substrates,” *Journal of turbomachinery*, vol. 108, no. 1, pp. 153–160, 1986.
- [194] M. Oldfield, “Impulse response processing of transient heat transfer gauge signals,” *Journal of Turbomachinery*, vol. 130, no. 2, p. 021023, 2008.
- [195] V. Iliopoulou, R. Denos, N. Billiard, and T. Arts, “Time-averaged and time-resolved heat flux measurements on a turbine stator blade using two-layered thin-film gauges,” *Journal of turbomachinery*, vol. 126, no. 4, pp. 570–577, 2004.
- [196] D. L. Schultz and T. Jones, “Heat-transfer measurements in short-duration hypersonic facilities.” Advisory Group for Aerospace Research and Development Paris (France), Tech. Rep., 1973.
- [197] N. Billiard, V. Iliopoulou, F. Ferrara, and R. Dénos, “Data reduction and thermal product determination for single and multi-layered substrates thin-film gauges,” *gas*, vol. 10, p. 1, 2002.
- [198] J. Crank and P. Nicolson, “A practical method for numerical evaluation of solutions of partial differential equations of the heat-conduction type,” in *Mathematical Proceedings of the Cambridge Philosophical Society*, vol. 43, no. 1. Cambridge University Press, 1947, pp. 50–67.
- [199] T. L. Bergman, F. P. Incropera, D. P. DeWitt, and A. S. Lavine, *Fundamentals of heat and mass transfer*. John Wiley & Sons, 2011.
- [200] R. J. Moffat, “What’s new in convective heat transfer?” *International Journal of Heat and Fluid Flow*, vol. 19, no. 2, pp. 90–101, 1998.

- [201] O. Popp, D. Smith, J. Bubb, H. Grabowski, T. Diller, J. Schetz, and W. Ng, "Investigation of heat transfer in a film cooled transonic turbine cascade: Part ii unsteady heat transfer," in *ASME Turbo Expo 2000: Power for Land, Sea, and Air*. American Society of Mechanical Engineers, 2000, pp. V003T01A011–V003T01A011.
- [202] S. Lavagnoli, C. De Maesschalck, and G. Paniagua, "Uncertainty analysis of adiabatic wall temperature measurements in turbine experiments," *Applied Thermal Engineering*, vol. 82, pp. 170–181, 2015.
- [203] S. Guo, M. Spencer, G. Lock, T. Jones, and N. Harvey, "The application of thin film gauges on flexible plastic substrates to the gas turbine situation," in *ASME 1995 International Gas Turbine and Aeroengine Congress and Exposition*. American Society of Mechanical Engineers, 1995, pp. V004T09A049–V004T09A049.
- [204] S. J. Thorpe, S. Yoshino, R. W. Ainsworth, and N. W. Harvey, "Improved fast-response heat transfer instrumentation for short-duration wind tunnels," *Measurement Science and Technology*, vol. 15, no. 9, p. 1897, 2004.

APPENDICES

A. FLUENT VALIDATION

A.1 Unsteady strong interactions in a turbine transonic turbine

The accuracy of the numerical results obtained with Fluent was assessed against the experimental data obtained in a transonic turbine stator [184]. The vane of this turbine stage, which blade profile is displayed in Figure A.1, operates at supersonic outlet conditions. Due to the supersonic outlet operation a trailing edge shock system is generated. For this numerical verification the domain was meshed following the same guidelines of the current investigation and the grid independency was carefully assessed. For the entire vane the near wall flow resolution ($y^+ < 0.5$) guaranteed a proper modulation of the viscous sublayer. The periodicity was assessed by setting the top and bottom surface of the domain as periodic translational boundary conditions. The turbulence closure in this simulations was achieved by exploiting the Langtry-Menter 4 equation Transitional SST model.

Figure A.2 left depicts the isentropic Mach number distribution along the suction side (SS) and pressure side (PS) of the stator vane. The adjacent trailing edge shock impingement in the suction side about 0.6 curve length. The Figure 90 right illustrates the Mach number contour, where the right trailing edge shock system is clearly revealed. The comparison of the numerical results with the empirical data depicts an agreement of around 3%.

A.2 Sod Shock Tube Validation

The robustness and accuracy of the numerical scheme was assessed through the Sod Shock Tube problem [185]. The comparison with the theoretical solution [186–189], characterizes the dynamic performance of the solver, which is clearly determine

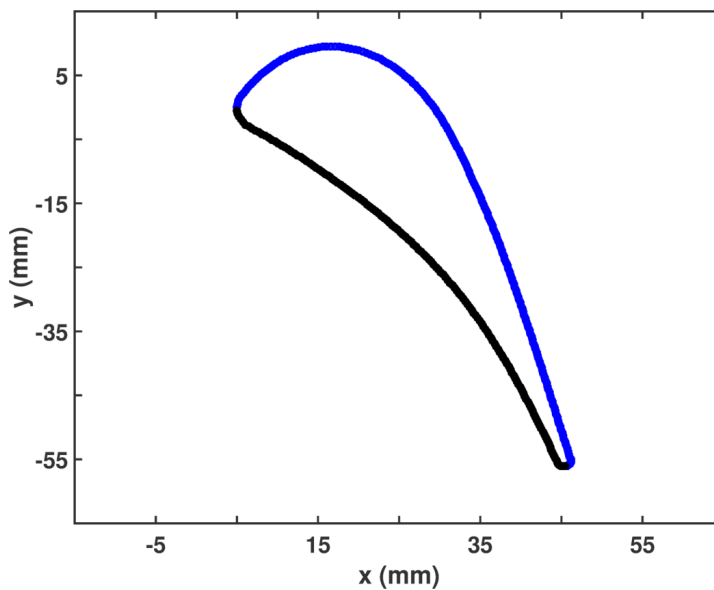


Fig. A.1. Transonic stator geometry for validation

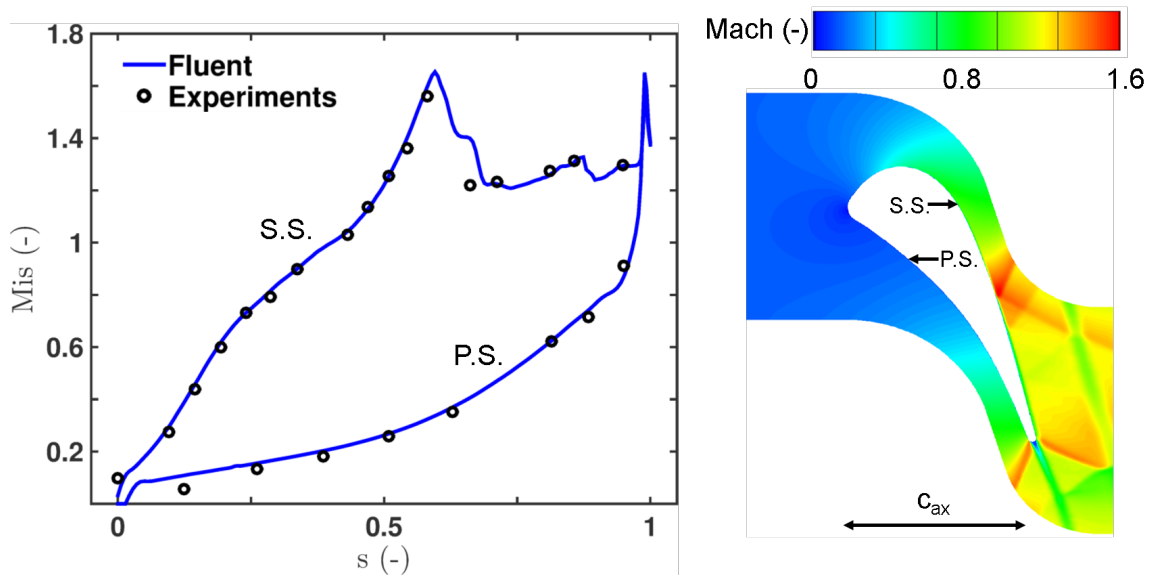


Fig. A.2. Left) Isentropic Mach number distribution along suction and pressure side, current CFD vs. experiments; Right) Mach number contour along the stator passage

by the speed of propagation of the characteristics and the discontinuities settled by their passage. This is a pure 1D numerical analysis where the domain is 1 meter

long. Prior to the test, the left volume contains a high pressure and temperature stagnant fluid. Whereas the right segment contains low pressure and temperature stagnant conditions. Both sections are numerically separated by a solid interface that is burst at $t=0$. Figure A.3 left illustrates the domain conditions 0.01 s after the solid interface removal. Following the burst, the hot, or high pressure segment, exude right running characteristics that increase the pressure of the fluid after its passage, while left running characteristics are emanated from the low pressure section, which reduce the static pressure.

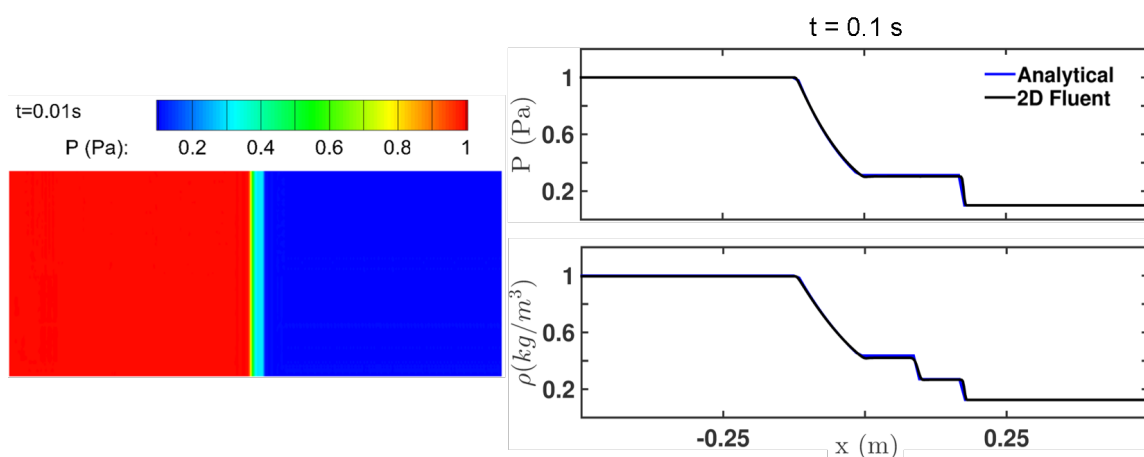


Fig. A.3. Sod Shock tube solution; Left) 2D Pressure contour 10ms after the membrane burst Right) Pressure and density distribution across the domain 100 ms after the membrane burst (Analytical and Current CFD tool)

The Figure A.3 right depicts the pressure and density inside of the domain for both analytic and numerical solution 100 ms after the burst of the isolating membrane. The density evolution clearly represents the location of the right and left running characteristic as well as the contact surface. Based on the comparison of the numerical results with the theoretical conditions an accurate prediction is assessed.

B. DOMAIN NUMERICAL DISCRETIZATION

B.1 Isothermal Flat Plate domain verification

To assess the best domain representation for the performed analysis a comparison between a extended numerical discretization and the current one is performed. Figure B.1 left represents a flat plate where the inlet boundary conditions is set directly upstream of the plate leading edge. Whereas Figure B.1 right depicts a flat plate domain where the inlet boundary conditions are imposed 0.2 m upstream of the plate and the domain extension is modeled by a symmetry plane.

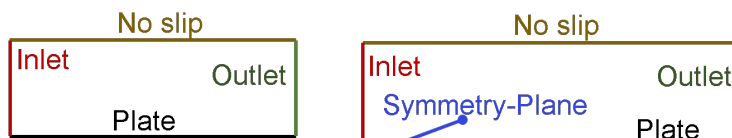


Fig. B.1. Domains to compare for flat plate research, Left) Regular flat plate (inlet at plate LE); Right) Extended inlet making use of symmetry plane

Figure B.2 represents the wall shear stress evolution along both domains for uniform inlet conditions. The results are identical for every axial location further than 0.05m the leading edge plate. For this comparison analysis the turbulence closure was achieved by the k- SST model, hence modeling fully turbulent boundary layer along the plate. However, for the extended domain a transition like wall shear stress distribution is found near plate leading edge. This phenomena has been previously found in the literature and it is known as the apparent transition [190], which occurs for the most extended 2-eqn turbulence closures when detailed axial and normal discretization are used. Based on this results the traditional domain without extension is employed for the current research.

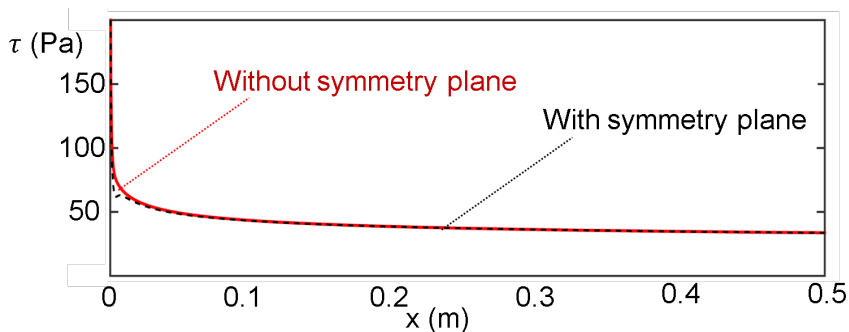


Fig. B.2. Skin friction distribution along the flat plate (Red, regular plate plate, Dashed-black, domain with symmetry plane upstream)

B.2 Isothermal separation domain verification

To guarantee the best domain representation for the performed analysis a comparison between a extended numerical discretization and the current one is performed. Figure B.3 top represents a domain where the inlet boundary conditions is set directly upstream of the smooth hump profile leading edge. Whereas the Figure B.3 bottom depicts a domain where the inlet boundary conditions are imposed 0.2 m upstream of the hump leading edge and the domain extension is modeled by a symmetry plane.

Figure B.4 represents the wall shear stress evolution along both domains for uniform inlet conditions. The results are identical for every axial location further than 0.05m the leading edge of the smooth hump profile. For this comparison analysis the turbulence closure was achieved by the k- SST model. Hence the flow is assume to be fully turbulent along the entire length. However, for the extended domain a transition like wall shear stress distribution is found at the hump leading edge. This phenomena has been previously found in the literature and it is known as the apparent transition [190], which occurs for the most extended 2-eqn turbulence closures when detailed axial and normal discretization are used. Based on this results the traditional domain without extension is employed for the current research.

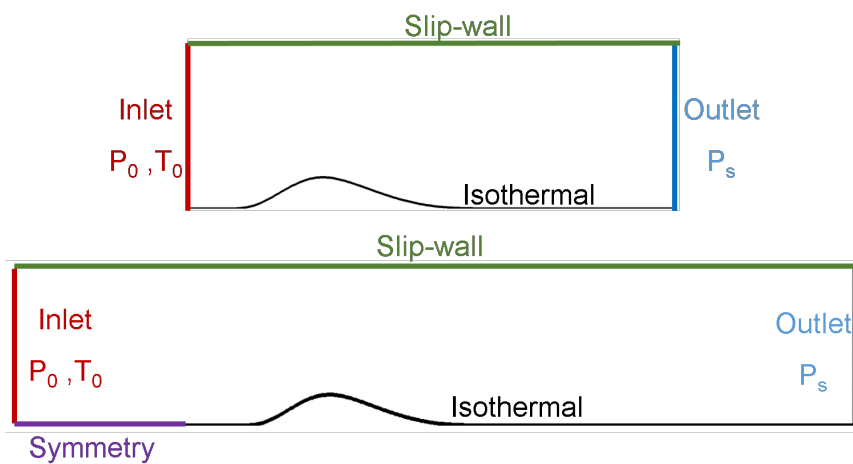


Fig. B.3. Domains to compare for flow separation research, Top) Regular domain (inlet at plate LE); Bottom) Extended inlet making use of symmetry plane

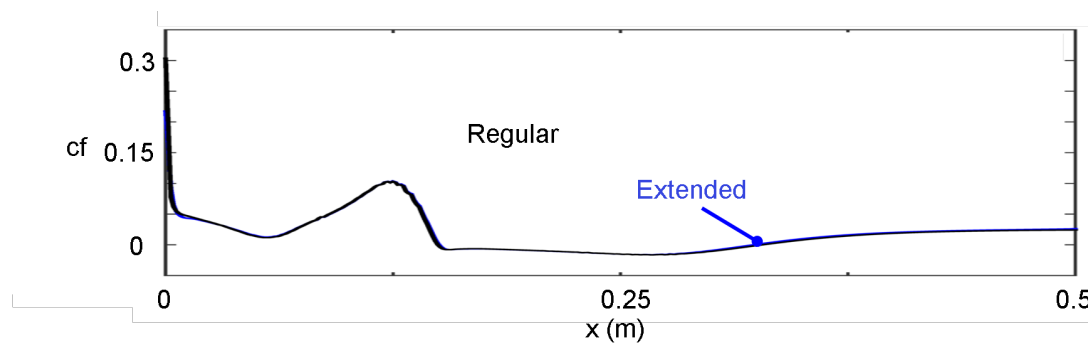


Fig. B.4. Skin friction distribution along the separation domain (Black regular plate, Blue, domain with symmetry plane upstream)

C. MOMENTUM INTEGRAL EQUATIONS REDUCTION

The second term of 2.84 can be integrated by parts

$$\int_0^\delta \left(\rho v \frac{\partial u}{\partial y} \right) dy = [\rho v u]_0^\delta - \int_0^\delta u \frac{\partial \rho v}{\partial y} dy \quad (\text{C.1})$$

Then applying the no slip condition and introducing the continuity equation 2.81

$$\begin{aligned} [\rho v u]_0^\delta - \int_0^\delta u \frac{\partial \rho v}{\partial y} dy &= -u_\delta \int_0^\delta \left(\frac{\partial \rho}{\partial t} \frac{\partial \rho u}{\partial x} + \frac{\partial \rho W}{\partial z} \right) dy + \\ &\int_0^\delta u \left(\frac{\partial \rho}{\partial t} \frac{\partial \rho u}{\partial x} + \frac{\partial \rho W}{\partial z} \right) dy \end{aligned} \quad (\text{C.2})$$

Introducing the new form of the second term of into 2.84 and rearranging

$$\begin{aligned} \int_0^\delta \frac{\partial \rho u}{\partial t} dy - u_\delta \int_0^\delta \frac{\partial \rho}{\partial t} dy + \int_0^\delta u \frac{\partial \rho}{\partial t} dy + \int_0^\delta \rho u \frac{\partial \rho}{\partial x} dy - u_\delta \int_0^\delta \frac{\partial \rho u}{\partial x} dy + \\ \int_0^\delta \frac{\partial \rho u}{\partial x} dy + \int_0^\delta \rho w \frac{\partial u}{\partial z} dy - u_\delta \int_0^\delta \frac{\partial \rho w}{\partial z} dy = - \int_0^\delta \frac{\partial p}{\partial x} dy + \frac{1}{Re} \int_0^\delta \frac{\partial \tau_{xx}}{\partial x} dy + \\ \frac{1}{Re} \int_0^\delta \frac{\partial \tau_{xy}}{\partial y} dy + \frac{1}{Re} \int_0^\delta \frac{\partial \tau_{xz}}{\partial z} dy \end{aligned} \quad (\text{C.3})$$

Some items can be included in the same integral

$$\begin{aligned} \underbrace{\int_0^\delta \frac{\partial \rho u}{\partial t} dy - u_\delta \int_0^\delta \frac{\partial \rho}{\partial t} dy}_I + \underbrace{\int_0^\delta \frac{\partial \rho u}{\partial t} dy - u_\delta \int_0^\delta \frac{\partial \rho u}{\partial x} dy}_II + \\ \underbrace{\int_0^\delta \frac{\partial \rho w u}{\partial z} dy - u_\delta \int_0^\delta \frac{\partial \rho w}{\partial z} dy}_III = - \underbrace{\int_0^\delta \frac{\partial p}{\partial x} dy}_IV + \underbrace{\frac{1}{Re} \int_0^\delta \frac{\partial \tau_{xy}}{\partial y} dy}_V + \\ \underbrace{\frac{1}{Re} \int_0^\delta \frac{\partial \tau_{xx}}{\partial x} dy}_VI + \underbrace{\frac{1}{Re} \int_0^\delta \frac{\partial \tau_{xz}}{\partial z} dy}_VII \end{aligned} \quad (\text{C.4})$$

To simplify the terms in equation C.4 the Leibniz rule is used to commute the integration and derivation operation

$$\frac{\partial}{\partial \alpha} \left(\int_0^\delta f dy \right) = \int_0^\delta \frac{\partial f}{\partial \alpha} dy + f(y = \delta) \frac{\partial \delta}{\partial \alpha} - f(y = 0) \frac{\partial 0}{\partial \alpha} \quad (\text{C.5})$$

Applying the Leibniz's rule to term I

$$\begin{aligned} & \int_0^\delta \frac{\partial \rho u}{\partial t} dy - u_\delta \int_0^\delta \frac{\partial \rho}{\partial t} dy = \\ \frac{\partial}{\partial t} \left(\int_0^\delta \rho u dy \right) - \rho_\delta u_\delta \frac{\partial \delta}{\partial t} - u_\delta \left(\frac{\partial}{\partial t} \left(\int_0^\delta \rho dy \right) - \rho_\delta \frac{\partial \delta}{\partial t} \right) = & \quad (\text{C.6}) \\ & \frac{\partial}{\partial t} \left(\int_0^\delta \rho u dy \right) + u_\delta \frac{\partial}{\partial t} \int_0^\delta \left(\rho dy \right) \end{aligned}$$

The definition of the displacement, momentum, pressure and density integral thicknesses together with the skin friction will be used to further simplify the terms of C.4

$$\delta^* = \int_0^\delta \left(1 - \frac{\rho u}{\rho_\delta u_\delta} \right) dy \quad (\text{C.7})$$

$$\theta = \int_0^\delta \frac{\rho u}{\rho_\delta u_\delta} \left(1 - \frac{u}{u_\delta} \right) dy \quad (\text{C.8})$$

$$\delta_p = \int_0^\delta \left(1 - \frac{p}{p_\delta} \right) dy \quad (\text{C.9})$$

$$\delta_\rho = \int_0^\delta \left(1 - \frac{\rho}{\rho_\delta} \right) dy \quad (\text{C.10})$$

$$c_f = \frac{2\mu_w}{\rho_\delta u_\delta^2 Re} \frac{\partial u}{\partial y} \Big|_w \quad (\text{C.11})$$

Taking advantage of the definition of the displacement thickness the first term of eq. C.6 can be rearranged:

$$\rho_\delta u_\delta \delta^* = \rho_\delta u_\delta \int_0^\delta \left(1 - \frac{\rho u}{\rho_\delta u_\delta} \right) dy = \int_0^\delta \rho_\delta u_\delta \left(1 - \frac{\rho u}{\rho_\delta u_\delta} \right) dy = \rho_\delta u_\delta \delta - \int_0^\delta \rho u dy \quad (\text{C.12})$$

$$\int_0^\delta \rho u dy = \rho_\delta u_\delta \delta - \rho_\delta u_\delta \delta^* \quad (\text{C.13})$$

Similarly, using the definition of the density boundary layer thickness C.10, the second terms of C.6 can be reformulated.

$$\rho_\delta \delta_\rho = \rho_\delta \int_0^\delta \left(1 - \frac{\rho}{\rho_\delta}\right) dy = \int_0^\delta \rho_\delta \left(1 - \frac{\rho}{\rho_\delta}\right) dy = \rho_\delta \delta - \int_0^\delta \rho dy \quad (\text{C.14})$$

$$\int_0^\delta \rho dy = \rho_\delta \delta - \rho_\delta \delta_\rho \quad (\text{C.15})$$

Introducing C.13 and C.15 on C.6 term I becomes:

$$\frac{\partial(\rho_\delta u_\delta \delta - \rho_\delta u_\delta \delta^*)}{\partial t} - u_\delta \frac{\partial(\rho_\delta \delta - \rho_\delta \delta_\rho)}{\partial t} \quad (\text{C.16})$$

$$\frac{\partial(\rho_\delta u_\delta (\delta - \delta^*))}{\partial t} - u_\delta \frac{\partial(\rho_\delta (\delta - \delta_\rho))}{\partial t} \quad (\text{C.17})$$

$$\rho_\delta (\delta - \delta^*) \frac{\partial u_\delta}{\partial t} + u_\delta \frac{\partial(\rho_\delta (\delta_\rho - \delta^*))}{\partial t} \quad (\text{C.18})$$

Using the Leibniz rule on term II:

$$\begin{aligned} \int_0^\delta \frac{\partial \rho u u}{\partial x} dy - u_\delta \int_0^\delta \frac{\partial \rho u}{\partial x} dy &= -u_\delta \frac{\partial}{\partial x} \left(\int_0^\delta \rho u u dy \right) - \rho_\delta u_\delta u_\delta \frac{\partial \delta}{\partial x} \\ -u_\delta \left(\frac{\partial}{\partial x} \left(\int_0^\delta \rho u dy \right) - \rho_\delta u_\delta \frac{\partial \delta}{\partial x} \right) &= \frac{\int_0^\delta \rho u u dy}{\partial x} - u_\delta \frac{\partial \left(\int_0^\delta \rho u dy \right)}{\partial x} \end{aligned} \quad (\text{C.19})$$

Introducing the definition of the momentum thickness and considering that ρ_δ and u_δ are independent of y :

$$\begin{aligned} \rho_\delta u_\delta^2 \theta &= \rho_\delta u_\delta^2 \int_0^\delta \frac{\rho u}{\rho_\delta u_\delta} \left(1 - \frac{u}{u_\delta}\right) dy = \int_0^\delta \rho_\delta u_\delta^2 \frac{\rho u}{\rho_\delta u_\delta} \left(1 - \frac{u}{u_\delta}\right) dy = \\ &= u_\delta \int_0^\delta \rho u dy - \int_0^\delta \rho u u dy = u_\delta (\rho_\delta u_\delta \delta - \rho_\delta u_\delta \delta^*) - \int_0^\delta \rho u u dy = \\ &= \rho_\delta u_\delta^2 (\delta - \delta^*) - \int_0^\delta \rho u u dy \end{aligned} \quad (\text{C.20})$$

$$\int_0^\delta \rho u u dy = \rho_\delta u_\delta^2 (\delta - \delta^*) - \rho_\delta u_\delta^2 \theta \quad (\text{C.21})$$

Then the term II is reduced to:

$$\begin{aligned} & \frac{\partial}{\partial x} \left(\int_0^\delta \rho u u dy \right) - u_\delta \frac{\partial}{\partial t} \left(\int_0^\delta \rho u dy \right) = \\ & \frac{\partial(\rho_\delta u_\delta^2 (\delta - \delta^*) - \rho_\delta u_\delta^2 \theta)}{\partial x} - u_\delta \frac{\partial(\rho_\delta u_\delta \delta - \rho_\delta u_\delta \delta^*)}{\partial x} = \\ & - \frac{\partial(\rho_\delta u_\delta^2 \theta)}{\partial x} - u_\delta \frac{\partial(\rho_\delta u_\delta (\delta - \delta^*))}{\partial x} + \frac{\partial(\rho_\delta u_\delta^2 (\delta - \delta^*))}{\partial x} = \\ & - \frac{\partial(\rho_\delta u_\delta^2 \theta)}{\partial x} - u_\delta (\rho_\delta (\delta - \delta^*)) \frac{\partial u_\delta}{\partial x} - u_\delta^2 \frac{\partial(\rho_\delta (\delta - \delta^*))}{\partial x} + \\ & (\rho_\delta (\delta - \delta^*)) 2u_\delta \frac{\partial u_\delta}{\partial x} + u_\delta^2 \frac{\partial(\rho_\delta (\delta - \delta^*))}{\partial x} = \\ & \rho_\delta u_\delta (\delta - \delta^*) \frac{\partial u_\delta}{\partial x} - \frac{\partial(\rho_\delta u_\delta^2 \theta)}{\partial x} \end{aligned} \quad (\text{C.22})$$

Invoking again the Leibniz rule over the term III

$$\begin{aligned} & \int_0^\delta \frac{\partial \rho w u}{\partial z} dy - u_\delta \int_0^\delta \frac{\partial \rho w}{\partial z} dy = \frac{\partial(\int_0^\delta \rho w u dy)}{\partial z} - \rho_\delta w_\delta u_\delta \frac{\partial \delta}{\partial z} - \\ u_\delta \left(\frac{\partial(\int_0^\delta \rho w dy)}{\partial z} - \rho_\delta w_\delta \frac{\partial \delta}{\partial z} \right) &= \frac{\partial(\int_0^\delta \rho w u dy)}{\partial z} - u_\delta \frac{\partial(\int_0^\delta \rho w dy)}{\partial z} \left(\int_0^\delta \rho u dy \right) \end{aligned} \quad (\text{C.23})$$

Similarly, term IV can also be simplified using Leibniz rule

$$- \int_0^\delta \frac{\partial p}{\partial x} dy = - \frac{\partial(\int_0^\delta p dy)}{\partial x} - p_\delta \frac{\partial \delta}{\partial x} \quad (\text{C.24})$$

Introducing the definition of the pressure boundary layer thickness:

$$p_\delta \delta_p = p_\delta \int_0^\delta \left(1 - \frac{p}{p_\delta} \right) dy = \int_0^\delta (p_\delta - p) dy = p_\delta \delta - \int_0^\delta p dy \quad (\text{C.25})$$

$$\int_0^\delta p dy = p_\delta \delta - p_\delta \delta_p = p_\delta (\delta - \delta_p) \quad (\text{C.26})$$

Term IV is expressed as:

$$-\int_0^\delta \frac{\partial p}{\partial x} dy = -\frac{\partial(p_\delta(\delta - \delta_p))}{\partial x} - p_\delta \frac{\partial \delta}{\partial x} = \frac{(p_\delta(\delta_p - \delta))}{\partial x} - p_\delta \frac{\partial \delta}{\partial x} \quad (\text{C.27})$$

Term V can be integrated across the normal direction taking advantage of the definition of the shear stress and applying the skin friction formulation (C.11)

$$\begin{aligned} \frac{1}{Re} \int_0^\delta \frac{\partial \tau_{xy}}{\partial x} dy &= \frac{1}{Re} \int_0^\delta \left(\rho \mu u \left(\frac{\partial v}{\partial x} + \frac{\partial u}{\partial y} \right) \right) dy = \\ \frac{1}{Re} \left(\mu \left(\frac{\partial v}{\partial x} + \frac{\partial u}{\partial y} \right) \Big|_\delta - \mu \left(\frac{\partial v}{\partial x} + \frac{\partial u}{\partial y} \right) \Big|_0 \right) &= \frac{1}{Re} \left(\mu \left(\frac{\partial v}{\partial x} + \frac{\partial u}{\partial y} \right) \Big|_\delta - \mu \left(\frac{\partial u}{\partial y} \right) \Big|_0 \right) = \\ \frac{1}{Re} \left(\mu \left(\frac{\partial v}{\partial x} + \frac{\partial u}{\partial y} \right) \Big|_\delta - c_f \frac{\rho_\delta u_\delta^2 Re}{2} \right) &= \\ \frac{1}{Re} \mu \left(\frac{\partial v}{\partial x} \Big|_\delta + \frac{\partial u}{\partial y} \Big|_\delta \right) - c_f \frac{\rho_\delta u_\delta^2}{2} & \end{aligned} \quad (\text{C.28})$$

Finally, terms VI and VII are rearranged taking advantage of the Leibniz rule

$$\frac{1}{Re} \int_0^\delta \frac{\tau_{xx}}{\partial x} dy = \frac{1}{Re} \left(\frac{\partial [\int_0^\delta \tau_{xx} dy]}{\partial x} - \tau_{xx} \Big|_\delta \frac{\partial \delta}{\partial x} \right) \quad (\text{C.29})$$

$$\frac{1}{Re} \int_0^\delta \frac{\partial \tau_{xz}}{\partial z} dy = \frac{1}{Re} \left(\frac{\partial [\int_0^\delta \tau_{xz} dy]}{\partial z} - \tau_{xz} \Big|_\delta \frac{\partial \delta}{\partial z} \right) \quad (\text{C.30})$$

Substituting the new definitions of the terms I to VII into C.4 it is reformulated as:

$$\begin{aligned} \rho_\delta (\delta - \delta^*) \left(\frac{\partial u_\delta}{\partial t} + u_\delta \frac{\partial u_\delta}{\partial x} \right) + u_\delta \frac{\partial (\rho_\delta (\delta_\rho - \delta^*))}{\partial t} - \frac{\rho_\delta u_\delta^2 \theta}{\partial x} + \frac{\partial \left(\int_0^\delta \rho u w dy \right)}{\partial z} \\ - u_\delta \frac{\partial \left(\int_0^\delta \rho u w dy \right)}{\partial z} = \frac{\partial (p_\delta (\delta_p - \delta))}{\partial x} - p_\delta \frac{\partial \delta}{\partial x} + \frac{\mu_\delta}{Re} \left(\frac{\partial v}{\partial x} + \frac{\partial u}{\partial y} \right) \Big|_\delta - c_f \frac{\rho_\delta u_\delta^2}{2} \\ + \frac{1}{Re} \left(\frac{\partial}{\partial x} \left[\int_0^\delta \tau_{xx} dy \right] - \tau_{xx} \Big|_\delta \frac{\partial \delta}{\partial x} \right) + \frac{1}{Re} \left(\frac{\partial}{\partial z} \left[\int_0^\delta \tau_{xz} dy \right] - \tau_{xz} \Big|_\delta \frac{\partial \delta}{\partial z} \right) \end{aligned} \quad (\text{C.31})$$

D. INSTRUMENTS CALIBRATION AND UNCERTAINTY EVALUATIONS

D.1 Pressure sensor calibration and drift pressure correction

The pressure readings are obtained with two different Scanivalve pressure scanners, the DSA3217 module with 16 channels and the MPS 4264 module with 64 channels. The DSA modules are sampled at 500 Hz while the MPS unit is sampled at 1 kHz. The pressure sensors are calibrated using the GE Druck DPI 612 pressure regulator. Up to eight different pressure levels are set for each of the modules to obtain the static calibration law. The length of the tubing guiding the pressure reading from the test article or the probe to the Scanivalve modules is minimized to enhance the frequency resolution. As an example the tubings of the wall pressure readings over the hump have a length of 0.1 m, ensuring a frequency response of the hardware of at least 1.5 kHz. The manufacturer uncertainty of each transducer is reported as 0.05 % of the pressure scanner range.

To correct for the sensor drift along the experimental campaign the readings from each one of the transducers are compared during the entire experiment, as depicted in Figure D.1 left. The pressure level prior to the experiment is measured with the pressure regulator, guaranteeing minimal uncertainty on the measurement. Taking the pressure regulator signal as a reference the drift of each one of the transducers is adjusted and the signal is corrected, as depicted in Figure D.1 right. To guarantee the absence of any drift change throughout the experiment the signal from each sensor is again compared to the reference value once the experiment is completed and the test section is at stagnant conditions.

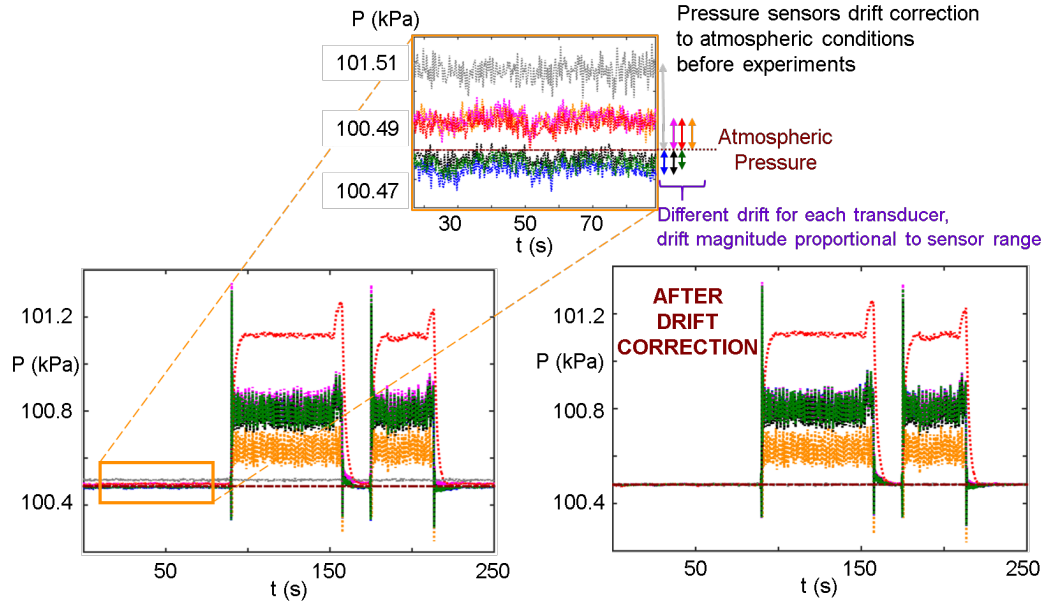


Fig. D.1. Pressure Stability correction

D.2 Hotwire calibration

The hotwire was calibrated in the PETAL Linear Wind tunnel with flat plate assembly and tested at 12 different points. Based on the voltage measured at the Constant Temperature Anemometer outlet and the velocity obtained from the total and static pressure readings, the hotwire operation in each condition was recorded. Following the approach outlined by Yasa et al. [191] the correlation factors n_h and A_h can be obtained evaluating a optimization routine which objective is to minimize the difference between the prescribed correlation and the calibration data set.

$$\frac{V_{CTA}}{OHR \times (R_0 - R_{cable})} = \left(A_h + \left(\frac{\rho_{film} u}{\mu_{film}} \right)^{n_h} \right) \times \left(\frac{T_{wire} + T}{T} \right)^{0.17} (T_{wire} - T_{gas}) \quad (D.1)$$

Where OHR is the over heat ratio applied to the hotwire sensor and the film subscript refers to the air properties evaluated at the film temperature, defined as $T_{film} = (T_0 + T_{wire})/2$.

The turbulence intensity can be computed directly based on the constant temperature anemometer voltage output (V_{CTA}) by

$$Tu = 2 \times 100 \times \frac{\sqrt{(V_{CTA} - \overline{V_{CTA}}) \times (V_{CTA} - \overline{V_{CTA}})}}{n_h \overline{V_{CTA}}^2} \quad (D.2)$$

The dissipative length scale, λ_x indicates the average dimension of the eddies that are responsible for the dissipation of the turbulence energy and can be obtained based on the expression:

$$\lambda_x = \frac{1}{\frac{2\pi^2}{xv^2(xv - \overline{xv})^2} \int_0^\infty f^2 E(f) df} \quad (D.3)$$

Where $E(f)$ is the energy density spectrum.

$$E(f) = \frac{\frac{abs(FFT(V_{CTA}))^2}{\#samples}}{f_{sampling}} \quad (D.4)$$

The integral length scale is equivalent to the measure of the largest eddy size in a turbulent fluid. The axial component of the integral length scale Λ_x :

$$\Lambda_x = xv \int_0^\infty CCF(xv)(t) dt \quad (D.5)$$

Where $CCF(xv)$ is the normal auto correlation function of the axial velocity.

D.3 Thermocouple calibration

The thermocouples produce a voltage proportional to the temperature difference between the reference cold junction and the joint temperature.

$$\Delta V = -S^e(T) \Delta T \quad (D.6)$$

$$V = \int_{T_{ref}}^{T_{sense}} (S_+^e(T) - S_-^e(T)) dT \quad (D.7)$$

$S^e(T)$ is the temperature dependent function, which is a function of the material and the type of joint. Type K thermocouples are selected due to their broad

range of operation and optimal sensitivity in the range of interest of the experimental campaign.

Each one of the thermocouples is individually calibrated using Fluke 9171 metrology well. Each sensor is soaked for at least 1 hour at 8 different temperatures inside of the well. Once the voltage reading and temperature inside of the well reach steady equilibrium both quantities are averaged during windows of 10 minutes. Linear correlation laws are then extracted between the well temperature and the voltage output of the sensor. If the correlation factor of the calibration is smaller than 0.9998 the calibration process is repeated. Figure D.2 represents the calibration points and extracted thermocouple correlation for two different transducers.

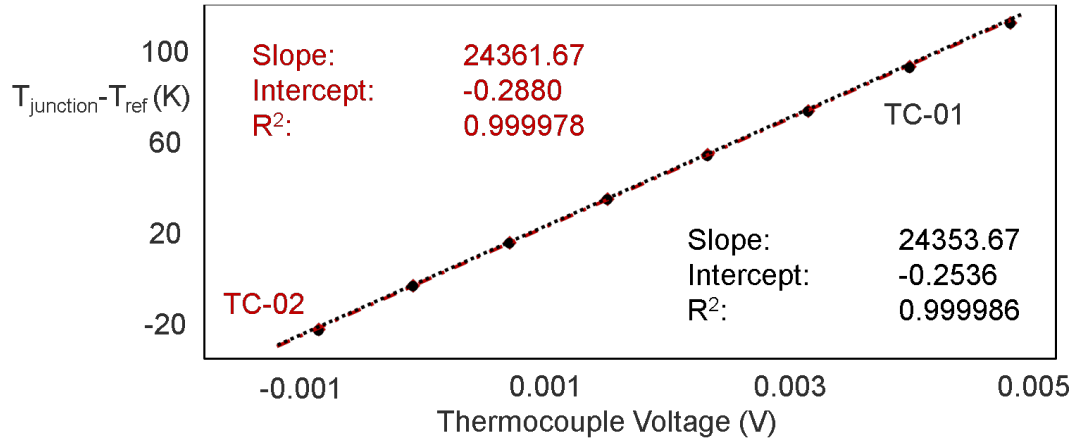


Fig. D.2. TC calibration

The relative temperature uncertainty is then computed as a function of the temperature and measured voltage during the calibration.

$$\frac{\partial T}{T} = \sqrt{\left(\frac{\text{slope} \times \text{voltage}}{T}\right)^2 \left(\left(\frac{\partial \text{slope}}{\text{slope}}\right)^2 + \left(\frac{\partial V}{V}\right)^2\right) + \left(\frac{\text{Intercept}}{T}\right)^2 \left(\frac{\partial \text{Intercept}}{\text{Intercept}}\right)^2} \quad (\text{D.8})$$

Figure D.3 depicts the associated uncertainty on the temperature measurement for each one of the calibrated points for both thermocouples

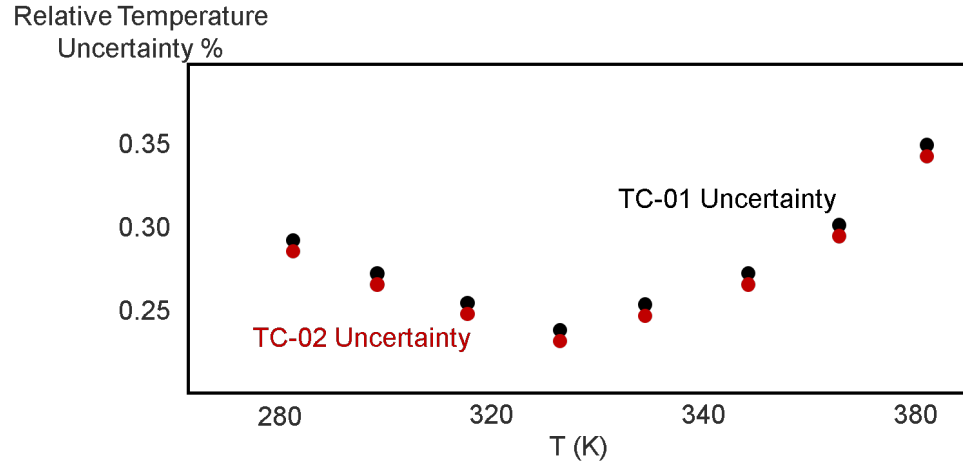


Fig. D.3. Thermocouple Uncertainty

D.4 Heat transfer calculation

D.4.1 One-Dimensional Numerical Heat Flux Approach to Solve Conduction

The classical data reduction technique used for thin-film gauges and wall mounted thermocouples is based on the resolution of the 1D unsteady heat conduction as given in the following equation:

$$\frac{1}{\alpha_t} \frac{\partial T}{\partial t} = \frac{\partial^2 T}{\partial x^2} \quad (\text{D.9})$$

Several techniques have been employed for thin film gauge data processing, consisting on analog circuits [192,193], fast Fourier transform techniques [194], or the numerical solution of the unsteady heat conduction equation in the gauge substrate [195]. These methods rely commonly on two assumptions: the substrate is considered as semi-infinite during the test duration; and the heat conduction occurs in a mono-dimensional manner. The data reduction technique consists on solving the 1D unsteady heat conduction equation imposing as the top boundary condition the temperature history provided by the thin film gauges in the airfoil surface. In this approach,

the bottom boundary condition is tracked in time and used as rear condition for the numerical solver.

Due to the existence of several substrates, an additional boundary condition must be imposed at the interface between each substrate, the heat flux continuity

$$-k_1 \left[\frac{\partial T}{\partial t} \right]_{x=L^-} = -k_2 \left[\frac{\partial T}{\partial t} \right]_{x=L^+} \quad (\text{D.10})$$

Various methodologies have been proposed to account for the presence of multi-layered substrates [192, 196, 197], considering the domain depicted in the Fig. D.4 left. The materials properties are listed in Table D.1.

Table D.1.
Material properties

	Cerakote	Aluminum	Unit
Thickness	0.4	50	mm
Density	1336	2700	kg/m ³
Heat Capacity	990	897	J/(kgK)
Thermal Conductivity	1.3	180	W/(mK)

A CrankNicholson numerical discretization is employed to solve the 1D unsteady heat conduction equation. It provides the temperature field in the substrate at every time step and, subsequently, the wall heat flux at the gauge location. The CrankNickolson method [198] is first-order accurate in space and second-order in time. It is based on the trapezoidal rule, giving second-order convergence in time. For example, in one dimension, if the partial differential equation is $(\partial u / \partial t) = F(u, x, t, (\partial u / \partial x), (\partial^2 u / \partial x^2))$ this method is a combination of the Forward Euler method at n , and the backward Euler method for $n+1$;

$$\frac{u_i^{n+1} - u_i^n}{\Delta t} = 1/2 \left[F_i^{n+1}(u, x, t, (\frac{\partial u}{\partial x}), (\frac{\partial^2 u}{\partial x^2})) + F_i^n(u, x, t, (\frac{\partial u}{\partial x}), (\frac{\partial^2 u}{\partial x^2})) \right] \quad (\text{D.11})$$

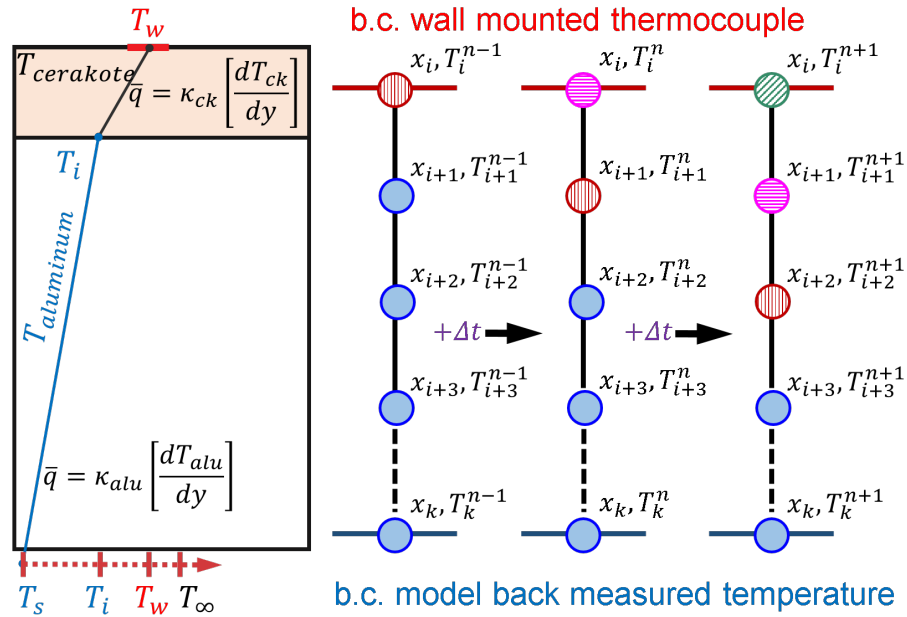


Fig. D.4. (Left) Heat conduction across multilayered substrates, (Right) Heat flux data reduction based on 1D semi-infinite assumption with a Crank Nicolson scheme

It is spatially implicit, hence, in order to solve the system of equations, the whole system must be solved at once due to its non-linearity nature. Based on its time evolution it can be written as an implicit RungeKutta method enhancing its numerical stability. The discretization characteristic of such a scheme is presented on the Fig. 3 right. This method is implemented in a numerical solver in order to post-process the wall temperature data. The tool is verified against the surface convection analytic solution from Incropera and coworkers [199] (Fig. D.5)

$$\frac{T(x, t) - T_i}{T_\infty - T_i} = \operatorname{erfc}\left(\frac{x}{2\sqrt{\alpha_t t}}\right) - \left[\exp\left(\frac{hx}{k} + \frac{h^2 \alpha_t t}{k^2}\right) \right] \left[\operatorname{erfc}\left(\frac{x}{2\sqrt{\alpha_t t}} + \frac{h\sqrt{\alpha_t t}}{k}\right) \right] \quad (\text{D.12})$$

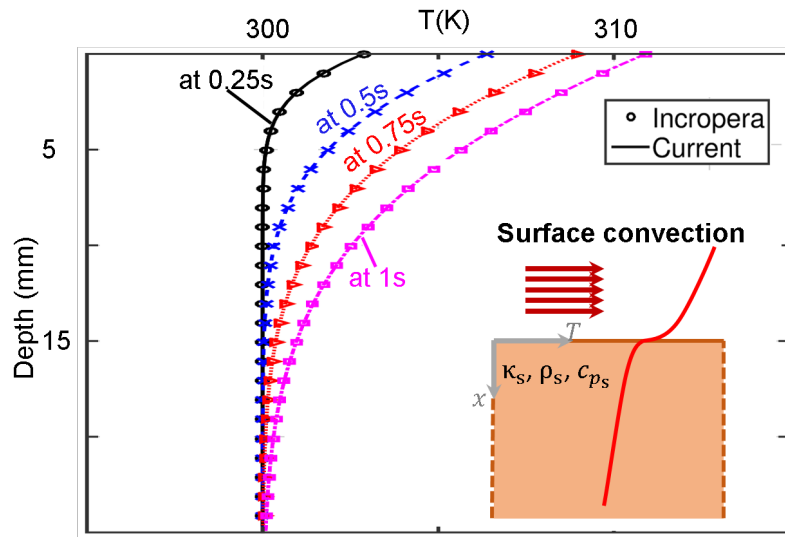


Fig. D.5. Validation of the code developed to solve the transient heat transfer

D.4.2 Adiabatic Convective Heat Transfer Coefficient

Given the substrate temporal evolution, the local convective heat transfer coefficient can be directly estimated. Prior studies proposed several approaches to compute the heat transfer coefficient in the quest for more accurate heat flux description. Moffat [200] and Popp et al. [201] introduced a method based on the definition of the adiabatic wall temperature. It consists of acquiring the wall temperature value, which results on null heat transfer between the fluid and the solid. This method was developed based on the realization of several experiments at the same aerothermal conditions, modifying only the test article wall temperature. As depicted in Fig. D.6, the heat transfer is represented against the wall temperature. As discussed by Lavagnoli et al. [202], the heat flux could be exponentially related with the adiabatic wall temperature and the temperature difference, Eq. D.13, albeit considering experimental window restrictions and the sensitivity of this method, the uncertainty results higher than the expected accuracy.¹

¹Material Published on Experimental Characterization of the Vane Heat Flux Under Pulsating Trailing Edge Blowing, J. Turbomachinery 139(6),2017

$$\bar{q} = h_{aw} \left(\frac{T_w}{T_{aw}} \right)^n (T_{aw} - T_w) \quad (\text{D.13})$$

The process could be similarly described making use of the Newton cooling law Eq. D.14, being the adiabatic wall temperature Refs. [203] [204].

$$\bar{q} = h_{aw}(T_{aw} - T_w) \quad (\text{D.14})$$

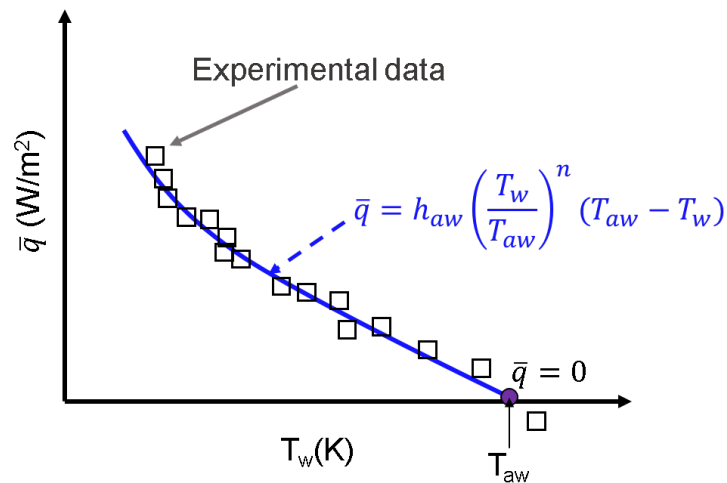


Fig. D.6. Heat transfer coefficient computation based on heat flux data and adiabatic wall temperature definition

Based on the total pressure and temperature evolution, the test duration is determined by the total pressure plateau and the total temperature steady behavior. The maximum oscillation of the free-stream temperature based on a root-mean-square deviation is limited to 2%, in order to avoid the effect of sudden wall temperature variations on the heat flux reduction process.

Applying the described methodology, the heat flux is represented against the wall temperature. Then making use of the adiabatic wall temperature definition, the adiabatic heat transfer coefficient is extracted.

The inverted C shape of the heat flux versus wall temperature (Fig. D.7 right) representation is due to the decay of the free-stream temperature by the end of the

experiment. The variations of the absolute temperature lead to sudden variation on the wall temperature. If the wall temperature is suddenly reduced and immediately raised up, it is reflected into a minor loop on the q versus T_w representation (Fig. D.7 right). Based on the high amplitude noise of the free-stream temperature and the consequent effect on the wall temperature evolution, the extraction of the heat transfer coefficient with polynomial fits results unfeasible. Additional attempts to improve the calculation of the heat transfer coefficient have been rejected due to its handicap to capture a realistic value during the blowdown. In order to compute the heat transfer coefficient over reasonable test windows a set of criteria are defined. This procedure was automatically applied to all the tests. The criteria consists on:

- test start, based on T_0 raise
- test end, based on T_0 sudden decay
- root-mean-square deviation (T_0) $< 2\%$ from down-sampled signal
- positive slope of the wall temperature
- negative slope of the heat flux
- minimum window size of 5 ms

Once all this criteria are met, the slope and intercept to the adiabatic heat flux condition are retrieved and hence the adiabatic heat transfer coefficient and adiabatic wall temperature are identified.

D.5 Uncertainty Evaluation

In order to quantify the uncertainty of the measurements all primary variables used in their derivation factors must be taken into account. The main sources of uncertainty in the methodology are summarized in Table D.2. All error evaluations are given at 95% confidence level.

The absolute uncertainty of each derived quantity is estimated based on the variable mean value and impact of the uncertainty of each one of the prime factors used

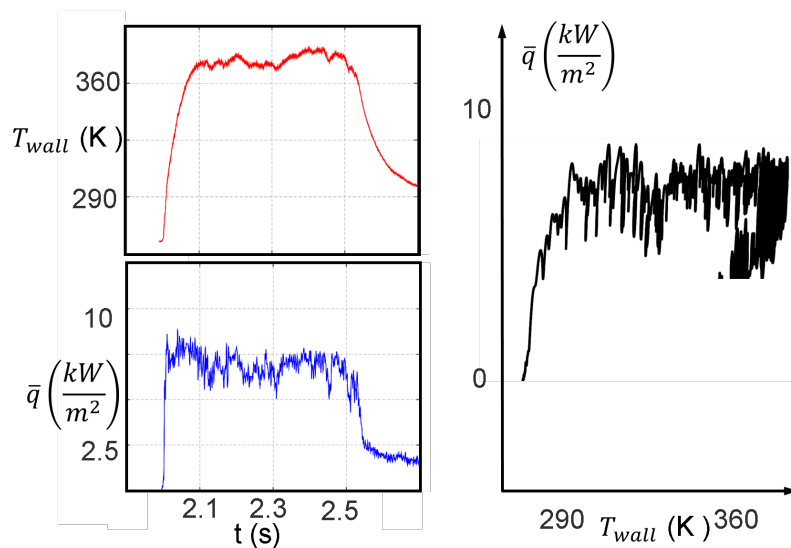


Fig. D.7. Methodology application

to derive that quantity. For example, Table D.3 represents the Venturi mass-flow uncertainty. The mass-flow through the critical Venturi depends only on 3 prime variables: total pressure, total temperature and discharge coefficient (obtained from Venturi calibration). Based on the mean value for each one of this quantities the mean mass-flow is obtained. Then additional evaluations of the massflow computation are repeated including the uncertainty of each one of the prime variables. A mass-flow derivation considering the mean value of the total pressure plus its uncertainty is evaluated keeping the other quantities at its mean value. The outcome of that evaluation reflects the mass-flow uncertainty associated to the total pressure uncertainty reading. The same procedure is repeated for each one of the prime variables and the global uncertainty is the square root of the sum of squares of the individuals uncertainties. Finally, the sensitivity of the derived variable to each one of the independent variables can also be obtained when dividing the outcome variation by the original independent absolute uncertainty. Similar procedures are followed for the uncertainty derivation on Reynolds number, Table D.4; flow velocity derived from P_0 , T_0 and P ,

Table D.5; hotwire flow velocity, Table D.8; heat flux, Table D.9; and heat transfer coefficient, Table D.10.

Table D.2.
Sensors Uncertainty

Variable/Sensor	Uncertainty	Unit
T_0 Piping	1	K
P_0 Venturi (Druck unit)	13800	Pa
P_0 Venturi (DSA unit)	1723	Pa
P_0 Test Section (MPS unit)	50	Pa
T_0 Test Section	0.3 %	K
cf Venturi Calibration	0.0178	(-)
Voltage HotWire	$1e^{-4}$	K
α HotWire	0.001	(-)

Table D.3.
Massflow Uncertainty

Quantity	Mean Value	Units	Absolute Uncertainty	Uncertainty % mean	Uncertainty with uncertainty	Massflow %	Δ Massflow %	Sensitivity
P_0	626328	Pa	1723	0.28	1.52	0.28	0.28	100.10
T_0	270	K	1	0.37	1.51	0.19	0.19	50.00
cf	1		0.0178	1.78	1.54	1.78	1.78	100.00
Massflow	1.51	kg/s				Massflow Uncertainty %	1.50	

Table D.4.
Reynolds Uncertainty

Quantity	Mean Value	Units	Absolute Uncertainty	Uncertainty % mean	Reynolds with uncertainty	Δ Reynolds %	Sensitivity
P_0	101885	Pa	50	0.05	1148340	4.38	8922
P	101325	Pa	50	0.05	1050066	4.55	9228
T_0	275	K	1	0.36	1095043	0.47	128.1
Reynolds	1100168				Reynolds Uncertainty %	3.07	

Table D.5.
Stream wise velocity Uncertainty

Quantity	Mean Value	Units	Absolute Uncertainty	Uncertainty % mean	xv with uncertainty	Δ xv %	Sensitivity
P_0	101885	Pa	50	0.05	30.11	2.12	4325
P	101325	Pa	50	0.05	28.96	1.78	3602
T_0	275	K	1	0.36	29.54	0.18	49.95
xv	29.48	m/s			xv Uncertainty %	2.77	

Table D.6.
Hotwire Calibration A factor

Quantity	Mean	Units	Absolute	Uncertainty	A_h factor	ΔA_h factor %	Sensitivity
	Value		Uncertainty	% mean	with uncertainty		
P_0	100598	Pa	50	0.05	$5.11e^{-7}$	2.64	5218
P	99674	Pa	50	0.05	$5.30e^{-7}$	2.71	5406
T_0	283.62	K	1	0.36	$5.21e^{-7}$	0.12	0.69
<i>WireResistance</i>	13.10	Ohm	0.01	0.08	$5.20e^{-7}$	0.08	101.27
α_h	$9e^{-4}$	1/K	$5e^{-5}$	5.56	$5.36e^{-7}$	0.08	1.39
Voltage	0.72	V	$1e^{-3}$	0.14	$5.20e^{-7}$	0.13	90.23
A_h factor	$5.2e^{-7}$	m/s			A_h factor Uncertainty %	3.79	

Table D.7.
Hotwire Calibration n factor

Quantity	Mean	Units	Absolute	Uncertainty	Uncertainty	n_h factor	Δn_h factor %	Sensitivity
	Value		Uncertainty	% mean	with uncertainty			
P_0	100598	Pa	50	0.05	0.71	0.26	532.38	
P	99674	Pa	50	0.05	0.71	0.26	527.04	
T_0	283.62	K	1	0.36	0.71	0.00	0.01	
<i>WireResistance</i>	13.10	Ohm	0.01	0.08	0.71	0.00	0.13	
α_h	$9e^{-4}$	1/K	$5e^{-5}$	5.56	0.71	0.00	0	
Voltage	0.72	V	$1e^{-3}$	0.14	0.71	0.01	7.69	
n_h factor	0.71	m/s			n_h factor	Uncertainty %	0.37	

Table D.8.
U from Hotwire Calibration

Quantity	Mean	Units	Absolute	Uncertainty	xv	Δ xv %	Sensitivity
	Value		Uncertainty	% mean	with uncertainty		
P_0	100598	Pa	50	0.05	33.48	0.00	0
P	99674	Pa	50	0.05	33.47	0.03	59.98
T_0	283.62	K	1	0.36	33.60	0.37	2.09
<i>Wire Resistance</i>	13.10	Ohm	0.01	0.08	33.44	0.11	140.62
α_h	$9e^{-4}$	1/K	$5e^{-5}$	5.56	34.93	0.11	1.93
Voltage	0.72	V	$1e^{-3}$	0.14	33.48	0.00	21.83
n_h factor	0.71		$2.6e^{-3}$	0.37	31.79	5.04	131.86
A_h factor	$5.2e^{-7}$		$1.97e^{-8}$	3.79	31.77	5.11	134.93
xv	33.48	m/s			xv Uncertainty %	7.19	

Table D.9.
Heat Flux Calibration

Quantity	Mean	Units	Absolute	Uncertainty	Heat Flux factor	Δ Heat	Sensitivity
	Value		Uncertainty	% mean	with uncertainty	Flux %	
Al thickness	0.05	m	$2e-4$	0.4	5745.44	0.01	2.86
Al κ	180	W/(mK)	7.2	4	5758.31	0.21	5.31
Al ρ	2700	kg/(m ³)	100	3.70	5755.54	0.16	4.43
Al c_p	897	J/(kgK)	10	1.11	5748.73	0.05	4.10
Cerakote thickness	$4e-4$	m	$5e-5$	12.50	6214.41	8.15	65.20
Cerakote κ	1.3	W/(mK)	0.1	7.69	6031.68	4.97	64.56
Cerakote ρ	1335.98	kg/(m ³)	45	3.37	5751.24	0.09	2.66
Cerakote c_p	990	J/(kgK)	25	2.53	5750.12	0.07	2.77
T_{wall}	340	K	1.5	0.44	5750.12	0.07	15.88
Heat Flux	5746.1	m/s			Heat Flux Uncertainty %	9.55	

Table D.10.
Adiabatic Heat Transfer Coefficient Calibration

Quantity	Mean Value	Units	Absolute Uncertainty	Uncertainty % mean	htc_{aw} factor with uncertainty	Δhtc_{aw} %	Sensitivity
Al thickness	0.05	m	$2e-4$	0.4	83.45	0.01	2.86
Al κ	180	W/(mK)	7.2	4	83.63	0.21	5.31
Al ρ	2700	kg/(m ³)	100	3.70	83.59	0.16	4.43
Al c_p	897	J/(kgK)	10	1.11	83.49	0.05	4.10
Cerakote thickness	$4e-4$	m	$5e-5$	12.50	90.26	8.15	65.20
Cerakote κ	1.3	W/(mK)	0.1	7.69	87.60	4.97	64.56
Cerakote ρ	1335.98	kg/(m ³)	45	3.37	83.53	0.09	2.66
Cerakote c_p	990	J/(kgK)	25	2.53	83.51	0.07	2.77
T_{wall}	340	K	1.5	0.44	81.41	2.45	556.42
htc_{aw}	83.45	m/s			htc_{aw} Uncertainty %	9.86	

VITA

VITA

Jorge Saavedra is currently in the 4th year of his doctoral studies at the Mechanical Engineering School of Purdue University. In December 2018, he will graduate with a focus in unsteady flow aerodynamics. He is an aerospace engineer by the Universidad Politecnica de Valencia. He is also a Research Master from the von Karman Institute for Fluid Mechanics in the Turbomachinery and Propulsion department . Mr. Saavedra is a member of a number of professional and student organizations including the American Society of Mechanical Engineers and the American Institute of Aeronautics and Astronautics.

During the past four years, Jorge has studied the influence of mean flow variations on the performance of aero-mechanical devices. He has analyzed the influence of sudden flow discharges and oscillations in subsonic and supersonic operations on a variety of test articles through computational and experimental resources. In the short term, he looks forward to apply the knowledge on the near wall flow evolution under mean flow transients to improve the performance and extend the operational envelope of compact heat exchangers and turbomachinery.

Outside of academics, Jorge is involved in Athletic activities. He spent 3 years serving at different roles in the Engineerig Athelic Club at Universidad Politecnica de Valencia and is one of the founders of the Engineers for Run athletic club in Lafayette. Jorge enjoys reading and studying military history books focused on Second World War troops deployment and the rapid growth of military aviation through the fist and second world war.

Education

Purdue University, West Lafayette, IN, USA Expected November 2018 Ph. D. Mechanical Engineering Title: Understanding the dynamic scales behind the flow establishment and the flow separation-reattachment process

Von Karman Institute for Fluid Dynamics, Rhode-Saint-Genese, Belgium 2014
 Research Master on Fluid Dynamics, Turbomachinery and Propulsion Title: Impli-
 cations of boundary layer establishment on heat transfer measurements Graduated
 with honors

Universidad Politecnica de Valencia, Valencia, Spain 2013 Combined M.S. and
 B.S, Aerospace Engineer Title: Development of a centrifugal compressor performance
 prediction model

Work Experience

2015 Graduate Research Assistant, Purdue Experimental Turbine Aero-thermal
 Laboratory (PETAL), Zucrow Laboratories, Purdue University Research Advisor:
 Guillermo Paniagua Management and control of short duration wind tunnel experi-
 ments. Analyzed the flow starting and flow separation-reattachment phenomena on
 low pressure turbine blades based on detailed numerical simulations.

Sept, 2018 Graduate Research Assistant, Visiting Collaborator, von Karman In-
 stitute for Fluid Mechanics Research Advisor: Olivier Chazot Start-up analysis of a
 hypersonic nozzle for short duration testing

2014 2015 Visiting Scholar, Zucrow Laboratories, Purdue University Research
 Advisor: Guillermo Paniagua Design, development and performance analysis of a
 transient wind tunnel for heat transfer and fundamental flow experiments.

2014 Graduate Researcher, von Karman Institute for Fluid Dynamics, Aerospace
 Department Research Advisor: Bayindir H. Saracoglu Heat transfer characterization
 of a transonic turbine vane based on wall temperature evolution during short duration
 experiments

2013 2014 Graduate Research Assistant, von Karman Institute for Fluid Dynam-
 ics, Turbomachinery and Propulsion Department Research Advisor: Guillermo Pani-
 agua and Sergio Lavagnoli Numerical analysis of the momentum and thermal bound-
 ary layer development during short duration wind tunnel experiments.

2012 2013 Graduate Research Assistant, Departamento de Maquinas y Motores
 Termicos (CMT), Universidad Politecnica de Valencia Research Advisor: Andres. O.

Tiseira Development of a simplified fluid dynamic code for the performance analysis of centrifugal compressors

2011 2012 Graduate Research Assistant, Departamento de Maquinas y Motores Termicos (CMT), Universidad Politecnica de Valencia Research Advisor: Pedro Piqueras Performance analysis of an axial turbine stage based on 3D Unsteady Reynolds Average Numerical Simulations.

Related Coursework

Multidisciplinary Design Optimization, Introduction to Measurement Techniques in Fluid Dynamics, Flow in Turbomachines, Advanced Course of Turbines, Aircrafts Design, Astronautics and Space Engineering, Aerospace Materials, Turbomachinery and Aeroacoustics, Turbulence Theory and Numerical Simulation, Advanced Heat Transfer

Technical Skills

- CFD (ANSYS, CFD++, Numeca, COMSOL)
- Programming (Matlab ,C++)
- FEA (ANSYS, COMSOL)
- CAD (Autodesk Inventor)
- Optimization (Matalb, Excel)
- Engine Modeling (GasTurb, GSP, TMATS) LabVIEW

Advising Experience

2017 Teaching Assistant for Uncertainty Quantification in Fluid Dynamics, Purdue University and von Karman Institute for Fluid Dynamics

2016 Student Research Advisor, Maurice J. Zucrow Laboratories, Purdue University. Advised three graduate, students on their dissertation: Application of high frequency temperature measurements for heat flux characterization, Development of high resolution Schlieren visualization for unsteady flow visualization and High frequency wall pressure characterization to retrieve unsteady blade loading

2015 Occasional lecturer, Principles of Turbomachinery and Air Breathing Propulsion, Mechanical Engineering, Purdue University Lecture introductory seminars to engine performance software for the students and provide support and assistance on their semester project.

2015 Student Research Advisor, Maurice J. Zucrow Laboratories, Purdue University. Advised two undergraduate students on their bachelor thesis work: Conception of a hypersonic wind tunnel for reentry analysis; Turbine stage numerical analysis for Biot number replication on short duration experiments. Guided a graduate student on his masters thesis: Implementation of Schlieren imaging techniques for blow-down wind tunnel experiments.

2013 2014 Student Research Advisor, von Karman Institute for Fluid Dynamics. Advised bachelor students on their research work: Lecture introductory seminars and provide assistance for different CFD solvers, preprocessing and post-processing tools: Gambit, ICEM, Ansys Workbench, Fluent, CFD++, COMSOL, OpenFoam and ParaView

2012 2013 Student Advisor, Departamento de Maquinas y Motores Termicos (CMT), Universidad Politecnica de Valencia. Advised two undergraduate students on their bachelor thesis work: Parametric analysis for centrifugal compressor and turbine predictive models development.

Honors and Awards

2018 ASME International Gas Turbine Institute Young Engineer Turbo Expo Participation Award

2016 ASME International Gas Turbine Institute Young Engineer Turbo Expo Participation Award

2013 NATO Fellowship, von Karman Institute for Fluid Dynamics research scholarship

Service and Leadership

2018 Reviewer, International Journal of Astronautics and Aeronautical Engineering

2017 Reviewer, Journal of Energies
 2017,2018 Reviewer, Journal of Fluid Mechanics
 2015 Reviewer, ASME Turbomachinery Technical Conference and Exposition
 2015 Reviewer, Journal of Heat transfer
 2016 Reviewer, ENIEF 2016 XXII Congress
 2015 2016 Reviewer, AIAA SciTech Forum and Exposition
 2011 2013 Vice President, Aerospace and Mechanical Engineers Graduate Athletes Association, Universidad Politecnica de Valencia
 2010 2011 Treasurer, Aerospace and Mechanical Engineers Graduate Athletes Association, Universidad Politecnica de Valencia

Publications

Peer-reviewed Journal Publications

Saavedra, J., Paniagua, G., Saracoglu, B. H. Experimental characterization of the vane heat flux under pulsating trailing edge blowing; Journal of Turbomachinery November 2016, doi:10.1115/1.4035211

Saavedra, J., Paniagua, G., Transient Performance of separated flows: characterization and active flow control , Journal of Engineering for Gas Turbine and Power, September 2018 doi: 10.1115/1.4040685

Saavedra, J., Paniagua, G., Chazot, O. Thermal boundary layer response to periodic fluctuations, Journal of Engineering for Gas Turbine and Power, Expected November 2018

Saavedra, J., Paniagua, G., Lavagnoli, S., 2017 On the transient response of the turbulent boundary layer inception in compressible flows, Journal of Fluid Mechanics, July 2018, doi:10.1017/jfm.2018.502

Sousa, J., Paniagua, G., Saavedra, J., 2017 Aerodynamic response of internal passages to pulsating inlet supersonic conditions, Computer and Fluids, March 2017, DOI: 10.1016/j.compfluid.2017.03.005

Paniagua, G., Gonzalez Cuadrado, D., Saavedra, J., Andreoli, V., Lawrence, D., Meyer, T., Meyer, S., Design of Purdue Experimental Turbine Aero-thermal Labora-

tory for optical and surface Aero-Thermal measurements Journal of Engineering for Gas Turbine and Power, Expected July 2018

Contributions to books

Saavedra, J., Paniagua, G., Chazot, O. Analysis of the mean flow unsteadiness impact on the near wall flow region; von Karman Institute Doctorate symposium April 2018,

Peer-reviewed Conference Publications

Paniagua, G., Gonzalez Cuadrado, D., Saavedra, J., Andreoli, V., Lawrence, D., Meyer, T., Meyer, S., Design of Purdue Experimental Turbine Aero-thermal Laboratory for optical and surface Aero-Thermal measurements Proc. ASME Turbo Expo 2016: Turbomachinery Technical Conference and Exposition, American Society of Mechanical Engineers, pp. V006T005A025, doi:10.1115/GT2016-58101

Saavedra, J., Paniagua, G., Saracoglu, B. H. Experimental characterization of the vane heat flux under pulsating trailing edge blowing; Proc. ASME Turbo Expo 2016: Turbomachinery Technical Conference and Exposition, American Society of Mechanical Engineers

Saavedra, J., Paniagua, G., Transient Performance of separated flows: characterization and active flow control Proc. ASME Turbo Expo 2018: Turbomachinery Technical Conference and Exposition, American Society of Mechanical Engineers

Saavedra, J., Paniagua, G., Chazot, O., Thermal boundary layer response to periodic fluctuations Proc. ASME Turbo Expo 2018: Turbomachinery Technical Conference and Exposition, American Society of Mechanical Engineers,

Conference Publications

Saavedra, J., Lavagnoli, S., Paniagua, G., 2015, Implications of boundary layer establishment on convective heat transfer experiments. Proceedings of the AIAA Science and technology Forum and Exposition. AIAA 2015-0258. DOI: 10.2514/6.2015-0258. eISBN: 978-1-62410-343-8. Kissimmee, USA. January

Braun, J., Saavedra, J., Paniagua, G. Evaluation of the unsteadiness across nozzles downstream of rotating detonator combustors; J. Braun, J. Saavedra, G. Paniagua;

55th AIAA Aerospace Sciences Meeting, AIAA SciTech Forum, (AIAA 2017-1063)
<http://dx.doi.org/10.2514/6.2017-1063>

Saavedra, J., Paniagua, G., Flow conditioning of subsonic and supersonic blow-down wind tunnels, Proceedings of the International Symposium of Air Breathing Engines 2017. Manchester, UK. ISABE 2017-22632.

G. Cuadrado, D., Saavedra, J., Andreoli, V., Paniagua G., Experimental calibration of a high speed blowdown wind tunnel, Proceedings of the International Symposium of Air Breathing Engines 2017. Manchester, UK. ISABE 2017-22636.

Padilla, I., Saavedra, J., Paniagua, G., Pinna, F., Analysis of the boundary layer stability to assess flow separation control capability in low pressure turbines, 7th European Conference on Computation Fluid Dynamics (ECFD 7) (ECCM-ECFD Conference).

Fisher, J., Saavedra, J., Paniagua, G., Meyer, T., Slipchenko, M., Development of high frequency particle image velocimetry to characterize separation regions downstream of a hump, XXIV Biennial Symposium on Measuring Techniques in Turbomachinery, Transonic and Supersonic Flow in Cascades and Turbomachines, (Prague August 2018).

Aye-Addo, N., Long, N., Paniagua, G., Saavedra, J., Development of laser lifetime pressure sensitive paint (PSP) technique for unsteady measurements, XXIV Biennial Symposium on Measuring Techniques in Turbomachinery, Transonic and Supersonic Flow in Cascades and Turbomachines, (Prague August 2018).

Conference Presentations

Experimental characterization of the vane heat flux under pulsating trailing edge blowing; Saavedra, J., Paniagua, G., Saracoglu, B. H.; Journal of Turbomachinery, Proc. ASME Turbo Expo 2016: Turbomachinery Technical Conference and Exposition, American Society of Mechanical Engineers ISBN: 978-0-7918-4978-1

Analysis of the mean flow unsteadiness impact on the near wall flow region; Saavedra, J.; von Karman Institute Ph.D, Symposium 2018, Sint Genesius-Rode, Belgium March5-7

Thermal boundary layer response to periodic fluctuations; Saavedra, J., Paniagua, G.; Computational Science and Engineering Student Conference, April 14th 2017, Purdue University

Memberships

- ASME Student member since 2014
- AIAA Student member since 2015